UNIWERSYTET MARII CURIE-SKŁODOWSKIEJ
W LUBLINIE

Wydział Chemii
Instytut Nauk Chemicznych

mgr Alicja Bosacka

BADANIA PROCESÓW ADSORPCYJNYCH I PRZEMIAN FAZOWYCH ZACHODZĄCYCH W PORACH MATERIAŁÓW ZRÓŻNICOWANYCH STRUKTURALNIE I CHEMICZNIE

RESEARCH ON ADSORPTION PROCESSES AND PHASE TRANSFORMATIONS OCCURRING IN THE PORES OF STRUCTURALLY AND CHEMICALLY DIFFERENTIATED MATERIALS

Rozprawa doktorska
wykonana w Katedrze Chemii Fizycznej
pod kierunkiem prof. dr hab. Anny Deryło-Marczewskiej
oraz dr Małgorzaty Zienkiewicz-Strzałki

Lublin 2023

Podziękowania

Paniom Promotor Prof. dr hab. Annie Deryło-Marczewskiej oraz dr Małgorzacie Zienkiewicz-Strzałce pragnę złożyć najserdeczniejsze podziękowania za merytoryczne rady, pomoc na każdym etapie pracy i ogrom życzliwości, której doświadczyłam. Jestem bardzo wdzięczna za wsparcie.

Dziękuję także współautorom artykułów oraz pozostałych prac naukowych za możliwość współpracy i wsparcie merytoryczne.

SPIS TREŚCI

1. Spis artykułów wchodzących w skład autoreferatu rozprawy doktorskiej

Lista artykułów stanowiących spójny tematycznie cykl rozprawy doktorskiej znajduje się w Tabeli 1.

Tabela 1. Spis artykułów wchodzących w skład rozprawy doktorskiej.

Skrót	Autorzy	Tytuł artykułu	Czasopismo	IF	MEiN
D1	Alicja Bosacka, Małgorzata Zienkiewicz-Strzałka, Anna Deryło-Marczewska, Małgorzata Wasilewska, Beata Podkościelna	Physicochemical and Adsorption Characteristics of Divinylbenzene-co-Triethoxyvinylsilane Microspheres as Materials for the Removal of Organic Compounds	Molecules	4,927	140
D2	Alicja Bosacka, Małgorzata Zienkiewicz-Strzałka, Anna Deryło-Marczewska, Agnieszka Chrzanowska, Małgorzata Wasilewska, Dariusz Sternik	Physicochemical, structural, and adsorption properties of chemically and thermally modified activated carbons	Colloids and Surfaces A: Physicochemical and Engineering Aspects	5,518	70
D3	Mariia Galaburda, Alicja Bosacka, Dariusz Sternik, Viktor Bogatyrov, Olena Oranska, Volodymyr Gun'ko Anna Deryło-Marczewska	Development, Synthesis and Characterization of Tannin/Bentonite-Derived Biochar for Water and Wastewater Treatment from Methylene Blue	Water	3,530	100

D4	Mariia Galaburda, Alicja Bosacka, Dariusz Sternik, Olena Oranska, Mykola Borysenko, Volodymyr Gun’ko, Anna Derylo-Marczewska	Physicochemical and Sorption Characteristics of Carbon Biochars Based on Lignin and Industrial Waste Magnetic Iron Dust	Water	3,530	100
D5	Alicja Bosacka, Małgorzata Zienkiewicz-Strzałka, Anna Deryło Marczewska, Małgorzata Sliwinska-Bartkowiak, Angelina Sterczyńska, Konrad Rotnicki, Dariusz Sternik	The influence of chemical and thermal modifications of ordered mesoporous carbon on the melting processes of water confined in pores	Microporous and Mesoporous Materials	5,876	100

Sumaryczny IF: 23,381

Łącza liczba punktów MEiN: 510

2. Streszczenie w języku polskim

Niniejsza rozprawa doktorska *Badania procesów adsorpcyjnych i przemian fazowych zachodzących w porach materiałów zróżnicowanych strukturalnie i chemicznie* stanowi cykl pięciu artykułów [**D1-D5**] i została przedstawiona w postaci autoreferatu. Celem rozprawy doktorskiej było zaprojektowanie, otrzymanie oraz analiza materiałów pod względem charakterystyk teksturalnych, morfologicznych i powierzchniowych oraz przebadanie wpływu ich właściwości na procesy adsorpcyjne i przemiany fazowe zachodzące w ograniczonych przestrzeniach porów.

Ze względu na bardzo szerokie wykorzystanie materiałów porowatych w technologii, nauce, ochronie środowiska, życiu codziennym prowadzi się badania nad otrzymywaniem nowych typów materiałów o właściwościach dopasowanych do konkretnych zastosowań. Z drugiej strony konkretne aplikacje wymagają szerszych badań nad procesami zachodzącymi w ograniczonych przestrzeniach porów, które mogą przebiegać odmiennie od procesów na powierzchniach płaskich i w fazach objętościowych. Z tego względu w literaturze naukowej tematyka dotycząca adsorbentów oraz procesów adsorpcyjnych jest szeroko reprezentowana. Stosunkowo nowy nurt badań dotyczy przemian fazowych zachodzących w mikro- i mezoporach, w tym procesów topnienia/krzepnięcia, co związane jest z wykorzystaniem materiałów porowatych w szerokich zakresach temperatury.

Problem zanieczyszczenia ścieków przemysłowych przez trudnorozpuszczalne w wodzie substancje organiczne (pochodne benzenu oraz syntetyczne barwniki, substancje niebezpieczne dla środowiska oraz zdrowia ludzi i zwierząt) pogłębia się, dlatego istotnie jest poszukiwanie nowych rozwiązań w uzdatnianiu wód z tych trudnych do usunięcia substancji z układów wodnych. Aspekt ten jest tym bardziej istotny, że zasoby wodne na świecie wyczerpują się. Jednym z najczęściej stosowanych sposobów oczyszczania wód i ścieków jest adsorpcja różnych substancji ze względu na prostotę jej zastosowania w porównaniu z innymi bardziej wymagającymi technikami oraz możliwość wyboru różnorodnych adsorbentów. Należy jednak podkreślić, że mimo iż na rynku dostępne są różne adsorbenty (zeolity, węgle, materiały krzemionkowe), nowe materiały o unikatowych właściwościach są stale poszukiwane i projektowane ze względu na ich zapotrzebowanie do specyficznych zastosowań (poszukiwane są adsorbenty efektywne, selektywne, odporne na działanie czynników chemicznych, fizycznych, czy biologicznych).

Kolejnym ważnym etapem pracy było badanie procesów topnienia/krzepnięcia w porach mezoporowatych węgli o zróżnicowanej chemii powierzchni. Ogólnie wiedza dotycząca procesów topnienia i krzepnięcia w porach jest istotna ze względu na możliwość jej wykorzystania do projektowania materiałów z praktycznym wykorzystaniem (adsorbenty, katalizatory, czy nanomateriały).

Szczególną uwagę zwrócono na możliwość użycia surowców naturalnych lub odpadów przemysłowych do syntezy materiałów ze względu na dbałość o środowisko naturalne.

W niniejszej rozprawie doktorskiej rozważono różne typy adsorbentów, które różniły się pod względem strukturalnym i chemicznym: organiczno-nieorganiczne materiały polimerowe na bazie dywinylobenzenu i trietoksywinylosilanu (adsorbenty **M1**), modyfikowane chemicznie i termicznie węgle aktywne (adsorbenty **M2**), organiczno-nieorganiczne materiały węglowe na bazie taniny i bentonitu (adsorbenty **M3**), organiczno-nieorganiczne materiały węglowe na bazie induliny i pyłu żelazowego (adsorbenty **M4**), oraz mezoporowate modyfikowane chemicznie i termicznie węgle (materiały **M5**).

W przypadku adsorbentów **M1, M3, M4** rozważono wpływ składu mieszaniny reakcyjnej natomiast dla adsorbentów **M2** wpływ zastosowanych modyfikacji na właściwości fizykochemiczne (teksturalne, morfologiczne, chemiczne) oraz adsorpcyjne. Otrzymane adsorbenty scharakteryzowano z wykorzystaniem szeregu metod badawczych: niskotemperaturowej adsorpcji-desorpcji azotu, mikroskopii elektronowej, dyfrakcji rentgenowskiej, niskokątowego rozpraszania promieni rentgenowskich, spektroskopii FT-IR/ATR, spektroskopii

Ramana, rentgenowskiej spektroskopii fotoelektronów, analizy termicznej sprzężonej ze spektrometrią mas. Właściwości adsorpcyjne otrzymanych materiałów względem pochodnych benzenu – fenolu, 4-nitrofenolu oraz nitrobenznenu lub barwnika (błękitu metylenowego), adsorbatów różniących się właściwościami (rozpuszczalnością/hydrofobowością, zdolnością do dysocjacji, wielkością cząsteczki, grupami funkcyjnymi), przebadano pod kątem analizy równowagi lub kinetyki adsorpcji.

Badane materiały wykazywały zróżnicowane fizykochemiczne właściwości (teksturalne, morfologiczne, chemiczne), które wpływały na efektywność adsorpcji. Otrzymano adsorbenty działające efektywnie i selektywnie w roztworach wodnych.

W pracy **D1** wykazano, że trietoksywinylosilan (TEVS) silnie rozwijał strukturę porowatą organiczno-nieorganicznych materiałów na bazie dywinylobenzenu (DVB). Ponadto, wykazano zróżnicowaną efektywność adsorpcji, która zależała od hydrofobowości adsorbatu (nitrobenzen>4-nitrofenol>fenol) dla wszystkich badanych układów (DVB:TEVS = 1:2, 1:1, 2:1). Badania kinetyki adsorpcji ujawniły wpływ takich czynników jak: właściwości hydrofobowe adsorbentu i adsorbatu, strukturalne właściwości adsorbentu, pęcznienie polimeru, oddziaływanie adsorbent-adsorbat.

W pracy **D2** udowodniono, że materiały w zależności od zastosowanej modyfikacji chemicznej oraz termicznej różnią się właściwościami fizykochemicznymi (teksturą, morfologią, właściwościami kwasowo-zasadowymi, stabilnością termiczną). Wykazano, że efektywność adsorpcji zależała od hydrofobowych właściwości adsorbatu (nitrobenzen>4-nitrofenol>fenol) oraz hydrofobowości węgli. Zaobserwowano wydłużony czas dyfuzji dla próbek o najwyższej zawartości tlenowych grup funkcyjnych będący wynikiem odziaływań cząsteczek adsorbatu z grupami tlenowymi na powierzchni węgli. Jednakże oddziaływania dyspersyjne pomiędzy elektronami π pierścienia aromatycznego adsorbatu a elektronami π warstw grafenowych adsorbentu przeważały.

W pracach **D3-D4** zbadano wpływ składu wyjściowej mieszaniny na właściwości fizykochemiczne pirolizowanych organiczno-nieorganicznych materiałów na bazie taniny i bentonitu bądź ligniny i magnetycznego pyłu żelazowego. Otrzymane organiczno-nieorganiczne materiały węglowe charakteryzowały się zróżnicowaną charakterystyką teksturalną, morfologiczną oraz adsorpcyjną. Wykazano wzrost zawartości mezoporów w całkowitej objętości porów wraz ze wzrostem udziału gliny lub magnetycznego komponentu. Większy udział mezoporów sprzyjał adsorpcji dużej cząsteczki barwnika – błękitu metylenowego. W pracy przedstawiono możliwości użycia naturalnych składników oraz odpadów przemysłowych (ochrona środowiska) do produkcji nowych typów adsorbentów.

W artykule **D5** potwierdzono skuteczność chemicznych oraz termicznych modyfikacji, które wpływały na procesy topnienia/krzepnięcia wody skondensowanej w porach. Zaobserwowano wprost proporcjonalną zależność pomiędzy właściwościami kwasowo-zasadowymi (stężeniem tlenowych grup funkcyjnych na powierzchni węgli) a przesunięciem w temperaturach topnienia wody zamkniętej w porach. Ponadto przeprowadzono analizę struktur lodu (odnotowano istnienie lodu o heksagonalnej, kubicznej i nieuporządkowanej strukturze).

Wyniki otrzymane w ramach realizacji rozprawy doktorskiej stanowią istotny wkład w rozwój badań nad otrzymywaniem i charakterystyką materiałów do zastosowań adsorpcyjnych oraz badań nad wpływem właściwości teksturalnych, a przede wszystkim powierzchniowych, na procesy topnienia/krzepnięcia w porach. Analiza tekstury, morfologii, chemii powierzchni, adsorpcji i stabilności termicznej jest istotna z fizykochemicznego punktu widzenia, jak i możliwych zastosowań materiałów w procesach, na przykład: oczyszczania, separacji, katalizy, magazynowania cieczy lub gazów, produkcji nanourządzeń, w nowoczesnych dziedzinach przemysłu. Dalsze plany badawcze zostaną rozszerzone o nowe adsorbenty o złożonej

budowie i specyficznej selektywności oraz będą skupione na procesach zachodzących w porach tych materiałów.

Słowa kluczowe: adsorbenty węglowe, adsorbenty nieorganiczno-organiczne, modyfikacje powierzchniowe, adsorpcja, topnienie/krzepnięcie wody w porach

3. Streszczenie w języku angielskim

The doctoral dissertation *Investigation of adsorption processes and phase transitions occurring in the pores of structurally and chemically diverse materials consists of a series of five articles* [**D1**-**D5**] and a self-report. The aim of the doctoral dissertation was to design, obtain and analyze materials in terms of textural, morphological and surface characteristics and to study the impact of their properties on adsorption processes and phase transformations taking place in limited pore spaces.

With regard to very wide use of porous materials in technology, science, environmental protection, and everyday life, research is being carried out to obtain new types of materials with properties tailored to specific applications. On the other hand, specific applications require more extensive research on processes occurring in limited pore spaces, which may be different from processes on flat surfaces and in bulk phases. Therefore, the subject of adsorbents and adsorption processes is widely represented in the scientific literature. A relatively new research trend concerns phase transformations taking place in micro- and mesopores, including melting/solidification processes, which is related to the use of porous materials in wide temperature ranges.

The problem of industrial wastewater pollution by organic substances that are difficult to dissolve in water (benzene derivatives and synthetic dyes, which are also dangerous to the environment and human and animal health) is getting worse, therefore it is important to look for new solutions in water treatment from these difficult-to-remove substances from water systems. This aspect is all the more important as the world's water resources are running out.

One of the most commonly used methods of water and wastewater treatment is the adsorption of various substances due to the simplicity of its use compared to other more demanding techniques and the possibility of choosing a variety of adsorbents. However, it should be emphasized that although there are various adsorbents available on the market (zeolites, carbons, silica materials), new materials with unique properties are constantly sought and designed due to their demand for specific applications (effective, selective, resistant to chemical, physical or biological factors).

An important aspect of the work was the study of melting/freezing processes in the pores of mesoporous carbons with different surface chemistry. In general, the knowledge about the processes of melting and freezing in pores is important due to the possibility of its usage in designing materials with practical application (adsorbents, lubricants or nanomaterials).

Particular attention was also given to the possibility of using natural resources or industrial waste for the synthesis of materials due to care for the natural environment.

In this doctoral thesis, various materials were considered, which differed in terms of structure and chemistry: organic-inorganic polymeric materials based on divinylbenzene and triethoxyvinylsilane (**M1** adsorbents), chemically and thermally modified active carbons (**M2** adsorbents), organic-inorganic carbonaceous materials based on tannin and bentonite (**M3** adsorbents), organic-inorganic carbonaceous materials based on indulin and iron dust (**M4** adsorbents), and mesoporous chemically and thermally modified carbons (**M5** materials).

For adsorbents **M1, M3, M4**, the influence of the composition of the reaction mixture, while for adsorbents **M2**, the influence of the applied modifications on the physicochemical (textural, morphological, chemical) and adsorption properties was considered. The obtained adsorbents were characterized using several research methods: low-temperature nitrogen adsorption-desorption, electron microscopy, X-ray diffraction, low-angle X-ray scattering, FT-IR/ATR spectroscopy, Raman spectroscopy, X-ray photoelectron spectroscopy, thermal analysis coupled with mass spectrometry. The adsorption properties of the obtained materials towards benzene derivatives - phenol, 4-nitrophenol and nitrobenzene or the dye - methylene blue, differing in properties (solubility/hydrophobicity, dissociation capacity, molecular size, functional groups) were tested by the analysis of equilibrium or adsorption kinetics.

In paper **D1**, it was shown that triethoxyvinylsilane (TEVS) strongly developed the porous structure of organic-inorganic materials based on divinylbenzene (DVB). In addition, different adsorption efficiency was shown, which depended on the hydrophobicity of the adsorbate (nitrobenzene>4-nitrophenol>phenol) for all the tested systems (DVB:TEVS = 1:2, 1:1, 2:1). Studies of adsorption kinetics revealed the effect of certain factors: hydrophobic properties of the adsorbent and adsorbate, structural properties of the adsorbent, swelling of the polymer, adsorbent-adsorbate interactions.

In the work **D2** it was proved that the materials, depending on the applied chemical and thermal modifications, differ in physicochemical properties (texture, morphology, acid-base properties, thermal stability). It was shown that the adsorption efficiency depended on the hydrophobic properties of the adsorbate (nitrobenzene>4-nitrophenol>phenol) and the carbon hydrophobicity. An extended diffusion time was observed for samples with the highest amount of oxygen functional groups, revealing interactions of adsorbate molecules with oxygen groups on the carbon surface. However, the dispersion interactions between the π electrons of the aromatic ring of the adsorbate and the π electrons of the graphene layers of the adsorbent were prevailing.

In works **D3-D4**, the influence of the composition of the initial mixture on the physicochemical properties of pyrolized organic-inorganic materials based on tannin and bentonite or lignin and magnetic iron dust was investigated. The obtained organic-inorganic carbon materials were characterized by diversified textural, morphological and adsorption characteristics. An increase in the share of mesopores in the total volume of pores was shown with an increase in the content of clay or a magnetic component, the participation of which promoted the adsorption of a large dye molecule - methylene blue. The work focuses on the aspect of the possibility of using natural ingredients and industrial waste (environmental protection) for novel adsorbent production.

In article **D5**, the effectiveness of chemical and thermal modifications that affected the processes of melting/freezing of condensed water in the pores was confirmed. A directly proportional relationship was observed between the acid-base properties (concentration of oxygen functional groups on the surface of carbons) and the shift in the melting temperatures of the water trapped in the pores. In addition, an analysis of ice structures was carried out (existence of ice with a hexagonal, cubic and disordered structure was noted).

The results obtained as part of the doctoral dissertation are a significant contribution to the development of research on the preparation and characterization of materials for adsorption applications and research on the influence of textural and, above all, surface properties, on melting/solidification processes in pores. The analysis of texture, morphology, surface chemistry, adsorption and thermal stability is important from the physicochemical point of view, as well as possible applications of materials in processes such as purification, separation, catalysis, storage of liquids or gases, production of nanodevices, in modern industries.

Further research plans will be extended to new adsorbents with a complex structure and specific selectivity, and will focus on the processes occurring in the pores of these materials.

Keywords: carbonaceous adsorbents, inorganic-organic adsorbents, surface modifications, adsorption, water melting/freezing in pores

4. Treść rozprawy doktorskiej

Przedstawiona rozprawa doktorska zatytułowana *Badania procesów adsorpcyjnych i przemian fazowych zachodzących w porach materiałów zróżnicowanych strukturalnie i chemicznie* stanowi zbiór pięciu oryginalnych prac badawczych. Prezentowana praca stanowi jedynie zwięzły opis metod badawczych i interpretacji wyników badań. Publikacje [D1-D5] oraz materiały uzupełniające [S1, S2, S5] znajdują się na stronach 67-204 autoreferatu.

4.1. Wprowadzenie

Materiały porowate są bardzo szeroko stosowane w różnych dziedzinach techniki, nauki, życia codziennego, ochronie środowiska. Ze względu na możliwe potrzeby ich wykorzystania badania prowadzone w wielu laboratoriach koncentrują się z jednej strony na projektowaniu i otrzymywaniu nowych materiałów o właściwościach dopasowanych do konkretnych zastosowań. Z drugiej strony konkretne aplikacje wymagają szerszych badań nad procesami zachodzącymi w ograniczonych przestrzeniach porów, które mogą przebiegać odmiennie od procesów na powierzchniach płaskich i w fazach objętościowych. Dlatego w literaturze naukowej tematyka dotycząca adsorbentów oraz procesów adsorpcyjnych jest szeroko reprezentowana. Stosunkowo nowy nurt badań dotyczy przemian fazowych zachodzących w mikro- i mezoporach, w tym procesów topnienia/krzepnięcia, co związane jest z wykorzystaniem materiałów porowatych w szerokich zakresach temperatury.

Zanieczyszczenia ścieków przemysłowych przez substancje organiczne takie jak pochodne benzenu oraz syntetyczne barwniki stanowią poważny problem, gdyż substancje te są słabo rozpuszczalne w wodzie i jednocześnie trudne do usunięcia z roztworów wodnych. Ponadto, substancje te są niebezpieczne dla środowiska oraz zdrowia ludzi i zwierząt [1,2,3]. Do oczyszczania wód z zanieczyszczeń stosowane są różne metody fizyczne, chemiczne lub fizykochemiczne, spośród których adsorpcja jest powszechnie stosowana ze względu na prostotę użycia, wysoką efektywność usuwania substancji, dostępność wielu adsorbentów o zróżnicowanej fizykochemicznej charakterystyce, oraz możliwość łatwego projektowania nowych, efektywnych i selektywnych adsorbentów [4,5].

Proces adsorpcji zależy od wielu czynników, w tym od natury adsorbatu, adsorbentu, roztworu oraz warunków prowadzenia procesu. W przypadku adsorbatu, proces adsorpcji zależy od jego struktury i wielkości cząsteczki oraz obecności różnych grup funkcyjnych, a także jego rozpuszczalności oraz zdolności do dysocjacji. Biorąc pod uwagę cechy adsorbentu, istotne są jego właściwości teksturalne, strukturalne oraz chemiczne (obecność grup funkcyjnych, zawartość popiołu). Poza właściwościami adsorbatu i adsorbentu należy również rozważyć właściwości roztworu (rodzaj rozpuszczalnika, pH, siła jonowa), a także sposób prowadzenia procesu, na przykład: temperaturę, czas. Należy podkreślić, że grupy funkcyjne obecne na powierzchni adsorbentu mogą odgrywać kluczową rolę w interakcjach adsorbent-adsorbat. Wymienić można różne mechanizmy oddziaływań adsorbent-adsorbat, z których główne mechanizmy rozważane w niniejszej rozprawie obejmowały odziaływania elektrostatyczne, hydrofobowe lub wiązanie wodorowe. Złożoność czynników, które mogą wpływać proces adsorpcji substancji sprawiają, że analiza i interpretacja danych jest skomplikowana [6, 7, 8, 9].

Stale poszukiwane są nowe materiały o ulepszonych właściwościach, charakteryzujące się wysoką efektywnością adsorpcji, stabilnością termiczną, długim czasem pracy, selektywnością, odpornością na działanie drobnoustrojów [10].

Opisane w literaturze badania obejmujące zjawiska topnienia/krzepnięcia wody skondensowanej w porach dotyczą charakteru przemian fazowych, przesunięć temperatury topnienia czy wpływu przemian teksturalnych/morfologicznych na procesy zachodzące w ograniczonych przestrzeniach porów. Procesy topnienia i krzepnięcia wody znajdującej się w porach jest istotne w wielu dziedzinach związanych z adhezją, adsorpcją, nanotechnologią. W literaturze opisano wpływ wielkości porów na przemiany fazowe w materiałach mikro- i mezoporowatych [11, 12, 13, 14]. Brak natomiast doniesień na temat możliwego wpływu chemii powierzchni materiałów (grupy funkcyjne obecne na powierzchni) na procesy topnienia/krzepnięcia przebiegające w małych porach dodatkowo zróżnicowanych powierzchniowo. Było to powodem podjęcia tego typu badań w niniejszej pracy, w której przeanalizowano wpływ właściwości chemicznych materiałów węglowych na procesy topnienia/krzepnięcia wody w porach.

Niniejsza rozprawa doktorska obejmuje zagadnienia projektowania, otrzymywania oraz badania unikatowych materiałów pod kątem określenia wpływu ich właściwości na charakter procesów adsorpcyjnych oraz przemian fazowych zachodzących w porach wypełnionych cieczą. Badania te są istotne z punktu widzenia zastosowań materiałów porowatych.

W ramach rozprawy doktorskiej *Badania procesów adsorpcyjnych i przemian fazowych zachodzących w porach materiałów zróżnicowanych strukturalnie i chemicznie* składającej się z cyklu pięciu publikacji rozważono różne typy materiałów o zróżnicowanej charakterystyce: organiczno-nieorganiczne materiały polimerowe w kształcie mikrosfer (**M1**), funkcjonalizowane węgle o granularnym kształcie ziaren (**M2**) oraz pirolizowane materiały organiczno-nieorganiczne (taninowo-bentonitowe oraz indulinowo-żelazowe), które otrzymano z surowców naturalnych lub odpadów przemysłowych (**M3**, **M4**), oraz modyfikowane powierzchniowo uporządkowane mezoporowate węgle (**M5**). Do otrzymania materiałów zastosowano różne procedury (polimeryzację suspensji, wytrawianie w kwasie i termiczne wygrzewanie lub mechanochemiczną aktywację ciał stałych w młynie kulowym i pirolizę w wysokiej temperaturze, syntezę materiału węglowego CMK-3 na bazie krzemionkowego templatu SBA-15) oraz chemiczne i termiczne modyfikacje.

W obrębie każdej serii materiałów sprawdzono wpływ składu mieszaniny reakcyjnej (organiczno-nieorganiczne materiały polimerowe oraz węglowe) oraz ilości tlenowych grup powierzchniowych (węgle aktywne oraz mezoporowate węgle) na właściwości fizykochemiczne, do przebadania których zastosowano wiele komplementarnych technik: niskotemperaturową adsorpcją-desorpcję azotu, mikroskopię elektronową, dyfrakcję rentgenowską, niskokątowe rozpraszanie promieni rentgenowskich, spektroskopię FT-IR/ATR, spektroskopię Ramana, rentgenowską spektroskopię fotoelektronów, analizę termiczną sprzężoną ze spektrometrią mas. Właściwości adsorpcyjne otrzymanych materiałów względem prostych substancji organicznych – fenolu, 4-nitrofenolu oraz nitrobenznenu lub barwnika – błękitu metylenowego przebadano pod kątem analizy równowagi lub kinetyki adsorpcji. Ponadto, procesy topnienia i krzepnięcia wody skondensowanej w porach modyfikowanych mezoporowatych węgli zbadano stosując dwie komplementarne techniki – skaningową kalorymetrię różnicową (DSC) oraz spektroskopię dielektryczną (ang. *Dielectric Spectroscopy*, DS).

Ważnym aspektem poruszanym w niniejszej rozprawie doktorskiej jest możliwość wykorzystania naturalnych składników takich jak tanina (organiczny związek z grupy garbników, pochodna fenoli), indulina (kraftowa lignina, polimer) lub odpadów przemysłowych (pył żelazowy o właściwościach magnetycznych) [15, 16].

4.2. Cel rozprawy doktorskiej

Głównym celem rozprawy doktorskiej opartej na cyklu publikacji [D1-D5] było zaprojektowanie, otrzymanie oraz kompleksowa analiza pięciu grup materiałów pod kątem określenia ich charakterystyk strukturalnych, teksturalnych, morfologicznych i powierzchniowych oraz przebadanie wpływu ich właściwości na procesy adsorpcyjne i przemiany fazowe zachodzące w ograniczonych przestrzeniach porów.

Przeprowadzona charakterystyka strukturalna, morfologiczna, teksturalna, chemiczna nowo otrzymanych materiałów umożliwiła analizę wpływu różnych czynników na procesy adsorpcji substancji organicznych z roztworów wodnych bądź zmian w procesach topnienia/krzepnięcia wody skondensowanej w porach. Główne założenia badawcze obejmowały:

- Zaprojektowanie oraz otrzymanie adsorbentów działających efektywnie, selektywnie względem wybranych substancji organicznych w roztworach wodnych
- Zbadanie wpływu składu mieszanin reakcyjnych lub modyfikacji powierzchniowych na właściwości fizykochemiczne adsorbentów (właściwości teksturalne, morfologiczne, strukturalne, chemiczne) oraz efektywność adsorpcji wskazanych substancji organicznych z roztworów wodnych
- Opis procesu adsorpcji substancji organicznych (pochodnych benzenu – fenolu, 4-nitrofenolu oraz nitrobenzenu) oraz barwnika – błękitu metylenowego z roztworów wodnych pod względem kinetyki lub równowagi adsorpcyjnej
- Możliwość wykorzystania naturalnych składników, takich jak: indulina, tanina) oraz odpadów przemysłowych, na przykład: pył żelazowy) do produkcji adsorbentów
- Zbadanie wpływu modyfikacji powierzchniowej mezoporowatych węgli na właściwości fizykochemiczne oraz procesy topnienia/krzepnięcia wody skondensowanej w porach modyfikowanych chemicznie i termicznie mezoporowatych węgli

Główne zadania wykonane w ramach realizacji rozprawy doktorskiej:

- Zaprojektowanie oraz otrzymanie materiałów o zróżnicowanej strukturze i chemii powierzchni (materiały organiczno-nieorganiczne i węglowe) poprzez zastosowanie różnych składników oraz procedur otrzymywania lub chemiczne i termiczne modyfikacje (mające na celu zróżnicowanie struktury i ilości grup funkcyjnych na powierzchni).
- Analiza strukturalna, teksturalna oraz morfologiczna materiałów (niskotemperaturowa adsorpcja-desorpcja azotu, dyfrakcja rentgenowska, mikroskopia elektronowa, spektroskopia Ramana).
- Określenie charakteru chemicznego (identyfikacja powierzchniowych grup funkcyjnych) (spektroskopia w poczerwieni, rentgenowska spektrometria fotoelektronów) oraz właściwości kwasowo-zasadowych (miareczkowanie potencjometryczne) materiałów.
- Badania kinetyki i równowagi adsorpcji (wykorzystanie spektrofotometrii UV-Vis) obejmujące określenie wpływu właściwości adsorbentów i adsorbatów na efektywność oraz szybkość procesu adsorpcji substancji organicznych (pochodnych benzenu oraz barwnika) z roztworów wodnych.
- Zastosowanie analizy termicznej do określenia stabilności termicznej adsorbentów oraz mechanizmu interakcji adsorbent-adsorbat (analizator termiczny sprzężony ze spektrometrem mas).
- Analiza procesów topnienia/krzepnięcia oraz przemian fazowych wody znajdującej się w porach modyfikowanych chemicznie i termicznie mezoporowatych węgli wsparta technikami DSC oraz DS.

4.3. Charakterystyka adsorbentów

Zestawienie adsorbentów badanych w niniejszej rozprawie doktorskiej znajduje się w Tabeli 2. Serie adsorbentów oznaczono jako M1-M5.

Tabela 2. Opis adsorbentów badanych w pracy doktorskiej.

Seria adsorbentów	**Nazwa serii materiałów stosowana w publikacji**	**Typ materiałów**	**Krótka charakterystyka materiałów**
M1	DVB-*co*-TEVS	Organiczno-nieorganiczne materiały polimerowe	Kopolimery otrzymane na bazie diwinylobenzenu oraz trietoksywinylosilanu [D1]
M2	AC-OX	Funkcjonalizowane grupami tlenowymi węgle mikroporowate	Węgle aktywne modyfikowane kwasem azotowym (V) i wygrzewane w temperaturach 180-800 °C [D2]
M3	TBC	Organiczno-nieorganiczne materiały węglowe	Materiały węglowe otrzymane na bazie taniny i bentonitu [D3]
M4	STInd	Organiczno-nieorganiczne materiały węglowe	Materiały węglowe otrzymane na bazie induliny oraz pyłu żelazowego [D4]
M5	OMC-OX	Funkcjonalizowane grupami tlenowymi węgle mezoporowate	Węgle mezoporowate modyfikowane kwasem azotowym (V) i wygrzewane w temperaturach 150-800 °C [D5]

Serie materiałów **M1-M5** otrzymano według poniżej opisanych procedur:

- Materiały **M1** otrzymano na bazie 1,4-dywinylobenzenu (DVB) i trietoksywinlosilanu (TEVS). Polimeryzację DVB z TEVS przeprowadzono w środowisku wodnym metodą polimeryzacji suspensji oraz stosując inicjator reakcji azobis(izobutyronitryl) (AIBN) oraz mieszaninę rozpuszczalników formujących strukturę porowatą – toluen oraz dekan-1-ol (*v/v* = 1/1). Polimeryzację prowadzono przez 12 godzin w 85 °C w systemie złożonym z kolby okrągłodennej, chłodnicy zwrotnej, mieszadła oraz termometru. Współczynniki molowe monomerów w mieszaninie reakcyjnej zaprezentowano w Tabeli 2. Schemat budowy chemicznej trietoksywinlyosilanu (TEVS), 1,4-diwynylobenzenu (DVB) oraz kopolimeru (DVB-*co*-TEVS) zaprezentowano na Rysunku 1 [D1].

Tabela 2. Skład mieszaniny reakcyjnej uwzględniający ilość monomerów (organiczno-nieorganiczne mikrosfery polimerowe).

Nazwa próbki	**Współczynniki molowe monomerów**	
	DVB	TEVS
DVB:TEVS = 1:2	1	2
DVB:TEVS = 1:1	1	1
DVB:TEVS = 2:1	1	0.5

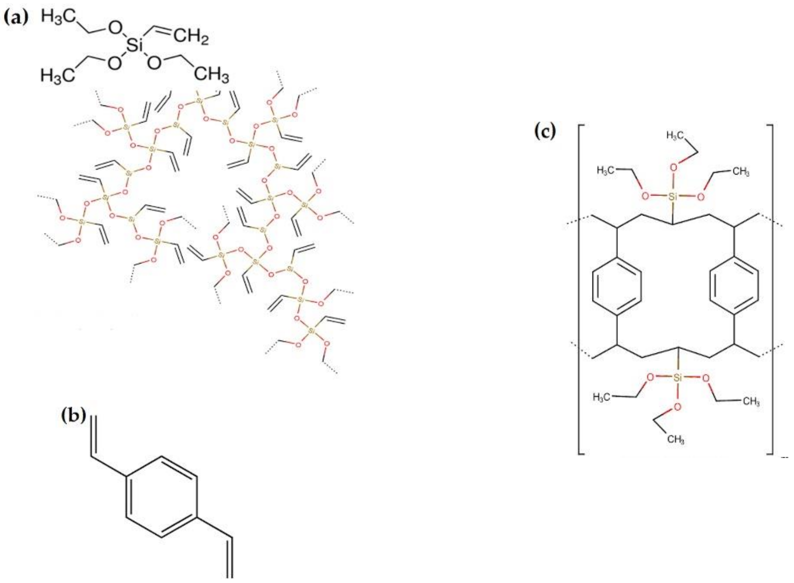

Rysunek 1. Budowa chemiczna trietoksywinylosilanu (TEVS) (a) i 1,4-diwinylobenzenu (DVB) (b) oraz schematyczna struktura kopolimeru (DVB-*co*-TEVS) (c).

- Materiały **M2** przygotowano wykorzystując dostępny komercyjnie węgiel aktywny GAC1240W Norit (USA) o ziarnistej budowie. Materiał węglowy modyfikowano 65% kwasem azotowym w temperaturze 80 °C przez 3 godziny w układzie wyposażonym w kolbę okrągłodenną, chłodnicę zwrotną i termometr zgodnie z procedurą opisaną w pracy [6]. Modyfikowany kwasem węgiel przepłukano dużą ilością wody destylowanej i wysuszono w temperaturze pokojowej. Wysuszony węgiel podzielono na porcje i wygrzewano w temperaturach 180, 280, 380, 480, 640 i 800 °C w piecu rurowym z podłączonym źródłem gazu obojętnego w celu zabezpieczenia materiału przed spaleniem [D2].

- Materiały **M3 i M4** otrzymano stosując dwuetapową procedurę: mechanochemiczną aktywację w młynie kulowym oraz pirolizę. Mechanochemiczna aktywacja w młynie pozwala na uzyskanie materiałów dwu- lub więcej składnikowych o wysokiej dyspersji faz bez użycia organicznych rozpuszczalników wykorzystując energię wytwarzaną podczas mielenia składników (praca młyna). Określone ilości wyjściowych składników: taniny i bentonitu (Tabela 3) lub induliny i pyłu żelazowego (Tabela 4) umieszczono w reaktorze ze stali nierdzewnej młyna kulowego (średnica kul wynosiła 5 mm). Proces mielenia prowadzono przez 6 godzin. Piroliza w piecu prowadzona była w atmosferze gazu obojętnego przez 2 godziny w temperaturze 800 °C. Schematy syntezy adsorbentów M3 i M4 pokazano na Rysunku 2 i 3 [D3, D4].

Tabela 3. Proporcje składników (g) wykorzystane do otrzymania organiczno-nieorganicznych materiałów węglowych na bazie taniny i bentonitu [D3].

Nazwa próbki	**Proporcje składników (g)**	
	Tanina	Bentonit
TC	10	0
TBC-1	10	10
TBC-2	20	10
TBC-3	30	10
TB-0,5	6	10

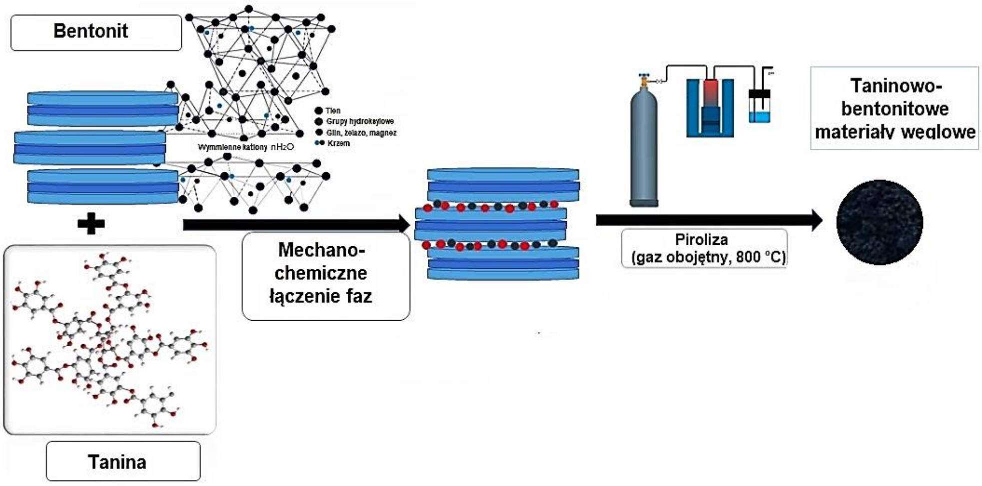

Rysunek 2. Schemat syntezy taninowo-bentonitowego materiału węglowego [D3].

Tabela 4. Stosunek komponentów (g) użytych do uzyskania organiczno-nieorganicznych materiałów węglowych na bazie induliny i pyłu żelazowego [D4].

Nazwa próbki	Stosunek komponentów (g)	
	Indulina	Pył żelazowy
STInd-1	12,5	5,0
STInd-2	12,5	4,0
STInd-3	12,5	3,0
STInd-4	12,5	1,3
Indulina/Węgiel	12,5	0,0

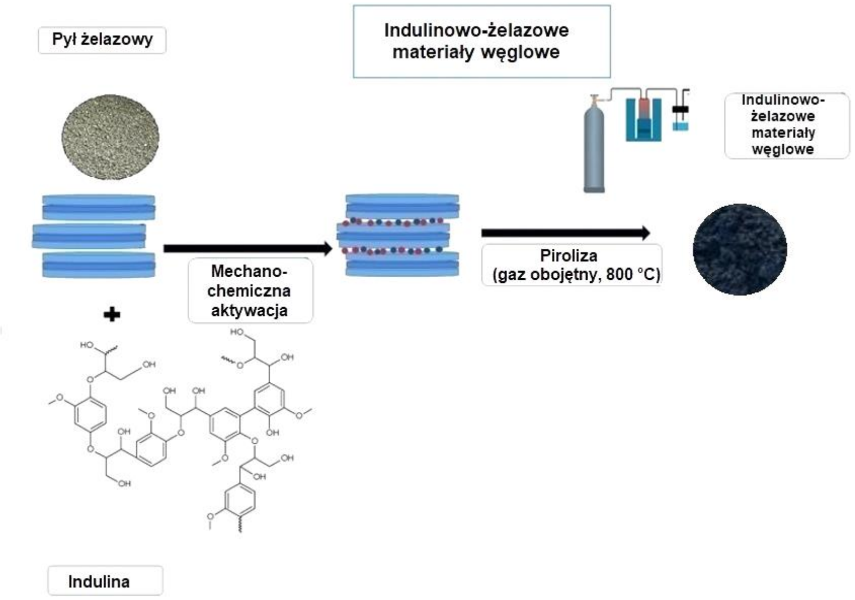

Rysunek 3. Schemat syntezy indulinowo-żelazowego materiału węglowego [D4].

Modyfikowane grupami tlenowymi mezoporowate węgle o uporządkowanej heksagonalnej strukturze (CMK-3) (materiały **M5**) otrzymano na bazie templatu krzemionkowego SBA-15 [D5]. W syntezie materiału SBA-15, przeprowadzonej według procedury opisanej w pracach [17,18], wykorzystano tetraetoksysilan (ang. *tetraethoxysilane*, TEOS) oraz trójblokowy kopolimer o nazwie *Pluronic P123*. Materiał węglowy otrzymano stosując dwustopniową impregnację w odpowiednich roztworach kwasu siarkowego i glukozy oraz przeprowadzając proces karbonizacji w temperaturze 700 °C. Otrzymany zwęglony materiał poddano wytrawianiu w etanolowo-wodnym roztworze (*v/v*% = 1/1) wodorotlenku potasu (~ 1 mol/l) w celu usunięcia matrycy krzemionkowej. Przepłukany dużą ilością wody destylowanej oraz wysuszony w temperaturze pokojowej materiał podzielono na porcje i poddano modyfikacji chemicznej oraz termicznej w 150, 400, 600 i 800 °C analogicznie jak w przypadku materiałów **M2** [D5]

4.4. Metody badawcze

Parametry teksturalne adsorbentów (**M1-M5**) zostały wyznaczone stosując niskotemperaturową analizę adsorpcji-desorpcji azotu w temperaturze −196 °C z wykorzystaniem porozymetru ASAP2020 lub ASAP2405N (Micromeritics, USA). Z izoterm adsorpcji oraz desorpcji azotu uzyskano wartości następujących parametrów: powierzchnię właściwą (S_{BET}) z liniowej zależności równania Brunauera, Emmetta i Tellera (BET), całkowitą objętość porów (V_t) (dla ciśnienia $p/p_0 \sim 0{,}99$) [19], powierzchnię zewnętrzną (S_{ext}) oraz objętość mikroporów (V_{mic}) metodą t-plot, i rozkład wielkości porów (ang. *Pore Size Distribution*, PSD) obliczony stosując nielokalną teorię funkcjonału gęstości (ang. *Non Local Density Functional Theory*, NLDFT) [20] lub procedurę Barretta, Joynera i Halendy (BJH) [21]. Średni hydrauliczny rozmiar porów (D_h) obliczono z zależności: $D_h = 4V_t/S_{BET}$. Przed pomiarami próbki odgazowano w celu usunięcia zaadsorbowanych zanieczyszczeń w określonych temperaturach [D1-D5].

Właściwości teksturalne modyfikowanych powierzchniowo węgli oraz materiałów polimerowych (M1, M2, M5) wyznaczono także stosując analizę niskokątowego rozpraszania promieni rentgenowskich (ang. *Small-Angle X-Ray Scattering*, SAXS). Analizę SAXS przeprowadzono za pomocą dyfraktometru Empyrean (PANalytical) z promieniowaniem CuKα. Rozkład promieni SAXS obejmował zakres kąta 2θ: 0,13-4 stopni [D1, D2, 22, 23].

Właściwości morfologiczne i strukturalne próbek zbadano wykorzystując skaningowy mikroskop elektronowy (ang. *Scanning Electron Microscop*, SEM) Quanta 250 FEG (FEI, USA) lub transmisyjny mikroskop elektronowy (ang. *Transsmition Electron Microscop*, TEM) Titan G2 60-300 (USA) [D1-D3, D5, 24].

W celu wyznaczenia właściwości kwasowo-zasadowych materiałów zastosowano miareczkowanie potencjometryczne suspensji. Analizę przeprowadzono wykorzystując układ wyposażony w biuretę automatyczną 765 Dosimat Metrohm (Herisau, Szwajcaria), pH-metr

PHM240 Radiometer (Kopenhaga, Dania), termostat Ecoline RE207 (Lauda, Niemcy) oraz naczynie kwarcowe o pojemności 50 ml. Celem wykonania pomiarów do naczynia kwarcowego odmierzono 30 ml elektrolitu (chlorku sodu) o stężeniu 0,1 mol/l, 0,3 ml kwasu solnego o stężeniu 0,2 lub 0,5 mol/l oraz dodano odpowiednią ilość adsorbentu (0,05 lub 0.1 g). Po osiągnięciu stałej temperatury (25 °C) oraz wartości pH, dodawany był roztwór wodorotlenku sodu o stężeniu 0,1 mol/l lub 0,2 mol/l. Analogiczny pomiar wykonano bez dodatku ciała stałego. Uzyskane wyniki przedstawiono w postaci zależności pH w funkcji ilości dodanego roztworu NaOH. Na podstawie zebranych danych wyznaczono punkt zerowego ładunku powierzchniowego pH_{PZC} [D1-D5, 25].

Charakter chemiczny adsorbentów zbadano stosując spektroskopię w podczerwieni wykorzystującą zjawisko osłabionego całkowitego wewnętrznego odbicia z transformatą Fouriera (ang. *Fourier Transform Infrared Spectroscopy/Attenuated Total Reflection*, FT-IR/ATR). Widma FT-IR/ATR rejestrowane były w zakresie 400-4000 cm^{-1} za pomocą spektroskopu Tensor 27 (Bruker, Niemcy) z przystawką ATR z wbudowanym diamentowym kryształem [D1, D3, 26].

Skład chemiczny powierzchni adsorbentów węglowych po modyfikacji w kwasie i wygrzewaniu w różnych temperaturach określono metodą rentgenowskiej spektroskopii fotoelektronów (ang. *Photoelectron X-Ray Spectroscopy*, XPS) wykorzystując wielokomorowy system wysokopróżniowy z analizatorem VG Scienta R4000 (ang. *Ultra-High Vaccum*, UHV). Uzyskano przeglądowe i szczegółowe widma XPS atomów węgla oraz tlenu (C1s i O1s) na podstawie których stwierdzono skuteczność przeprowadzonych modyfikacji powierzchni [D2, D5, 27].

Identyfikacja faz materiałów węglowych otrzymanych z surowców naturalnych (taniny i induliny) (M3, M4) przeprowadzono wykorzystując dyfrakcję rentgenowską (ang. *X-Ray Diffraction*, XRD) oraz spektroskopię Ramana. Dyfraktogramy rejestrowano przy kącie 2θ = 5-80° za pomocą dyfraktometru DRON-4-07 wykorzystującą wiązkę promieniowania CuKα w geometrii Bragga-Brentano. Widma Ramana zarejestrowano w zakresie 3200-150 cm^{-1} z wykorzystaniem spektroskopu Via Reflex DMLM Leica Research Grade (Wielka Brytania) [D3, D4, 28].

Analizę termiczną obejmującą termograwimetrię (ang. *Thermogravimetry*, TG) polegającą na pomiarze ubytków masy podczas ogrzewania lub chłodzenia materiału, analizę pochodnej krzywej termograwimetrycznej (ang. *Derivative Thermogravimetry*, DTG) pomagającej w interpretacji wyników TG (wyznaczenie krzywej DTG umożliwia dokładniejsze wyodrębnienie nakładających się na siebie etapów, które są słabo widoczne na krzywej TG), analizę termiczną różnicową (ang. *Differential Thermal Analysis*, DTA) polegającą na rejestracji różnicy temperatury między próbką badaną i referencyjną (wykonanie pomiaru DTA umożliwia badanie efektów cieplnych towarzyszącym procesom zachodzącym podczas ogrzewania materiału), skaningową kalorymetrię różnicową (ang. *Differential Scanning Calorimetry*, DSC) polegającą na pomiarze zmiany różnicy strumienia cieplnego powstającego między próbką badaną i odniesienia w trakcie ogrzewania materiału (analiza DSC pozwala wyszczególnić przemiany fazowe i strukturalne zachodzące w próbce) przeprowadzono na aparacie STA 449 Jupiter F1 Netzsch (Niemcy) (Materiały M1-M3) lub Q 1500D Paulik (Węgry) w atmosferze gazu obojętnego (Materiały M4). Próbki o kreślonych masach umieszczono w tyglach i ogrzewano w szerokim zakresie temperaturowym stosując narost temperaturowy 10 °C /min. Produkty gazowe ulatniające się podczas rozkładu materiałów analizowano stosując kwadrupolową spektrometrię mas (ang. *Quadrupole Mas Spectrometry*, QMS). Pomiary wykonano na spektrometrze mas QMS 403C Aeölos (Niemcy) w zakresie od 10 do 300 amu. Analiza produktów gazowych materiałów z zaadsorbowaną substancją umożliwiła pełniejszą interpretację mechanizmu oddziaływań adsorbent-adsorbat [D1-D4, 29, 30].

Badania równowagi adsorpcji substancji organicznych z roztworów wodnych (pH~7) na adsorbentach przeprowadzono metodą statyczną wykorzystując spektrofotometr UV-Vis Carry 4000 Varian (Australia) do określania stężeń równowagowych adsorbatu. Adsorbenty o określonych masach (~0,05 g) umieszczono w kolbach stożkowych 50 lub 100 ml. Odważone ciała stałe skontaktowano z odpowiednimi roztworami substancji organicznych o określonych stężeniach i objętościach. Proces adsorpcji prowadzono w wytrząsarce New Brunswick Scientific Shaker (USA) zapewniającej stałą prędkość mieszania oraz temperaturę (25 °C). Po ustaleniu równowagi (2-7 dni w zależności od badanego układu) mierzono absorbancję. Na podstawie uzyskanych danych wyznaczono stężenie substancji rozpuszczonej, które obliczono z maksymalnej absorbancji przy określonej długości fali A = f(λ). Zaadsorbowaną ilość substancji organicznych obliczono z równania bilansu masy (1). Procent usunięcia substancji organicznej wyznaczono z równania (2). Do analizy teoretycznej równowagi adsorpcyjnej w przypadku adsorbentów M2 wykorzystano uogólnioną postać izotermy Langmuira (ang. *Generalized Lagmuir,* GL) (3). Równanie GL można uprościć do izotermy Langmuira, gdy $m = n = 1$, uogólnionej izotermy Freundlicha, gdy $n = 1$ oraz do izotermy Tótha, gdy $m = 1$. W pracach dotyczących adsorpcji substancji organicznych na adsorbentach M3 oraz M4 zastosowano izotermę adsorpcji Langmuira (4) lub modyfikowaną postać izotermy Langmuira (5) oraz izotermę Freundlicha (6). W przypadku materiałów M3 oraz M4 zbadano również wpływ pH oraz czas kontaktu [D2-D5].

$$a = \frac{(c_0 - c_{eq}) \cdot V}{w} \tag{1}$$

$$\%_{us} = \frac{(c_0 - c_{eq}) \cdot 100}{C_0} \tag{2}$$

$$\frac{a}{a_m} = \left[\frac{(\overline{K} \cdot c_{eq})^n}{1 + (\overline{K} \cdot c_{eq})^n}\right]^{\frac{m}{n}} \tag{3}$$

$$\frac{c_{eq}}{a} = \frac{c_{eq}}{a_m} + \frac{1}{K_L \cdot a_m} \tag{4}$$

$$a = a_m \frac{K_{ML} \cdot c_{eq}}{\left(c_S - c_{eq}\right) + K_{ML} \cdot c_{eq}} \tag{5}$$

$$a = K_F \cdot C_{eq}^{\frac{1}{n}} \tag{6}$$

gdzie: a to ilość zaadsorbowana (mg/g), C_0 to początkowe stężenie substancji organicznej (mg/l), V to objętość roztworu, w to masa adsorbentu, $\%_{us}$ jest to procent usunięcia substancji organicznej, a_m to maksymalna ilość zaadsorbowana (mg/g), m i n to parametry heterogeniczności, $\overline{K}$ jest stałą równowagi adsorpcji związaną z charakterystyczną energią funkcji rozkładu, K_L stała równowagi Langmuira, K_{ML} to modyfikowana stała równowagi Langmuira, C_S to wartość nasyconego stężenia substancji rozpuszczonej (mg/l), K_F to stała Freundlicha [31, 32, 33, 34, 35].

Charakterystykę fizykochemiczną substancji organicznych wykorzystanych jako adsorbaty w układach wodnych przedstawiono w Tabeli 3. Substancje organiczne różnią się budową cząsteczki, masą molową, rozpuszczalnością, stałą jonizacji, temperaturą topnienia, temperaturą wrzenia [D1-D4].

Tabela 3. Charakterystyka fizykochemiczna adsorbatów [D1-D4].

Nazwa adsorbatu	**Fenol**	**4-Nitrofenol**	**Nitrobenzen**	**Błękit metylenowy**
Chemiczna formuła	C_6H_5OH	$C_6H_5NO_3$	$C_6H_5NO_2$	$C_{16}H_{18}ClN_3S$
Budowa cząsteczki	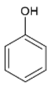	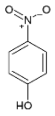	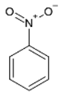	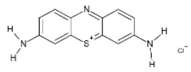
Masa molowa (g/mol)	94,11	139,11	123,11	319,90
Rozpuszczalność w wodzie w 20 °C (g/100 ml)	8,30	1,16	0,19	4,36
Stała jonizacji, pK_a	9,99	7,15	-	3,80
Temperatura topnienia (°C)	40,5	114,0	5,7	190
Temperatura wrzenia (°C)	181,7	279,0	210,9	-

Badania kinetyki adsorpcji przeprowadzono na serii materiałów **M1, M2**. Pomiary kinetyczne przeprowadzono za pomocą spektrofotometru UV-Vis Cary 100 Varian (Australia) z celą przepływową zapewniającą możliwość ciągłej rejestracji widma. Adsorbent o masie 0,1 g umieszczono w naczyniu kwarcowym oraz dodano 100 ml wodnego roztworu substancji organicznej o określonym stężeniu początkowym (c_0). System wyposażony był w mieszadło oraz termostat zapewniający stałą temperaturę (25 °C). W określonych odstępach czasowych rejestrowano widma absorpcyjne, a roztwór zawracano do naczynia reakcyjnego. Widmo absorbancji rejestrowano przy długości fali w zakresie od 200 do 450 nm. Stężenie substancji zaadsorbowanej dla układów eksperymentalnych obliczono z zarejestrowanych widm.

Krzywe kinetyczne zanalizowano za pomocą kilku równań: równania pierwszego i drugiego rzędu (ang. *First Order Equation*, FOE i *Second Order Equation*, SOE) oraz równania pseudo pierwszego i drugiego rzędu (ang. *Pseudo First Order Equation*, PFOE i *Pseudo Second Order Equation*, PSOE), mieszane równanie pierwszego i drugiego rzędu (ang. *Mixed Order Equation*, MOE), oraz równania fraktalne (f-MOE, f-FOE, f-SOE), równanie multieksponencjalne (ang. *Multiexponential Equation*, m-exp), model dyfuzji wewnątrzcząstkowej w porach znany jako model Cranka (ang. *Intraparticle Diffusion Model*, IDM), oraz model dyfuzji w porach (ang. *Pore Diffusion Model*, PDM) [D1, D2, 31, 32, 33, 34, 35].

Różnicowa kalorymetria skaningowa (DSC) i spektroskopia dielektryczna (DS) zostały zastosowane do badań procesów topnienia/krzepnięcia wody znajdującej się w porach mezoporowatych węgli. Pomiary DS przeprowadzono przy użyciu kondensatora ze stali nierdzewnej wyposażonego w analizator impedancji Solartron 1260 (Wielka Brytania) do pomiaru pojemności (C) w funkcji temperatury (T) i częstotliwości (ω). Zastosowano cykliczne pole elektryczne w zakresie częstotliwości od 1 do 106 Hz w różnych temperaturach (od 140 K do 304 K) i stosując narost temperaturowy odpowiednio 0,8 K/min lub 0,6 K/min podczas procesów chłodzenia lub grzania. Próbki umieszczono między płytami kondensatora w postaci zawiesiny węgla z wodą. Zespolona przenikalność elektryczna jest zdefiniowana jako: $\varepsilon^* = \varepsilon' + i\varepsilon''$. Temperaturę topnienia T_m wyznaczono jako zmianę wartości przenikalności elektrycznej ε' (lub pojemności elektrycznej C) temperatury topnienia $\varepsilon' = C/C_0$, gdzie C_0 jest pojemnością pustego kondensatora, *ε”* jest urojoną częścią przenikalności elektrycznej i wyraża się zależnością $\varepsilon'' = tg\delta \cdot \varepsilon'$, gdzie $tg\delta$ to straty dielektryczne. Czas relaksacji dielektrycznej oszacowano, dopasowując model relaksacji orientacyjnej Debye'a do widma dyspersji złożonej przenikalności elektrycznej w pobliżu rezonansu. Pomiary DSC przeprowadzono za pomocą aparatu TG/DTA/DSC STA 449 Jupiter F1 Netzsch (Niemcy). W tym celu 20 mg przesączonej zawiesiny umieszczono w aluminiowym tyglu przykrytym aluminiową pokrywą i zakapsułkowano. Pusty tygiel użyto jako próbka odniesienia. Pomiary prowadzono w obecności powietrza syntetycznego o natężeniu przepływu 50 ml/min w zakresie temperatur od -100 do +60 °C i szybkości ogrzewania 5 °C/min. Przed pomiarami próbki suszono przez 12 godzin w temperaturze 60 °C [D5, 11, 13, 14].

4.5. Omówienie wyników

4.5.1. Charakterystyka fizykochemiczna i adsorpcyjna materiałów M1

Koopolimery na bazie dywinylobenzenu i trietoksywinylosilanu (DVB-*co*-TEVS) o sferycznym kształcie zsyntezowano stosując różne stosunki molowe monomerów (1:2, 1:1 i 2:1). Zdjęcia z obrazowania SEM przedstawiono na Rysunku 4. Otrzymane mikrosfery charakteryzowały się zróżnicowaną morfologią oraz średnicą ziaren w zakresie 50-200 µm. Mikrosfery o stosunku molowym 1:2 charakteryzowały się nieidealnym kulistym kształtem oraz charakteryzowały się największą chropowatością powierzchni, podczas gdy materiały o proporcji składników 2:1 charakteryzowały się najbardziej regularnym kształtem oraz homogeniczną i gładką powierzchnią. Próbka o stosunku molowym 1:1 wykazała właściwości pośrednie. Wykazano wyraźny efekt porotwórczy TEVS [36, 37].

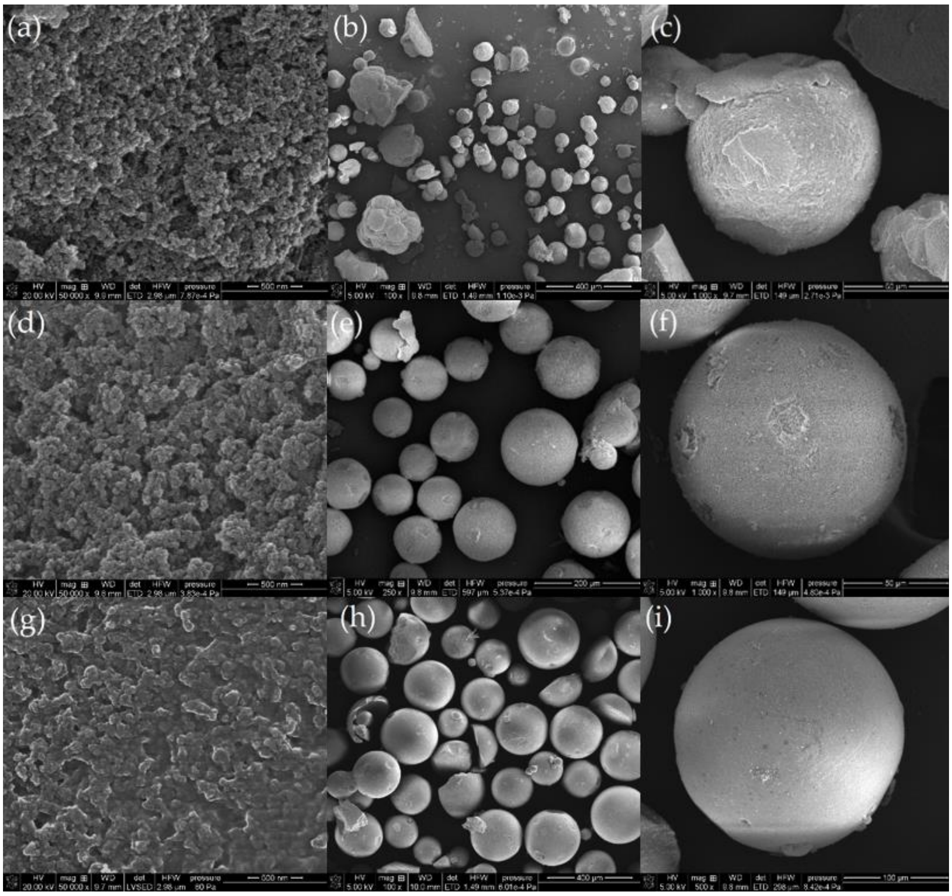

Rysunek 4. Obrazy mikroskopowe SEM dla materiału DVB-*co*-TEVS o stosunkach molowych składników mieszaniny reakcyjnej 1:2 (a, b, c), 1:1 (d, e, f), 2:1 (g, h, i) przedstawione w różnych przybliżeniach [D1].

Dane z niskotemperaturowej adsorpcji-desorpcji azotu zaprezentowano w Tabeli 5. Kształty izoterm wykazały, że materiały na bazie dywinylobenzenu i trietoksywinylosilanu zawierają znaczną ilość mezoporów i niewielką ilość mikroporów. Potwierdzono, że zmiany w parametrach strukturalnych związane są z ilością nieorganicznego składnika (TEVS), który rozwija strukturę porowatą. Natomiast zwiększenie ilości DVB powoduje zwiększenie wielkości porów. Zmiany we właściwościach teksturalnych potwierdzono poprzez analizę SAXS [36, 37].

Tabela 5. Parametry teksturalne organiczno-nieorganicznych mikrosfer polimerowych otrzymane z niskotemperaturowej adsorpcji-desorpcji azotu [D1].

DVB-*co*-TEVS	S_{BET} **(m^2/g)**	V_t **(cm^3/g)**	V_{mic} **(cm^3/g)**	BJH_{ADS} **(nm)**	D_h **(nm)**	S_{SAXS} **(m^2/g)**
1:2	521	0,84	-	4,8	6,4	610
1:1	402	0,74	-	5,1	7,4	480
2:1	316	0,54	0,01	5,8	6,8	390

Skuteczność połączenia faz sprawdzono stosując technikę FT-IR/ATR. Charakterystyczne drgania pochodzące od faz diwinylobenzenu i trietoksywinylosilanu zaobserwowano w przypadku każdej z próbek. Pasmo położone przy liczbie falowej 1000-1110 cm^{-1} związane jest z występowaniem symetrycznych drgań rozciągających grup Si-O-C, których obecność potwierdza wbudowanie TEVS w strukturę polimeru. Pasmo to nie jest widoczne na widmie DVB (S1). Pik o największej intensywności zaobserwowany został w próbce o najwyższej zawartości trietoksywinylosilanu [38, 39, 40, 41].

Kinetykę adsorpcji fenolu, 4-nitrofenolu i nitrobenzenu przebadano dla serii otrzymanych materiałów. Najwyższy spadek stężenia adsorbatu zanotowano w przypadku układów z nitrobenzenem, najniższy dla fenolu. Ubytki w stężeniach adsorbatów związane były z ich właściwościami (głównie hydrofobowością – rozpuszczalnością w wodzie). W przypadku adsorpcji nitrobenzenu największe ubytki adsorbatu z roztworu wodnego zaobserwowano w przypadku najbardziej hydrofobowego materiału DVB:TEVS = 2:1. Dla 4-nitrofenolu i fenolu największe ubytki adsorbatu stwierdzono dla DVB:TEVS = 1:1. Efektywność adsorpcyjna materiałów DVB:TEVS = 2:1 i DVB:TEVS = 1:2 w stosunku do różnych adsorbatów była podobna, natomiast adsorbent DVB:TEVS = 1:1 wykazywał odmienne właściwości. Profile kinetyczne ujawniły ogólny wpływ kilku czynników: właściwości hydrofobowych adsorbatu, strukturalnych właściwości adsorbentu, pęcznienia polimeru, oddziaływania adsorbent-adsorbat. Badania potwierdziły efektywność procesu adsorpcji [42].

Analiza termiczna organiczno-nieorganicznych materiałów na bazie DVB i TEVS wykazała, że są stabilne termicznie do co najmniej 330 °C, dzięki czemu mogą być stosowane w stosunkowo szerokim zakresie temperatur. Ubytki masy dla wszystkich materiałów z zaadsorbowanymi organicznymi substancjami były większe w porównaniu z czystymi materiałami DVB-TEVS sugerujące stosunkowo słabe oddziaływania adsorbent-adsorbat o charakterze fizycznym [D1].

4.5.2. Charakterystyka fizykochemiczna i adsorpcyjna materiałów M2

Materiały węglowe ze zróżnicowaną koncentracją grup tlenowych na powierzchni zostały otrzymane metodą mokrej impregnacji w kwasie azotowym (V) oraz modyfikacji temperaturowej [6]. Parametry otrzymane z izoterm adsorpcji-desorpcji azotu pokazane są w Tabeli 6. Właściwości teksturalne zbadano kompleksowo z zastosowaniem analizy mikroskopowej, porozymetrycznej oraz SAXS. Otrzymano komplementarne wyniki badań.

Wykazano, że zastosowane modyfikacje nie zmieniają znacząco rozkładu porów (rozkład porów otrzymany metodą NLDFT), wartości promienia hydraulicznego (D_h) są także porównywalne i wynoszą ~2 nm, natomiast widoczne są różnice w wielkościach powierzchni (S_{BET}) i całkowitych objętościach porów (V_t) (Tabela 6). Utlenienie w kwasie powoduje znaczną redukcję tych wartości, natomiast wygrzewanie w coraz wyższych temperaturach, ich stopniowy wzrost. Zmniejszenie wielkości powierzchni i porowatości próbki potraktowanej kwasem azotowym (V) mogą być związane z zapadaniem się niektórych ścianek porów. Ponadto, spadki te mogą być skorelowane z obecnością tlenowych grup powierzchniowych mogących blokować wejście porów ograniczając dostępną przestrzeń materiału węglowego. Na skutek termicznego wygrzewania i usuwania grup funkcyjnych przestrzeń ta zostaje ponownie otwarta. Niezależnie od temperatury wygrzewania udział mikroporów w ogólnej liczbie porów maleje. To może sugerować łączenie się mikroporów w większe struktury porów w przypadku materiałów modyfikowanych w wyższych temperaturach. Analiza kształtu izoterm adsorpcji-desorpcji potwierdziła mikroporowaty charakter analizowanych materiałów typu I z pętlą histerezy H4 zgodnie z klasyfikacją IUPAC.

Obrazy ze skaningowego mikroskopu elektronowego węgli aktywnych ujawniły różnice w morfologii. Obrazowanie SEM próbki niemodyfikowanej wykazało relatywnie wysoki stopień gładkości powierzchni ziaren. Modyfikacje kwasem azotowym, poza wprowadzeniem grup tlenowych, spowodowały zmiany w morfologii próbek. Powierzchnia wytrawiona kwasem była pełna nieregularności (powstanie defektów powierzchniowych). Zmiany mikrostrukturalne nasiliły się w wyniku zastosowania modyfikacji temperaturowych, które udostępniły wolną przestrzeń porów na skutek usunięcia grup tlenowych [D2, 6, 43].

Tabela 6. Parametry teksturalne węgli aktywnych modyfikowanych chemicznie i termicznie otrzymane z izoterm adsorpcji-desorpcji azotu [D2].

Nazwa próbki	**S_{BET} (m^2/g)**	**V_t (cm^3/g)**	**V_{mic} (cm^3/g)**	**V_{mic}/V_t**	**D_h (nm)**	**S_{SAXS} (m^2/g)**
AC	900	0,52	0,20	0,38	2,30	945
AC-OX	631	0,32	0,13	0,41	2,05	700
AC-OX-180	661	0,34	0,10	0,29	2,08	706
AC-OX-280	689	0,36	0,11	0,31	2,11	713
AC-OX-380	694	0,36	0,10	0,28	2,09	736
AC-OX-480	715	0,37	0,10	0,27	2,08	741
AC-OX-600	714	0,38	0,10	0,26	2,12	747
AC-OX-800	759	0,40	0,10	0,24	2,12	755

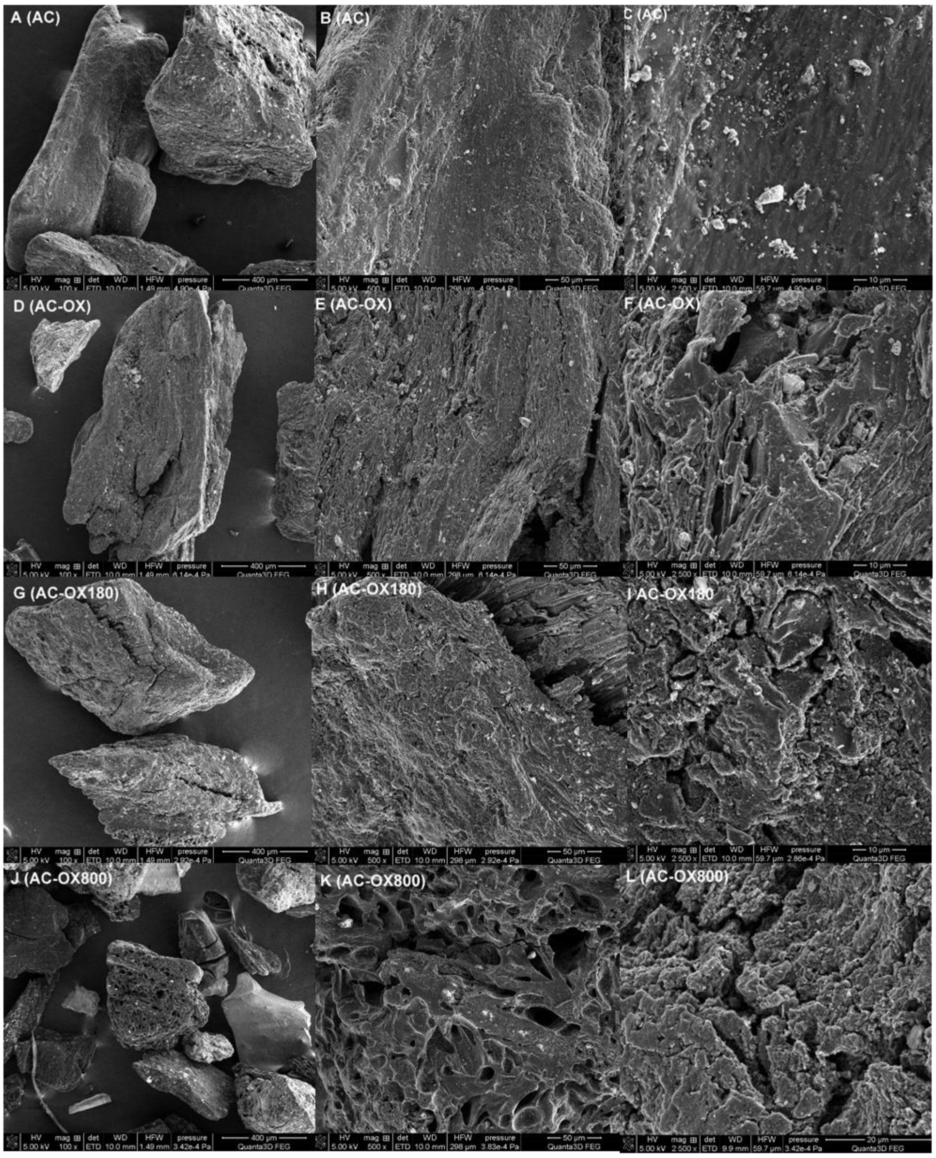

Rysunek 5. Obrazy SEM węgli aktywnych: niemodyfikowanego (a-c), modyfikowanego kwasem (d-f), wygrzewanego w 180 °C po modyfikacji w kwasie (g-i), oraz wygrzewanego w 800 °C po modyfikacji w kwasie (j-l) [D2].

Analiza XPS potwierdziła skuteczność wprowadzenia grup tlenowych oraz ich stopniowego usuwania w wyniku zastosowania modyfikacji temperaturowych. Uzyskano materiały o zróżnicowanej koncentracji powierzchniowych grup tlenowych. Miareczkowanie potencjometryczne wykazało zróżnicowane właściwości kwasowo-zasadowe adsorbentów (wartości pH_{PZC} od 3,6 do 11,5).

Badania kinetyki i równowagi adsorpcji z wodnych roztworów (pH~7) substancji organicznych (fenolu, 4-nitrofenolu i nitrobenzenu) przeprowadzono dla całej serii materiałów węglowych. Na podstawie badań równowagowych adsorpcji odnotowano wzrost ilości zaadsorbowanej wraz ze wzrostem temperatury modyfikacji materiałów węglowych (związany ze wzrostem hydrofobowych właściwości węgla) (Rysunek 6).

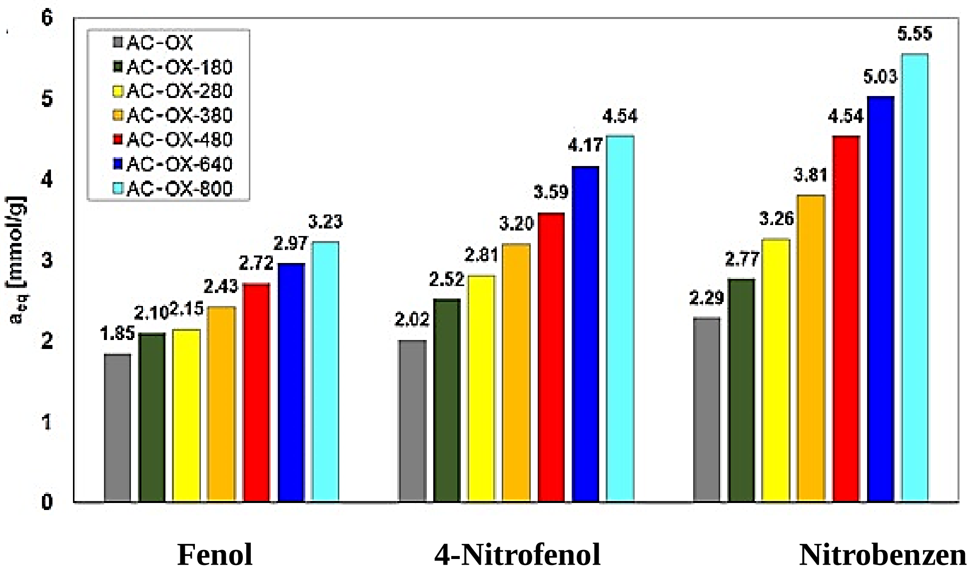

Rysunek 6. Maksymalne ilości zaadsorbowane na badanych węglach aktywnych [D2].

Przeprowadzone pomiary kinetyczne ujawniły wpływ właściwości powierzchni na proces adsorpcji. Wartości czasu połówkowego adsorpcji ($t_{1/2}$) potwierdziły największą szybkość adsorpcji w przypadku nitrobenzenu (adsorbat charakteryzujący się największą hydrofobowością, a zatem najsilniejszymi oddziaływaniami z płaszczyznami grafenowymi węgla). W badanych układach doświadczalnych przeważały oddziaływania dyspersyjne pomiędzy elektronami π pierścienia aromatycznego adsorbatu a elektronami π warstw grafenowych adsorbentu. W przypadku 4-nitrofenolu i fenolu (adsorbaty charakteryzujące się mniejszą hydrofobowością) proces adsorpcji przebiegał wolniej w wyniku interakcji z tlenowymi grupami funkcyjnymi. W przypadku tych adsorbatów odnotowano zwiększenie $t_{1/2}$

spowodowane oddziaływaniami z grupami funkcyjnymi adsorbentu, co wydłużało proces dyfuzji. Stwierdzono również zmniejszenie wartości $t_{1/2}$ wraz ze wzrostem temperatury modyfikacji węgli [44, 45].

Analiza termiczna wykazała, że materiały są stabilne termicznie w szerokim zakresie temperatur (główny rozkład matrycy następuje w temperaturze powyżej 500 °C). Całkowity ubytek masy adsorbentów zmniejszał się wraz z temperaturą modyfikacji termicznej, a powierzchniowe grupy funkcyjne były systematycznie usuwane w trakcie procesu. Badania przeprowadzone na próbkach węgli z zaadsorbowanymi substancjami organicznymi wykazały, że nitrobenzen był najsilniej związany z węglem [D2].

4.5.3. Charakterystyka fizykochemiczna i adsorpcyjna materiałów M3

Materiały węglowe na bazie taniny i bentonitu zbadano pod kątem właściwości teksturalnych, morfologicznych, strukturalnych, termicznych oraz adsorpcyjnych względem barwika – błękitu metylenowego.

Parametry obliczone z izoterm niskotemperaturowej adsorpcji-desorpcji azotu przedstawiono w Tabeli 7. Węgle na bazie taniny i bentonitu charakteryzowały się większą powierzchnią właściwą (S_{BET}) oraz większym udziałem mikroporów w całkowitej porowatości w porównaniu do czystego bentonitu. Izotermy według klasyfikacji IUPAC można opisać jako typ mieszany I i IV wynikający z obecności zarówno mikro- jak również mezoporów (pętla histerezy H4).

Tabela 7. Parametry materiałów organiczno-nieorganicznych otrzymanych na bazie taniny i bentonitu, określone z izoterm adsorpcji-desorpcji azotu [D3].

Nazwa próbki	S_{BET} (m^2/g)	V_t (cm^3/g)	V_{mic} (cm^3/g)	V_{meso} (cm^3/g)	V_{mic}/V_t	V_{meso}/V_t
TBC-1	128	0,09	0,06	0,02	0,72	0,20
TBC-2	194	0,13	0,10	0,02	0,80	0,13
TBC-3	230	0,14	0,11	0,02	0,81	0,12
TC	380	0,23	0,20	0,02	0,86	0,10
TBC-0,5	86	0,08	0,05	0,03	0,61	0,39
Bentonit pirolizowany	3	0,01	-	0,01	0,59	0,39
Bentonit	86	0,12	0,01	0,08	0,08	0,70

Analiza SEM została wykorzystana do oceny morfologii karbonizowanych materiałów. Obrazowanie SEM wykazało, że węgiel występuje w formie cząstek o nieregularnym kształcie o rozmiarach 1-1,5 µm i składa się z amorficznych struktur węgla położonych w warstwowej strukturze bentonitu. W wyniku wprowadzania węgla w przestrzenie międzypłaszczyznowe materiału bentonitowego podczas procesów modyfikacji i pirolizy zaobserwowano strukturalną degradację. Warstwowa struktura bentonitu uległa zniszczeniu podczas pirolizy z powodu usunięcia wody znajdującej się między warstwami bentonitu oraz dihydroksylacji.

Właściwości kwasowo-zasadowe materiałów zbadano stosując miareczkowanie potencjometryczne. Obojętny charakter pirolizowanej taniny może być spowodowany usunięciem grup tlenowych (głównie fenolowych) (pH~7). Materiały TBC-1, TBC-2, TBC-3 wskazują na obecność grup o charakterze kwasowym (pH_{PZC} = 5,84, 6,39, 6,41). Materiał TBC-0,5 oraz bentonit pirolizowany i bentonit ujawniły obecność grup funkcyjnych o charakterze zasadowym (pH_{PZC} = 8,55, 7,90 i 8,42).

Dane dyfrakcyjne (XRD) potwierdziły, że główna faza krystaliczna bentonitu odpowiadała montmorylonitowi, jednakże wykryto też śladowe ilości kwarcu i muskowitu. Wzrost zawartości taniny w mieszaninie reakcyjnej prowadził do wzrostu zawartości węgla w materiałach po karbonizacji. Analiza XRD potwierdziła, że piroliza niszczy strukturę krystaliczną montmorylonitu (zanik piku podstawowego (001, 2θ = 6°). Wzrost intensywności piku przy 2θ = 25° oraz spadek intensywności pików kwarcu i muskowitu wskazują na wzrost zawartości węgla amorficznego w materiale. Biorąc pod uwagę karbonizowaną taninę, widoczne były dwa charakterystyczne piki przy 2θ = 25° i 50° potwierdzające przeważający udział węgla amorficznego. Ogólnie syntetyzowane materiały są połączeniem bentonitu o zdegradowanej strukturze i węgla amorficznego, który częściowo powstaje w przestrzeni międzypłaszczyznowej warstw bentonitu [46].

Spektroskopię Ramana wykorzystano do uzyskania dodatkowych informacji o strukturze węglowej. Widma zarejestrowano w zakresie 200–3200 cm^{-1}, na których widoczne są dwa charakterystyczne pasma D i G (~1350 i 1600 cm^{-1}). Pasmo D reprezentuje częściowe defekty sieci węglowej, które mogą być głównie spowodowane zniekształceniem strukturalnym (odpychanie pierścieni aromatycznych), natomiast pasmo G odpowiada płaskim drgania atomów węgla w hybrydyzacji sp^2 struktury grafitowej. Szerokie pasma D i G o dużej intensywności wskazują na wysoki stopień nieuporządkowania węgla. Stosunek intensywności pasma I_D/I_G określa stopień grafityzacji materiału. Wartość I_D/I_G nie wykazała istotnej zmiany dla serii materiałów, można zatem stwierdzić, że bentonit nie wpływa na cechy strukturalne fazy węglowej. Stosunek D/G wynosi ~0,8 potwierdzając, że warstwy węglowe są głównie amorficzne (z licznymi defektami i nieuporządkowanymi) [47].

Na widmach FT-IR analizowanych materiałów taninowo-bentonitowych widoczne są piki pochodzące od charakterystycznych drgań fazy montmorylonitowej jednak zarejestrowano też osłabienie intensywności pików względem bentonitu [48, 49, 50].

Analiza termiczna materiałów węglowych na bazie taniny i bentonitu wykazała, że materiały są stabilnie termiczne w szerokim zakresie temperatur a ich główny rozkład następuje w zakresie temperatur 500-600 °C. Maksimum piku na krzywej DTG przesuwa się nieznacznie w kierunku wyższych temperatur dla materiałów z dodatkiem bentonitu (TBC) w porównaniu do próbki kontrolnej (TC).

Badania adsorpcyjne błękitu metylenowego wykazały znaczny wzrost pojemności adsorpcyjnej materiałów przygotowanych z dodatkiem glinokrzemianu w mieszaninach reakcyjnych w porównaniu z próbką kontrolną (TC). Może to być skorelowane z największym udziałem mikroporów w całkowitej porowatości, utrudniających dyfuzję dużych cząsteczek barwnika. Najlepsze właściwości adsorpcyjne stwierdzono dla materiału TBC-0,5 z największym udziałem bentonitu (a_m = 5,78 mg/g) który charakteryzował się najwyższym udziałem mezoporów w całkowitej objętości porów. W przypadku trzech pozostałych próbek TBC-1, TBC-2 i TBC-3 (a_m = 3,90; 4,74; 5,26 mg/g) udział mikro- i mezoporów był porównywalny, natomiast większe różnice występowały w wielkościach powierzchni właściwej (S_{BET}). Dane eksperymentalne zostały opisane z wykorzystaniem izotermy Lagmuira. Sprawdzono, że model Freundlicha, również dobrze opisuje układy eksperymentalne.

Rozważając możliwy mechanizm adsorpcji na taninowo-bentonitowych materiałach węglowych wyróżniono najbardziej prawdopodobne: odziaływania hydrofobowe, elektrostatyczne oraz odziaływania wodorowe (Rysunek 7). Cząsteczka błękitu metylenowego jest naładowana dodatnio i może oddziaływać elektrostatycznie z ujemnie naładowanymi lub bogatymi w elektrony ugrupowaniami. Tworzenie wiązania wodorowego jest możliwe pomiędzy grupami zawierającymi wodór (Si-O-H, C-O-H, Me-O-H) oraz atomami azotu. Jednakże przeważają interakcje π-π między pierścieniami aromatycznymi cząsteczek barwnika i strukturami grafenowymi węgla [51].

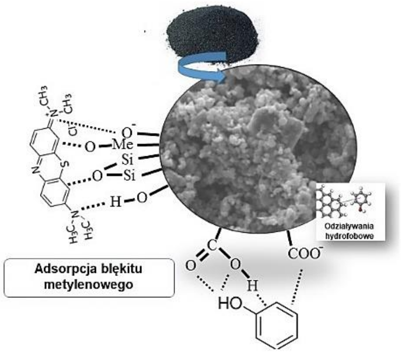

Rysunek 7. Przewidywany mechanizm adsorpcji błękitu na taninowo-bentonitowych materiałach węglowych [D3].

4.5.4. Charakterystyka fizykochemiczna i adsorpcyjna materiałów M4

Zsyntezowane indulinowo-żelazowe materiały węglowe zostały scharakteryzowane pod względem właściwości teksturalnych, strukturalnych, termicznych i adsorpcyjnych.

Parametry otrzymane z niskotemperaturowych izoterm adsorpcji-desorpcji azotu przedstawiono w Tabeli 8. Powierzchnie właściwe (S_{BET}) oraz całkowite objętości porów (V_t) pirolizowanych indulinowo-żelazowych materiałów (S_{BET} = 290-330 m^2/g, V_t = 0,132-0,142 cm^3/g) są znacznie większe niż pirolizowanej induliny (S_{BET} = 7 m^2/g, V_t = 0,007 cm^3/g). Ponadto, odnotowano znaczący udział mikroporów (V_{mic}/V_t = 0,894-0,942) oraz pewien wkład mezoporów (V_{meso}/V_t = 0,058-0,106) w całkowitej objętości porów otrzymanych materiałów. Zmiany w wartościach S_{BET}, V_{mic}, V_{meso} związane były ze składem mieszaniny reakcyjnej. Zwiększenie ilości żelazowego wypełniacza w materiałach spowodowało nieznaczne zmniejszenie powierzchni właściwej oraz ilości mikroporów oraz wzrost liczby mezoporów. Izotermy adsorpcji-desorpcji azotu dla próbek na bazie induliny można opisać jako typ mieszany I i IV (pętle histerezy H1 i H4) według klasyfikacji IUPAC, co wiąże się z występowaniem struktur mikro- i mezoporowatych. Rozkłady wielkości porów (IPSD) potwierdziły, że rozmiary porów mieszczą się głównie w zakresie mikroporowatym, jednakże odnotowano istnienie także porów z zakresu mezoporów [52, 53].

Tabela 8. Parametry materiałów organiczno-nieorganicznych na bazie induliny i pyłu żelazowego, otrzymane z izoterm adsorpcji-desorpcji azotu [D4].

Nazwa próbki	S_{BET} (m^2/g)	V_t (cm^3/g)	V_{mic} (cm^3/g)	V_{meso} (cm^3/g)	V_{mic}/V_t	V_{meso}/V_t
STInd-1	290	0,132	0,118	0,014	0,894	0,106
STInd-2	315	0,142	0,128	0,014	0,901	0,099
STInd-3	313	0,140	0,129	0,011	0,921	0,079
STInd-4	330	0,139	0,131	0,008	0,942	0,058
Indulin/Carbon	7	0,007	-	0,007	-	-

Na podstawie danych XRD wykazano, że głównymi składnikami pyłu magnetycznego są fazy Fe_3O_4, α-Fe_2O_3, SiO_2 i $CaCO_3$. Podczas karbonizacji tlenki żelaza ulegają redukcji do α-Fe. Ponadto w pirolizowanych materiałach wykryto fazy FeO i Fe_3O_4. Zwiększający się udział węgla amorficznego (obecność pików przy $2\theta = 26$ i 50° na dyfraktogramie) zaobserwowano wraz ze wzrostem ilości taniny w materiale. Poza obecnością węgla amorficznego, zarejestrowano obecność grafitu ($2\theta = 31°$). Spektroskopia Ramana ujawniła istnienie dwóch charakterystycznych pasm G i D (~1600, 1310 oraz 2600 cm^{-1}). Szerokie i intensywne pasma D i G analizowanych próbek ujawniły wysoki stopień nieuporządkowania węgla. Wysokie wartości stosunku intensywności pasma D do G uzyskano w zakresie 0,9-1,3 co potwierdziło obecność faz amorficznych w strukturze badanych materiałów węglowych. Widoczny pik będący nadtonem przy ~2600 cm^{-1} odpowiada grafitowi pirolitycznemu o wysoce uporządkowanej strukturze. Największą intensywność piku odnotowano w przypadku próbki z największą zawartością fazy żelazowej. Wzrost ilości żelazowego wypełniacza prowadził do zwiększenia krystaliczności frakcji grafitopodobnej [54, 55].

Analiza termiczna przeprowadzona w szerokim zakresie temperaturowym wykazała wysoką stabilność termiczną adsorbentów. Analiza krzywych DTA ujawniła istnienie szeregu nakładających się na siebie procesów związanych z adsorpcją tlenu, spalaniem węgla, utlenianiem cząstek metali w powietrzu czy usuwaniem grup funkcyjnych. Wykazano zwiększenie stabilności termicznej pirolizowanych materiałów z dodatkiem pyłu żelazowego w porównaniu do pirolizowanej taniny [56].

Miareczkowanie potencjometryczne ujawniło zasadowy charakter analizowanych materiałów (pH_{PZC} = 7,38-9,41) i wykazało spadek w wartości punktu zerowego ładunku powierzchniowego wraz ze zwiększeniem ilości fazy żelazowej w karbonizowanych materiałach.

Adsorpcję błękitu metylenowego z roztworów wodnych przeprowadzono całej serii otrzymanych materiałów. Wykazano, że materiały z dodatkiem magnetycznego wypełniacza (a_m = 4,53-9,71 mg/g) wykazują większą efektywność adsorpcji niż karbonizowana lignina (a_m = 0,44 mg/g). Różnice w maksymalnej ilości zaadsorbowanej można wiązać z charakterystyką teksturalną materiałów oraz innymi właściwościami powierzchni (głównie właściwościami kwasowo-zasadowymi). Materiały z większą ilością wypełniacza charakteryzują się większą ilością mezoporów w całkowitej objętości porów, które mogą ułatwiać penetrację dużej cząsteczki barwnika do wnętrza porów. Parametry obliczono stosując zmodyfikowaną izotermę Langmuira oraz rówanie Freundlicha. Współczynniki korelacji o wartości powyżej 0,9 wykazały, że obie izotermy mogą być zastosowane do scharakteryzowania procesu adsorpcji [57, 58, 59].

Uproszczony mechanizm adsorpcji błękitu metylenowego na serii adsorbentów M4 pokazano na Rysunku 8. Biorąc pod uwagę możliwe interakcje można wyróżnić: oddziaływania hydrofobowe, elektrostatyczne, ale także wiązanie wodorowe analogicznie jak w przypadku serii adsorbentów M3 [D4].

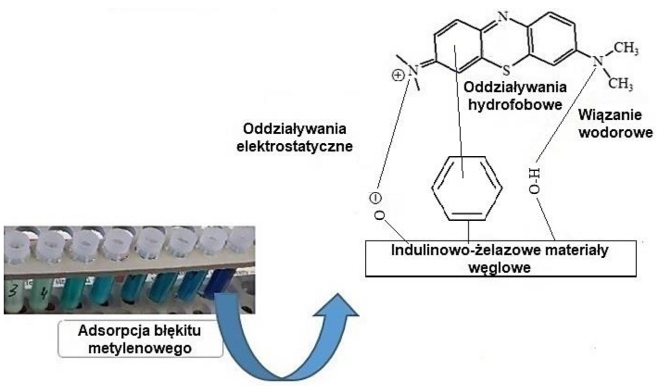

Rysunek 8. Przewidywany mechanizm adsorpcji na indulinowo-żelazowych materiałach węglowych [D4].

4.5.5. Charakterystyka fizykochemiczna materiałów M5 oraz badania przemian fazowych wody

Modyfikowane w kwasie azotowym (V) i wygrzane w różnych temperaturach mezoporowate węgle zbadano pod względem właściwości fizykochemicznych oraz procesów topnienia/krzepnięcia wody w porach.

Parametry teksturalne otrzymane z niskotemperaturowej adsorpcji-desorpcji azotu pokazane są w Tabeli 9.

Tabela 9. Parametry teksturalne modyfikowanych węgli mezoporowatych [D5].

Sample name	S_{BET} (m^2/g)	V_t (cm^3/g)	V_{mic} (cm^3/g)
MC	375	0,40	0,06
MC-OX	174	0,19	0,04
MC-OX-150	178	0,20	0,04
MC-OX-400	214	0,24	0,04
MC-OX-600	317	0,27	0,08
MC-OX-800	325	0,32	0,08

Analiza izoterm adsorpcji-desorpcji azotu w przypadku materiału MC wsparta techniką TEM oraz SAXS wykazała uporządkowaną heksagonalną strukturę o symetrii *P6mm*. Zaobserwowano częściową destrukcję uporządkowanej struktury na skutek zastosowanych modyfikacji: utleniania w kwasie oraz termicznego wygrzewania wcześniej utlenionego materiału węglowego. Modyfikacja w kwasie materiału węglowego powoduje zmniejszenie jego powierzchni właściwej (S_{BET}) oraz całkowitej objętości porów (V_t), ale ma niewielki wpływ na zmianę stopnia uporządkowania (dane SAXS), natomiast wygrzewanie w coraz wyższych temperaturach powoduje stopniowy wzrost wartości tych parametrów oraz znaczącą utratę uporządkowania (dane SAXS). Zjawisko to można wyjaśnić blokowaniem wejścia porów przez grupy tlenowe oraz ich odblokowywanie w procesie termicznego usuwania. Poza udziałem mezoporów w całkowitej objętości porów, odnotowany istotny udział mikroporów. Ponadto, podczas wygrzewania materiałów w wysokich temperaturach, część ścianek ulega zniszczeniu, mniejsze pory mogą łączyć się w większe.

Technika XPS wykazała zróżnicowaną koncentrację powierzchniowych grup tlenowych, natomiast miareczkowanie potencjometryczne odmienny charakter kwasowo-zasadowy badanych materiałów (pH_{PZC} = 4,4-7,0).

Procesy topnienia/krzepnięcia otrzymanych materiałów analizowano technikami DSC oraz DS. Wyznaczono wartości temperatury topnienia wody objętościowej niezwiązanej w porach ($T_{m,b}$) oraz wody znajdującej się w mezoporach ($T_{m,p1}$) oraz mikroporach ($T_{m,p2}$). Na podstawie różnic pomiędzy $T_{m,b}$ oraz $T_{m,p1}$ lub $T_{m,p2}$ obliczono wartości przesunięć temperatur ΔT (Tabela 10). Należy podkreślić, że obie techniki wykazały bardzo podobne zmiany w temperaturach topnienia/krzepnięcia wody skondensowanej w porach oraz różnice w wartościach ΔT. Utlenienie w kwasie spowodowało obniżenie temperatury topnienia wody związanej w porach, natomiast termiczne modyfikacje stopniowy wzrost tych wartości. Zależność pomiędzy temperaturami topnienia wody, a ilością grup tlenowych na powierzchni materiałów węglowych (kwasowością) potwierdza korelacja pomiędzy pH_{PZC} a ΔT (R^2>0,95). Obserwowane zmiany procesów topnienia/krzepnięcia w porach można wyjaśnić zróżnicowaniem oddziaływań adsorbat-adsorbent i adsorbat-adsorbat. Adsorbat o charakterze hydrofobowym silnie oddziałuje z węglowymi płaszczyznami grafenowymi węgla, natomiast adsorbat hydrofilowy wykazuje duże powinowactwo do tlenowych warstw powierzchniowych. W przypadku badanych modyfikowanych materiałów o różnych właściwościach kwasowo-zasadowych skutkuje to osłabieniem oddziaływań bocznych między cząsteczkami wody w przypadku utlenionych węgli ze względu na ich zaangażowanie w interakcje z grupami powierzchniowymi. Natomiast w przypadku materiałów o małej liczbie grup tlenowych przeważają oddziaływania boczne między cząsteczkami wody, a ich oddziaływania z warstwami grafenowymi węgla są słabsze. Obserwowany spadek temperatur topnienia wody w porach materiałów utlenionych można więc wiązać ze zmniejszeniem oddziaływań bocznych niezbędnych do powstania fazy stałej. Natomiast wzrost interakcji między cząsteczkami wody a grupami powierzchniowymi węgla powoduje wzrost temperatury topnienia.

Tabela 10. Temperatury topnienia wody objętościowej i wody w porach węgli MC, MC-OX, MC-OX-150, MC-OX-600 i MC-OX-800; dane otrzymane z pomiarów DSC/DS [D5].

Nazwa próbki	$T_{m,b}$ **[K]**	$T_{m,p1}$ **[K]**	$T_{m,p2}$ **[K]**	ΔT_1 **[K]**	ΔT_2 **[K]**
MC	$274_{DSC}/273_{DS}$	$226_{DSC}/226_{DS}$	$254_{DSC}/253_{DS}$	$-48_{DSC}/-47_{DS}$	$-20_{DSC}/-20_{DS}$
MC-OX	$274_{DSC}/274_{DS}$	$217_{DSC}/217_{DS}$	$239_{DSC}/239_{DS}$	$-57_{DSC}/-57_{DS}$	$-35_{DSC}/-35_{DS}$
MC-OX-150	$274_{DSC}/274_{DS}$	$217_{DSC}/217_{DS}$	$239_{DSC}/239_{DS}$	$-57_{DSC}/-57_{DS}$	$-35_{DSC}/-35_{DS}$
MC-OX-400	$274_{DSC}/274_{DS}$	$221_{DSC}/221_{DS}$	$242_{DSC}/242_{DS}$	$-53_{DSC}/-53_{DS}$	$-32_{DSC}/-32_{DS}$
MC-OX-600	$274_{DSC}/274_{DS}$	$223_{DSC}/224_{DS}$	$243_{DSC}/243_{DS}$	$-51_{DSC}/-50_{DS}$	$-31_{DSC}/-31_{DS}$
MC-OX-800	$274_{DSC}/274_{DS}$	$225_{DSC}/225_{DS}$	$246_{DSC}/247_{DS}$	$-49_{DSC}/-48_{DS}$	$-28_{DSC}/-29_{DS}$

Poza badaniami przesunięć temperatur topnienia w porach analizie poddano formy struktur lodu związanego w porach materiałów węglowych. Stwierdzono istnienie trzech charakterystycznych czasów relaskacji związanych z istnieniem różnych struktur lodu: głównie heksangonalnego, kubicznego, a także odnotowano istnienie lodu o nieuporządkowanej strukturze. Należy podkreślić konieczność dalszych badań, aby zbadać możliwe formy krystaliczne w układzie porów o zróżnicowanej chemii powierzchni. Biorąc pod uwagę zastosowania materiałów porowatych w technice, badania przemian fazowych w szerokim zakresie temperatur mają duże znaczenie [D5].

5. Podsumowanie

W pracy doktorskiej *Badania procesów adsorpcyjnych i przemian fazowych zachodzących w porach materiałów zróżnicowanych strukturalnie i chemicznie* zbadano pięć serii materiałów (materiały **M1-M5**). Materiały analizowano różnymi technikami badawczymi: niskotemperaturowa adsorpcja-desorpcja azotu, mikroskopia elektronowa, dyfrakcja rentgenowska, niskokątowe rozpraszanie promieni rentgenowskich, spektroskopia FT-IR/ATR, spektroskopia Ramana, rentgenowska spektroskopia fotoelektronów, analiza termiczna sprzężona ze spektrometrią mas, skaningowa kalorymetria różnicowa, spektroskopia dielektryczna.

W przypadku materiałów **M1** wykazano, że dodatek trietoskywinylosilanu (TEVS) do 1,4-dywinylobenzenu (DVB) wpływał na rozwinięcie struktury materiałów. Dla wszystkich badanych materiałów najwyższy ubytek stężenia adsorbatu stwierdzono dla nitrobenzenu, a najniższy dla fenolu, co było związane z właściwościami adsorbatów (różnice w ich rozpuszczalności/hydrofobowości). Wykazano także zróżnicowaną selektywność materiałów względem rozważanych układów adsorpcyjnych. Badania kinetyki adsorpcji ujawniły ogólny wpływ kilku czynników: właściwości hydrofobowych/hydrofilowych, strukturalnych właściwości adsorbentu, pęcznienia polimeru, oddziaływań adsorbent-adsorbat.

W przypadku materiałów **M2** udowodniono skuteczność modyfikacji chemicznej oraz modyfikacji termicznych. Otrzymane modyfikowane węgle aktywne były zróżnicowane pod względem właściwości teksturalnych, morfologicznych oraz chemii powierzchni. Modyfikacja materiałów w kwasie spowodowała redukcje w wielkościach powierzchni właściwej (S_{BET}) oraz całkowitej objętości porów (V_t), natomiast dalsze modyfikacje termiczne w coraz wyższych temperaturach spowodowały wzrost tych wielkości związanych z usuwaniem tlenowych grup powierzchniowych mogących blokować dostępną przestrzeń porów. Stopniowy wzrost maksymalnych ilości zaadsorbowanych zaobserwowano dla wszystkich badanych układów wraz ze spadkiem ilości tlenowych grup funkcyjnych (wzrost zasadowych właściwości materiałów). Najwyższe wartości adsorpcji uzyskano w przypadku nitrobenzenu charakteryzującego się największą hydrofobowością, a najniższe dla fenolu o najmniejszej hydrofobowości, pośrednie dla 4-nitrofenolu o pośredniej hydrofobowości.

Badania kinetyki adsorpcji ujawniły wydłużony czas dyfuzji w przypadku próbek o najwyższej koncentracji grup tlenowych ujawniający odziaływania cząsteczek adsorbatu z grupami tlenowymi na powierzchni węgli. Jednakże oddziaływania dyspersyjne pomiędzy elektronami π pierścienia aromatycznego adsorbatu a elektronami π warstw grafenowych adsorbentu są także zauważalne.

W przypadku adsorbentów **M3-M4** wykazano wyraźny efekt składu mieszanin na właściwości teksturalne, morfologiczne, strukturalne, termiczne i adsorpcyjne taninowo-bentonitowych lub indulinowo-żelazowych materiałów węglowych. Wykazano, że zwiększenie ilości bentonitu lub magnetycznego pyłu żelazowego wpływało na zwiększenie udziału mezoporów w całkowitej porowatości materiałów, których istnienie wspomagało dyfuzję dużej cząsteczki barwnika. Najwyższą maksymalną adsorpcję odnotowano dla materiału z największą ilością gliny lub żelazowego wypełniacza (największy udział mezoporów). Ponadto pirolizowane materiały dwufazowe charakteryzowały się znacznie lepszymi właściwościami teksturalnymi oraz adsorpcyjnymi w porównaniu do materiałów otrzymanych na bazie jedynie pirolizowanej taniny lub induliny. Przewidywany mechanizm adsorpcji obejmował istnienie odziaływań: hydrofobowych (odziaływania pomiędzy pierścieniem barwnika a płaszczyznami grafenowymi węgla), elektrostatycznych (pomiędzy dodatnio naładowaną cząsteczką barwnika a ujemnie naładowanymi grupami funkcyjnymi) oraz możliwe występowanie wiązania wodorowego. Ważnym aspektem prac D3 i D4 była możliwość wykorzystania odpadów przemysłowych lub surowców naturalnych, których ilość na świecie drastycznie rośnie. Powoduje to wzrost intensywności badań związanych z ich ponownym wykorzystaniem/przetwarzaniem.

W przypadku materiałów **M5** wykazano zróżnicowaną charakterystykę fizykochemiczną mezoporowatych sorbentów zsyntezowanych na bazie matrycy krzemionkowej (SBA-15). Analiza teksturalna wykazała, ze otrzymano materiał o uporządkowanej heksagonalnej strukturze, która uległa częściowemu zniszczeniu na skutek zastosowanych modyfikacji. Zróżnicowana chemia powierzchni (różna ilość tlenowych grup powierzchniowych, zróżnicowany charakter kwasowo-zasadowy) znacząco wpłynęła na przesunięcia temperatur topnienia wody w porach mezoporowatych materiałów, co powiązano ze zróżnicowaniem oddziaływań adsorbat-adorbent i adsorbat-adsorbat. Poza badaniami przesunięć temperatur topnienia wody związanej w porach spowodowanymi ich modyfikacjami, zidentyfikowano także możliwe struktury lodu (heksagonalny, kubiczny oraz nieuporządkowany). Wiedza na temat procesów topnienia/krzepnięcia w porach jest ważna ze względu na możliwość zastosowania jej w praktyce (adsorbenty, materiały techniczne, zastosowania nanotechnologiczne).

Wszystkie analizowane adsorbenty charakteryzowały się wysoką stabilnością termiczną (rozkład w temperaturach powyżej 350 °C) jednak zwiększanie ilości niektórych składników mieszaniny reakcyjnej powodowało wzrost wytrzymałości termicznej materiałów. Materiały węglowe charakteryzowały się nieco wyższą wytrzymałością termiczną niż materiały polimerowe. Analiza MS produktów gazowych pozwoliła na pełniejszą interpretację mechanizmu odziaływań adsorbent-adsorbat.

Wyniki otrzymane w ramach realizacji rozprawy doktorskiej stanowią istotny wkład w rozwój badań nad otrzymywaniem i charakterystyką materiałów do różnego typu zastosowań. Kompleksowa charakterystyka tekstury, morfologii, chemii powierzchni, adsorpcji i stabilności termicznej wsparta różnymi technikami, jest potrzebna zarówno z fizykochemicznego punktu widzenia, jak i możliwych zastosowań materiałów.

Przyszłe zadania badawcze zostaną rozszerzone o opracowywanie oraz badania nowych materiałów o złożonej strukturze i specyficznej selektywności jako potencjalnych materiałów do oczyszczania wód i ścieków lub materiałów do ściśle sprecyzowanych zastosowań.

6. Stosowane skróty i symbole

Stosowany w pracy doktorskiej wykaz skrótów i symboli znajduje się w Tabeli 9 oraz 10.

Tabela 9. Wykaz ważnych skrótów stosowanych w rozprawie doktorskiej.

Skrót	**Wyjaśnienie skrótu**	**Objaśnienie z języka angielskiego**
AIBN	Azobis(izobutyronitryl)	*Azobisisobutyronitrile*
ATR	Osłabione całkowite wewnętrzne odbicie	*Attenuated Total Reflectance*
BET	Teoria Brunauera, Emetta i Tallera	*Brunauer, Emmett and Teller*
BJH	Rozkład wielkości porów Baretta, Joynera i Halendy	*Barrett- Joyner-Halenda*
D	Rozprawa doktorska	*Dissertation*
DS	Spektroskopia dielektryczna	*Dielectric spectroscopy*
DSC	Skaningowa kalorymetria różnicowa	*Differential Scanning Calorimetry*
DTA	Różnicowa analiza termiczna	*Differential Thermal Analysis*
DTG	Pochodna krzywej termograwimetrycznej	*Derivative Thermal Analysis*
DVB	Dywinylobenzen	*Divinylobenzene*
FT-IR	Spektroskopia w podczerwieni z transformacją Fouriera	*Fourier Transform Infrared Spectroscopy*

GAC	Granulowany węgiel aktywny	*Granulated Activated Carbon*
GL	Uogólniona postać izotermy Langmuira	*Generalized Langmuir*
FOE	Równanie kinetyki adsorpcji I rzędu	*First Order Equation*
IF	Wskaźnik cytowań	*Impact Factor*
L	Izoterma Langmuira	*Langmuir Isotherm*
MOE	Równanie mieszane kinetyki I i II rzędu	*Mixed Order Equarion*
MEiN	Ministerstwo Edukacji i Nauki	-
MS	Spektrometria mas	*Mass Spectrometry*
NLDFT	Nielokalna teoria funkcjonału gęstości	*Non-Local Denisty Fuctional Theory*
SAXS	Niskokątowe rozpraszanie promieni rentgenowskich	*Small-Angle X-Ray Scaterring*
SEM	Skaningowa mikroskopia elektronowa	*Scanning Electron Microscopy*
TG	Termograwimetria	*Thermogravimetry*
PSD	Rozkład wielkości porów	*Pore Size Distribution*
T	Izoterma Tótha	*Tóth Isotherm*
TEM	Transmisyjna spektroskopia elektronowa	*Transmission Electron Microscopy*
TEOS	Tetraetoksysilan	*Tetraethoxysilane*
TEVS	Trietoskywinylosilan	*Triethoxyvinylosilane*
UHV	Skrajnie wysoka próżnia	*Ultra High Vaccum*

S	Materiał uzupełniający do artykułu	*Supplementary Material*
UV-Vis	Nadfiolet - Światło widzialne	*Ultraviolet-Visible*
XPS	Rentgenowska spektroskopia fotoelektronów	*X-Ray Photoelectron Spectroscopy*
XRD	Dyfrakcja rentgenowska	*X-Ray Diffraction*

Tabela 10. Wykaz najważniejszych używanych symboli.

Symbol	**Objaśnienie symbolu**
A	Absorbancja
a_{eq}	Ilość substancji zaadsorbowanej w równowadze
a_m	Maksymalna ilość zaadsorbowana
c_{eq}	Stężenie adsorbatu w stanie równowagi
c_0	Początkowe stężenie roztworu adsorbatu
D_h	Hydrauliczny promień porów
m, n	Parametry heterogeniczności
K	Stała równowagi
p/p_0	Ciśnienie względne
pH_{PZC}	Punkt zerowego ładunku
$t_{1/2}$	Czas połówkowy
V	Objętość roztworu
V_{mic}	Objętość mikroporów
V_{meso}	Objętość mezoporów
V_t	Całkowita objętość porów
T_m	Temperatura topnienia
$T_{m,b}$	Temperatura topnienia wody objętościowej
$T_{m,p1}$	Temperatura topnienia wody skondensowanej w mezoporach

$T_{m,p2}$	Temperatura topnienia wody skondensowanej w mikroporach
S_{BET}	Powierzchnia BET
w	Masa adsorbentu
ΔT	Różnica pomiędzy $T_{m,b}$ i $T_{m,\, p1}$ lub $T_{m,p2}$
λ	Długość fali

7. Życiorys naukowy

Praca:

- 10/2022-obecnie – zatrudnienie na stanowisku asystenta badawczo-dydaktycznego w Katedrze Podstaw Techniki Wydziału Inżynierii Produkcji Uniwersytetu Przyrodniczego w Lublinie

Edukacja:

- 2018-2023 – Studia stacjonarne III stopnia na kierunku chemia realizowane w ramach projektu *Międzynarodowe Studia Doktoranckie z Chemii* na Uniwersytecie Marii Curie-Skłodowskiej w Lublinie
- 2016-2017 – Studia podyplomowe przygotowujące do nauczania chemii w szkole na III i IV etapie edukacyjnym prowadzone przez Wydział Chemii UMCS
- 2013-2018 – Studia stacjonarne I oraz II stopnia na kierunku chemia o specjalności analityka chemiczna na Uniwersytecie Marii Curie-Skłodowskiej w Lublinie
- 2010-2013 – V Liceum Ogólnokształcące im. Marii Skłodowskiej-Curie w Lublinie, klasa o profilu biologiczno-chemicznym

Publikacje i monografie (Numer ORCID: 0000-0002-3437-8509):

I. Publikacje:

1. Alicja Bosacka, Małgorzata Zienkiewicz-Strzałka, Małgorzata Śliwińska Bartkowiak, Angelina Sterczyńska, Dariusz Sternik, Konrad Rotnicki, Microporous and Mesoporous Materials 2023, 351, 112477, https://doi.org/10.1016/j.micromeso.2023.112477
2. Mariia Galaburda, Alicja Bosacka, Dariusz Sternik, Olena Oranska, Mykola Borysenko Volodymyr Gun'ko, Anna Derylo-Marczewska, *Physicochemical and Sorption Characteristics of Carbon Biochars Based on Lignin and Industrial Waste Magnetic Iron Dust*, Water 2023, 15(1), 189, https://doi.org/10.3390/w15010189

3. Mariia Galaburda, Alicja Bosacka, Dariusz Sternik, Viktor Bogatyrov, Olena Oranska, Volodymyr Gun'ko, Anna Deryło-Marczewska, *Development, Synthesis and Characterization of Tannin/Bentonite-Derived Biochar for Water and Wastewater Treatment from Methylene Blue,* Water 2022, 14(15), 2407, https://doi.org/10.3390/w14152407
4. Alicja Bosacka, Małgorzata Zienkiewicz-Strzałka, Anna Deryło-Marczewska, Agnieszka Chrzanowska, Małgorzata Wasilewska, Dariusz Sternik, *Physicochemical, structural, and adsorption properties of chemically and thermally modified activated carbons,* Colloids and Surfaces A: Physicochemical and Engineering Aspects 2022, 647, 129130, https://doi.org/10.1016/j.colsurfa.2022.129130
5. Alicja Bosacka, Małgorzata Zienkiewicz-Strzałka, Anna Deryło-Marczewska. Małgorzata Wasilewska, Beata Podkościelna, *Physicochemical and Adsorption Characteristics of Divinylbenzene-co-Triethoxyvinylsilane Microspheres as Materials for the Removal of Organic Compounds,* Molecules 2021, 26(8), 2396, https://doi.org/10.3390/molecules26082396
6. Alicja Bosacka, Małgorzata Zienkiewicz-Strzałka, *Actual challenges, opportunities, and perspectives of composite materials*, Annales Universitatis Mariae Curie-Skłodowska Lublin-Polonia Sectio AA, 2019, 74(1), DOI: 10.17951/aa.2019.74.1.41-54

II. Monografie:

1. Agnieszka Chrzanowska, Anna Wiejak, Anna Deryło-Marczewska, Alicja Bosacka, Rozdział w tomie *Nauka i przemysł – metody spektroskopowe w praktyce, nowe wyzwania i możliwości*, Synteza i właściwości mezokomórkowych pianek krzemionkowych, Wydawnictwo UMCS, 2022, s.428-431, ISBN: 978-83-227-9602-3
2. Alicja Bosacka, Victoriia Paientko, Olena Orańska, Yurii Lytvynenko, Natalia Stolyarchuk, Roman Kozakevych, Stanislaw Sevstynow, Natalia Hurieva, Ivan Shersheniuk, Aleksander Matkovsky, Volodymyr Gun'ko, Małgorzata Zienkiewicz-Strzałka, Anna Deryło-Marczewska, Agnieszka Chrzanowska, Rozdział w tomie *Nauka*

i przemysł – lubelskie spotkania studenckie, Composites based on kaolin, activated carbon, and lavender as cosmetic ingrediesnts, Wydawnictwo UMCS, 2022, s.306-309, ISBN: 978-83-227-9603-0

3. Alicja Bosacka, Anna Deryło-Marczewska, Beata Podkościelna, Rozdział w monografii *Proceedings of the 17th International Students Conference in Modern Analytical Chemistry, Faculty of Science of Charles University,* FTIR/ATR technique in the analysis of divinylbenzene silica composite, Praga 2021, s. 115-120, ISBN: 978-80-7444-089-2
4. Alicja Bosacka, Anna Deryło-Marczewska, Małgorzata Zienkiewicz-Strzałka, Rozdział w materiale pokonferencyjnym *Nauka i przemysł – lubelskie spotkania studenckie*, Synteza i badania nieorganiczno-organicznych materiałów kompozytowych, Wydawnictwo UMCS, 2019, s.20-23, ISBN: 978-83-227-9220-9
5. Alicja Bosacka, Małgorzata Zienkiewicz-Strzałka, Rozdział w monografii *Kwadrans dla Chemii. Zjazd Wiosenny Sekcji Studenckiej Polskiego Towarzystwa Chemicznego*, Oficyna Edukacyjna Krzysztof Pazdro, Obecne trendy w syntezie materiałów kompozytowych, Ustroń 2019, s. 33-40 ISBN: 978-83-7594-191-3

Konferencje międzynarodowe:

I. Komunikaty:

- 11-16.09.2022 – International Conference Nanomaterials: Applications and Properties IEEE-NAP 2022 (Kraków, Lublin), Autorzy: Alicja Bosacka, Viktoriia Paientko, Aleksander Matkovsky, Volodymyr Gun'ko, Anna Derylo-Marczewska, Tytuł prezentacji: *Preparation of kaolin-carbon-orange peel powder composites by knife- or planetary ball milling*
- 24-25.11.2021 – Conference of Young Scientists IGIC-2021 V.I. Vernadsky IGIC of NAS of Ukraine, Autorzy: Alicja Bosacka, Viktoriia Paientko, Olena Oranska, Roman Kozakevych, Natalia Stolyarchuk, Yurii Lytvynenko, Aleksander Matkovsky, Volodymyr

Gun'ko, Anna Deryło-Marczewska, Tytuł prezentacji: *Kaolin/carbon composites mechanochemical synthesis and structural characteristics*

- 20-23.09.2021 – 12th International Conference on "Instrumental Methods of Analysis", IMA 2021 (Thessaloniki, Grecja), Autorzy: Alicja Bosacka, Anna Deryło-Marczewska, Beata Podkościelna, Tytuł prezentacji: *Chemically and thermally modified activated carbons for the removal of aromatic compounds*
- 16-17.09.2021 – 17th International Students Conference on "Modern Analytical Chemistry", 17th ISC (Praga, Czechy), Autorzy: Alicja Bosacka, Anna Deryło-Marczewska, Beata Podkościelna, Tytuł prezentacji: *FTIR/ATR technique in the analysis of divinylbenzene-silica composite*
- 17-18.09.2020 – 16th International Students Conference on "Modern Analytical Chemistry", 16th ISC (Praga, Czechy), Autorzy: Alicja Bosacka, Anna Deryło-Marczewska, Beata Podkościelna, Tytuł prezentacji: *FTIR analysis of organic-inorganic nanocomposite systems*

II. Postery:

- 19-20.10.2022 – Conference of Institute of Surface Chemistry NASU, ISC 2022 (Kijów, Ukraina), Autorzy: Alicja Bosacka, Małgorzata Zienkiewicz-Strzałka, Anna Deryło-Marczewska, Tytuł posteru: *Chemical and thermal modifications of carbons*
- 04-09.09.2022 – European Colloid and Interface Society, ECIS 2022 (Chania, Grecja), Autorzy: Alicja Bosacka, Małgorzata Zienkiewicz-Strzałka, Anna Deryło-Marczewska, Agnieszka Chrzanowska, Małgorzata Wasilewska, and Beata Podkościelna, Tytuł posteru: *Physicochemical and adsorption properties of polymer microspheres as materials for the removal of organic compounds*
- 03-04.03.2022 – Ecological and Environmental Chemistry 2022, EEC-2022 (Kiszyniów, Mołdawia), Autorzy: Mariia Galaburda, Viktor Bogatyrov, Alicja Bosacka, Olena Oranska, Volodymyr Gun'ko, Anna

Deryło-Marczewska, Tytuł posteru: *Physicochemical And Sorption Characteristics of Lignin-Based Materials*

- 29-30.11.2021 – 2nd International Scientific Conference on Contemporary Problems of Geology and Geoecology of Mining (Kijów, Ukraina), Autorzy: Alicja Bosacka, Viktoriia Paientko, Olena Oranska, Roman Kozakevych, Natalia Stolyarchuk, Yurii Lytvynenko, Aleksander Matkovsky, Wołodymyr Gun'ko, Anna Deryło-Marczewska, Tytuł posteru: *Physicochemical and adsorption characteristics of thiomethacrylate-co-divinylbenzene microspheres*
- 20-23.09.2021 – 12th International Conference on Instrumental Methods of Analysis, IMA 2021 (Thessaloniki, Grecja), Autorzy: Alicja Bosacka, Anna Deryło-Marczewska, Agnieszka Chrzanowaska, Małgorzata Wasilewska, Dariusz Sternik, Beata Podkościelna Tytuł posteru: *Physicochemical and adsorption characteristics of thiomethacrylate-co-divinylbenzene microspheres*
- 5-10.09.2021 – European Colloid and Interface Society, ECIS 2021 (Ateny, Grecja), Autorzy: Alicja Bosacka, Anna Deryło-Marczewska, Agnieszka Chrzanowska, Małgorzata Wasilewska, Beata Podkościelna, Tytuł posteru: Physicochemical and adsorption characteristics of S,S'-thiodi-4,1-phenylenebis(thiomethacrylate)-co-divinylbenzene microspheres as materials for the removal of aromatic compounds
- 3-5.12.2019 – X-Ray Investigations of Polymer Structure, XIPS 2019 (Ustroń, Polska), Autorzy: Alicja Bosacka, Małgorzata Zienkiewicz-Strzałka, Beata Podkościelna, Tytuł posteru: X-ray investigations of hybrid composite systems based on the polymer module
- 18-22.06.2019 – 17th European Student Colloids Conference (Warna, Bułgaria), Autorzy: Alicja Bosacka, Anna Deryło-Marczewska, Małgorzata Zienkiewicz-Strzałka, Tytuł posteru: Synthesis and study of ordered mesoporous materials

III. Zgłoszony referat:

- 18.02.2022 – Planta Plus 2022 (Kijów, Ukraina), Autorzy: Alicja Bosacka, Victoriia Paientko, Olena Oranska, Roman Kozakevych, Aleksander Matkovsky, Volodymyr Gun'ko, Anna Deryło-Marczewska, Tytuł referatu: Kinetic release of anthocyanins and chlorophylls by kaolin-carbon-plant composites
- 18-19.11.2021 – Conference of Chemistry, Bio- and Nanotchnologies, Ecology and Economy in the Cosmetics Industry (Charków, Ukraina), Autorzy: Victoriia Paientko, Alicja Bosacka, Olena Oranska, Ludmila Golovkova, Aleksander Matkovsky, Volodymyr Gun'ko, Anna Deryło-Marczewska, Tytuł referatu: Composite fillers of dessert-stuffs for controling delivery of bioactive substances

Konferencje krajowe:

I. Komunikaty:

- 23.01.2021 – National Scientific Conference "Knowledge - Key to Success", Fundacja Promovendi (on-line), Autorzy: Alicja Bosacka, Tytuł prezentacji: *Kinetic studies of hybrid polymer materials*
- 24.11.2020 – Konferencja „OMNIBUS" cz. VI Marta Rachwał Konferencje Naukowe (Kraków, Polska, on-line), Autorzy: Alicja Bosacka, Tytuł prezentacji: *Otrzymywanie i badania modyfikowanych mezoporowatych materiałow węglowych*
- 14.11.2020 – National Scientific e-Conference "e-Factory of Science, Fundcja Promovendi (on-line), Autorzy: Alicja Bosacka, Tytuł prezentacji: *Suspension potentiometric titration of the functionalized ordered mesoporous carbon*
- 26.09.2020 – National Scientific Conference "Understand the Science". Fundacja Promovendi (on-line), Autorzy: Alicja Bosacka, Tytuł prezentacji: *Morphology studies of the functionalized porous samples*
- 08.08.2022 – 1st on-line Summer School. Fundcja Promovendi (on-line), Autorzy: Alicja Bosacka, Tytuł prezentacji: *FTIR/ATR technique in the analysis of inorganic-organic composites*

- 06.06.2020 – National Scientific Conference. Science and Young Researchers. Fundacja Promovendi (on-line), Autorzy: Alicja Bosacka, Tytuł prezentacji: *Study of functionalized materials by XPS technique*
- 02.03.2019 – National Scientific Conference for PhD Students, Fundacja Promovendi (Kraków, Polska), Autorzy: Alicja Bosacka, Tytuł prezentacji: *Nanocomposites and their applications*

II. Postery:

- 11-16.09.2022 – Konferencja Polskiego Towarzystwa Chemicznego (Lublin, Polska), Autorzy: Anna Derylo-Marczewska, Małgorzata Wasilewska, Alicja Bosacka, Cezary Zasada, Beata Podkościelna, Tytuł posteru: *Badanie właściwości fizykochemicznych mikrosfer polimerowych otrzymywanych na bazie diwinylobenzenu*
- 28-29.06.2022 – Ogólnopolskie Sympozjum Nauka i Przemysł – metody spektroskopowe w praktyce, nowe wyzwania i możliwości (Lublin, Polska), Autorzy: Agnieszka Chrzanowska, Anna Wiejak, Anna Deryło-Marczewska, Alicja Bosacka Tytuł posteru: *Synteza i właściwości mezokomórkowych pianek krzemionkowych*
- 27.06.2022 – XI Ogólnopolskie Sympozjum Nauka i przemysł – lubelskie spotkania studenckie, NPLSS 2022 (Lublin, Polska), Autorzy: Alicja Bosacka, Victoriia Paientko, Olena Orańska, Yurii Lytvynenko, Natalia Stolyarchuk, Roman Kozakevych, Stanisław Sevastynov, Natalia Hurieva, Ivan Shersheniuk, Aleksander Matkovsky, Volodymyr Gun'ko, Małgorzata Zienkiewicz-Strzałka, Anna Deryło-Marczewska, Agnieszka Chrzanowska, Tytuł posteru: *Composites based on kaolin, activated carbon, and lavender as cosmetic ingredients*
- 03.04.2020 – XI Ogólnopolska Konferencja Naukowa Młodzi Naukowcy w Polsce - Badania i Rozwój (Lublin, Polska), Autorzy: Alicja Bosacka, Tytuł posteru: *Technika XPS w badaniach modyfikowanych powierzchniowo mezoporowatych materiałów węglowych*

- 22.11.2019 – X Ogólnopolska Konferencja Naukowa Młodzi Naukowcy w Polsce - Badania i Rozwój (Lublin, Polska), Autorzy: Alicja Bosacka, Tytuł posteru: *Charakterystyka, otrzymywanie i badania hybrydowych materiałów kompozytowych*
- 24.06.2019 – IX Ogólnopolskie Sympozjum Nauka i przemysł – lubelskie spotkania studenckie, NPLSS-2019, Autorzy: Alicja Bosacka, Małgorzata Zienkiewicz-Strzałka, Anna Deryło-Marczewska, Tytuł posteru: *Synteza i badania nieorganiczno-organicznych materiałów kompozytowych*
- 10-14.04.2019 – Zjazd Wiosenny Sekcji Studenckiej Polskiego Towarzystwa Chemicznego (Ustroń, Polska), Autorzy: Alicja Bosacka, Tytuł posteru: *Węgiel aktywny i jego właściwości adsorpcyjne*
- 23-24.03.2019 – XI Interdyscyplinarna Konferencja Naukowa TYGIEL 2019 "Interdyscyplinarność kluczem do rozwoju" (Lublin, Polska), Autorzy: Alicja Bosacka, Tytuł posteru: *Materiały porowate w badaniach procesów adsorpcji*
- 02.03.2019 – National Scientific Conference for PhD Students, Fundacja Promovendi (Kraków, Polska), Autorzy: Alicja Bosacka, Tytuł posteru: *Synthesis and application of biocomposites*
- 8.12.2018 – Zjazd zimowy Sekcji Studenckiej Polskiego Towarzystwa Chemicznego, (Warszawa, Polska), Autorzy: Alicja Bosacka, Małgorzata Zienkiewicz-Strzałka, Tytuł posteru: *Obecne trendy w syntezie materiałów kompozytowych*

Szkoły letnie:

- 18-20.05.2022 – Międzynarodowa Szkoła Letnia *SchoolChem 2022* organizowana przez Wydział Chemii Uniwersytetu Marii Curie-Skłodowskiej (Lublin, Polska)
- 7-20.07.2019 – Międzynarodowa Szkoła Letnia *Measurement Science in Chemistry Summer School* współorganizowana przez Uniwersytet Tartu w Estonii (Lyon, Francja)

Staże naukowe:

- 01.07.2022-06.08.2022 – staż naukowy na Wydziale Chemii Uniwersytetu Vigo (Vigo, Hiszpania). Realizowana podczas stażu tematyka badawcza: *Zastosowanie materiałów węglowych do adsorpcji galusanu propylu oraz kwasu galusowego – kinetyka, równowaga, dopasowanie modeli, odzysk substancji*
- 01.10.2021-23.02.2022 – staż naukowy w Instytucie Chemii Powierzchni Narodowej Akademii Nauk (Kijów, Ukraina). Realizowana podczas stażu tematyka badawcza: *Synteza i badania fizykochemiczne materiałów do zastosowań kosmetycznych, spożywczych oraz adsorpcyjnych*

Projekty naukowe i inne efekty pracy naukowej:

- 26.09.2022 – Współautor w zgłoszeniu *Know how.* Tytuł zgłoszenia: *Multifunctionality of black paste based on kaolin-carbon-silica composite doped with herbs: whitening, cleansing, treatment,* Ministerstwo Edukacji i Nauki Ukrainy, Biblioteka Naukowo-Techniczna Ukrainy, Nr 281/1 (2022) (Kijów, Ukraina)
- 15.07.2022 – Współautor w zgłoszeniu *Know how.* Tytuł zgłoszenia *Carbon containing materials for cosmetic purposes,* Ministerstwo Edukacji i Nauki Ukrainy, Biblioteka Naukowo-Techniczna Ukrainy, Nr 268/1 (2022) (Kijów, Ukraina)
- 15.07.2022 – Współautor w zgłoszeniu *Know how.* Tytuł zgłoszenia *Nanostructured fillers and additions of synthetic and natural origin for the imporovement of bioavailability of active components,* Ministerstwo Edukacji i Nauki Ukrainy, Biblioteka Naukowo-Techniczna Ukrainy, Nr 267/1 (2022) (Kijów, Ukraina)
- 2018-2023 – Udział w projekcie *Międzynarodowe Studia Doktoranckie z Chemii, Program Operacyjny Wiedza Edukacja Rozwój, OŚ PRIORYTETOWA III SZKOLNICTWO WYŻSZE DLA GOSPODARKI I ROZWOJU, Działanie 3.2 Studia doktoranckie*

Stypendia:

- Stypendium motywacyjne z projektu *Od studenta do eksperta – ochrona środowiska w praktyce*. Umowa nr UDA-POKL.04.01.02-00-085/09-02 (Studia I stopnia)

Członkostwo w kołach naukowych i stowarzyszeniach:

- Członkostwo w *Polskim Towarzystwie Inżynierii Rolniczej*, Oddział w Lublinie (od 12/2022)
- Członkostwo w *Sekcji Studenckiej Polskiego Towarzystwa Chemicznego* (Studia I-III stopnia)
- Członkostwo w Kole Naukowym *Alkahest* działającym na Wydziale Chemii UMCS (Studia I-III stopnia)

Szkolenia i kursy:

- 24.03-05.05.2020 – Szkolenie *Estimation of Measurement. Uncertainty in Chemical Analysis* organizowane przez Uniwersytet w Tartu w Estonii (26 godzin)
- 21.10-09.12.2019 – Kurs *TELC B2*, Centrum Nauczania i Certyfikacji Języków Obcych UMCS (20 godzin)
- 26.11.2018-07.02.2019 – Szkolenie *LC-MS Validation* organizowane przez Uniwersytet Tartu w Estonii (52 godziny)
- 16.12.2018 – Szkolenie *Auditor Wewnętrzny Systemu Zarządzania wg normy PN-EN ISO/IEC 17025 w laboratorium analitycznym*, Wydział Chemii UMCS (8 godzin)

Znajomość języków obcych:

- Znajomość języka angielskiego na poziomie B2 potwierdzone certyfikatem TELC B2

8. Oryginalne artykuły naukowe i oświadczenia

Teksty publikacji D1-D5 wraz z materiałami dodatkowymi S1, S2, S5 oraz oświadczeniami:

[D1] Alicja Bosacka, Małgorzata Zienkiewicz-Strzałka, Anna Deryło-Marczewska, Małgorzata Wasilewska, Beata Podkościelna, Physicochemical and Adsorption Characteristics of Divinylbenzene-co-Triethoxyvinylsilane Microspheres as Materials for the Removal of Organic Compounds, Molecules 2021, 26(8), 2396, https://doi.org/10.3390/molecules26082396 wraz z materiałem dodatkowym [S1]

molecules

MDPI

Article

Physicochemical and Adsorption Characteristics of Divinylbenzene-*co*-Triethoxyvinylsilane Microspheres as Materials for the Removal of Organic Compounds

Alicja Bosacka *, Małgorzata Zienkiewicz-Strzalka, Małgorzata Wasilewska, Anna Derylo-Marczewska * and Beata Podkościelna

Institute of Chemical Sciences, Faculty of Chemistry, Maria Curie-Sklodowska University,
Maria Curie-Sklodowska Sq. 3, 20-031 Lublin, Poland; malgorzata.zienkiewicz@poczta.umcs.lublin.pl (M.Z.-S.);
malgorzata.wasilewska@poczta.umcs.lublin.pl (M.W.); beatapod@poczta.umcs.lublin.pl (B.P.)
* Correspondence: alicja.bosacka@poczta.umcs.lublin.pl (A.B.); annad@hektor.umcs.lublin.pl (A.D.-M.);
Tel.: +48-81-53-777-66 (A.D.-M.)

Abstract: In this work, organic-inorganic materials with spherical shape consisting of divinylbenzene (DVB) and triethoxyvinylsilane (TEVS) were synthesized and investigated by different complementary techniques. The obtained microspheres may be applied as sorbent systems for the purification of organic compounds from water. The hybrid microspheres combine the properties of the constituents depending on the morphologies and interfacial bonding. In this work, the influence of the molar ratio composition of crosslinked monomer (DVB) and silane coupling agent (TEVS) (DVB:TEVS molar ratios: 1:2, 1:1 and 2:1) on the morphology and quality of organic-inorganic materials have been examined. The materials were analysed using small angle X-ray scattering (SAXS) analysis, low-temperature nitrogen sorption, scanning electron microscopy (SEM) and Fourier transform infrared spectroscopy (FTIR) to provide information on their structural and surface properties. Moreover, thermal analysis was performed to characterize the thermal stability of the studied materials and the adsorbent-adsorbate interactions, while adsorption kinetic studies proved the utility of the synthesized adsorbents for water and wastewater treatment.

Keywords: polymer-inorganic materials; nanostructures; microspheres; adsorption kinetics

Citation: Bosacka, A.; Zienkiewicz-Strzalka, M.; Wasilewska, M.; Derylo-Marczewska, A.; Podkościelna, B. Physicochemical and Adsorption Characteristics of Divinylbenzene-*co*-Triethoxyvinylsilane Microspheres as Materials for the Removal of Organic Compounds. *Molecules* **2021**, *26*, 2396. https://doi.org/10.3390/molecules26082396

Academic Editor:
Bhanu P. S. Chauhan

Received: 27 February 2021
Accepted: 16 April 2021
Published: 20 April 2021

1. Introduction

The development of industry and technology has contributed to the increase in demand for materials with well-defined characteristics and combining several features of different solids in one type of structure [1–3]. Hybrid organic-inorganic materials are the answer to the growing needs of the material market [4,5]. One of the most important actual challenges in designing these combined systems is how to keep or increase the best properties of each component while rejecting or decreasing their limitations [6]. Organic-inorganic materials based on a polymer matrix are some of the most frequently obtained types of hybrid systems because of their ease of synthesis and further modification [7,8].

Generally, polymers have many desirable physical properties including tensile strength, modulus, toughness, or viscoelasticity. Nevertheless, because of their worse mechanical and thermal properties in comparison to metals or ceramics, numerous polymers have restricted use in engineering applications [9,10]. The mechanical and thermal properties of polymers can be improved by combining them in organic-inorganic systems. The connection between the polymer and the inorganic phase improves its strength and toughness. Moreover, the inorganic component provides the mechanical and thermal stability and usually leads to many other desired chemical and physical properties of the hybrid materials [11–15].

Hybrid organic-inorganic materials with spherical shapes (microspheres) can be prepared by different methods (polymerization, extraction, dispersion, solvent evaporation or emulsion techniques). In this work the suspension polymerization method was used to obtain polymer-silane microspheres. Generally, suspension polymerization is a reaction in which a monomers mixture with an initiator is dispersed in a continuous aqueous phase with the addition of a small amount of a suspension agent (stabilizer) [16–18]. The method as well as conditions of synthesis reaction have an influence on the properties of polymer-inorganic microspheres. The adsorption properties of hybrid microspheres result from their porous structures which develop during the polymerization reaction. The amounts, shapes and sizes of pores depend on pore-forming diluents applied to expand the polymer matrix, however, the major factor in developing the surface area is the crosslinking agent (the higher amount of crosslinker, the higher the surface area) [19–22].

Water is an essential compound used for many purposes, from drinking to industrial processes. Both drinking and industrial water must in many cases be treated before use due to the presence of various harmful contaminants [23–25]. Among the different wastewater treatment methods, adsorption is widely used because of its simplicity, good treatment efficiency, the availability of a wide variety of adsorbents, and relatively low costs. Aliphatic or aromatic organic substances including aldehydes, amines, nitrides, pesticides, pharmaceuticals and dyes are generally compounds that are difficult to decompose in water [26–32]. Therefore, the development of effective, inexpensive and selective sorbents is a crucial issue. Traditional sorbents may have many limitations: they can be susceptible to contamination and microbial growth, they may have poor mechanical and thermal stability, not enough efficiency and short life-time. The solution is to combine several solids in one in order to obtain materials with improved properties [25,29].

Adsorption processes of different aromatic compounds from solutions have been widely studied to find the dependencies between the sorption effectiveness and the properties of the adsorbate and adsorbent. Generally, the adsorption effectiveness should be treated as a result of the combined properties of the adsorbent, adsorbate and solvent as well as the parameters of the adsorption process. The affinity of various substances for solid materials depends on many factors: the structure and size of the adsorbate molecules, type of functional groups, solubility, interactions (mainly intra- or inter- molecular hydrogen bonds), as well as the properties of the solvent, and the surface and structure of the adsorbents. Therefore, data interpretation is a complex matter [33,34].

In this work, divinylbenzene-*co*-triethoxyvinysilane (DVB-TEVS) microspheres were synthesized by a copolymerization reaction at three different molar ratios 1:2, 1:1 and 2:1, in which the DVB is the organic phase and TEVS, an inorganic one. The divinylbenzene molecule has an aromatic ring linked with two vinyl groups structure (Figure 18b) while the TEVS used as a crosslinking agent is an inorganic compound with formula ($Si(OCH_3)_3CH_2$) (Figure 18a). Organic-inorganic materials similar to DVB-TEVS are described in the literature, however, there is still an ongoing search for new materials showing high efficiency and selectivity towards various groups of pollutants. The proposed organic-inorganic microspheres show promising properties, especially as adsorbents for the removal of heavy ions and organic compounds from aqueous solutions and selective materials for solid-phase extraction techniques, because of their well-developed porous structures. Also, these materials are characterized by good thermal resistance [35–42].

The obtained samples were analyzed by various techniques. Small angle X-ray diffraction analysis (SAXS) provided detailed information about the structure of these microspherical complex systems. To strengthen and confirm the correctness of the SAXS analysis, these results were correlated and completed with low-temperature nitrogen sorption analysis, scanning electron microscopy (SEM) and also Fourier transform infrared spectroscopy/attenuated total reflection (FTIR/ATR) spectroscopy. In addition, a thermal analysis was conducted to assess the thermal properties of the obtained materials. Moreover, regarding the application in water remediation systems the adsorption properties of the hybrid materials were investigated by kinetic studies.

2. Results and Discussion

2.1. Materials Characteristics

2.1.1. SEM Studies

The effect of the proportions of reacting TEVS and DVB components on the properties of the newly synthesized materials was investigated via scanning electron microscopy (SEM) and further correlated and developed by SAXS and nitrogen adsorption/desorption analysis. It was found that the copolymerization of divinylbenzene with triethoxyvinylsilane by the suspension polymerization method led to obtaining well-defined polymeric-inorganic microspheres. The SEM results presented in Figure 1 show low and high magnification images of the final microspheres.

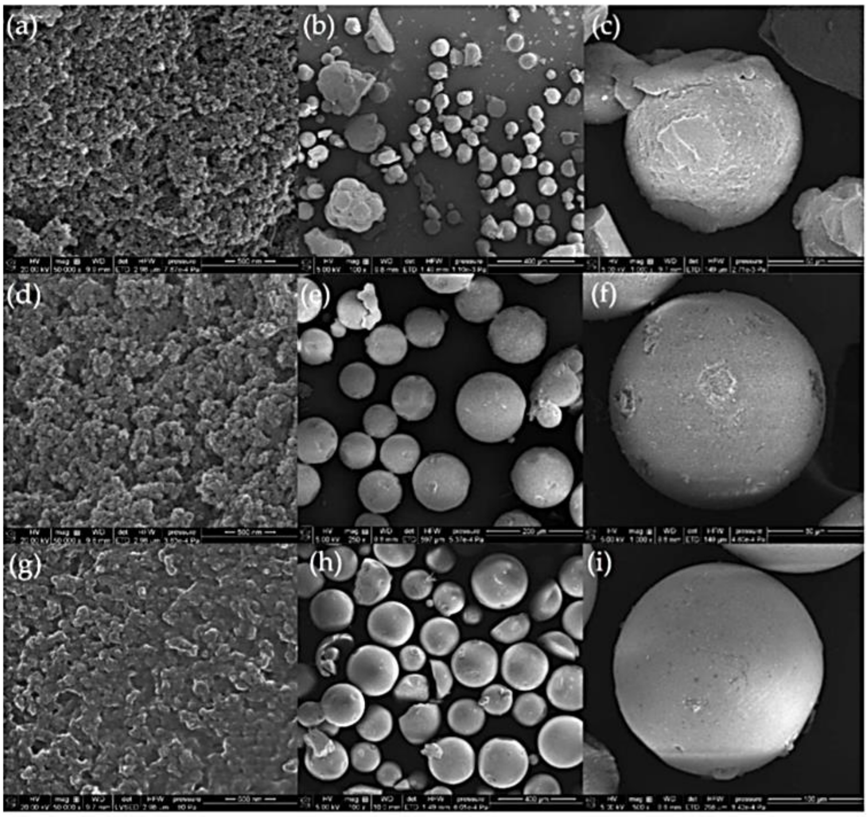

Figure 1. SEM images of DVB:TEVS = 1:2 (**a**–**c**), DVB:TEVS = 1:1 microspheres (**d**–**f**) and DVB:TEVS = 2:1 microspheres (**g**–**i**) in different magnification.

The particles of the studied inorganic-organic materials have spherical shapes with gradually changing surface smoothness and diameters ranging from 50 μm to 200 μm. Moreover, the applied polymerization conditions yielded about 80% microspheres in the range of 100–150 μm. Depending on the molar ratio of components in the reaction mixture, differences in the morphology and porosity of the final microspheres were observed. When the ratio of organic to inorganic phases was 1:2, the spherical morphology of the material is disturbed with many deviations from the ideal spherical form, the material is heterogeneous, and several defects are observed (Figure 1a–c). The most regular shape, the highest homogeneity, and the lowest porosity were observed for the DVB:TEVS = 2:1 sample (Figure 1g–i). In this case, the surface of the spheres is the most uniform and smooth. The DVB:TEVS = 1:1 sample, shows intermediate morphological and pore properties in comparison to the materials synthesized at proportions DVB:TEVS = 2:1 and DVB:TEVS = 1:2 (Figure 1d–f).

The DVB:TEVS = 1:2 spheres are characterized by the most developed surface with the highest degree of roughness. The observed differences in the surface layers of the polymer spheres depending on the fraction of individual components indicate a clear pore-forming nature of the inorganic TEVS component and its role in the formation of an extensive surface on the created materials. The use of a silane coupling agent with a branched crosslinking nature may be responsible for the assembly of an increased porous network. The TEVS contains three ethoxy groups that occupy an area close to the Si atoms, thus limiting the formation of a polymer network in their vicinity and creating a porous system. In this case, the TEVS monomer is responsible for the observed hierarchical roughness and surface vinyl terminations [43,44]. The DVB monomer and crosslinker with its simple unidirectional structure guide the materials into a more monolithic form [45,46].

Depending on the need to create materials for various applications (catalyst supports, adsorbents), strict control of the number of ingredients of different natures has a significant impact on the ultimate morphology and allows obtaining more or less heterogeneous and porous materialstructures.

2.1.2. FTIR/ATR Analysis

FTIR/ATR spectroscopy was applied to assess the advancement in the phase bonding of the organic-inorganic microspheres. The building of dual systems is associated with the content of both polymeric as well as silane phases. Therefore, the characteristic vibrations from divinylbenzene and triethoxyvinylsilane have been observed (Figure 2). The spectra show bands at 1000–1110 cm^{-1} associated with the asymmetrical stretching vibrations of Si-O-C groups, which confirm the incorporation of TEVS into the polymeric structure of the synthesized material. This peak is not observed for divinylbenzene (Figure S1, Supplementary Material). The TEVS introduction into the polymeric phase has been found for all studied materials. However, the peak with the highest intensity is observed for the sample with the highest amount of triethoxyvinylsilane [33]. The existence of stretching bonds C–H of methyl ($-CH_3$), ethyl ($-CH_2-CH_3$) ~2900 cm^{-1} and vinyl groups ($-CH=CH_2$) ~3080 cm^{-1} and ~2998 cm^{-1} and aromatic ring of divinylbenzene ~3020 cm^{-1} are observed. The peak intensity of aromatic ring for DVB:TEVS materials is associated with the sample composition. For DVB:TEVS = 1:2 this peak intensity is the lowest. The stretching vibrations of C=C from vinyl groups are found at 1650 cm^{-1}. The ring stretches of aromatic ring are visible at 1600, 1500 and 1450 cm^{-1}, respectively. The deformation vibrations of methyl and ethyl groups are observed in the range of 1470–1350 cm^{-1}. Moreover, in the range of 900–650 cm^{-1} is possible to see deformation bands of C-H groups at benzene ring, therefore, the presence out of plane ring and H bending vibrations at 695 and 750 cm^{-1} is detected. Besides, the out of plane bending and twisted vibrations of vinyl groups at 908 and 991 cm^{-1} are observed [36–42].

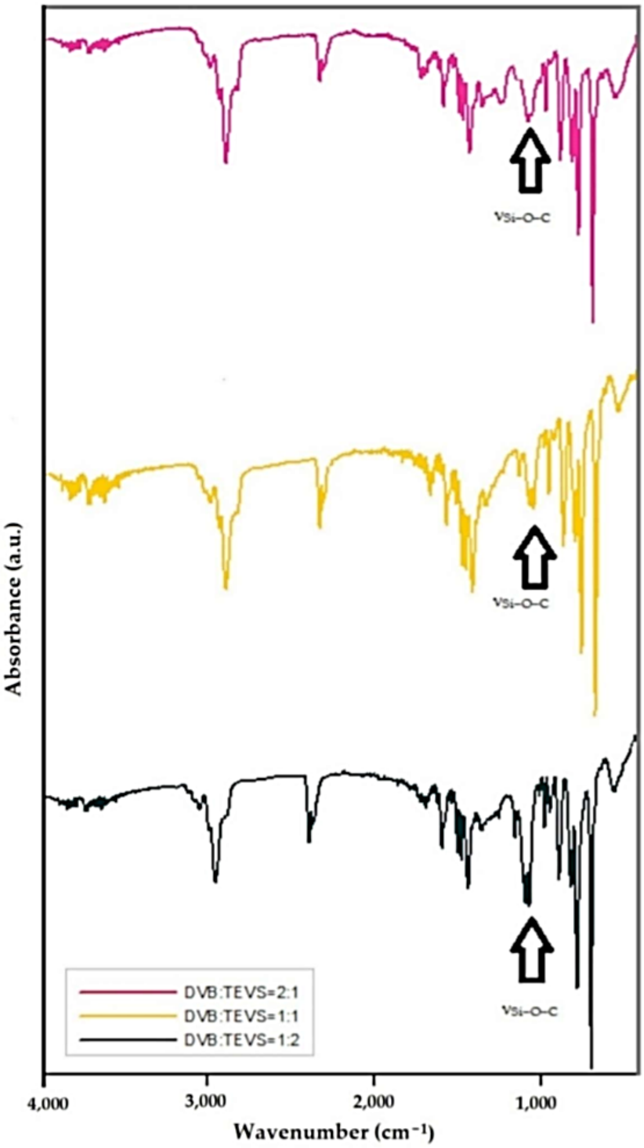

Figure 2. FTIR/ATR spectra for DVB:TEVS materials with phase ratios: 2:1, 1:1 and 1:2.

2.1.3. SAXS Investigation

Investigation of new materials requires the detailed analysis of structural aspects due to their importance in adsorption/desorption or immobilization processes. In this part, the microstructure of organic-inorganic materials was investigated by small-angle X-ray scattering. Table 1 includes the investigated materials and selected microstructure parameters determined from SAXS analysis.

Table 1. Structural parameters of the investigated organic-inorganic systems.

Sample	R [a][Å]	PDDF [b] [Å]	D_{max} (PDDF) [c] [Å]	R_g[Å] (Sphere) [d]		Porod Approximation				Specific Surface Area	
				PDDF [e]	Guinier [f]	K [g]	Q [h] [$Å^{-1}$]	C_0 [i]	S/V [$Å^{-1}$]	S_{SAXS} [j] [m^2/g]	S_{BET} [m^2/g]
DVB:TEVS = 1:2	45	110(Spherical) 45(Rod-type cross-section)	399	125	115	0.798	34.7	12.1	0.061	610	521
DVB:TEVS = 1:1	35	140	420	112	101	0.649	27.8	11.8	0.048	480	402
DVB:TEVS = 2:1	30	179	504	110	95	0.511	29.6	13.3	0.039	390	316

[a] The volume-weighted particle size distribution Dv(R) as the maximum value of the function. [b] Pair distance distribution function PDDF as the maximum value of the function. [c] Maximum dimension D_{max} means also R-value (distance) at which PDDF goes to 0. This parameter is defined as diameter across the longest dimension of the particles and is zero for $r > D_{max}$. [d] Radius of gyration as the mean square distance from the center of their distribution. R_g provides a measure of the overall size of the scattering objects. [e] R_g determined from p(r) function is proportional to the normalized second moment of p(r) (Equation.(4)) from the whole scattering curve. [f] The Guinier plot, as ln(I(q)) vs. q^2 was used to determine the R_g from the slope of the Guinier plot. [g] Porod constant is proportional to the surface area and the square of the electron density contrast. [h] Scattering invariant Q is proportional to the mean-square density fluctuation of scattering volume. $Q = 2\pi^2 \cdot \Delta\rho^2 \cdot V$ where volume V and scattering contrast Δρ. For calculation Q invariant the scattering intensities to q = 0 and also towards large q should be extrapolated. [i] Bacground constant which illustrates asymptotic decay of the SAXS curve at the high q values. [j] Surface area by SAXS calculated by Equation (2).

Figure 3a shows logarithmic plots of the experimental scattering intensity I(q) as a function of the modulus of the scattering vector, q, corresponding to organic-inorganic samples with different component fractions. The scattering curve is continuous and contains no pronounced extremes or peaks. The lack of a sharp interference peak on the SAXS profile suggests the absence of the regular superstructural forms of domains [47]. The experimental scattering curve includes the sum of the scattering of various phases and their interactions [48,49]. The nature of the scattering curve is similar for all studied samples. However, some differences in the level of scattering were observed. It was found that the introduction of the greater amount of TEVS into the polymeric body raises the intensity of scattering at low-angles.

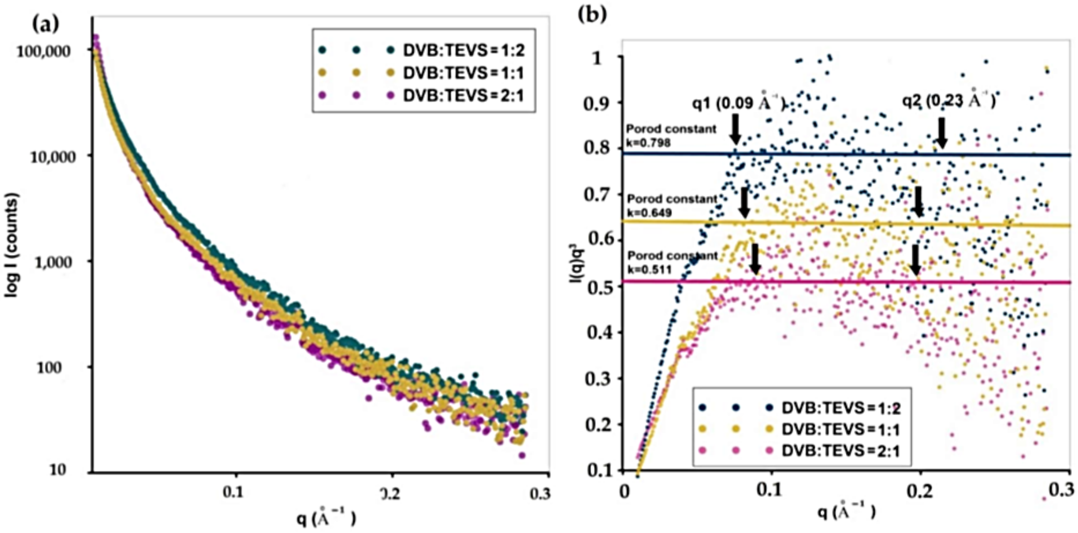

Figure 3. *Cont.*

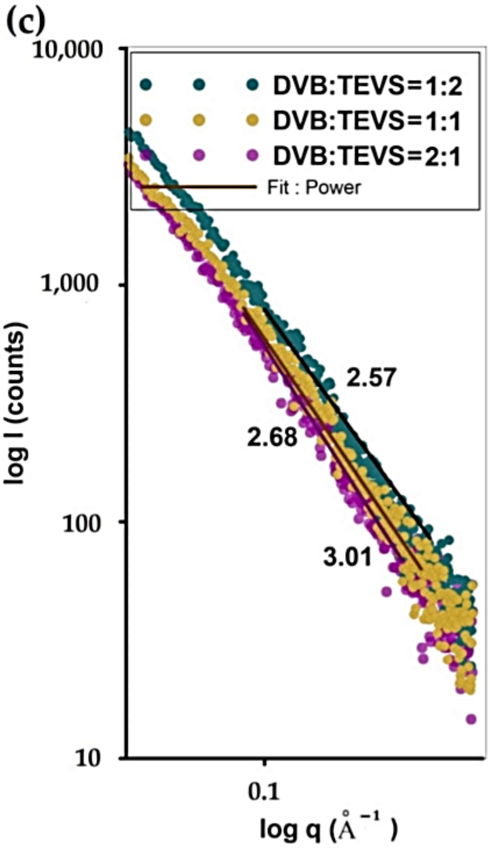

Figure 3. Experimental SAXS profiles corresponding to hybrid microspheres with various amounts of organic and inorganic components (**a**) Porod plots, and Porod constants determined from experimental patterns (**b**). The black arrows show the range of scattering vector suitable for the Porod linear range. The log-log plots of SAXS intensity in the power-law range (**c**).

The highest level of scattering was observed for DVB:TEVS = 1:2 sample, whereas the lowest was noticed for DVB:TEVS = 2:1. Due to the presence of scattering objects (polymer domains) in the materials' body, their size and relative quantity may be responsible for the scattering capacity and observed differences. Although all tested materials have a similar type of morphology, polymer domains in the DVB:TEVS = 1:2 sample should be marked as more visible. The phenomenon can be associated with the enhanced porosity of material as a result of greater amount of TEVS. In the case of this sample (DVB:TEVS = 1:2), increased porosity is associated with a higher amount of crosslinking agent and may cause the presence of additional nanometer forms (pores) able to generate the scattering effect [50,51]. In this way, a comparison of the level of scattering by hybrid samples can provide information about the degree of surface homogeneity [52,53].

The scattering properties of organic-inorganic materials can be discussed by Porod law. In this case, the scattering effect at large q values is applied. According to Porod law, the scattering curves of particle systems and porous materials with smooth surfaces decay proportionally to q^{-3} at large angles ($I(q) \approx k_3/q^3$ for smeared data). When Porod's law is observed for experimental data (like in Figure 3b), it is a good indication of well-defined interfaces between regions of different electron density. Here, the scattered intensity is proportional to the reciprocal of suitable power of scattering vector ($I(q) \sim k^4$ for non-smeared SAXS data and $I(q) \sim k^3$ for smeared SAXS data). Figure 3b shows the calculated Porod plots for investigated samples. Porod curves display a plateau and the SAXS data asymptotically approaches a constant value. The procedure allows evaluating the Porod constant k based on the asymptotic decay of the scattering curve at the higher angles. The amplitude of the asymptote is proportional to the particle's surface-area-to-volume ratio and concentration. The most important feature of the Porod law suggests that the Porod constant is proportional to the surface area and the square of the electron density contrast. In this case, a simple comparison of the Porod constant allows illustrating the differences in the specific surface of materials in a way that is much simpler and faster than conventional methods of testing porosity. Comparing the absolute S/V values calculated from the Porod approximation, a clear decrease in the value for the sample containing the majority of the organic phase is visible. The S/V values equal 0.061 $Å^{-1}$, 0.048 $Å^{-1}$ and 0.039 $Å^{-1}$ for DVB:TEVS = 1:2, DVB:TEVS = 1:1, and DVB:TEVS = 2:1 samples, respectively. This suggests creating an extended three-dimensional surface of material containing mostly an inorganic blowing agent and a significant reduction of this surface by increasing the degree of smoothness using larger amounts of the organic phase. The estimated values of the interface surface from SAXS data (S_{SAXS}) are given in Table 1 and are equal to 521, 402 and 311 m^2/g, respectively. Comparison of the specific surface area determined by using two different methods (low-temperature nitrogen sorption method: Brunauer–Emmett–Teller (BET) and SAXS indicates a correlation between both techniques for evaluating structural characteristics generated by polymer-domains and pores. Slight differences indicate a low amount of closed porosity of the microspheres.

Small-angle X-ray scattering allows conducting statistical analysis of scatters nanostructures. Figure 4a shows the volume-weighted particle (or pore) size distribution Dv(R) from the scattering curve of an ensemble of spherical particles (or pores) with homogeneous inner electron density distribution. Here, the size of the scattering objects can be determined. In this case, all nanometer objects are very similar (they have similar sizes). The difference concerns the relative number of these objects, which is reflected in the intensity of the maxima of Dv(R) curves. For the DVB:TEVS = 1:2 sample (Figure 4a) the size of most inhomogeneities is estimated to 40 nm, however, a significant amount of these objects is in the range from 20 nm to 100 nm. The size of scattering objects was significantly lower for DVB:TEVS = 1:1 and DVB:TEVS = 2:1 samples. Here the Dv(R) function points to the significant number of objects with dimensions of 35 nm and 20–30 nm for DVB:TEVS = 1:1 and DVB:TEVS = 2:1, respectively. Moreover the radius of gyration as the mean square distance from the center of their distribution provides a measure of the overall size of the scattering objects. Here, the DVB:TEVS = 1:2 sample exhibit some cylinder geometry as cross-sectional dimension of the objects in comparison to typical spherical scatters. For DVB:TEVS = 1:1 and DVB:TEVS = 2:1 samples the fit of the PDDF function (pair distance distribution function) was satisfactory only for spherical systems (additional calculations were performed but not presented here). The roughness of the surface was evaluated by investigation of the Porod exponent (Figure 4c). The slope of a log-log plot of intensity vs. q vector shows the fractal dimension of the scattering object. At high q values, the q^{-3} function illustrates the smooth interfaces. The log-log plots of investigated samples shows the linear range of Porod range. The Porod exponent for scattering from materials is between 2 and 3 for a surface fractal in three-dimensional space. The obtained results suggest the smooth surface for DVB:TEVS = 2:1 microspheres.

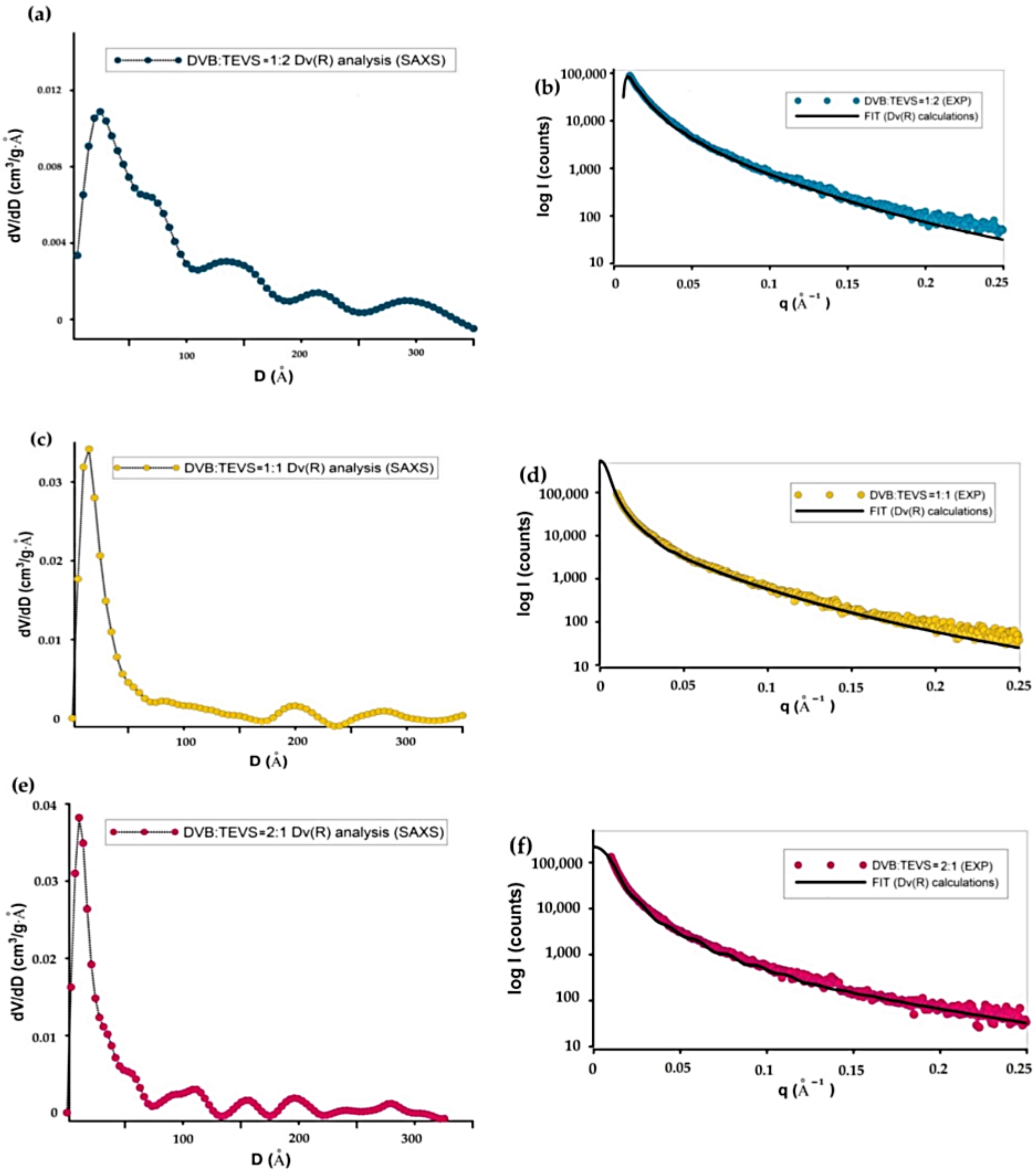

Figure 4. Particle Size Distribution by volume analysis Dv(R) for investigation systems: DVB:TEVS = 1:2 (**a**), DVB:TEVS = 1:1 (**c**) and DVB:TEVS = 2:1 (**e**). The insets of plots correspond to fit curves extrapolated for experimental SAXS data (**b**,**d**,**f**).

2.1.4. Nitrogen Low-Temperature Sorption Analysis

The porosity characteristics of polymeric-inorganic microspheres were determined on the basis of low-temperature nitrogen adsorption-desorption measurements. In Figures 5 and 6 the isotherms and pore size distributions are presented for all studied DVB-TEVS materials. The structure parameters are presented in Table 2. The differences in the isotherm course and nitrogen uptake reflect an essential variation of the porous structure. The shape of adsorption isotherms indicates a small content of micropores and significant content of mesopores. The difference between the adsorption and desorption is observed for all samples as elongated hysteresis loop of H1 type. The decrease of nitrogen adsorption, specific surface area and pore total volume is well correlated with DVB:TEVS ratio, more TEVS content the higher structure parameters. The highest specific surface areas (S_{BET}) are for DVB:TEVS = 1:2, the medium for DVB:TEVS = 1:1 and the lowest for DVB:TEVS = 2:1 with values: 521, 402, 316 m^2/g, respectively. It is evident that the addition of crosslinking agent TEVS develops porous structure of organic-inorganic materials. The increase of pore size as the average value with increase of DVB content is observed, however, the differences are not significant. The pore size distribution functions for all studied materials show similar tendencies as those obtained from SAXS data. Generally, the determined values are in good agreement with data from SEM microscopy and SAXS analysis.

Table 2. The values of parameters characterizing the porous structure of DVB-TEVS.

Sample	Surface Area (S_{BET}) [m^2/g]		Pore Volume [cm^3/g]		Pore Size [nm]	
	$S_{BETTotal}$ [a]	S_{MIC} [b]	V_{Total} [c]	V_{MIC} [d]	D_h [e]	BJH_{ADS} [f]
DVB:TEVS = 1:2	521	-	0.84	-	6.4	4.8
DVB:TEVS = 1:1	402	2.5	0.74	-	7.4	5.1
DVB:TEVS = 2:1	316	27	0.54	0.01	6.8	5.8

[a] S_{BET}, the BET specific surface area; [b] S_{MIC}, the micropore surface area; [c] V_t, the total pore volume; [d] V_{MIC}, the micropore volume; [e] D_h, the average hydraulic pore diameter (4V/A); [f] BJH_{ADS}, average BJH adsorption pore diameter.

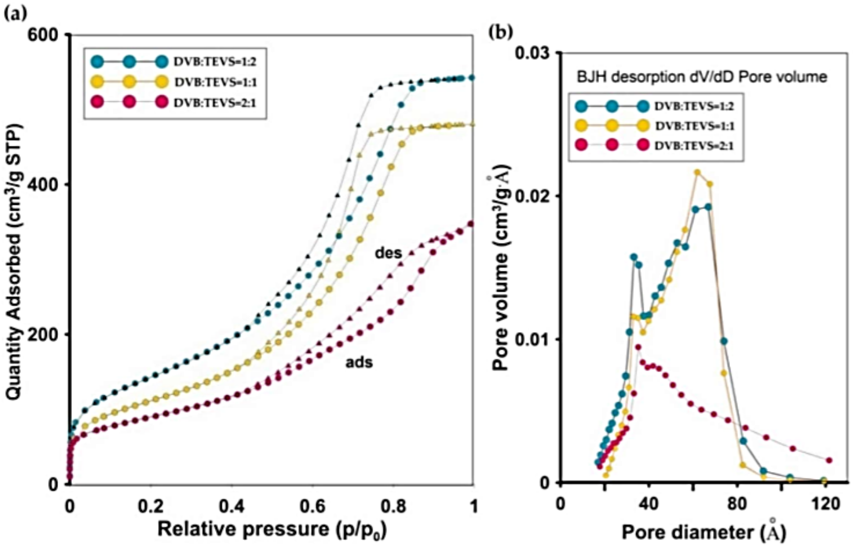

Figure 5. *Cont.*

(c)

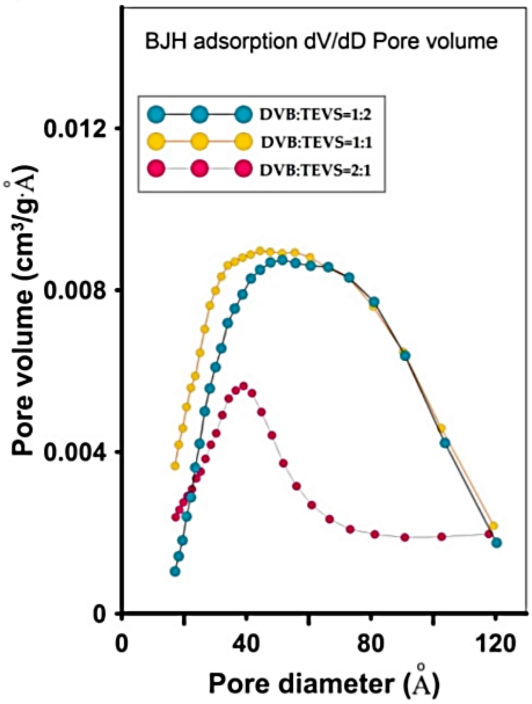

Figure 5. The nitrogen adsorption-desorption isotherms for DVB-TEVS materials (**a**), pore size distributions by the Barrett–Joyner–Halenda (BJH) with Halsey-Faas correction for desorption (**b**) and adsorption data (**c**).

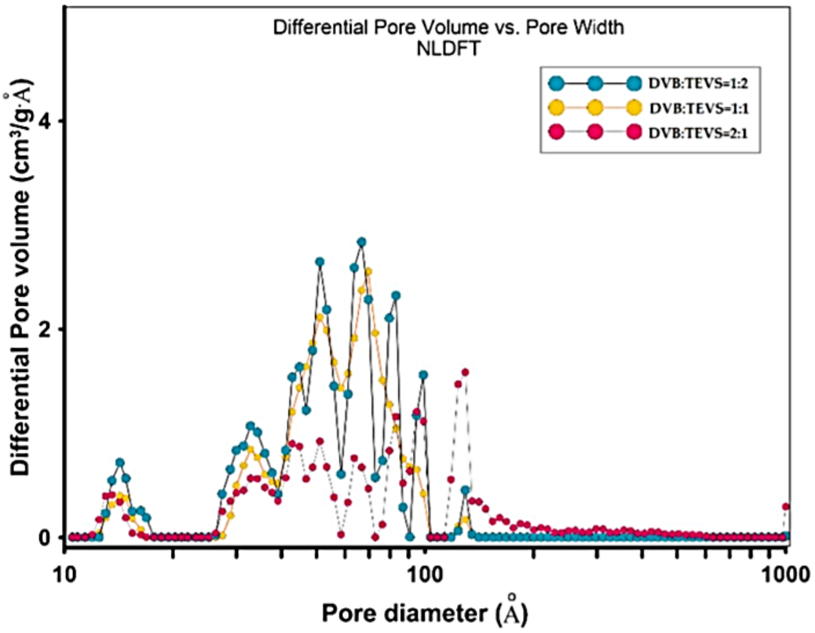

Figure 6. Pore size distributions obtained by Density Functional Theory with Model: N2 @ 77 K, Slit Pores. Method: Non-negative Regularization: 0.01000 and Standard Deviation of Fit: 6.62419 cm^3/g STP.

2.2. Adsorption Studies

In order to investigate the adsorption effectiveness of the synthesized microspheres the kinetic profiles for nitrobenzene (NB), 4-nitrophenol (4-NP) and phenol (P) adsorption from aqueous solutions were measured. In Figure 7, Figure 8 and Figure S2 (Supplementary Material) the concentration and adsorption profiles on DVB:TEVS = 2:1, DVB:TEVS = 1:2 and DVB:TEVS = 1:1 materials are compared.

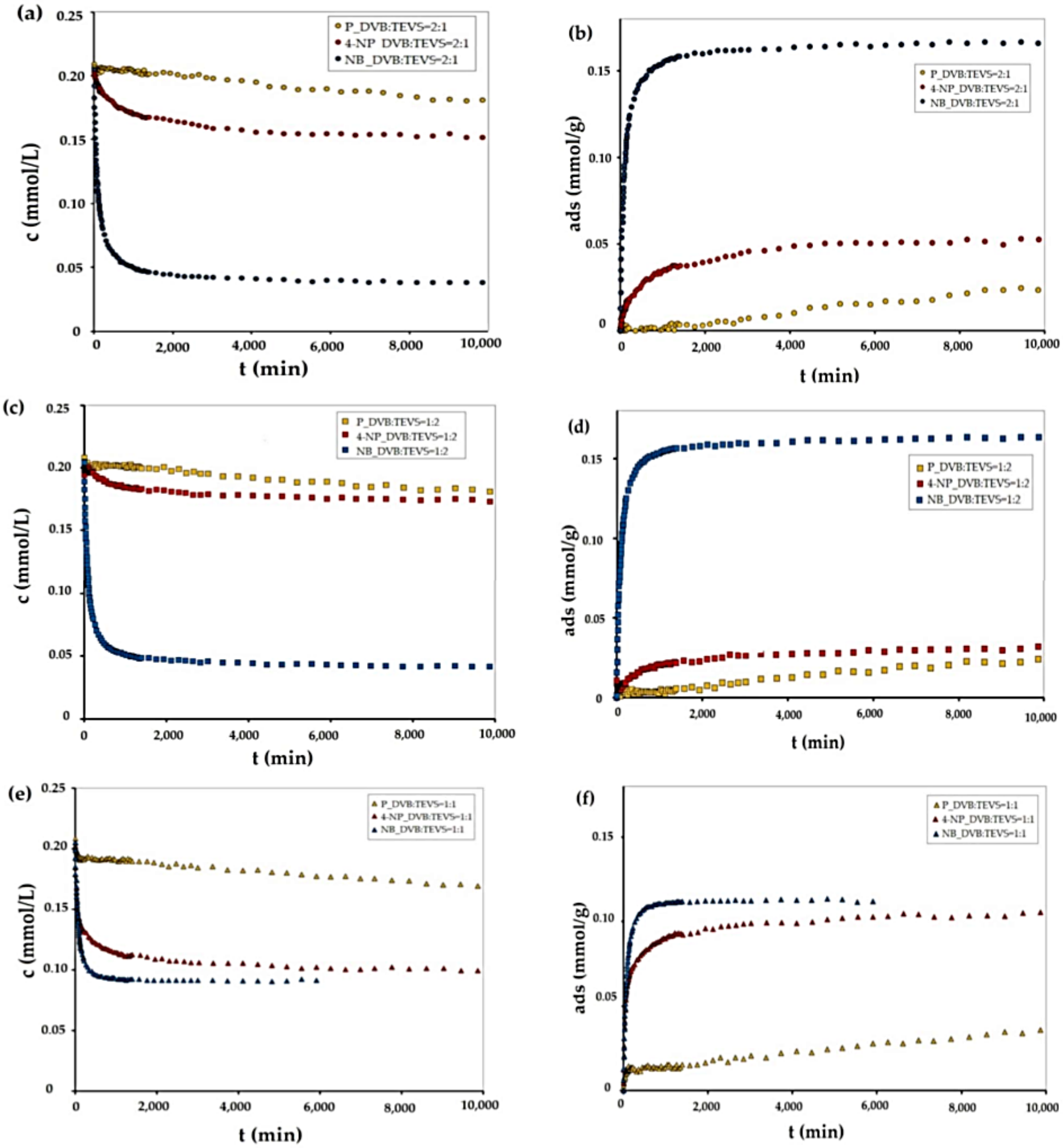

Figure 7. Adsorption kinetics for NB, P and 4-NP on DVB:TEVS = 2:1 (**a**,**b**), DVB:TEVS = 1:2 (**c**,**d**) and DVB:TEVS:1:1 (**e**,**f**) microspheres presented as changes in concentration over time and changes in adsorption over time.

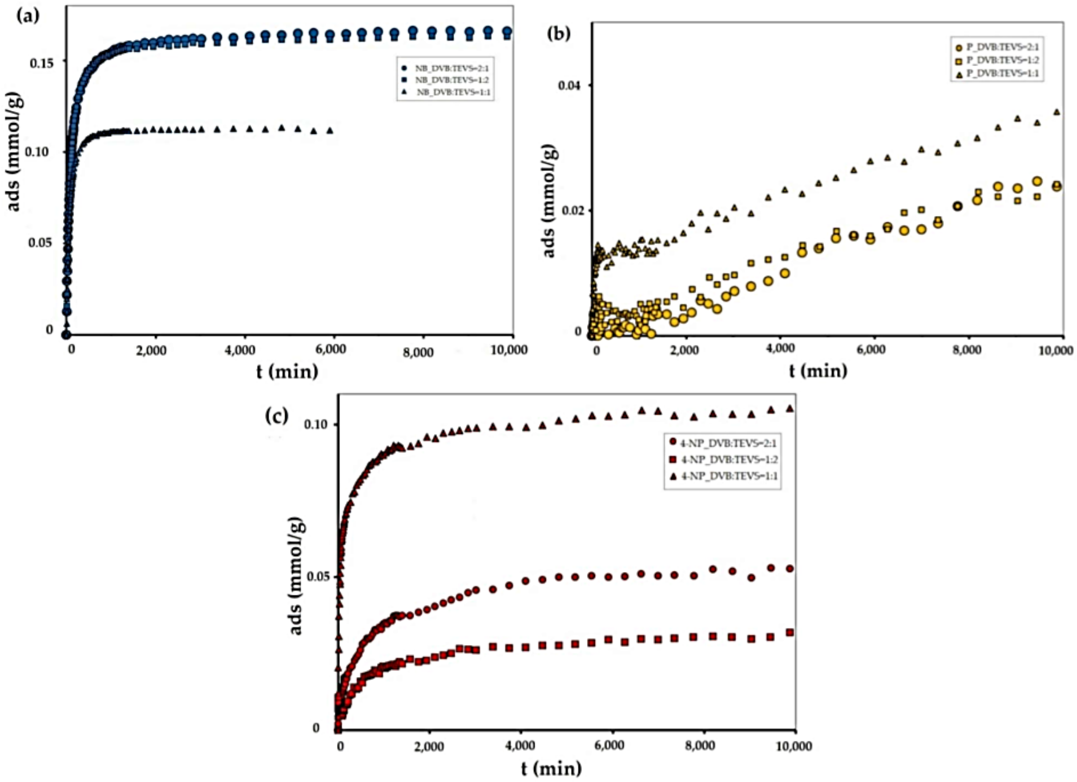

Figure 8. Adsorption kinetics for NB (**a**), P (**b**) and 4-NP (**c**) on DVB:TEVS = 2:1, DVB:TEVS = 1:2 and DVB:TEVS = 1:1 materials presented as changes in adsorption over time.

Let us first discuss the differentiation of adsorbate affinity to a given material. Based on the analysis of kinetic data presented in Figure 7, one can find that for all tested materials the strongest decrease of adsorbate concentration is observed for nitrobenzene, and the lowest for phenol. This effect can be explained based on the differences in solute solubility, whereby compounds with a lower solubility in water generally have a greater affinity to the hydrophobic surface of the adsorbent [33]. Next one can discuss the differentiation of the adsorption properties of all DVB-TEVS materials towards various solutes. Basing on the analysis of data presented in Figure 8 and Figure S2, we can find the differences in the amount and rate of concentration loss from the solution of nitrobenzene, phenol and 4-nitrophenol. In the case of nitrobenzene adsorption (Figure 8a and Figure S2a), the greatest adsorbate losses from the solution are noted for the experimental system with the most hydrophobic DVB:TEVS = 2:1, slightly smaller for the least hydrophobic DVB:TEVS = 1:2, and the smallest for DVB:TEVS = 1:1 with intermediate properties. In the case of 4-nitrophenol and phenol adsorption the greatest adsorbate losses are observed for DVB:TEVS = 1:1. Comparing the adsorption effectiveness of the obtained materials towards different adsorbates one can find a relatively large degree of similarity between the DVB:TEVS = 2:1 and DVB:TEVS = 1:2, however, DVB:TEVS = 1:1 shows quite different properties. Such a differentiated behaviour may be explained taking into account not only the hydrophobic/hydrophilic properties, but also the structural adsorbent characteristics and polymer swelling which can be responsible for penetration of adsorbate molecules into the material structure. As it will be discussed later basedon the thermal analysis data, the interactions of solute molecules with DVB-TEVS microspheres have physical character. Thus, the measured kinetic profiles reveal the global effect of all these factors.

The obtained experimental data were analysed using many equations and adsorption kinetics models. The relative standard deviations obtained in fitting procedure are listed in Table 3. It was observed that the best quality of fitting to the kinetic data was obtained for a multi-exponential equation, which parameters are summarized in Table 6. As can be seen, adsorption in the investigated experimental systems is a complex process, which kinetics can be described by two or three terms of the m-exp equation. The fitting quality is very good, which is confirmed by low values of relative standard deviations $SD(c)/c_o$ in the range from 0.205% to 0.805% and low values of determination factors 1-R^2 in the range from 4.2×10^{-4} to 5.4×10^{-2}. Additionally, the u_{eq} parameter values confirm the differences in the adsorption values. Moreover, for all tested systems, the half time $t_{1/2}$ values are determined, which are defined as the time needed to obtain a half of the concentration change. The obtained half-time values confirm the differences in the adsorption rates of NB, P and 4-NP. Additionally, based on the analysis of the data presented in Figure 7, Figure 8 and Figure S2, and in Table 4 it may be found that the highest adsorption kinetics for all tested adsorbates was recorded in the system with the DVB:TEVS = 1:1.

Summing up the discussion on DVB-TEVS adsorption effectiveness one can find that the synthesized materials show remarkable selectivity towards various adsorbates. Depending on the synthesis procedure it is possible to obtain the materials which are characterized by divergent uptakes and kinetic characteristics.

Table 3. Relative standard deviations SD(c)/co (%) for m-exp, FOE, SOE, MOE, f-FOE, f-SOE, F-MOE, McKay pore diffusion (PDM) and IDM model (Crank).

System	m-exp (%)	FOE (%)	SOE (%)	MOE (%)	f-FOE (%)	f-SOE (%)	f-MOE (%)	IDM (%)	PDM (%)
NB/DVB:TEVS = 2:1	0.544	3.200	0.703	0.935	1.281	0.635	0.651	5.81	24.78
NB/DVB:TEVS = 1:2	0.469	2.480	0.695	0.699	1.310	0.498	0.501	7.21	25.92
NB/DVB:TEVS = 1:1	0.205	1.227	0.995	0.999	0.473	0.581	0.395	15.36	24.75
P/DVB:TEVS = 2:1	0.805	0.802	0.818	0.794	0.685	0.680	0.684	10.36	23.89
P/DVB:TEVS = 1:2	0.704	0.776	0.782	0.772	0.763	0.750	0.711	9.06	22.56
P/DVB:TEVS = 1:1	0.506	1.455	1.450	1.459	1.330	1.351	1.351	6.87	18.96
4-NP/DVB:TEVS = 2:1	0.397	1.277	0.791	0.796	0.407	0.427	0.408	8.78	29.56
4-NP/ DVB:TEVS = 1:2	0.572	0.801	0.704	0.708	0.750	0.704	0.709	9.64	28.25
4-NP/DVB:TEVS = 1:1	0.669	3.519	4.949	1.889	1.737	0.999	9.694	13.53	21.64

Table 4. Optimized parameters of m-exp equation.

System	f_1, log k_1	f_2, log k_2	f_3, log k_3	u_{eq}	$t_{1/2}$ (min)	$SD(c)/c_o$ (%)	1-R^2
NB/DVB:TEVS = 2:1	0.095,0.116	0.627,−1.90	0.278,−2.81	0.805	73.1	0.544	$5.2 \cdot 10^{-4}$
NB/DVB:TEVS = 1:2	0.080,−0.967	0.715,−1.968	0.205,−2.851	0.788	75.9	0.469	$9.6 \cdot 10^{-4}$
NB/DVB:TEVS = 1:1	0.056,0.187	0.686,−1.809	0.258,−2.451	0.553	55.9	0.205	$4.2 \cdot 10^{-4}$
P/DVB:TEVS = 2:1	0.005,−0.788	0.995,−4.881	-	0.148	52334.6	0.805	$5.4 \cdot 10^{-2}$
P/DVB:TEVS = 1:2	0.018,−0.889	0.982,−4.939	-	0.154	52334.6	0.704	$5.1 \cdot 10^{-2}$
P/DVB:TEVS = 1:1	0.056,−1.452	0.006,−0.816	0.938,−4.870	0.168	46568.7	0.506	$1.6 \cdot 10^{-2}$
4-NP/DVB:TEVS = 2:1	0.124,−1.332	0.368,−2.518	0.508,−3.380	0.256	483.9	0.397	$2.3 \cdot 10^{-3}$
4-NP/DVB:TEVS = 1:2	0.130,1.063	0.450,−2.839	0.370,−4.040	0.180	803.6	0.572	$1.4 \cdot 10^{-2}$
4-NP/DVB:TEVS = 1:1	0.049,−0.071	0.598,−1.607	0.353,−2.972	0.499	51.8	0.669	$2.4 \cdot 10^{-3}$

2.3. Thermal Analysis

Thermal analysis is a very useful technique for the characterization of materials, which may be also helpful in investigations of adsorbate-adsorbent interactions. The thermal properties of pure polymer-silane hybrids and the materials loaded with organic adsorbates were investigated using TG, DTG and DSC techniques. In Figure 9, the TG, DTG and DSC curves measured for the synthesized DVB-TEVS materials are presented. One can state that they show similar thermal behaviour with several stages of the thermal degradation. The data obtained from TG/DTG/DSC curves are summarized in Table 5. The thermal analysis proved that up to 170 °C the materials are highly thermally stable. The exothermic peaks visible on DSC curve starting at 170 °C may be associated with the additional crosslinking processes related to the presence of tetrafunctional DVB monomer. The main step related to thermal destruction of crosslinked microspheres follows at temperatures 330–550 °C with the maximum at about 450 °C. In this stage an 84–85% decrease in the weight of studied materials is observed. In the 550–950 °C temperature range the weight loss is below 3%. The total mass loss is similar for all DVB-TEVS materials and it is about 87%. These results confirm that the materials are thermally stable up to at least 330 °C and the main destruction process occurs at about 450 °C, therefore, the synthesized materials may be applied in relatively wide temperature ranges. These observations were confirmed with the data of identification of thermal destruction products by mass spectrometry (MS) analysis. The MS profiles for DVB:TEVS = 1:1 are shown in Figures 10 and 11. The MS analysis confirms that the initial decomposition of these materials happens below 200 °C, and the major material destruction process is above 330 °C. Moreover, the MS data indicate that the thermal behaviour of DVB-TEVS materials is strictly connected with the presence of the 1,4-divinylbenzene matrix. The course of TG, DTG and DSC curves as well as MS spectra for the DVB:TEVS materials (Figures 9 and 10) and pure DVB (presented in Figures S3–S5, (Supplementary Material)) are similar. Many signals from the defragmentation of the aromatic structure of divinylbenzene are visible: water (m/z = 18), vinyl group (m/z = 27), ethyl group (m/z = 29), benzene (m/z = 78), phenyl group (m/z = 77), benzyl group (m/z = 91). In addition, the gaseous MS profiles of thermal degradation of the studied materials confirm the presence of triethoxyvinylsilane coupling agent (Figure S6 for DVB:TEVS = 1:1, Supplementary Material) (m/z = 189) and absence of TEVS in pure polymer.

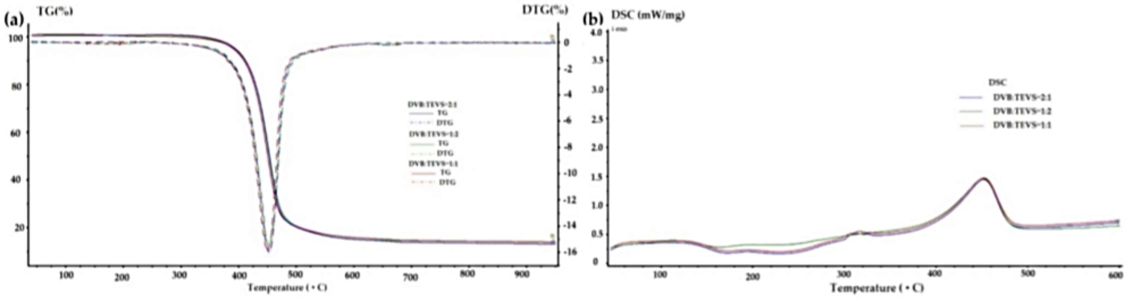

Figure 9. TG, DTG (**a**) and DSC (**b**) curves for DVB-TEVS materials measured in helium conditions.

Table 5. TG, DTG and DSC data obtained in helium atmosphere for DVB-TEVS materials.

Sample	TG [%]				DTG	DSC	
	m_{IDT} (170–330 °C)	m_{loss} 330–550 °C	m_{loss} 550–950 °C	m_{loss} TOTAL	T_d [°C]	T_d [°C]	ΔH_d [J/g]
DVB:TEVS = 1:2	1.39	83.99	1.47	86.85	453	453	150.8
DVB:TEVS = 1:1	0.92	83.87	1.89	86.68	450	453	145.7
DVB:TEVS = 2:1	0.36	85.06	2.13	87.55	453	453	147.4

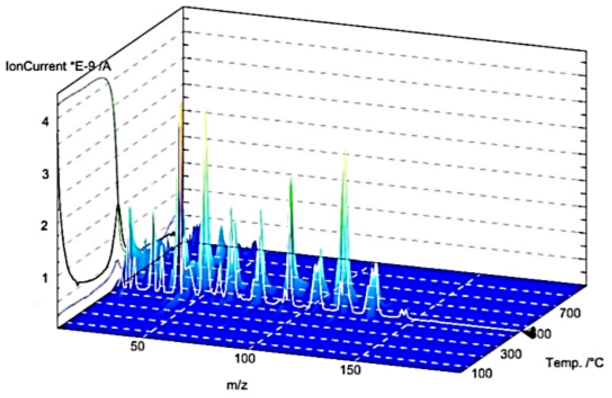

Figure 10. 3D MS profile registered during decomposition of pure DVB:TEVS = 1:1.

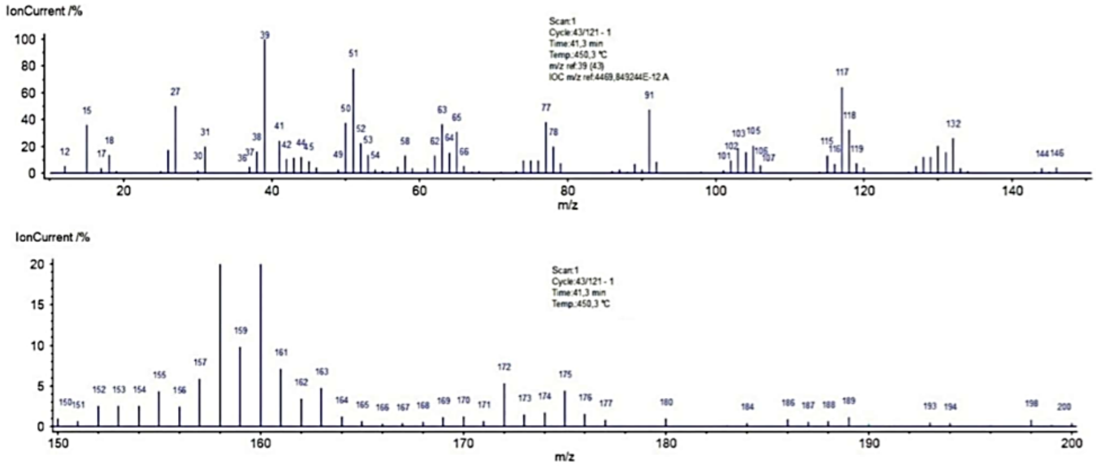

Figure 11. MS spectra of DVB:TEVS = 1:1 decomposition at 450 °C.

Taking into consideration the TG, DTG and DSC curves obtained for the materials loaded with organic solutes (Figure 12, Figure 13, Figure 14 and Table 6) one can find small differences for various adsorbates. In the range of 170–330 °C the weight losses for all materials with adsorbed organic solutes are higher than in the case of pure DVB-TEVS materials (0.4–1.4%) suggesting relatively weak adsorbent-adsorbate interactions of physical nature. However, for 4-NP and P the weight loss is higher (2.6–4%) in comparison to the NB (0.7–1.3%)-containing sample.

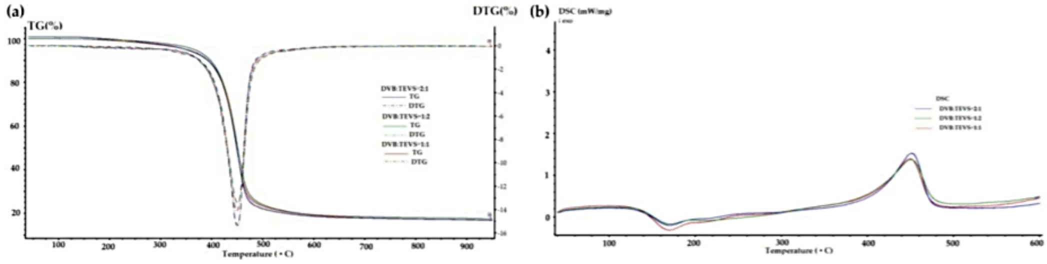

Figure 12. TG, DTG (**a**) and DSC (**b**) curves for DVB-TEVS materials measured in helium conditions after adsorption of P.

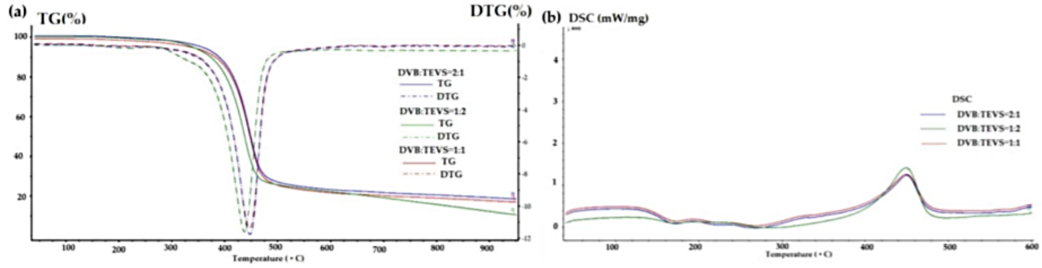

Figure 13. TG, DTG (**a**) and DSC (**b**) curves for DVB-TEVS materials measured in helium conditions after adsorption of 4-NP.

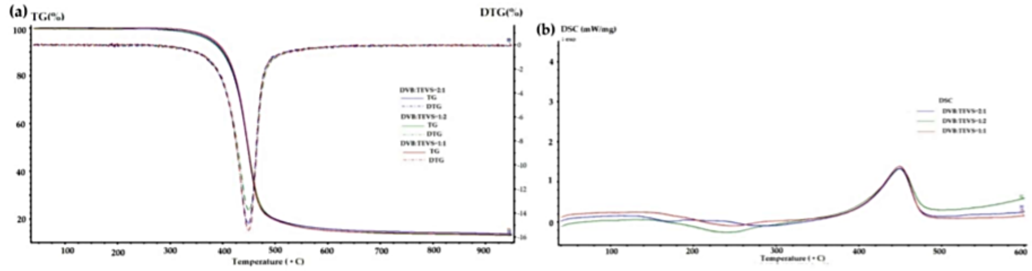

Figure 14. TG, DTG (**a**) and DSC (**b**) curves for DVB-TEVS materials measured in helium conditions after adsorption of NB.

Table 6. TG, DTG and DSC data obtained in helium atmosphere for DVB-TEVS materials with loaded P, 4-NP and NB.

Sample	TG [%]				DTG	DSC	
	m_{IDT} (170–330 °C)	m_{loss} 330–550 °C	m_{loss} 550–950 °C	m_{loss} TOTAL	T_d [°C]	T_d [°C]	ΔH_d [J/g]
P_DVB:TEVS = 1:2	2.61	75.69	3.11	81.41	450	452	164.8
P_DVB:TEVS = 1:1	3.41	75.86	3.60	82.87	450	452	167.1
P_DVB:TEVS = 2:1	3.98	76.76	2.73	83.47	450	452	198.2
NP_DVB:TEVS = 1:2	3.70	72.62	8.50	84.82	440	449	191.1
NP_DVB:TEVS = 1:1	3.19	72.51	6.02	81.72	449	449	134.5
NP_DVB:TEVS = 2:1	3.25	72.53	5.96	81.74	449	449	135.8
NB_DVB:TEVS = 1:2	1.24	80.20	2.97	84.41	450	450	170.2
NB_DVB:TEVS = 1:1	0.67	83.25	2.67	86.59	449	450	199.5
NB_DVB:TEVS = 2:1	1.29	81.61	2.90	85.80	448	450	186.9

The TG, DTG and DSC results were completed by mass spectrometry analysis. The 3D MS profiles and MS spectra for DVB:TEVS = 1:1 with adsorbed organic substances are presented in Figures 15 and 16. The gaseous MS profiles of DVB-TEVS materials after adsorption (Figure 17) revealed that in the case of 4-NP certain amounts of nitrogen compounds released above 170 °C are found: nitrogen oxide (*m/z* = 30), nitrogen dioxide (*m/z* = 46) and also small amounts of nitrophenol (*m/z* = 139) and nitrobenzene (*m/z* = 123). These products of thermal decomposition confirm the adsorption 4-NP and explain the higher mass losses in the range of 170–330 °C. In the case of NB adsorption larger amounts of nitrogen compounds evaporate up to 100 °C (the MS signals recorded at low temperatures), thus, it explains lower mass losses in the range 170–330 °C in comparison to 4-NP. The main step of the destruction of microspherical structures with residues of adsorbates occurs runs at a maximum of 450 °C.

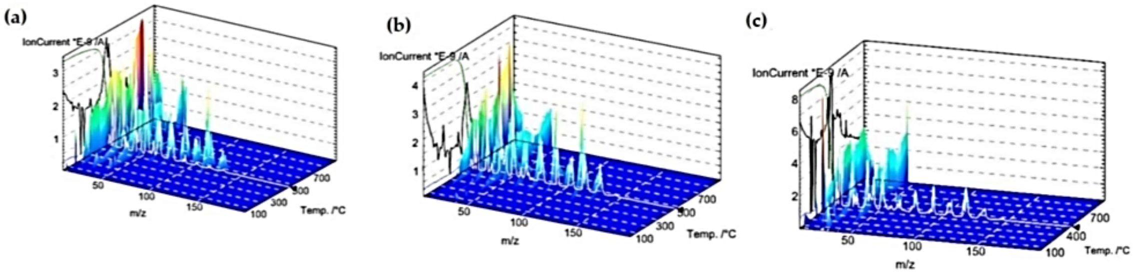

Figure 15. 3D MS profiles registered during decomposition of DVB:TEVS = 1:1 after adsorption of P (**a**), 4-NP (**b**) and NB (**c**).

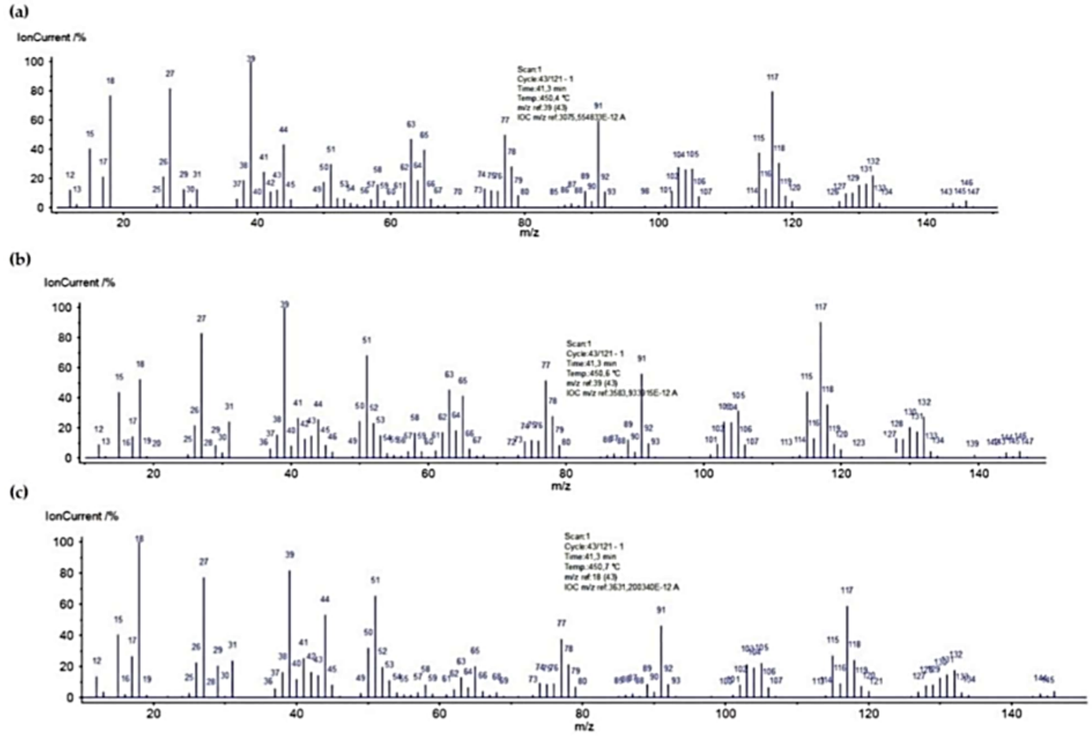

Figure 16. MS profiles registered during decomposition of DVB:TEVS = 1:1 after adsorption of P (**a**), 4-NP (**b**) and NB (**c**).

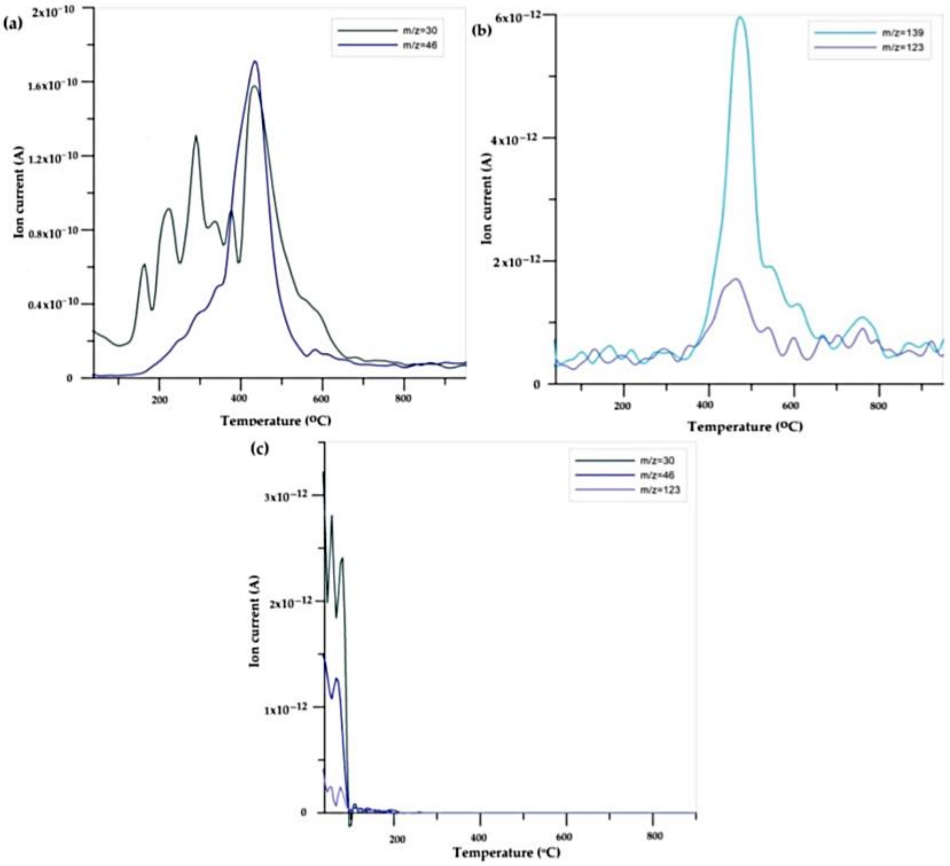

Figure 17. MS gaseous profiles registered during decomposition of DVB:TEVS = 1:1 after adsorption of 4-NP m/z = 30 and 46 (**a**) and m/z = 139 and 123 (**b**) and of NB m/z = 30, 46 and 123 (**c**).

3. Experimental and Calculation Procedures

3.1. Chemicals

Triethoxyvinylsilane (TEVS), decan-1-ol and poly(vinyl alcohol) (PVA) were purchased in Fluka AG (Buchs, Switzerland). α,α'-Azoiso-bis-butyronitrile (AIBN) and DVB (62.2% of 1,4-divinylbenzene, 0.2% of 1,2-divinylbenzene and ethylvinylbenzene) were obtained from Merck (Darmstadt, Germany). Prior to use DVB and TEVS were washed with 3% aqueous sodium hydroxide solution. Acetone and toluene have been obtained from Avantor Performance Materials Poland S.A. (Gliwice, Poland). The organic substances used in kinetic experiment: phenol and 4-nitrophenol were bought from Merck and the nitrobenzene from Avantor Performance Materials Poland S.A.

The structures of TEVS and DVB, as well as the model of the hybrid chain are shown in Figure 18. The properties of organic compounds used as the adsorbates in the kinetic studies are presented in Table 7.

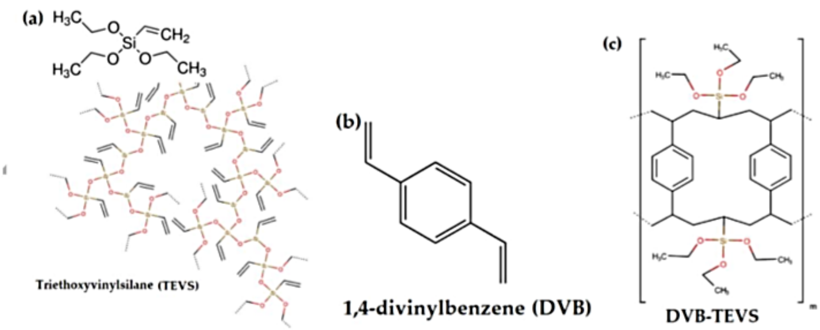

Figure 18. The chemical structure of inorganic (**a**) and organic (**b**) components of hybrid materials as well as the schematic structure of the copolymer (**c**).

Table 7. The physicochemical properties of used adsorbates.

Adsorbate	**Chemical Formula**	**Molecular Weight [g/mol]**	**Water Solubility [g/100 mL at 20 °C]**	**Ionization Constant pKa**	**Melting Point [°C]**	**Boiling Point [°C]**	**Chemical Safety**
Phenol (P)	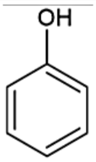	94.11[1]	8.3[1]	9.99[1]	40.5[1]	181.7[1]	Corrosive Acute toxic Health hazard[1]
Nitrobenzene (NB)	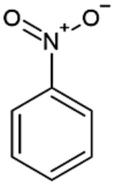	123.11[1]	0.19[1]	—	5.7[1]	210.9[1]	Acute toxic Health hazard[1]
4-Nitrophenol (4-NP)	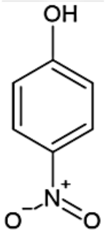	139.11[1]	1.6[1]	7.15[1]	113[1]	279[1]	Irritant Health hazard[1]

[1] https://pubchem.ncbi.nlm.nih.gov (accessed on 01 February 2021).

3.2. Materials Synthesis

Copolymerization of 1,4-divinylbenzene with triethoxyvinylsilane was performed in the aqueous medium by using a suspension polymerization method. In synthesis vessel 75 mL of redistilled water and 1 g of poly(vinyl alcohol) were placed and stirred for 1 h at 80 °C in a three-necked flask fitted with a mechanical stirrer, thermometer and air cooler. Then, the solutions containing DVB and a corresponding amount of TEVS, the initiator AIBN (1 wt%) and the mixture of pore-forming diluents (toluene and 1-decanol, taken in 1/1 (*v*/*v*) proportions) were added while stirring to the aqueous medium. The mixture was stirred at 350 rpm for 12 h at 85 °C. The obtained microspheres were washed with distilled water (2 L), filtered, dried and extracted in a Soxhlet apparatus with boiling acetone for 3 h. The amounts of individual components in reaction mixtures are presented in Table 8.

Table 8. Compositions of reaction mixtures in organic-inorganic materials synthesis.

Sample	**Monomers**		**Pore-Forming Diluents**	
	DVB-TEVS Molar Ratios		**Toluene and Decano-1-ol Volumes [cm^3]**	
DVB:TEVS = 1:2	1	2	5	5
DVB:TEVS = 1:1	1	1	5	5
DVB:TEVS = 2:1	1	0.5	5	5

3.3. *Investigation Methods*

3.3.1. Scanning Electron Microscopy (SEM)

The surface morphology of the samples was studied by the field emission Scanning Electron Microscopy (SEM) employing a Quanta^{TM} 3D FEG (FEI Company, Hillsboro, OR, USA) apparatus operating at 5 kV. A high vacuum (4×10^{-4} Pa) mode was applied for imaging the investigated samples. Prior to measurement, the samples were mounted on aluminum stubs and sputtered with gold.

3.3.2. Nitrogen Adsorption-Desorption Measurements

The porosity of the materials was examined applying low-temperature nitrogen adsorption-desorption isotherms at 77 K. The values of the parameters characterizing the properties of analyzed samples were obtained: the BET specific surface area (S_{BET}) (assessed from the linear BET plot of adsorption data), the total pore volume (V_t) (from the adsorption value at the relative pressure p/p_o~0.99), the micropore volume (V_{mic}) (from the t-plot), and the pore size distributions (PSD) followed by the Barrett, Joyner, and Halenda (BJH) procedure and the Non-Local Density Functional Theory (NLDFT) approach (ASAP 2020 analyzer, Micromeritics, USA Before the measurement, volatile materials adsorbed on the surface were driven by thermal degassing. In this procedure, the precisely weighed amount of the samples (~0.15 g) were outgassed at 120 °C and pressure of 1 mmHg for 24 h in a degas port of analyser.

3.3.3. Small-Angle X-ray Scattering (SAXS)

Small X-ray scattering (SAXS) experiments were carried out by the Empyrean X-ray diffraction platforms (PANalytical), in transmission geometry CuKα radiation with a wavelength (λ) of 1.5418 Å was used at 40 kV and 40 mA configuration at room temperature. The X-ray source consisted of an anode Cu source with a line focus type. SAXS measurements were performed using a 10 mm fixed mask, Cu 0.2 mm beam attenuator and PIXcel3D area detector. SAXS is an analytical technique that measures the X-ray intensities scattered by a sample as a function of the scattering angle (scattering vector q). Scattering vector q is given by $q = 4\pi \sin(\theta/2)/\lambda$, where λ is the wavelength of the X-ray beam and θ is the scattering angle. Measurements were made at a small angle in the range of 0.2 to 4.0deg of 2θ.

The Porod approximation was applied to SAXS data processing to assess the interface between the matrix and the distracting objects (pores). Porod constant (k_p) can be applied for determination of the specific surface area of the two-phase system using X-ray scattering at small-angle:

$$\frac{S}{V} = \frac{4p(1-p)k_p}{Q_p} \tag{1}$$

where p and (1-p) are the volumes of two phases, k_p is the Porod's constant, and Q_p is the Porod's invariant which is proportional to the mean-square density fluctuation of the whole scattering volume. If S/V is calculated by $D_v(R)$ or Porod algorithm, the specific surface area from SAXS (S_{SAXS}) can be calculated according to the equation:

$$S_{SAXS}\left[\frac{m^2}{g}\right] = \frac{10000 \cdot \frac{S}{V}\left[A^{-1}\right]}{d\left[\frac{g}{cm^3}\right]} \tag{2}$$

where S/V is the surface divided by volume ratio calculated from the distribution curve and d is the mass density [54,55].

3.3.4. Fourier Transformed Infrared/Attenuated Total Reflection Analysis (FTIR/ATR)

Fourier Transformed Infrared connected with Attenuated Total Reflection (FTIR/ATR) analysis was conducted by using IR spectrometer TENSOR 27 (Brucker, Germany) equipped with the diamond crystal. The spectra were recorded in the spectral range of 400–4000 cm^{-1}.

3.3.5. Thermal Analysis

Thermal analysis was carried out on a TG/DTA/DSC apparatus (STA 449 Jupiter F1, Netzsch, Selb, Germany). Samples of mass 20 mg placed in alumina crucibles and heated from 30 to 1200 °C under helium atmosphere with flow rate 50 $mL \cdot min^{-1}$ and heating rate 10 $°C \cdot min^{-1}$. The gaseous products emitted during decomposition of materials after adsorption were analysed by Quadrupole Mass Spectroscopy (QMS 403C Aeölos, Selb, Germany). The QMS data in the range from 10 to 300 amu were recorded.

3.3.6. Adsorption Studies

Kinetic measurements were conducted using a UV-Vis spectrophotometer Cary 100 (Varian, Australia) with a flow working cell for periodic measurements of a solution concentration in a closed system. In all cases, 100 mg of sample was placed in a quartz vessel connected with a stirrer (110 rpm) and thermostatic system (25 °C) and filled with 100 mL solutes. Each of the samples was treated with three aqueous solutions of organic compounds: phenol, 4-nitrophenol, and nitrobenzene. The initial concentration of solutions in all cases was equal to 0.205 mmol/L. At definite time intervals, the solution samples were gathered in a flow cell, and absorption spectra were measured, and the solution was turned back to the reaction vessel. The absorbance spectrum was recorded for wavelength ranges from 200 to 450 nm. The concentration in the function of time profiles for the experimental systems was calculated from the recorded spectra.

The kinetic curves were analysed using several equations: first-order equation (FOE), the second-order equation (SOE) and pseudo first and second-order equations (PFOE and PSOE), the so-called mixed 1,2-order equation (MOE), the fractal-like MOE equation (f-MOE), the fractal-like first-order equation (f-FOE) and the fractal-like second-order equation (f-SOE), the so-called multiexponential equation (m-exp), the intraparticle diffusion model (IDM), and the pore diffusion model (PDM). The basic and pseudo first-order equations (FOE and PFOE can be expressed by a linear relationships (3) or (4):

$$ln(a_{eq} - a) = ln(a_{eq} - a_o) - k_1 \tag{3}$$

where a is the temporary adsorbed amount, a_o is the initial amount, a_{eq} is the equilibrium adsorbed amount, k_1 is the adsorption rate coefficient.

$$ln(c_{eq} - c) = ln(c_{eq} - c_o) - k_1 \tag{4}$$

where c is the temporary adsorbate concentration, c_o is the initial concentration, c_{eq} is the equilibrium concentration, k_1 is the same as in Equation (3).

The second-order and pseudo second order equations (SOE and PSOE) can be noted as:

$$a = a_{eq}[k_2 t/(1 + k_2 t)] \tag{5}$$

The linear forms of SOE and PSOE equations are:

$$t/a = (1/a_{eq})(1/k_2 + t) \tag{6}$$

$$a = a_{eq} - (1/k_2)(a/t) \tag{7}$$

where $k_2 = k_{2a}a_{eq}$ and k_{2a} are the rate coefficients for pseudo-second order kinetics.

The generalization of the first and second order kinetics is the 1,2-mixed-order kinetic equation (MOE) which is the combination of the first and second order units and can be expressed as a relative adsorption progress in time (F):

$$F = a/a_{eq} = \frac{1 - exp(-k_1 t)}{1 - f_2 exp(-k_1 t)} \tag{8}$$

$$ln\left(\frac{1-F}{1-f_2 F}\right) = -k_1 t \tag{9}$$

where $f_2 < 1$ is the normalized share of the second order process in the kinetics. In some cases, the MOE equation is reduced to the simple kinetic equations of the first ($f_2 = 0$) and the second order ($f_2 = 1$) type. Non-ideality effects can be considered using fractal-like equations (f-FOE, f-SOE and f-MOE) in which fractal coefficient f is used.

The multi-exponential equation (m-exp) is applied to describe numerous first-order processes or the follow up processes and has the following forms:

$$c = \left(c_o - c_{eq}\right) \sum\nolimits_{i=1}^{n} f_i exp(-k_i t) + c_{eq} \tag{10}$$

$$c = c_o - c_o u_{eq} \sum\nolimits_{i=1}^{n} f_i [1 - exp(-k_i t)] \tag{11}$$

where k_i is the rate coefficient, $u_{eq} = 1 - c_{eq}/c_o$ is the relative loss of adsorbate from the solution, and "i" is the term of m-exp equation.

The Intraparticle Diffusion Model (IDM, Crank) characterizes the adsorption processes on the spherical adsorbent grains. When the concentration of adsorbate is constant the equation can be expressed as:

$$F = 1 - \frac{6}{\pi^2} \sum_{n=1}^{\infty} \frac{1}{n^2} exp\left(\frac{-\pi^2 \cdot n^2 \cdot D_a \cdot t}{r^2}\right) \tag{12}$$

where r is the radius of adsorbent particle, D_a is the effective diffusion coefficient and is given in equation:

$$D_a = \frac{D}{\tau_p \cdot (1 + \rho \cdot K_H \cdot \varepsilon_p)} \tag{13}$$

where D is the molecular diffusion coefficient, τ_p is the dimensionless pore tortuosity factor, ρ is the particle density, ε_p is the particle porosity and K_H is the Henry adsorption constant.

The Pore Diffusion Model (PDM, McKay) describe adsorption on porous solids which combines the transfer resistance of adsorbate particles through the surface layer, the proportional penetration of the adsorbate into the adsorbent grains, the sharp boundary between the space in which the equilibrium state is determined and the space without the adsorbate, and can be expressed by the mathematic formula:

$$\frac{dF}{d\tau_s} = \frac{3\left(1 - u_{eq} \cdot F\right) \cdot (1 - F)^{\frac{1}{3}}}{1 - B \cdot (1 - F)^{\frac{1}{3}}} \tag{14}$$

where u_{eq} is the relative adsorbate loss, the parameter $B = 1 - 1/B_i$ and $B_i = K_f/D_p$ is the Biot number, D_p is the pore diffusion coefficient, K_f is the external mass transfer coefficient, τ_s is the undersized model time [32,56,57].

4. Conclusions

Divinylbenzene-*co*-triethoxyvinylsilane microspheres were synthesized at different component molar ratios (DVB:TEVS = 1:2, DVB:TEVS = 1:1 and DVB:TEVS = 2:1). The obtained materials were characterized by differentiated morphology and porosity. The DVB:TEVS = 1:2 microspheres showed many deviations from the ideal spherical form, while the DVB:TEVS = 2:1 microspheres were characterized by the most regular shape, uniform and smooth surface. FTIR/ATR spectroscopy confirmed the incorporation of TEVS into the polymeric structure of the synthesized materials. The SAXS and nitrogen adsorption-desorption techniques produced similar results regarding the structural characteristics of the copolymers. The specific surface areas determined by both methods were similar with slight differences indicating a low amount of closed porosity. The correlation between the structure parameters (specific surface area and pore total volume) and DVB:TEVS ratio was found.

The adsorption properties of the synthesized microspheres towards nitrobenzene, 4-nitrophenol and phenol were studied by kinetic measurements. Generally, the differences in the amount and rate of concentration loss from the solutions of all solutes were observed. For all tested materials the strongest decrease of adsorbate concentration was found for nitrobenzene, and the lowest for phenol which was connected with adsorbate solubility/hydrophobicity. For nitrobenzene adsorption the greatest adsorbate losses from the solution were observed in the case of the most hydrophobic DVB:TEVS = 2:1, however, for 4-nitrophenol and phenol adsorption the greatest adsorbate losses were found for DVB:TEVS = 1:1. The adsorption effectiveness of DVB:TEVS = 2:1 and DVB:TEVS = 1:2 materials towards different adsorbates was similar, however, DVB:TEVS = 1:1 showed quite different properties. The measured kinetic profiles revealed the global effect of several factors: the hydrophobic/hydrophilic properties, the structural adsorbent characteristics, the polymer swelling, the adsorbent-adsorbate interactions.

The thermal analysis proved that the synthesized DVB-TEVS materials were thermally stable up to at least 330 °C, thus, they may be applied in relatively wide temperature ranges. The weight losses for all materials with adsorbed organic solutes were higher in comparison to pure DVB-TEVS materials suggesting relatively weak adsorbent-adsorbate interactions of physical nature. The MS gaseous profiles revealed certain amounts of nitrogen compounds confirming adsorption of 4-nitrophenol and nitrobenzene.

The synthesized polymeric materials showed remarkable selectivity towards various organic adsorbates confirmed by divergent uptakes and kinetic characteristics. They seem to be promising materials for adsorption and separation techniques.

Supplementary Materials: The following are available online. Figure S1: FTIR/ATR spectra of DVB, Figure S2: Adsorption kinetics for NB (a), P (b) and 4-NP (c) on DVB:TEVS = 2:1, DVB:TEVS = 1:2 and DVB:TEVS = 1:1 presented as changes in concentration over time, Figure S3: TG/DTG/DSC curves of DVB, Figure S4: 3D MS profile of thermal decomposition of DVB, Figure S5: MS spectra of thermal degradation of DVB at 450 °C and Figure S6: MS profiles of gaseous products of thermal degradation of DVB:TEVS = 1:1 and DVB (m/z = 189).

Author Contributions: Conceptualization, A.B, M.Z.-S., A.D.-M. and B.P.; Material synthesis, B.P.; Investigation, A.B., M.Z.-S. and M.W.; Methodology, A.B., M.Z.-S., M.W. and A.D.-M., Supervision, A.D.-M. and M.Z.-S.; Writing—original draft, A.B.; M.Z.-S., A.D.-M. and M.W. Writing—review and editing, A.B., A.D.-M., M.Z.-S., M.W. and B.P. All authors have read and agreed to the published version of the manuscript.

Funding: This research received no external funding.

Institutional Review Board Statement: Not applicable.

Informed Consent Statement: Informed consent was obtained from all subjects involved in the study.

Data Availability Statement: The data are available by corresponding author.

Conflicts of Interest: The authors declare no conflict of interest.

Sample Availability: Samples of the compounds are available from the authors.

References

1. Chujo, Y. Organic-inorganic hybrid materials. *Curr. Opin. Solid State Mater. Sci.* **1996**, *1*, 806–811. [CrossRef]
2. Tiwari, I.; Mahanwar, P.A. Polyacrylate/silica hybrid materials: A step towards multifunctional properties. *J. Dispers. Sci. Technol.* **2019**, *40*, 925–957. [CrossRef]
3. Saha, P.; Chowdhury, S.; Kim, M.C.; Kim, J.K. MultiComponent Materials. In *Multicomponent Polymeric Materials*, 1st ed.; Kim, J.K., Thomas, S., Saha, P., Eds.; Springer: Dordrecht, The Netherlands, 2016; Volume 223, pp. 3–12.

4. Timin, A.; Rumyantsev, E.; Solomonov, E. Synthesis and application of amino-modified silicas containing albumin as hemoadsorbents for bilirubin adsorption. *J. Non-Cryst. Solids* **2014**, *385*, 81–88. [CrossRef]
5. Kubota, Y.; Nishizaki, Y.; Ikeya, H. Organic–silicate hybrid catalysts based on various defined structures for Knoevenagel condensation. *Microporous Mesoporous Mater.* **2004**, *70*, 135–149. [CrossRef]
6. Gomez-Romero, P. Hybrid Organic–Inorganic Materials—In Search of Synergic Activity. *Adv. Mater.* **2001**, *13*, 163–174. [CrossRef]
7. Kawaguchi, H. Functional polymer microspheres. *Prog. Polym. Sci.* **2000**, *25*, 1171–1210. [CrossRef]
8. Wang, Z.; Lei, F.; Li, W.; Li, P.; Wang, T.; Qin, L.; Cheng, G.; Sun, Y. Preparationof rosin-based polymer microspheres as a stationary phase inhigh-performance liquid chromatography to separate polycyclic aromatic hydrocarbons and alkaloids. *e-Polymers* **2019**, *19*, 290–296. [CrossRef]
9. Schmidt, G.; Malwitz, M.M.; Shankar, R. Properties of polymer–nanoparticle composites. *Curr. Opin. Colloid Interface Sci.* **2003**, *8*, 103–108. [CrossRef]
10. Mammeri, F.; Le Bourhis, E.; Rozes, L.; Sanchez, C. Mechanical properties of hybrid organic–inorganic materials. *J. Mater. Chem.* **2005**, *15*, 3789–3811. [CrossRef]
11. Lu, S.; Chun, W.; Yu, J.; Yang, X. Preparation and Characterization of the Mesoporous SiO_2–TiO_2/Epoxy Resin Hybrid Materials. *J. Appl. Polym. Sci.* **2008**, *109*, 2095–2102. [CrossRef]
12. Zoppi, R.A.; DeCastro, C.R.; Yoshida, I.V.P. Hybrids of SiO_2 and poly(amide6-b-ethyleneoxide). *Polymer* **1997**, *38*, 5708–5712. [CrossRef]
13. Causin, V. Polymers: An Overview. In *Polymers on the Crime Scene*, 1st ed.; Causin, V., Ed.; Springer: Cham, Switzerland, 2015; pp. 9–52.
14. Mascia, L.; Capra, C.; Lavorgna, M. Organic-Inorganic Hybrid Fillers for the Controlled Release of Antioxidants. *Macromol. Symp.* **2007**, *247*, 129–139. [CrossRef]
15. Ogoshi, T.; Chujo, Y. Synthesis of anionic polymer–silica hybrids by controlling pH in an aqueous solution. *J. Mater. Chem.* **2005**, *15*, 315–322. [CrossRef]
16. Yap, H.Y.; Soon, C.F.; Nor, N.H.M.; Saripan, M.S.; Sahdan, M.Z.; Tee, K.S. Synthesis and characterization of polymeric microspheres by using suspension polymerization technique. *ARPN J. Eng. Appl. Sci.* **2016**, *11*, 11808–11811.
17. Santos, J.C.; Lopes, C.N.; Reis, M.M.; Giudici, R.; Sayer, C.; Machado, R.A.F.; Araujo, P.H.H. Comparison of techniques for the determination of conversion during suspension polymerization reactions. *Braz. J. Chem. Eng.* **2008**, *25*, 399–407. [CrossRef]
18. Bansal, H.; Kaur, S.P.; Gupta, A.K. Microsphere methods of preparation and applications; a comparative study. *Int. J. Pharm. Sci. Rev. Res.* **2011**, *10*, 69–78.
19. Lebedev, E.V. Hybrid organic-inorganic polymer systems: Synthesis, structure, and properties. *Theor. Exp. Chem.* **2011**, *46*, 5708–5712. [CrossRef]
20. Mahfouz, M.G.; Killa, H.M.; Sheta, M.E.; Moustafa, A.H.; Tolba, A.A. Synthesis, characterization, and application of polystyrene adsorbents containing tri-n-butylphosphate for solid-phase extraction of uranium(VI) from aqueous nitrate solutions. *J. Radioanal. Nucl. Chem.* **2016**, *309*, 729–741. [CrossRef]
21. Maciejewska, M. Characterization of macroporous1-vinyl-2-pyrrolidone copolymers obtained by suspension polymerization. *J. Appl. Polym. Sci.* **2011**, *124*, 568–575. [CrossRef]
22. Ali, S.W.; Malik, M.A.; Yasin, T. Economical and environmentally friendly synthesis of strongcation-exchange resins frommacroporous styrene-divinylbenzene copolymers. *Polym. Bull.* **2016**, *73*, 559–570. [CrossRef]
23. Srivastava, S.; Zare, E.N.; Makvandi, P.; Zheng, X.; Iftekhar, S.; Wu, A.; Padil, V.V.T.; Mokhtari, B.; Varma, R.S.; Tay, F.R.; et al. Cytotoxic aquatic pollutants and their removal by nanocomposite-based sorbents. *Chemosphere* **2020**, *258*, 127324. [CrossRef]
24. Younas, F.; Mustafa, A.; Faroogi, Z.U.R.; Wang, X.; Younas, S.; Mohy-Ud-Din, W.; Hameed, M.A.; Abrar, M.M.; Maitlo, A.A.; Noree, S.; et al. Current and Emerging Adsorbent Technologies for Wastewater Treatment: Trends, Limitations, and Environmental Implications. *Water* **2021**, *13*, 215.
25. Sheth, Y.; Dharaskar, S.; Khalid, M.; Sonawane, S. An environment friendly approach for heavy metal removal from industrial wastewater using chitosan based biosorbent: A review. *Sustain. Energy Technol. Assess.* **2021**, *43*, 100951.
26. Aldawsari, A.M.; Alsohaimi, I.; Hassan, H.M.A.; Abdalla, Z.E.A.; Hassan, I.; Berber, M.R. Tailoring an efficient nanocomposite of activated carbon-layered double hydroxide for elimination of water-soluble dyes. *J. Alloy.* **2021**, *857*, 157551. [CrossRef]
27. Karimi-Maleh, H.; Ayati, A.; Davoodi, R.; Tanhaei, B.; Karimi, F.; Malekmohammadi, S.; Orooji, Y.; Fu, L.; Sillanpää, M. Recent advances in using of chitosan-based adsorbents for removal of pharmaceutical contaminants: A review. *J. Clean. Prod.* **2021**, *291*, 125880. [CrossRef]
28. Kambarova, E.A.; Gawrilenko, M.A.; Bektenov, N.A. Zeolites modified with polyethylenepolyamine and epoxy resin to extract lead ions from wastewater. *Bull. Tomsk Polytech. Univ. Geo Assets Eng.* **2021**, *1*, 7–13.
29. Wang, M.; Gengxian, L.; Chunlong, X.; Xudong, J.; Rubing, W.; Qingquan, L.; Xiyun, C. Facile preparation of cyclodextrin polymer materials with rigid spherical structure and flexible network for sorption of organic contaminants in water. *Chem. Eng. J.* **2021**, *411*, 128489. [CrossRef]
30. Budnyak, T.M.; Błachnio, M.; Slabon, A.; Jaworski, A.; Tertykh, V.A.; Deryło-Marczewska, A.; Marczewski, A.W. Chitosan Coated Silica as Effective and Sustainable Material for Acid Orange 8 Dye Capturing: Effect of Temperature in AdsorptionEquilibrium and Kinetics. *J. Phys. Chem. C* **2020**, *28*, 15312–15323. [CrossRef]

31. Derylo-Marczewska, A.; Blachnio, M.; Marczewski, A.W.; Swiatkowski, A.; Buczek, B. Adsorption of chlorophenoxy pesticides on activated carbon with gradually removed external particle layers. *Chem. Eng. J.* **2017**, *308*, 408–418. [CrossRef]
32. Blachnio, M.; Derylo-Marczewska, A.; Charmas, B.; Zienkiewicz-Strzalka, M.; Bogatyrov, V.; Galaburda, M. Active Carbonfrom Agricultural Wastes for Adsorption of Organic Pollutants. *Moelcules* **2020**, *25*, 5105. [CrossRef]
33. Blachnio, M.; Derylo-Marczewska, A.; Marczewski, A.W.; Seczkowska, M. Phenoxyacid pesticide adsorption on activatedcarbon– equilibrium and kinetics. *Chemosphere* **2019**, *214*, 349–360.
34. Derylo-Marczewska, A.; Marczewski, A.W. Effect of adsorbate structure on adsorption from solutions. *Appl. Surf. Sci.* **2002**, *196*, 264–272. [CrossRef]
35. Derylo-Marczewska, A.; Miroslaw, K.; Marczewski, A.W.; Sternik, D. Studies of adsorption equilibria and kinetics of o-,m-,p-nitro-and chlorophenols on microporous carbons from aqueous solutions. *Adsorption* **2010**, *16*, 359–375. [CrossRef]
36. Podkoscielna, B.; Sobiesiak, M. Synthesis and characterization of organic–inorganic hybrid microspheres. *Adsorption* **2016**, *22*, 631–638. [CrossRef]
37. Podkoscielna, B.; Fila, K.; Gil, M.; Nowak, J. Synthesis and characterization of new hybrid microspheres with amide functionalization. *Adsorpt. Sci. Technol.* **2017**, *35*, 422–431. [CrossRef]
38. Goliszek, M.; Poskoscielna, B.; Fila, K.; Riazanova, A.V.; Aminzadeh, S.; Sevastyanova, O.; Gunko, V.M. Synthesis and structure characterization of polymeric nanoporous microspheres with lignin. *Cellulose* **2018**, *25*, 5843–5862. [CrossRef]
39. Fila, K.; Bolbukh, Y.; Goliszek, M.; Podkoscielna, B.; Gargol, M.; Gawdzik, M. Synthesis and characterization of mesoporous polymeric microspheres of methacrylic derivatives of aromatic thiols. *Adsorption* **2019**, *35*, 429–442. [CrossRef]
40. Podkoscielna, B.; Kolodynska, D.; Podkoscielny, P. Chemical modification of commercial St-DVB microspheres and their application for metal ions removal. *Adsorption* **2019**, *25*, 529–544. [CrossRef]
41. Santa Maria, L.C.; Costa, M.A.S.; Santos, F.A.M.; Wang, S.H.; Silva, M.R. Preparation and characterization of polymer metalcomposite microspheres. *Mater. Lett.* **2006**, *60*, 270–273. [CrossRef]
42. Wawrzykiewicz, M.; Podkoscielna, B.; Podkoscielny, P. Application of Functionalized DVB-co-GMA Polymeric Microspheres in the Enhanced Sorption Process of Hazardous Dyes from Dyeing Baths. *Molecules* **2020**, *25*, 5247. [CrossRef]
43. Hamid, J.N.; Fariba, D.; Reza, M.A. Effects of triethoxy and triphenylvinylsilanes on the porous structure of cross-linked poly(methylmethacrylate) beads. *e-Polymers* **2008**, 1–11. [CrossRef]
44. Naghash, H.; Karimzadeh, A.; Momeni, A.; Massah, A.; Alian, H. Preparation and Properties of Triethoxyvinylsilane-Modified Styrene-Butyl Acrylate Emulsion Copolymers. *Turk. J. Chem.* **2007**, *31*, 257–269.
45. Lee, J.; Hwang, D.; Shim, S.; Rhym, Y.-M. Controlling Morphology of Polymer Microspheres by Shirasu Porous Glass (SPG) Membrane Emulsification and Subsequent Polymerization: From Solid to Hollow. *Macromol. Res.* **2010**, *18*, 1142–1147. [CrossRef]
46. Yu, B.; Xu, T.; Cong, H.; Peng, Q.; Usman, M. Preparation of Porous Poly(Styrene-Divinylbenzene) Microspheres and TheirModification with Diazoresin for Mix-Mode HPLC Separations. *Materials* **2017**, *10*, 440. [CrossRef]
47. Walenta, E. Small angle X-ray scattering. *Acta Polym.* **1985**, *36*, 296. [CrossRef]
48. Li, T.; Senesi, A.J.; Lee, B. Small Angle X-ray Scattering for Nanoparticle Research. *Chem. Rev.* **2016**, *116*, 11128–11180. [CrossRef]
49. Putnam, C.D.; Hammel, M.; Hura, G.L.; Tainer, J.A. X-ray solution scattering (SAXS) combined with crystallography andcomputation: Defining accurate macromolecular structures, conformations and assemblies in solution. *Q. Rev. Biophys.* **2007**, *40*, 191–285. [CrossRef]
50. McDermott, A.G.; Budd, P.M.; McKeown, N.B.; Colina, C.M.; Runt, J. Physical aging of polymers of intrinsic microporosity: A SAXS/WAXS study. *J. Mater. Chem. A* **2014**, 2, 11742–11752. [CrossRef]
51. Saurel, D.; Segalini, J.; Jauregui, M.; Pendashteh, A.; Daffos, B.; Simon, P.; Casas-Cabanas, M. A SAXS outlook on disorderedcarbonaceous materials for electrochemical energy storage. *Energy Storage Mater.* **2019**, *21*, 162–173. [CrossRef]
52. Williams, J.A.; Rindone, G.E.; Mckinstry, H.A. Small-Angle X-Ray Scattering Analysis of Nucleation in Glass: I Matrix Scattering and Sample Surface Effects. *J. Am. Ceram. Soc.* **1981**, *64*, 697–702. [CrossRef]
53. Sharma, J. Characterization of Polymer Blends by X-Ray Scattering: SAXS and WAXS. In *Characterization of Polymer Blends*; Thomas, S., Grohens, Y., Jyotishkumar, P., Eds.; Wiley Online Library: New York, NY, USA, 2014; pp. 209–236.
54. Zienkiewcz-Strzalka, M.; Pikus, S. The study of palladium ions incorporation into the mesoporous ordered silicates. *Appl. Surf. Sci.* **2012**, *261*, 616–622. [CrossRef]
55. Zienkiewcz-Strzalka, M.; Pikus, S. Synthesis of photoactive AgCl/SBA-15 by conversion of silver nanoparticles into stable AgCl nanoparticles. *Appl. Surf. Sci.* **2013**, *265*, 904–911. [CrossRef]
56. Marczewski, A.W.; Derylo-Marczewska, A.; Slota, A. Adsorption and desorption kinetics of benzene derivatives on mesoporous carbons. *Adsorption* **2013**, *19*, 391–406. [CrossRef]
57. Chrzanowska, A.; Derylo-Marczewska, A.; Wasilewska, M. Mesocellular SilicaFoams (MCFs) with Tunable Pore Size as a Support for Lysozyme Immobilization: Adsorption Equilibrium and Kinetics, Biocomposite Properties. *Mol. Sci.* **2020**, *21*, 5479. [CrossRef]

Supplementary material for the paper:

Physicochemical and Adsorption Characteristics of Divinylbenzene-*co*-Triethoxyvinylsilane Microspheres as Materials for the Removal of Organic Compounds

Alicja Bosacka*, Małgorzata Zienkiewicz-Strzalka, Małgorzata Wasilewska, Anna Derylo-Marczewska* and Beata Podkoscielna

Institute of Chemical Sciences, Faculty of Chemistry, Maria Curie-Sklodowska University, Maria Curie-Sklodowska Sq. 3, 20-031 Lublin, Poland;

malgorzata.zienkiewicz@poczta.umcs.lublin.pl (M.Z.-S.); malgorzata.wasilewska@poczta.umcs.lublin.pl (M.W.); beatapod@poczta.umcs.lublin.pl (B.P.);

* Correspondence: alicja.bosacka@poczta.umcs.lublin.pl (A.B.); annad@hektor.umcs.lublin.pl (A.D.-M.); Tel.: +48-81-53-777-66 (A.D.-M.);

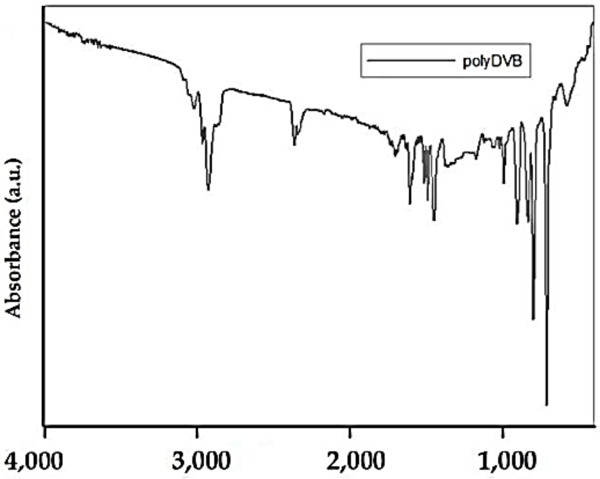

Figure S1. FTIR/ATR spectra of DVB.

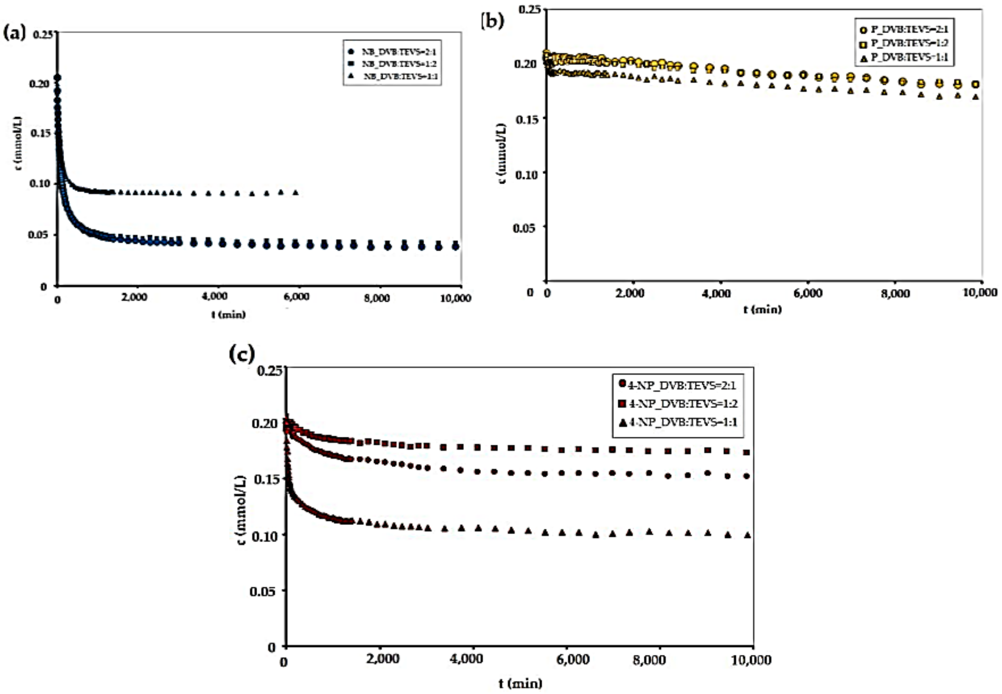

Figure S2. Adsorption kinetics for NB (**a**), P (**b**) and 4-NP (**c**) on DVB:TEVS=2:1, DVB:TEVS=1:2 and DVB:TEVS=1:1 presented as changes in concentration over time.

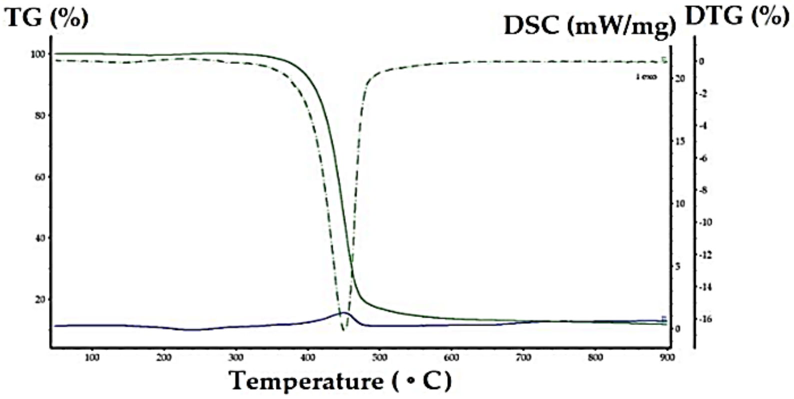

Figure S3. TG/DTG/DSC curves of DVB.

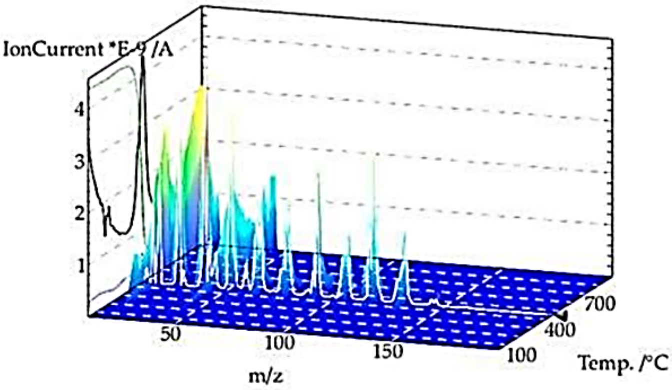

Figure S4. 3D MS profile of thermal decomposition of DVB.

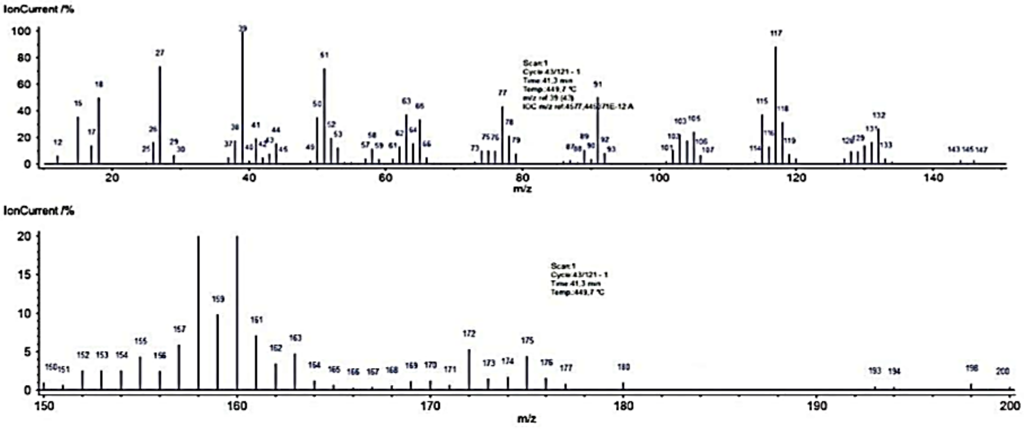

Figure S5. MS spectra of thermal degradation of DVB at 450 ◦C.

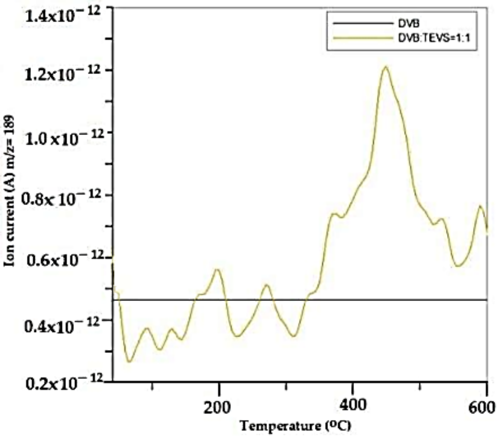

Figure S6. MS profiles of gaseous products of thermal degradation of DVB:TEVS=1:1 and DVB (m/z=189).

[D2] Alicja Bosacka, Małgorzata Zienkiewicz-Strzałka, Anna Deryło-Marczewska, Agnieszka Chrzanowska, Małgorzata Wasilewska, Dariusz Sternik, Physicochemical, structural, and adsorption properties of chemically and thermally modified activated carbons, Colloids and Surfaces A: Physicochemical and Engineering Aspects 2022, 647, 129130, https://doi.org/10.1016/j.colsurfa.2022.129130 wraz z materiałem dodatkowym [S2]

Colloids and Surfaces A: Physicochemical and Engineering Aspects 647 (2022) 129130

Contents lists available at ScienceDirect

Colloids and Surfaces A: Physicochemical and Engineering Aspects

journal homepage: www.elsevier.com/locate/colsurfa

Physicochemical, structural, and adsorption properties of chemically and thermally modified activated carbons

Alicja Bosacka *, Małgorzata Zienkiewicz-Strzałka, Anna Deryło-Marczewska *, Agnieszka Chrzanowska, Małgorzata Wasilewska, Dariusz Sternik

Institute of Chemical Sciences, Faculty of Chemistry, Maria Curie-Sklodowska University, Maria Curie-Sklodowska Sq. 3, 20-031 Lublin, Poland

HIGHLIGHTS

- Gradual increase of carbon surface area and pore volume with increasing modification temperature.
- Systematic increase of adsorption capacity with increasing modification temperature.
- Decrease in adsorption half-times with increasing modification temperature for all selected adsorbates.
- Distinct changes of adsorption half-times correlated with carbon surface properties.
- Systematic decrease of total weight losses for carbon samples with increasing modification temperature.

GRAPHICAL ABSTRACT

ARTICLE INFO

Keywords:
Activated carbon
Surface functionalization
Oxidation
Adsorption kinetics
Adsorbent-adsorbate interactions

ABSTRACT

In this work, granular activated carbon (GAC1240W Norit N.V.) was chemically and thermally modified to diverse its acid-base character. The main aim of this work was to assess the efficiency of surface modifications of activated carbons (ACs) concerning studying the differentiation of their affinity towards aromatic organic compounds of various properties. For this purpose, the comprehensive characteristics of oxidized activated carbon (AC-OX) and oxidized thermally modified carbons at 180, 280, 380, 480, 640, and 800 °C (AC-OX, AC-OX-180, 280, 380, 480, 640, and 800) were analyzed using several analytical techniques:low-temperature nitrogen sorption (porosity characteristics), potentiometric titration of suspension (SPT) (acid-base properties), X-ray photoelectron spectroscopy (XPS) (quality and quantity analysis of elements), thermal analysis (TA) coupled with mass spectrometry (MS) (materials thermal stability, identification of gaseous products emitted during thermal decomposition). To verify the applicability of adsorbents for removing selected organic compounds, the equilibrium and kinetic experimental data were measured and analyzed by applying various equations and models.

---

* Corresponding authors.
E-mail addresses: alicja.bosacka@poczta.umcs.lublin.pl (A. Bosacka), anna.derylo-marczewska@mail.umcs.pl (A. Deryło-Marczewska).

https://doi.org/10.1016/j.colsurfa.2022.129130
Received 13 March 2022; Received in revised form 27 April 2022; Accepted 28 April 2022

1. Introduction

Activated carbons (ACs) are a good deal of research due to their unique physicochemical properties. ACs are non-hazardous materials with a well-developed porous structure and usually with a significant share of microspores [1–4]. AC surface consists of three major sections: carbon basal planes (above 90% of the surface composition), heterogeneous sites (oxygen-containing groups mostly situated at the edges of basal graphite planes), and inorganic ash [5,6]. The rich surface of activated carbons in combination with thermal, chemical, and mechanical resistance makes these materials excellent adsorbents for water or wastewater purification, especially from organic compounds that are hard to decompose in water [7–11]. Despite these valuable features of activated carbons, surface functionalization is often a desirable operation as it may improve the sorption uptake of ACs and makes the adsorbent more selective [12,13].

The surface chemistry of activated carbons can be modified by various methods: the action of plasma, microwaves, or treatment in acid. Oxidation is a procedure by which hydroxyl, carbonyl, carboxyl, phenolic, lactone, ketone, or other oxygen functional groups can be embedded on the carbon surface. This process can be performed in a gaseous or liquid medium (dry – stream activated by ozone, carbon dioxide, or oxygen plasma or wet oxidation – using oxidizers: hydrogen peroxide, nitric acid, sulfur acid, or manganate potassium [12,14–16]. Likewise, surface modification can be performed by thermal treatment procedures that remove surface functional groups and also improve the thermal properties of a given material. The action of differentiated temperatures onto the surface abundant in oxygen species improve selective adsorption of hazardous substances from water or wastewater because of the distinction in quality and quantity of surface functional groups. Directly, their nature influences the type of interactions occurring between adsorbate and adsorbent phases. The acidic (or basic) active centers present on the carbon surface affect the charge, hydrophobicity, or electric density of graphene layers. The sorption capacity of activated carbons is also related to the adsorbate characteristics: its molecular weight, ionization strength (pKa), substituent type, or solubility (hydrophobicity) [1,7,17]. An important factor influencing the sorption efficiency is also solvent [18,19], therefore, different sorption mechanisms can be proposed: dispersion, donor-acceptor, hydrogen bonding to explain the adsorbent-adsorbate interactions, but this field is still not fully understood because of many factors that may affect the sorption capacity [20,21].

In this paper, the granular activated carbon (GAC1240W) was subjected to chemical (in concentrated nitric acid) and thermal (at various temperatures) modifications to diversify the chemical character of its surface. The obtained adsorbents were investigated using the following analytical techniques: low-temperature sorption, suspension potentiometric titration (SPT), X-ray photoelectron spectroscopy (XPS), thermal analysis(TA) combined with quadrupole mass spectrometry (QMS). The main aim of this work was to examine the influence of type and concentration of surface groups of activated carbons on the sorption mechanism towards selected aromatic organic solutes with the differentiated physicochemical characteristics: phenol (P), 4-nitrophenol (4-NP), and nitrobenzene (NB).

2. Experimental

2.1. Chemicals

Granulated activated carbon GAC1240W NoritN.V. Company (Klazienaveen, Drenthe, the Netherlands)(AC) was purchased from Sigma-Aldrich (Oakville, Ontario, Canada, USA). The AC producers and suppliers'description is in Table S1 (Supplementary material). Nitric acid (concentrated, 65%) used for GAC surface functionalization was bought from Avantor Performance Materials Poland S.A (Gliwice, Poland). Substances for the adsorption and equilibrium studies: phenol (P) and 4-nitrophenol (4-NP) were delivered by Merck (Darmstadt, Germany) and nitrobenzene (NB) by Avantor Performance Materials Poland S.A (Gliwice, Poland). Aqueous solutions for adsorption studies were prepared with the usage of deionized water. The physicochemical properties of aromatic compounds used as adsorbents are presented in Table S2 (Supplementary material) [22].

2.2. Material preparation

Initially, the AC material was washed with deionized water, sieved, and dried at room temperature. The dried AC was subjected to chemical treatment by 65% nitric acid at 80 °C over 3 h in the system equipped with a reflux condenser and magnetic stirrer according to the procedure proposed by Swiatkowski at all [20]. The oxidized AC (AC-OX) was transferred to the Büchner funnel and washed with at least 5 L of deionized water and dried at room temperature. The dried AC-OX was divided into portions, placed into the tube flow furnace, and heated at 180, 280, 380, 480, 640, and 800 °C for 3 h with a 5 °C/min heating rate and under nitrogen as protection against the material combustion.

2.3. Methods

2.3.1. Small-angle X-ray scattering (SAXS)

SAXS analysis was carried out by an Empyrean diffractometer (PANalytical) with CuKα radiation using the SAXS/WAXS stage and capillary mode. The SAXS configuration includes a range of 0.13–4.0 degrees of 2θ. The device was powered by a high-voltage X-ray generator and generator settings of 40 kV and 40 mA. The single-scan mode and reflection geometry were applied during SAXS measurements. The incident beam path consisted of a line focus type, W/Si, graded X-ray mirror with an elliptical shape. The primary beam was measured using a beam attenuator Cu 0.2 mm. The measurements were carried out using a PIXcel1D detector receiving slit with an active length of 0.05 mm. The relevant parameter of SAXS analysis was the momentum transfer or scattering vector q defined as $q = 4\pi\sin\theta/\lambda$, where 2θ is the scattering angle, λ is the X-ray wavelength (1.5418 Å). The corresponding range of q values was 0.0095–0.28 $Å^{-1}$. Background scattering was performed by air scattering measure with an empty sample holder. The measurement time was 2300 s for each carbon sample. Dv(R) calculations were performed using the indirect Fourier transformation technique applied in EasySAXS software. In this case, Tikhonov's regularization algorithm was applied [23].

2.3.2. Scanning electron microscopy (SEM)

Morphological/textural properties of samples were examined using Scanning Electron Microscopy (SEM) equipped with Quanta TM 3D FEG (FEI Company, Hillsboro, OR, USA) apparatus operating at 5 kV and high vacuum ($4 \cdot 10^{-4}$ Pa) condition.

2.3.3. Nitrogen sorption

Porosity properties of activated carbons were determined by the nitrogen low-temperature sorption isotherms using the ASAP2020 apparatus (Micromeritics Incorporation, Nocross, Georgia, USA) at 77 K. From the isotherms, values of the following parameters were obtained: BET specific surface area (S_{BET}) (calculated according to the standard BET method [24]), total pore volume (V_t) (assessed from and the nitrogen adsorption at $p/p_o \sim 0.99$), external surface area (S_{ext}), and micropore volume (V_{mic}) (both calculated from t-plot method), average hydraulic pore diameter (calculated according to the equation: $D_h = 4V_t/S_{BET}$), and pore size distributions (PSD) (calculated by Non-Local Density Functional Theory (NLDFT) [25]. Before the measurements, the samples were outgassed for 24 h at 90 °C and pressure of 1 mmHg in a degas port analyzer to remove physically adsorbed contaminants.

2.3.4. X-ray photoelectron spectroscopy (XPS)

Qualitative and quantitative investigations of ACs were conducted

Table 1
Structural parameters obtained from nitrogen sorption and SAXS measurements.

Samplename	Surface area (m^2/g)		Pore volume (cm^3/g)			Pore size (nm)	Porosity by SAXS	
	S_{BET}[a]	S_{ext}[b]	V_t[c]	V_{mic}[d]	V_{mic}/V_t[e]	D_h[f]	S/V[g] ($Å^{-1}$)	S_{SAXS}[h] (m^2/g)
AC	900	523	0.52	0.20	0.38	2.30	0.189	945
AC-OX	631	327	0.32	0.13	0.41	2.05	0.140	700
AC-OX-180	661	419	0.34	0.10	0.29	2.08	0.141	706
AC-OX-280	689	432	0.36	0.11	0.31	2.11	0.143	713
AC-OX-380	694	450	0.36	0.10	0.28	2.09	0.147	736
AC-OX-480	715	492	0.37	0.10	0.27	2.08	0.148	741
AC-OX-640	714	482	0.38	0.10	0.26	2.12	0.149	747
AC-OX-800	759	515	0.40	0.10	0.24	2.12	0.151	755

[a] S_{BET}, the BET specific surface area.
[b] S_{ext}, the external surface area.
[c] V_t, the total pore volume.
[d] V_{mic}, the micropore volume.
[e] V_{mic}/V_t, the quotient of V_{mic} and V_t.
[f] D_h, the average hydraulic pore diameter.
[g] S/V, the surface to volume ratio calculated from distribution curve.
[h] S_{SAXS}, the surface area by SAXS calculated by equation: $S_{SAXS} = (1000 \cdot S/V)/d$, where d is the carbon mass density (~2 g/cm^3).

by X-ray Photoelectron Spectroscopy (XPS). For this target, the multi-chamber Ultra-High Vacuum (UHV) system (Prevac 2009, Rogow, Poland) with the hemispherical analyzer (VG Scienta R4000) by monochromatic AlKa radiation from high-intensity source MX-650, Scienta (Uppsala, Sweden) and the average depth of analysis ~5 nm was applied. All of the binding energies were calibrated to the C1s peak. High-resolution XPS data were obtained for C1s and O1s signals. The data progress of deconvolution of C1s and O1s peaks was carried out by CasaXPS software (Casa Software Ltd.).

2.3.5. *Suspension potentiometric titration (SPT)*

Suspension potentiometric titration (SPT) measurements were performed using a system consisting of a pH meter (PHM240 Radiometer, Copenhagen, Denmark), an autoburet 765 Dosimat (Metrohm, Herisau, Switzerland), and a thermostat (Ecoline RE207, Lauda, Germany). Before the measurements, the quartz vessel was filled with 30 mL of electrolyte (0.1 mol/dm^3 NaCl) with the addition of 0.3 mL of 0.5 mol/dm^3 HCl. After 1 h of equilibration of the system in terms of established pH and temperature, 0.05 g of activated carbon previously dried for 3 h at 80 °C was added. The suspension of carbon in the electrolyte with the addition of hydrochloric acid was gradually titrated with 0.2 mol/dm^3 of NaOH. In addition, during the measurements, the system was protected against contamination with carbon dioxide through the action of an inert gas atmosphere (nitrogen with a purity of 99.0) [17].

2.3.6. *Thermal analysis (TA)*

Thermal analysis (TA) was performed using TG/STA/QMS Netzschapparatus (STA 449 Jupiter F1/QMS 403C Aëolos, Selb, Germany). The thermal analysis equipment calibration was performed using a sapphire. Before measurements, the sample of mass ~18 mg was placed in an alumina crucible and heated from 30 to 1200 °C under nitrogen conditions with a flow rate of 25 mL·min^{-1} and heating rate 10 °C·min^{-1}. Argon was used as a protective gas. The gaseous products emitted during the decomposition of ACs were analyzed by Quadrupole Mass Spectrometer (QMS). The QMS data in the range from 10 to 200 amu were recorded.

2.3.7. *Adsorption studies*

Adsorption equilibrium measurements were carried out by using a UV-Vis spectrophotometer (Cary 4000, Varian, Melbourne, Victoria, Australia) at wavelength 200–450 nm for establishing the adsorbate concentrations. Before measurements, the ACsample of mass ~0.05 g was placed in the 100 mL Erlenmeyer flask and then 5 mL of solvent was added. The sample with 5 mL of deionized water and fixed pH was degassed for 15 min using the water pump. After 15 min of degassing, the stock solution of the given concentration was prepared, added to carbon slurry and the vessel was placed into the incubator shaker for 7 days at 25 °C (110 rpm) (New Brunswick Scientific, Edison, New Jersey, USA). After, the equilibrium achievement, the solute concentration was determined based on the obtained data and calculated from the maximum absorbance peak A = f(λ). The adsorbed amount was calculated from the mass balance equation:

$$a_{eq} = \frac{(c_o - c_{eq}) \cdot V}{m} \tag{1}$$

where a_{eq} is the adsorbed amount, c_o is the initial concentration, c_{eq} is the equilibrium concentration, V is the adsorbate volume and m is the adsorbent mass [26].

The received equilibrium data were studied using the Generalized Langmuir (GL) isotherm equation:

$$\theta = \left[\frac{(\overline{K} \cdot c_{eq})^n}{1 + (\overline{K} \cdot c_{eq})^n}\right]^{\frac{m}{n}} \tag{2}$$

where θ is the relative adsorption (surface coverage), $\theta = a_{eq}/a_m$, and a_m is the adsorption capacity, m and n are the heterogeneity parameters ($0<m$, $n<1$), $\overline{K}$ is the adsorption equilibrium constant related to the characteristic energy of the distribution function. In some cases, the form of the GL isotherm is changed to simple equations as follows: $m=n=1$ in the Langmuir isotherm (L); $m=n$ in the Langmuir-Freundlich isotherm (LF); $n = 1$ in the Generalized Freundlich isotherm (GF); $m = 1$ in the Tóth isotherm (T) [27–29].

Adsorption kinetic measurements were conducted using a UV-Vis spectrophotometer (Cary 100, Varian, Melbourne, Victoria, Australia) equipped with a working cell allowing the cyclic solution measurements in a closed system. The sample of mass ~0.1 g was loaded into a quartz vessel connected with a magnetic stirrer (EUROSTAR 20, IKA, Poznan, Poland) (110 rpm) and thermostat (Ecoline RE207, Lauda, Germany) (25 °C) and poured with a solution of phenol (P), 4-nitrophenol (4-NP), and nitrobenzene (NB) with the initial concentration of 0.205 mmol/L. At definite time intervals, the solution was gathered in a flow cell, the absorption spectra were measured at the wavelength range of 200–450 nm and the solution was returned to the reaction vessel. Concentrations in the function of time profiles for the experimental systems were calculated from the recorded spectra. The Supporting data were analyzed using various adsorption kinetic equations and models presented in Table S3 [29–38].

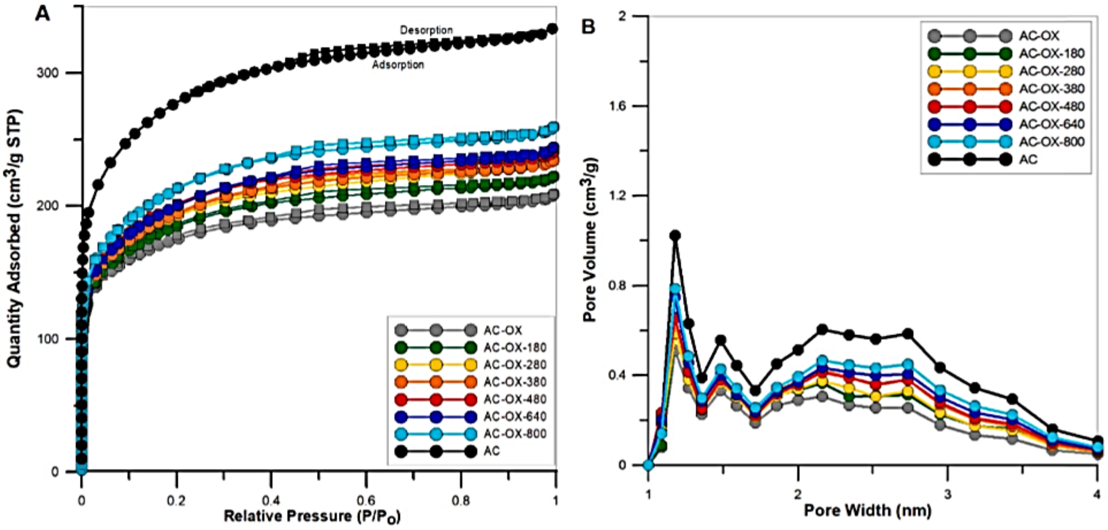

Fig. 1. Nitrogen adsorption-desorption isotherms (A), and pore size distributions calculated by using the non-local density functional theory (NLDFT) (B) for the studied ACs.

3. Results and discussion

3.1. Porosity properties

Porosity properties of chemically and thermally modified activated carbons were examined using low-temperature nitrogen adsorption-desorption measurements at 77 K. Analysing the structural parameters obtained from the experimental data one can state that the unmodified AC has a well-developed internal structure with a significant share of micropores. It is characterized by high specific surface area S_{BET}= 900 m^2, external surface area S_{ext} = 523 m^2, total pore volume V_t = 0.52 cm^3/g, and micropore volume V_{mic} = 0.2 cm^3/g (Table 1). The values of structural parameters of functionalized ACs are presented also in Table 1. Likewise, the isotherms of adsorption-desorption and pore size distributions calculated by NLDFT approach for the studied ACs are presented in Fig. 1. In general, the low-temperature adsorption-desorption isotherms of nitrogen are typical for microporous materials of I type with hysteresis loops of H4 characteristic for materials with a quite narrow pore size distributions according to the IUPAC classification [39,40].

The obtained data indicate that the chemical and thermal modifications of GAC carbon change its porous structure. Taking into account the isotherms (Fig. 1A) and the surface area values presented in Table 1 one can state that chemical oxidation of AC by nitric acid causes a reduction in the surface area sizes by 30–40%, however, further thermal treatments cause a gradual increase of a few percent in these values with increasing heating temperature. Also, the value of total pore volume decreases (from 0.52 to 0.32 cm^3/g) after an oxidation process and

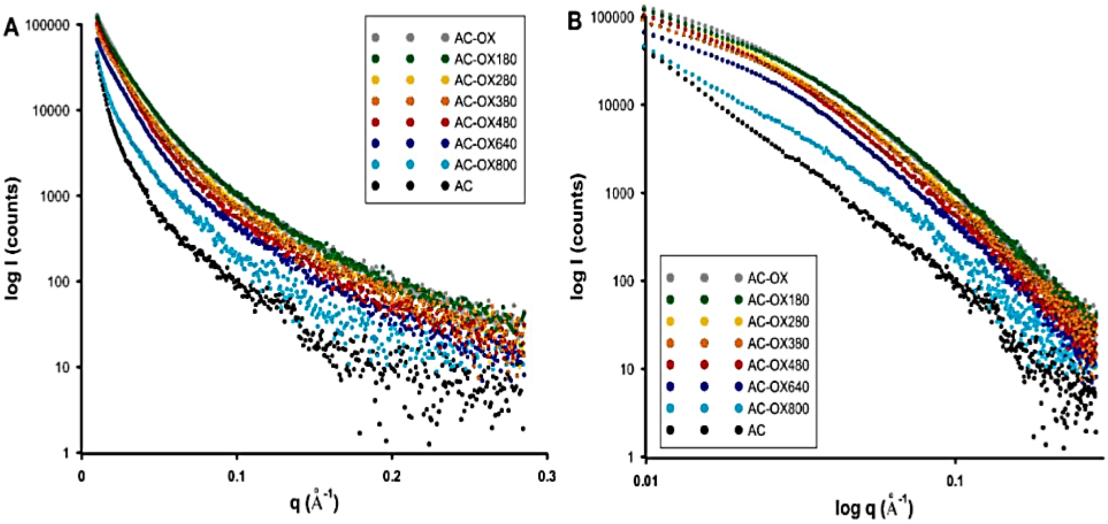

Fig. 2. Experimental SAXS curves of the investigated materials. The intensity *versus* momentum transfer q (length of scattering vector)is plotted in log-linear (a), and log-log (b) plots of ACs.

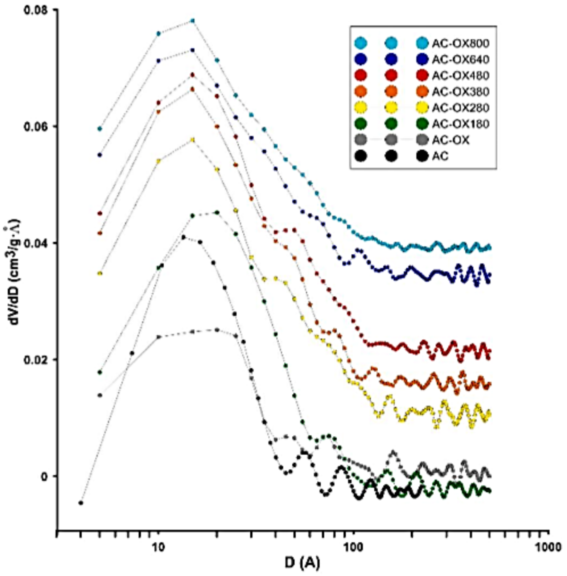

Fig. 3. Pore size distribution by volume analysis Dv(R) for investigated ACs.

further, it gradually increases with the temperature of thermal modification (from 0.34 to 0.40 cm^3/g). The similar character of changes in V_t and S_{BET}after oxidation and thermal treatment processes indicates an etching of carbon surface and gradual removal of oxidation residues with temperature increase. The micropore volume is also reduced after nitric acid treatment (from 0.20 to 0.13 cm^3/g), however, the changes after thermal modifications are insignificant (V_{mic}~0.10 cm^3/g). The initial decrease in the porosity parameters is related to the treatment of the material by an oxidation liquid. The literature data show that reduction of the surface area and porosity of the sample treated in nitric acid may be associated with the collapse of some pore walls. In addition, the oxygen surface groups can be considered as active centers which are located on the entrance of pores, therefore, the decrease in these values may be related to an increase in the number of oxygen surface groups that can be expected to be immersed inside or block the entrance of pores, thus limiting the accessible space of carbon material. An increase in surface areas after thermal heating is caused by the removal of oxygen surface groups that may be inside or block the entry of certain pores [7,10,16]. Regardless of the annealing temperature, the share of micropores in the total number of pores is decreasing. This may suggest the merging of micropores into larger pore structures and the development of non-microporous porous structures at higher temperatures from AC-OX-180 to AC-OX-800 (which is illustrated by a gradual increase in the specific surface area of materials and total pore volumes).

Considering the pore size distributions obtained by the NLDFT method shown in Fig. 1B, it can be claimed that for all examined ACs they are very similar and the pore sizes are in the range of 1–4 nm. Only some distinctions in the pore volumes are reported, mainly after the oxidation process, however, thermal treatment does not cause large differences. In addition, the value of the average hydraulic pore diameter is comparable (~2 nm) for all tested ACs (Table 1).

3.2. *Structural features by SAXS*

The experimental SAXS profiles of investigated ACs are shown in Fig. 2. All the considered carbon systems are capable of scattering X-rays in the range of low angles. Some differentiation of the scattering effect was observed depending on the tested system in terms of scattering intensity and curvature of scattering profiles. The factor responsible for the occurrence of the SAXS effect, in this case, is the three-dimensional porous structure which determines the difference in electron density between the carbon layers and the pore void spaces. The intensity of the SAXS effect is the lowest for a sample of unmodified carbon sample (AC) and increases successively depending on the thermal post-synthesis treatment (the lowest scattering intensity for AC-OX-800, the highest for AC-OX-180). The increase in scattering intensity may be related to the increase in the number of scattering centers, *i.e.*, pores with nano dimensions. Here, the mild temperature conditions generate the presence of nano-sized pores sensitive to the scattering effect of X-rays, as evidenced by its highest intensity. The high temperature changes the micropores into larger systems, the SAXS effect is weaker, but the overall surface area of the carbon material after high-temperature treatment may increase. Such observations are confirmed by direct porosity analysis (low-temperature nitrogen adsorption/desorption isotherms).

The volume-weighted particle size distribution Dv(R) function can be used for a detailed description of the size distribution of scattering objects (pores) (Fig. 3). Particle size distributions (Dv(R) were determined by using the indirect Fourier transformation procedure establishing a spherical morphology of scattering objects. By analyzing the SAXS data in the form of calculated heterogeneity size distributions, gradual and successive changes in the dimensions of these characteristic elements were observed. As the temperature of the post-synthesis treatment increases, the SAXS curves show an increase in the pore sizes(from 180 °C to 800 °C). The surface-to-volume ratio S/V was determined from Dv(R) function (Table 1). By taking into account the mass density of a typical porous carbon sample as 2 g/cm^3, the specific surface area of the pores was calculated from this value to 945 m^2/g and 700 m^2/g for AC and AC-OX samples respectively and further from 705 m^2/g to 755 m^2/g for thermally treated samples (Table 1). These results are in good agreement with those obtained from the same samples using the gas adsorption (BET) method. Note that the minor oscillations are non-avoidable artefacts originating from the indirect Fourier Transformation (FT) method during calculations. Nevertheless, the SAXS method, which remains definitely more sensitive to the presence of a porous system even in the area of closed pores (inaccessible for the gas adsorption-desorption method), indicates a reduction in the pore surface after the oxidation process and a gradual increase in this surface under temperature conditions.

3.3. *General morphology and microstructure*

The results obtained by low-temperature nitrogen adsorption-desorption and small-angle X-ray scattering techniques were compared with those from scanning electron microscopy. For all investigated samples general morphological/textural changes can be observed. The SEM images of four AC samples are presented in Fig. 4 and show variable morphology/texture depending on the applied modification. SEM images of the unmodified (AC) sample at different magnifications (Fig. 4A-C) indicate a relatively high degree of grain surface smoothness. The surface of this carbon is compact and almost free of cracks and large open spaces. The textural properties of the same sample change in an oxidation process by nitric acid (AC-OX). One can observe the appearance of many irregularities. Gaps appear and small pores begin to form larger patterns (Fig. 4D-F). This state is connected with the process of acid etching that besides oxidation may cause partial destruction of the micropore walls and the formation of surface defects [41]. Further microstructural changes are aggravated after the application of thermal treatment. Temperature modification gradually opens more porous areas (Fig. 4G-I and Fig. 4J-L) because of the gradual removal of post-synthesis traces. For the sample heated at 800 °C, the morphology/texture indicates the much-increased surface heterogeneity. The enlarged porosity facilitates access to pores with small diameters. Thus, the carbons in the process of oxidation and temperature treatment underwent quite significant morphological modification.

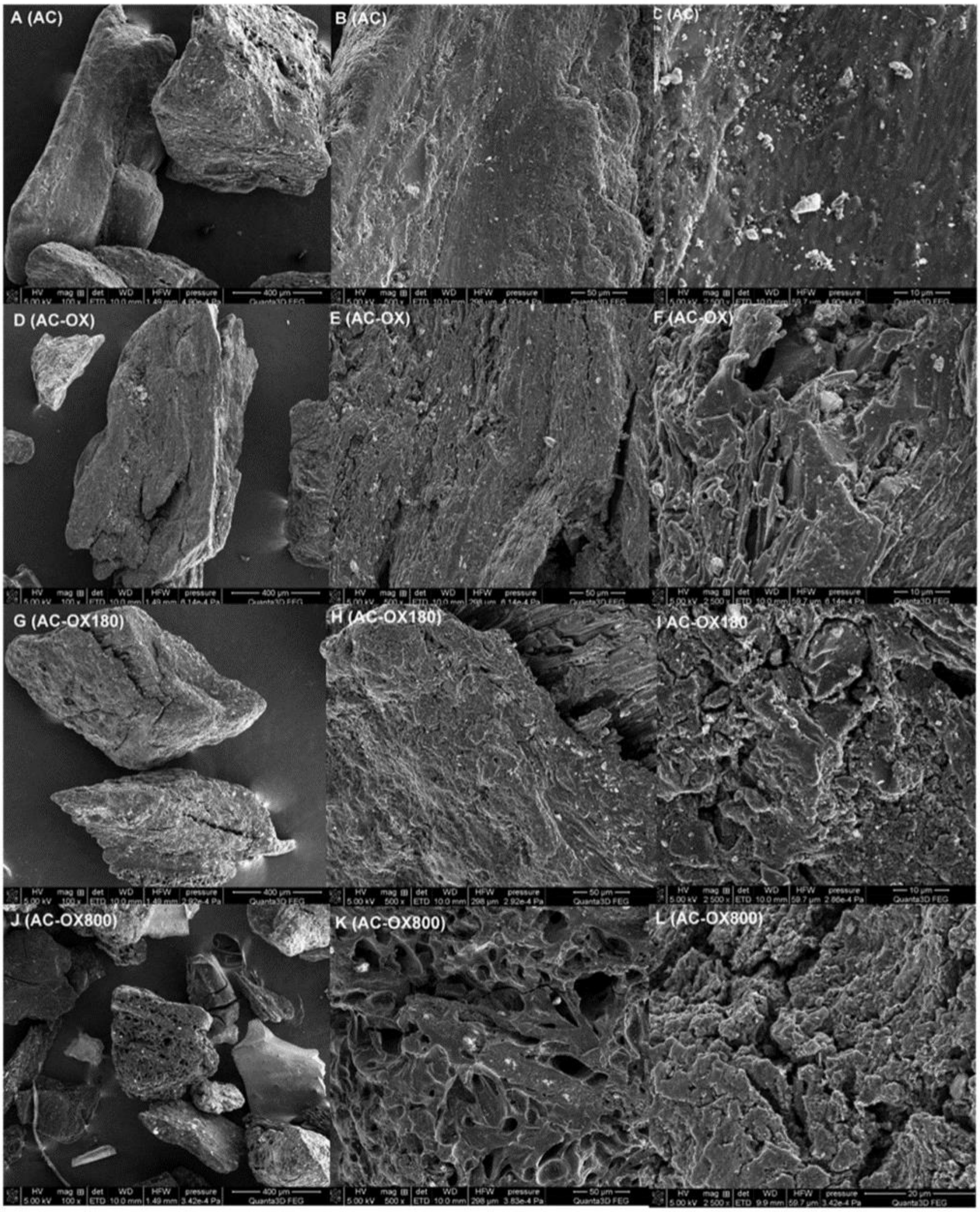

Fig. 4. SEM images of AC (A-C), AC-OX (D-F), AC-OX-180 (G-I), and AC-OX-800 (J-L).

Table 2
Quantitative results of XPS analysis of ACs.

Samplename	Binding Energy (eV)			FWHM			% Atomic Concentration			% Mass Concentration		
Name	C 1s	O 1s	Si 2p	C 1s	O 1s	Si 2p	C 1s	O 1s	Si 2p	C 1s	O 1s	Si 2p
AC	284.7	533.7	104.7	2.41	3.46	2.97	85.9	10.4	3.7	79.2	12.8	8.0
AC-OX	284.7	532.2	104.7	2.46	3.87	5.67	79.7	16.7	3.6	72.2	20.2	7.6
AC-OX-180	284.7	532.7	105.2	2.43	3.78	4.55	81.6	15.2	3.2	74.4	18.7	6.9
AC-OX-280	284.7	533.2	105.7	2.44	4.52	5.27	81.6	14.8	3.6	74.6	17.7	7.7
AC-OX-380	284.7	532.2	105.7	2.41	4.54	6.24	82.5	13.5	4.2	75.0	16.3	8.7
AC-OX-480	284.7	532.2	104.2	2.41	4.11	6.77	85.3	11.2	3.5	78.7	13.8	7.5
AC-OX-640	284.7	533.2	106.7	2.39	6.09	5.12	88.0	10.7	1.3	83.4	13.6	3.0
AC-OX-800	284.7	533.7	105.2	2.36	4.19	4.79	90.2	7.2	2.6	85.3	9.0	5.7

3.4. The qualitative and quantitative surface composition and chemical state analysis

The surface properties of ACs were investigated by X-ray photoelectron spectroscopy (XPS). The overview spectra of the functionalized oxidized carbons are present in Fig. S1 (Supplementary material). On the survey spectra, three characteristic peaks with the high-intensity carbon C 1 s, oxygen O 1 s, and silicon Si 2p are visible. The position of peaks of the studied carbons expressed by their binding energy (eV) and other parameters: full width at half maximum (FWHM), % atomic concentration, % mass concentration are presented in Table 2.

Generally, bands at 284.7 eV correspond with carbon C 1s, 532.2–533.7 eV with oxygen O1s, and 104.7–106.7 eV with silicon Si 2p. The comparison of qualitative and quantitative analysis in terms of C1s, O1s, and Si2p elements of the studied ACs expressed by % atomic (at%) or % mass (wt%) concentration is presented in Fig. 5. The % atomic concentration C 1s of initial AC was 85.9, O1s – 10.4, and Si 2p – 3.7. The % mass concentration of C 1s of AC was 79.2, O1s – 12.8, and Si 2p – 8.0. The chemical treatment of the initially activated carbon in oxyacid caused a reduction in the amount of carbon C 1 s from 85.9 to 79.7 at% (from 79.2 to 72.2 wt%) and an increase in the number of oxygen O1s from 10.4 to 16.7 at% (from 12.8 to 20.2 wt%). The C 1s content increase from 79.7 to 90.2 at% (72.2–85.3 wt%) and O 1s decrease from 16.7 to 7.2 at% (20.2–9.0 wt%) for chemically and thermally modified activated carbons is reported. Moreover, the analyzed activated carbons contain also a certain amount of silicon Si 2p below 5% and 9% of atomic and mass concentration, respectively. The silicon can be residue after the manufacturing process of activated carbon. Generally, the overview XPS analysis revealed that thermal treatment of previously oxidized activated carbons causes gradual changes in the content of both carbon C 1s and oxygen O 1s elements (the number of carbon decreases, oxygen increases). In addition, for the sample treated at 800 °C (AC-OX-800) the content of carbon C 1s is even higher

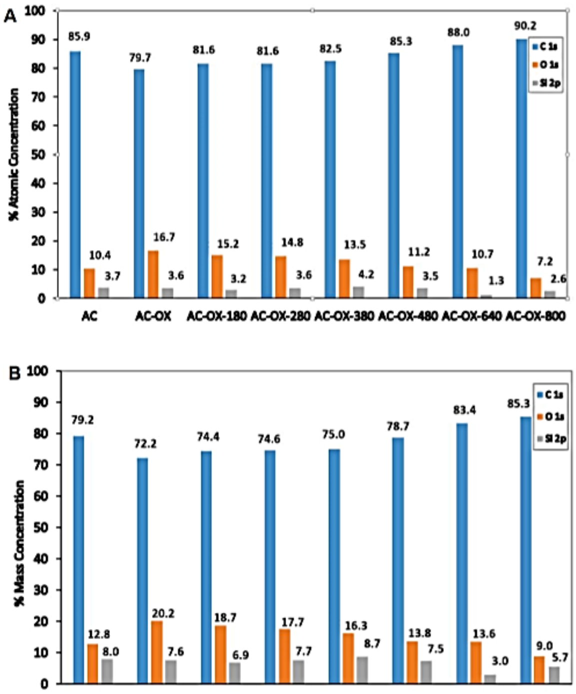

Fig. 5. The % atomic (A) and mass (B) concentration of C 1s, O 1s, and Si 2p of ACs.

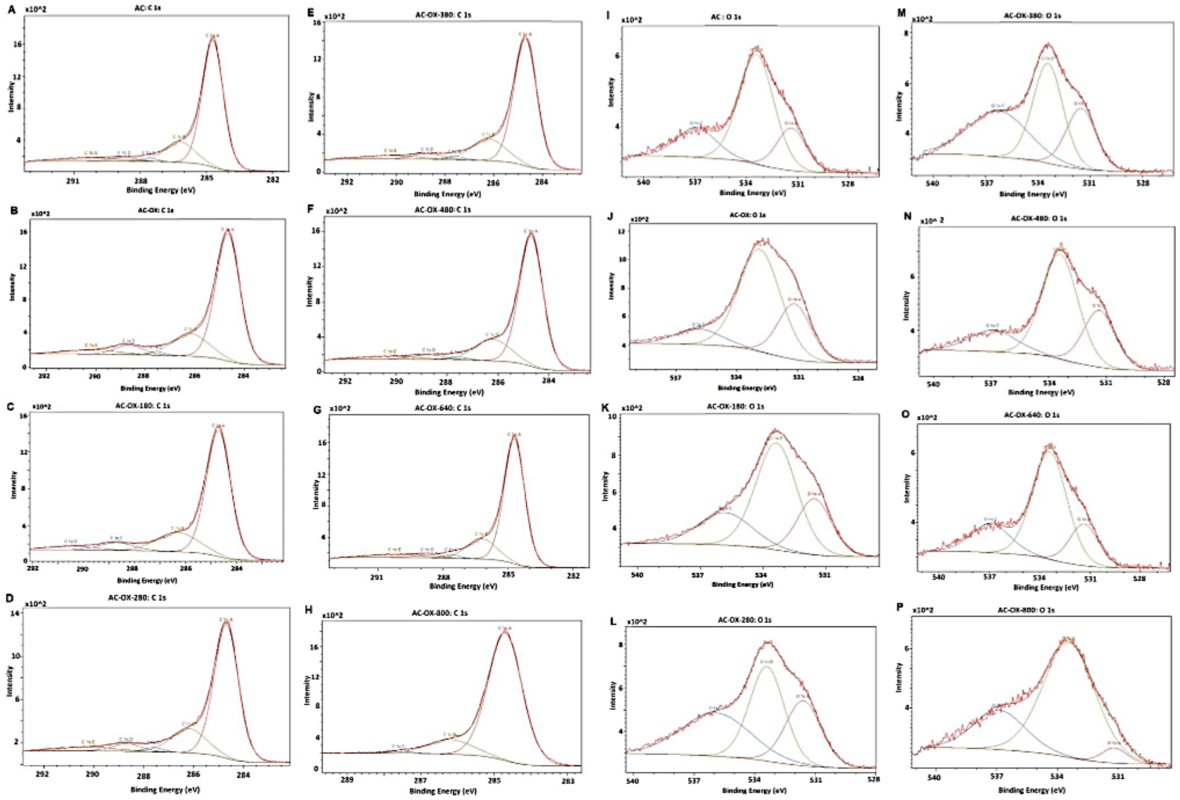

Fig. 6. Detailed spectra of C 1s (A-H) and O 1s (I-P) of the studied ACs.

and oxygen O 1s lower than for pure AC because of the removal of a higher quantity of surface functional groups, however, even a sample heated at such a high temperature as 800 °C was not completely removed from oxygen groups.

The detailed spectra of carbon C 1 s as well as an oxygen O 1 s species of functionalized ACs are presented in Fig. 6. The values of integrated parameters (binding energy, FWHM, % atomic concentration) and also assigned surface functional groups are presented in Table 3. The detailed analysis of the studied samples revealed the existence of surface carbon groups: single-bonded carbon with another carbon (C 1s A, 284.7 eV, C-C), ether (C 1s B, 286.2 eV, C-O-R, R = OH or C), carbonyl (C 1s C, 287.6 eV, C=O), carboxyl (C 1s D, 288.7 eV, O-C=O), and also carbonate (C 1s E, 290.2 eV, H_2CO_3) The detailed qualitative analysis of oxygen surface groups was also performed. The oxygen in the form of carboxyl (O 1s A, ~531.5 eV, O-C=O), silicon dioxide (O 1s B, ~533 eV, SiO_2), and from adsorbed water (O 1s C, ~536 eV, H_2O) was detected. The studied samples are characterized by different proportions of the indicated functional groups located onto the surface (Fig. 7). Concerning carbon functional groups (Table 3 and Fig. 7A), it is confirmed that each of the studied samples is loaded with the highest amount of C-C and C-O-H or C-O-C. The presence of carbonyl, carboxyl, carbonate groups onto the ACs surfaces is also detected but in smaller quantities. Only in sample AC-OX-180, the C=O group was not found. Additionally, thermal treatment at 800 °C caused surface depletion from O-C=O and H_2CO_3 species. Taking into account, the oxygen species (Table 3 and Fig. 7B): the highest degree of ACs surface coverage is by silicon dioxide groups. The rest of the surface is covered by carboxyl group or adsorbed water and their proportions are differentiated depending on the sample.

3.5. Acid-base properties

The acid-base properties of functionalized activated carbons were examined by potentiometric titration of suspension (SPT). The SPT experiment was conducted for all modified activated carbons. The dependence of surface charge density on pH is presented in Fig. 8. The point of zero charge (pH_{PZC}), which may be estimated from the experimental curves, is the pH value at which the surface charge is equal to zero. If the surface is negatively charged the material can adsorb cations. On the other hand, if it is positively charged it can adsorb anions.

The analyzed activated carbons are both positively and negatively charged but the acid-base characteristics are differentiated depending on the modification process (Fig. 8). The AC-OX carbon is to a greater extent negatively charged in the pH range > 3.6 as its pH_{PZC} is 3.6, therefore, could have a greater affinity to cations. The opposite situation is observed for the sample treated at 800 °C where its pH_{PZC} is 11.5 and thus rather positive charged till a pH < 11.5.

The samples treated at temperatures 180–640 °C have intermediate properties between AC-OX and AC-OX-800, however, the effect of increasing the pH_{PZC} with a higher temperature of thermal treatment is evident.

The value of pH_{PZC} of unmodified activated carbon (AC) is equal to 10.8. The oxidation process by nitric acid decreases the pH_{PZC}value from 10.8 to 3.6. Taking into account the curves presented in Fig. 8, one can state that the influence of thermal treatment of the studied samples on pH_{PZC} values is evident. The lowest value of $pH_{PZC} = 3.6$ is reported for the chemically modified sample without treatment (AC-OX sample). The values of pH_{PZC} for thermally modified samples: AC-OX-180, 280, 380, 480, 640, and 800 are 4.1, 5.7, 7.8, 9.9, 10.7, and 11.5, respectively. The highest pH_{PZC} is reported for the sample thermally treated at 800 °C

Table 3
The detailed data of XPS analysis of ACs samples.

AC								**Samplename**
AC-OX								
AC-OX-180								
AC-OX-280								
AC-OX-380								
AC-OX-480								
AC-OX-640								
AC-OX-800								
O 1s C	**O 1s B**	**O 1s A**	**C 1s E**	**C 1s D**	**C 1s C**	**C 1s B**	**C 1s A**	**Name**
536.9	533.4	531.2	290.2	288.7	287.6	286.2	284.7	**Binding Energy (eV)**
535.9	532.9	531.1	290.2	288.7	287.6	286.2	284.7	
535.8	533.4	531.5	-	290.5	288.7	286.3	284.7	
535.9	533.4	531.6	290.2	288.7	287.6	286.2	284.7	
536.3	533.4	531.5	290.2	288.7	287.6	286.2	284.7	
536.9	533.4	531.4	290.2	288.7	287.6	286.2	284.7	
536.9	533.4	531.4	290.2	288.7	287.6	286.2	284.7	
536.9	533.4	531.2	-	-	287.6	286.2	284.7	
2.70	2.15	2.00	2.50	1.24	0.81	1.63	1.11	**FWHM**
2.70	2.42	1.92	2.50	1.36	0.75	1.73	1.15	
3.00	2.31	1.92	-	2.18	1.56	1.93	1.12	
4.00	2.02	2.08	2.50	1.39	0.87	1.65	1.15	
4.00	2.01	2.02	2.50	1.35	0.80	1.64	1.11	
2.90	2.19	1.96	2.50	1.42	0.88	1.64	1.09	
2.70	2.40	2.01	2.70	1.33	0.81	1.60	1.11	
3.00	3.04	1.47	-	-	0.90	1.45	1.09	
15.6	58.8	25.6	5.4	1.9	1.5	17.4	73.8	**% AtomicConcentration**
10.6	62.4	27.0	5.2	6.0	1.3	18.5	69.0	
21.6	54.7	23.7	4.2	6.1	-	18.7	71.0	
34.8	38.0	27.2	4.5	4.8	1.7	18.4	70.6	
36.3	39.6	24.1	4.2	4.2	1.5	18.4	72.1	
15.4	57.0	27.6	3.5	3.8	1.4	18.4	73.4	
18.7	61.4	19.9	4.6	3.3	1.6	17.3	74.1	
24.1	71.3	4.6	-	-	1.1	13.1	85.8	
H_2O	SiO_2	O-C=O	H_2CO_3	O-C=O**	C=O*	C-O-R*	C-C	**Identyfiedgroup**

*R= OH orC
(AC-OX-180: O-C═O)
* *(AC-OX-180: H_2CO_3)

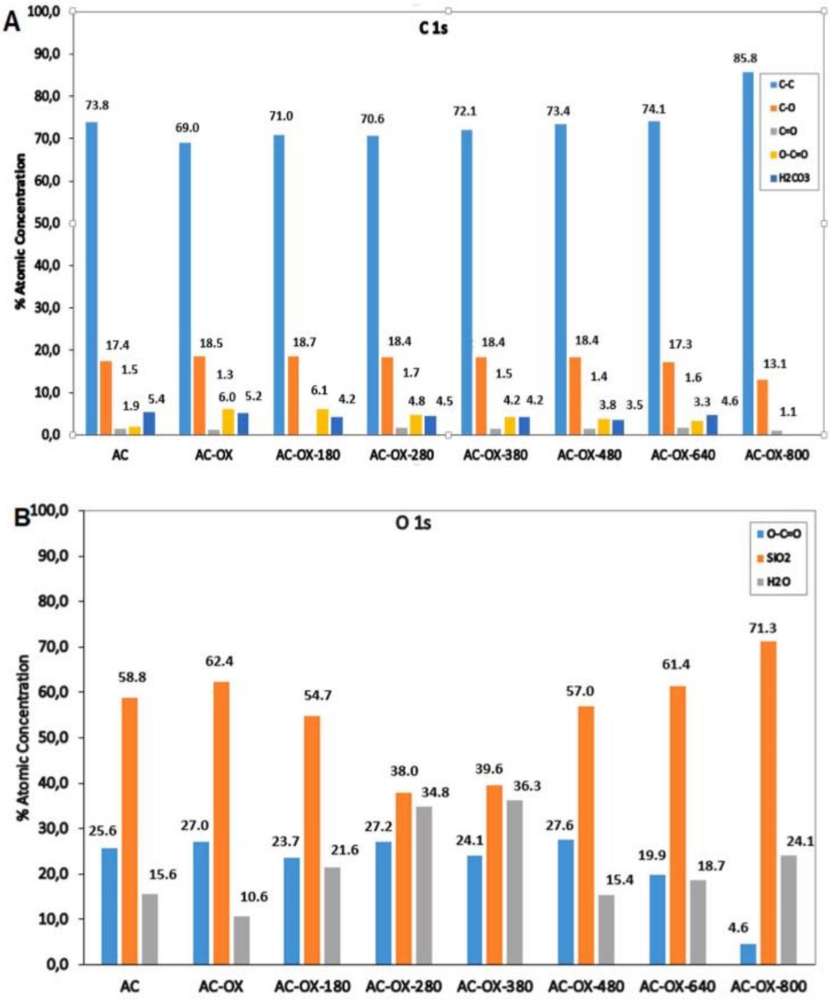

Fig. 7. The % atomic concentration of the particular carbon surface groups of C 1s (A), and O 1s (B) of ACs.

($pH_{PZC} = 11.5$) and this value is even higher than in the case of the initial activated carbon (pH = 10.8) because of the removal of the most functional groups from its surface. The value of pH_{PZC} of the sample heated at 640 °C is close to the value of initial carbon.

Overall, the suspension potentiometric titration studies revealed the differentiated acid-base character of the studied samples. AC-OX sample shows the most acidic, AC-OX-800, the most basic from the analyzed ACs. The rest of the studied carbons (AC-OX-180, AC-OX-280, AC-OX-380, AC-OX-480, AC-OX-640) have intermediate acid-base properties between AC-OX and AC-OX-800. Generally, the data obtained by XPS and PTS are in good agreement.

3.6. *Adsorption properties*

To estimate the adsorption properties of the tested ACs, the studies of the sorption equilibrium and kinetics of nitrobenzene (NB), 4-nitrophenol (4-NP) and phenol (P)for AC-OX, AC-OX-180, AC-OX-280, AC-OX-380, AC-OX-480, AC-OX-640, and AC-OX-800 were performed. In Fig. 9 and Fig. S2 (Supplementary material), the adsorption isotherms and capacities for the studied experimental systems are compared. In Fig. 10 and Fig. S3 (Supplementary material) the concentration and adsorption profiles are shown for all studied carbon materials.

First, let's follow the maximum adsorption amounts for selected adsorbates on active carbons. Based on the analysis of the data shown in Fig. 9, for all tested aromatic organic compounds, a clear increase in the adsorption value is observed with the increase in the temperature of the adsorbent modification; the highest for systems with AC-OX-800, and the lowest for AC-OX. For the studied experimental systems, the maximum adsorption values are 2.29, 2.77, 3.26, 3.81, 4.54, 5.03 and 5.55 mmol/g for AC-OX, AC-OX-180, AC-OX-280, AC-OX-380, AC-OX-480, AC-OX-640, and AC-OX-800 (Fig. 9A), respectively. In a certain part, this effect may be due to differences in the structural properties of the tested carbon materials (increase of specific surface area and pore volume). However, the most important effect on adsorption is connected with strong changes in surface characteristics of adsorbents (number and type of surface functional groups, acid-base properties). Thus, the interactions between the adsorbate molecules and the surface of active carbons should be considered. In the investigated experimental systems the dispersion interactions between the π electrons from the aromatic ring of the adsorbate and the π electrons in the adsorbent graphene layers prevail [29,42]. At the same time, taking into account that the adsorption was carried out from aqueous solutions, a certain share of

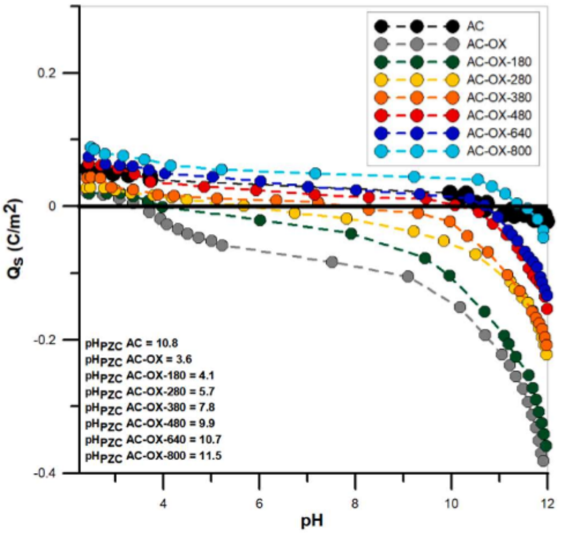

Fig. 8. Surface charge density in the function of pH, $Q_s = f$ (pH) of all tested ACs.

competitive adsorption between the adsorbate and water molecules in the studied samples should be expected. Therefore, hydrogen bonds can also occur here, both between the surface groups of the adsorbents and the functional groups of solutes, as well as the surface groups of activated carbon and water molecules [6,29]. Additionally, it should be noted that under the experimental conditions (pH=7), the active carbons AC-OX, AC-OX-180 and AC-OX-280 have a negative charge, and AC-OX-380, AC-OX-480, AC-OX-640 and AC-OX-800 have a positive charge (potentiometric titration data). At the same time, the adsorbates are partially or completely dissociated. Therefore, the electrostatic repulsion interactions may weaken adsorption, however, the electrostatic attraction can promote greater adsorption. Generally, an increase in the basic character (increasing pH_{PZC} values) of the tested carbon materials supports the adsorption of compounds of acidic chemical nature. Moreover, bearing in mind that the amount of oxygen functional groups of the investigated activated carbons decreases with the increasing modification temperature of the materials, their hydrophobicity increases. Therefore, in the systems with AC-OX-800, between the molecules of aromatic organic compounds and the adsorbent, the strongest hydrophobic interactions occur, which favors the adsorption process. Based on the analysis of data presented in Fig. 10A, B and S2 (Supplementary material), the highest amount of adsorption was observed for nitrobenzene and the lowest for phenol. The maximum adsorption values are in the range: 2.29 – 5.55, 2.02 – 4.54 and 1.85 – 3.23 mmol/g, respectively for NB, 4-NP and P (Fig. 10A and B). This relationship can be explained based on the differences in the water solubility of these compounds. Among the studied adsorbates, phenol is the best soluble in water, and nitrobenzene is the worst. This means that among the aromatic organic compounds selected for research, NB is more hydrophobic, which in turn indicates its greater affinity for the hydrophobic surface of the activated carbon, which promotes greater adsorption [29,42].

The obtained experimental data of the adsorption equilibrium were analyzed employing the Generalized Langmuir equation and its parameters are summarized in Table 4. In the case of nitrobenzene adsorption, for most experimental systems, the heterogeneity parameter n is equal to 1, which indicates that the GL isotherm simplifies to the GF equation. However, for the adsorption on AC-OX and AC-OX-480, the heterogeneity parameter m is equal to 1, which in turn means that the GL isotherm reduces to the equation T [27–29]. For the adsorption of 4-nitrophenol and phenol, only for 4-NPAC-OX-380 and PAC-OX systems, the Tóth isotherm was used to describe the adsorption process. For the remaining adsorption systems, the Generalized Freundlich isotherm was used. Based on the data collected in Table 4, the average heterogeneity effect was observed for all investigated experimental systems. Additionally, the adjusted values of the sorption capacity for individual samples are comparable to the values designated experimentally. The quality of fit is very good, which is confirmed by the values of the determination coefficients,R^2 ranging from 0.928 to 1; and standard deviations, *SD (a)* ranging from 0.034 to 0.308.

Let us proceed to the analysis of the adsorption rate of selected aromatic organic compounds on the tested carbon materials. Based on the analysis of the kinetic data presented in Fig. 10 and S3 (Supplementary material), in the investigated experimental systems, similar relationships in the adsorption rate were observed concerning the results of the adsorption equilibrium studies. Considering the data presented in Fig. 10A, C, E, it was shown that the loss of adsorbate concentration from the solution increases with the modification temperature increase; the highest was observed for systems with AC-OX-800, and the lowest for AC-OX. In addition, by analyzing the data collected in Fig. 10B, D and F, the highest adsorption for AC-OX-800 is also shown. Based on the analysis of Fig. S3 (Supplementary material), it is shown that for most of the experimental systems, the greatest loss of concentration from the solution and the greatest relative adsorption is observed for samples with nitrobenzene, and the smallest with phenol. The obtained experimental adsorption data were analyzed employing many equations and models of adsorption kinetics (the relative standard deviations are listed in Table 5). Based on the analysis of the data listed in Table 5, it is visible that the best quality of fit is obtained using the multi-exponential equation, the parameters of which are presented in Table 6. Considering the data in Table 6, it can be seen that the adsorption of selected aromatic organic compounds on the studied activated carbons is a complex process, the rate of which can be described by 2 or 3 terms of the m-exp equation. At the same time, in the case of nitrobenzene adsorption, if 3 terms of the m-exp equation are used to describe the rate of this process, the first of them is very small, ranging from 0.005 to 0.024. The fitting quality is very good, which is confirmed by low values of relative standard deviations *SD(c)/co* in the range from 0.041% to 0.858% and low values of indetermination factors 1-R^2in the range from $1.0 \cdot 10^{-5}$ to $7.8 \cdot 10^{-4}$. Moreover, the values of the u_{eq} parameter correspond to the differences in the adsorption amount of selected adsorbates on individual activated carbons. In particular, these relationships are most pronounced for the phenol experimental systems. This is because in this experimental part low initial concentrations of the tested aromatic organic compounds were used, and phenol shows the weakest affinity to the studied carbon materials. Additionally, the half time $t_{1/2}$ was estimated for all experimental systems. It is defined as the time it takes to recover half of the concentration change. The determined values of the half-times are 108.4–224.4, 123.1–628.2 and 141.7–682.1 min for the activated carbon samples with NB, 4-NP and P, respectively. This in turn confirms the highest adsorption rate for NB, the solute of the highest hydrophobicity showing the strongest interactions with carbon basal planes. However, for two other adsorbates characterized by lower hydrophobicity a certain share of interactions with oxygen functional groups may be expected which reveals in prolongation of adsorption rate. It was also observed that the values of the $t_{1/2}$ parameter decreased with the increasing modification temperature of activated carbon, which confirms the greatest adsorption kinetics on AC-OX-800 material. In Fig. S4 (Supplementary material) some simple correlations are presented confirming this tendency: $t_{1/2}$*vs.* pH_{PZC},$t_{1/2}$ *vs.*at%(O 1 s),$t_{1/2}$ *vs.* T.The higher number of acidic surface groups, the higher $t_{1/2}$, which confirms the interactions of some solute molecules with adsorbent surface sites extending the diffusion process. Moreover, a correlation between the adsorption half-time and specific surface ($t_{1/2}$*vs.* S_{BET}) may be observed, which confirms also the influence of adsorbent pore structure.

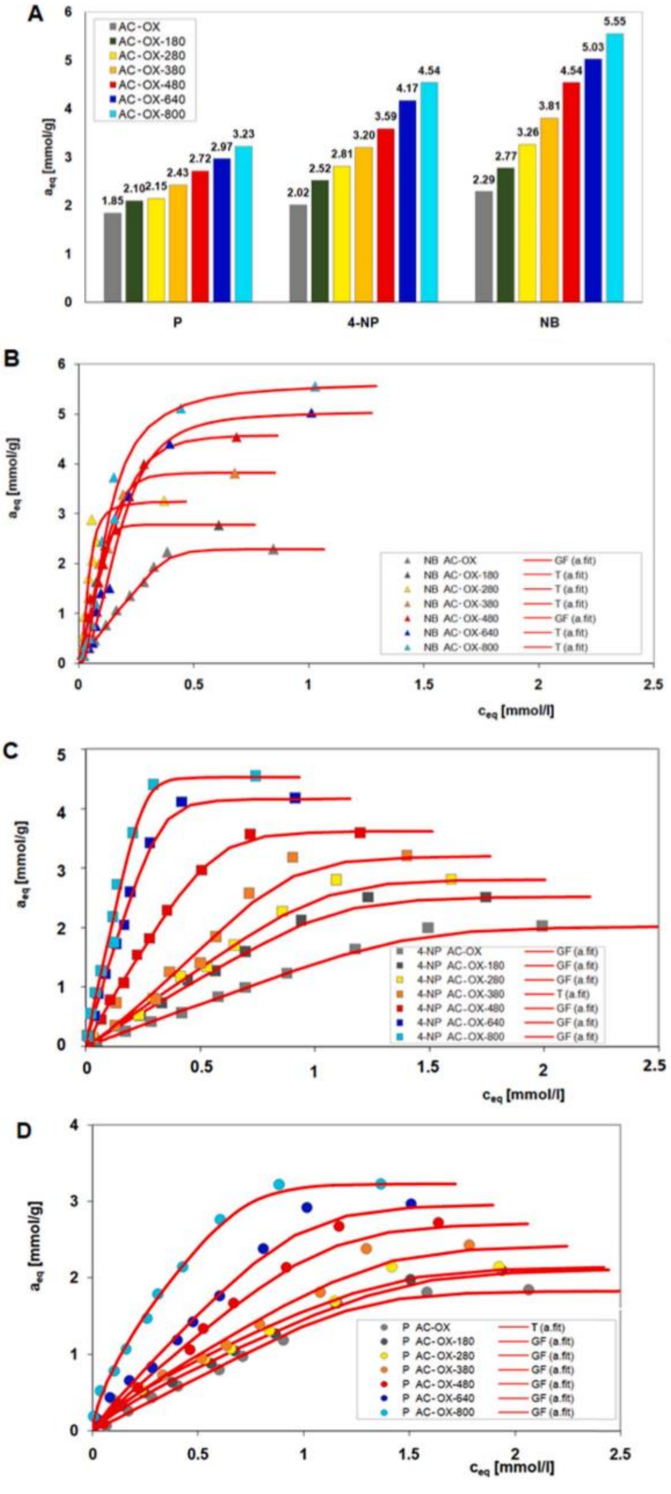

Fig. 9. Comparison of the adsorption amounts (A), and the adsorption isotherms (B-D) on AC-OX, AC-OX-180, AC-OX-280, AC-OX-380, AC-OX-480, AC-OX-640, AC-OX-800 for 4-NP, NB, and P.

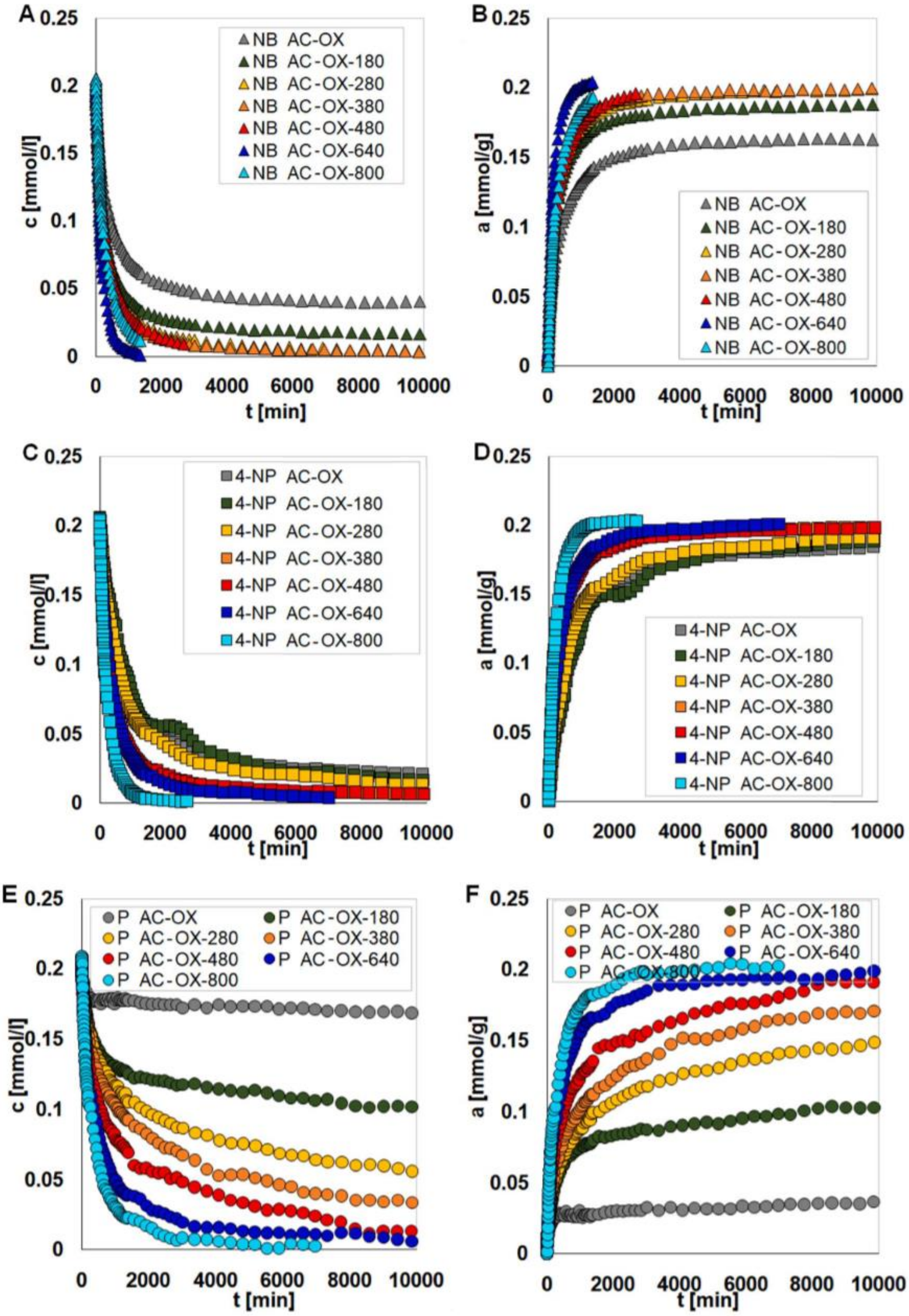

Fig. 10. Adsorption kinetics on AC-OX, AC-OX-180, AC-OX-280, AC-OX-380, AC-OX-480, AC-OX-640, AC-OX-800 presented as changes in concentration (A, C, E), or adsorption over time (B, D, F) for NB (A, B), 4-NP (C, D), and P (E, F).

Table 4
Parameters of the Generalized Langmuir equation characterizing adsorption of NB, 4-NP and P from dilute aqueous solutions on AC-OX, AC-OX-180, AC-OX-280, AC-OX-380, AC-OX-480, AC-OX-640, AC-OX-800.

System	Isotherm type	a_m	m	n	logK	R^2	SD (a)
NB AC-OX	GF	2.29	0.90	1	0.40	0.995	0.063
NB AC-OX-180	T	2.78	1	0.61	0.89	0.995	0.070
NB AC-OX-280	T	3.25	1	0.48	1.30	0.928	0.308
NB AC-OX-380	T	3.83	1	0.41	0.74	0.992	0.118
NB AC-OX-480	GF	4.59	0.92	1	0.58	0.991	0.162
NB AC-OX-640	T	5.04	1	0.81	0.64	0.991	0.176
NB AC-OX-800	T	5.65	1	0.75	1.07	0.987	0.244
4-NPAC-OX	GF	2.02	0.97	1	-0.16	1.000	0.021
4-NP AC-OX-180	GF	2.52	0.97	1	-0.05	0.998	0.049
4-NP AC-OX-280	GF	2.81	0.89	1	-0.03	0.997	0.057
4-NP AC-OX-380	T	3.20	1	0.69	0.04	0.977	0.179
4-NP AC-OX-480	GF	3.62	0.92	1	0.23	0.999	0.055
4-NP AC-OX-640	GF	4.16	0.90	1	0.46	0.998	0.069
4-NP AC-OX-800	GF	4.53	0.93	1	0.58	0.984	0.225
P AC-OX	T	1.83	1	0.45	-0.12	0.996	0.042
P AC-OX-180	GF	2.11	0.82	1	-0.19	0.998	0.034
P AC-OX-280	GF	2.15	0.76	1	-0.18	0.993	0.067
P AC-OX-380	GF	2.43	0.84	1	-0.16	0.983	0.117
P AC-OX-480	GF	2.72	0.90	1	-0.07	0.996	0.063
P AC-OX-640	GF	2.97	0.91	1	-0.02	0.995	0.083
P AC-OX-800	GF	3.23	0.67	1	0.11	0.997	0.066

3.7. Thermal analysis

Thermal properties (stability, decomposition stages, gaseous products) during heating of ACs in nitrogen atmosphere were examined by TG/DTG/DSC/MS-coupled techniques.The thermogravimetry (TG), the derivative thermogravimetry (DTG), and the differential scanning calorimetry(DSC) curves, as well as thermal analysis parameters of pure functionalized ACs, are given in Fig. 11 and Table 7, respectively. By analyzing the TG and DTG curves, it is visible that the thermal degradation of studied materials is a multi-stage process in the temperature range of 40–1200 °C. The initial decomposition stage is observed in the temperature range of 40–180 °C with peaks minimum from 53.6 to 89.4 °C ($T_{min,\ IDT}$) on the DTG curves with initial weight loss ($m_{loss,\ IDT}$) in the range of 0.23–4.64%. This phenomenon is associated with the removal of hygroscopic water from the surface of ACs as evidenced by the endothermic peak on the DSC curve, (Fig. 11). One can find that total weight loss ($m_{loss,\ TOTAL}$) systematically decreases after thermal modification of ACs at higher temperatures as follows: AC-OX>AC-OX-180 >AC-OX-280 >AC-OX-380 >AC-OX-480 >AC-OX-640 >AC-OX-800, the highest and lowest weight loss for the initial AC-OX (4.64%) and thermally treated at 800 °C (AC-OX-800) samples (0.76%) is established. Also, on the DSC curves for the oxidized ACs samples before and after thermal modification at 180, 240, 380, 680, 800 °C, the endothermic peaks in the low-temperature region with T_{peak1} at 61.2–89.4 °C (Table 7) are reported. The main stage of the ACs decomposition process is observed in the temperature range of 350–950 °C with the greatest weight loss (m_{loss2} ~ 12–25%) and minimum on the DTG curve at T_{min2}~666–724 °C. It was found that as the temperature of the material modification process increases, the T_{min2} in the DTG curves shifts towards higher temperatures. Comparison of the total mass loss of carbon samples without and with thermal treatment indicates that total weight loss ($m_{loss,\ TOTAL}$) significantly reduces after temperature modification, and it is attributed to the main destruction of carbon materials. Generally, a higher weight loss for the initial AC-OX sample (~41.1%) in comparison to the AC samples after thermal modification at 180 (~37.9%), 280 (33.1), 380 (32.6), 480 (28.2), 640 °C(26.3%)is observed. These results significantly confirm that the AC-OX sample is characterized by the most acidic surface (highest weight loss ~41.1) while for AC-OX-800 most alkaline surface is observed (the lowest mass loss ~19.9%). This difference is associated with a higher amount of oxygen functional groups on the surface of the AC-OX carbon, and the gradual changes in the weight loss for the studied material (decreasing with increasing temperature) follow different concentrations of surface oxygen groups onto their surface. In addition, peaks on the DSC curves with a minimum at T_{peak2} (444–524 °C) are observed, associated with the desorption of quite strongly bonded surface oxygen groups in exothermic processes. Generally, up to 950 °C, the most functional groups are desorbed from the surface of all tested samples. At temperature below 350 °C for two, the most acidic samples AC-OX and AC-OX-180 additional smaller peaks on the DTG curves at T_{min1} = 275.3 °C(m_{loss1} = 4.69%) in the case of AC-OX, and T_{min1}

Table 5
Relative standard deviations SD(c)/c_o (%) for m-exp, FOE, SOE, MOE, f-FOE, f-SOE, F-MOE, McKay pore diffusion (PDM), and IDM model (Crank).

System	m-exp (%)	FOE (%)	SOE (%)	MOE (%)	f-FOE (%)	f-SOE (%)	f-MOE (%)	IDM (%)	PDM (%)
NB AC-OX	0.561	3.722	1.069	1.075	0.884	0.704	0.708	6.65	31.03
NB AC-OX-180	0.605	3.761	0.362	0.364	1.240	0.363	0.365	9.05	22.56
NB AC-OX-280	0.645	3.826	0.637	0.466	1.166	0.562	0.557	8.79	31.27
NB AC-OX-380	0.577	3.718	0.949	0.482	1.181	0.690	0.688	9.09	31.04
NB AC-OX-480	0.318	3.033	1.248	0.611	0.936	0.985	0.982	34.77	55.73
NB AC-OX-640	0.706	1.579	4.886	0.809	1.078	1.715	1.730	32.90	61.96
NB AC-OX-800	0.644	3.086	2.152	0.779	1.303	1.342	1.303	36.82	64.96
4-NP AC-OX	0.647	3.368	1.733	1.743	2.001	1.743	1.751	4.38	33.17
4-NP AC-OX-180	0.858	2.991	2.089	2.101	2.306	2.066	2.078	11.08	34.41
4-NP AC-OX-280	0.219	2.683	1.454	1.462	1.633	1.339	1.333	9.13	34.99
4-NP AC-OX-380	0.041	0.140	0.192	0.050	0.138	0.176	0.049	17.51	4.40
4-NP AC-OX-480	0.662	3.371	1.132	0.910	1.124	1.060	0.861	9.08	34.63
4-NP AC-OX-640	0.533	2.536	2.429	0.811	0.770	1.356	0.707	10.96	33.64
4-NP AC-OX-800	0.671	1.762	4.883	0.723	1.044	1.731	0.629	13.27	32.56
P AC-OX	0.474	1.274	0.962	0.968	1.060	0.865	0.870	14.16	20.25
P AC-OX-180	0.452	2.838	1.344	1.352	1.263	0.873	0.878	10.00	28.72
P AC-OX-280	0.519	3.660	2.261	2.275	0.673	0.466	0.470	1.12	29.22
P AC-OX-380	0.515	4.497	2.742	2.758	1.183	0.956	0.892	3.14	30.13
P AC-OX-480	0.774	5.548	3.207	3.226	1.869	1.601	1.390	4.43	29.28
P AC-OX-640	0.738	4.846	2.019	2.031	2.390	1.860	1.870	8.04	32.12
P AC-OX-800	0.837	4.319	2.406	1.956	2.532	2.086	1.967	27.07	41.83

Table 6
Optimized parameters of m-exp equation.

System	f_1, log k_1	f_2, log k_2	f_3, log k_3	u_{eq}	$t_{1/2}$ (min)	SD (c)/c_o (%)	1-R^2
NB AC-OX	0.018, 1.301	0.414, – 2.053	0.568, – 2.956	0.796	224.4	0.561	$4.1\cdot10^{-4}$
NB AC-OX-180	0.012,– 1.301	0.536, – 2.091	0.452, – 2.903	0.907	186.5	0.605	$3.7\cdot10^{-4}$
NB AC-OX-280	0.024,1.301	0.514, – 2.134	0.462, – 2.914	0.968	185.7	0.645	$3.6\cdot10^{-4}$
NB AC-OX-380	0.012, 1.301	0.493, – 2.042	0.495, – 2.818	0.972	182.7	0.577	$2.9\cdot10^{-4}$
NB AC-OX-480	0.013, 1.301	0.398, – 2.023	0.589, – 2.779	0.956	170.1	0.318	$9.5\cdot10^{-5}$
NB AC-OX-640	0.005, 1.301	0.555, – 2.002	0.440, – 2.496	1.000	162.1	0.706	$4.1\cdot10^{-4}$
NB AC-OX-800	0.436, 2.071	0.564, – 2.750	–	1.000	108.4	0.644	$4.0\cdot10^{4}$
4-NP AC-OX	0.172, – 1.990	0.628, – 2.754	0.200, – 3.636	0.919	628.2	0.647	$2.6\cdot10^{-4}$
4-NPAC-OX-180	0.042, – 1.712	0.677, – 2.795	0.281, – 3.777	0.979	465.9	0.858	$3.0\cdot10^{-4}$
4-NP AC-OX-280	0.103, – 2.003	0.697, – 2.775	0.200, – 3.658	0.957	465.9	0.219	$1.2\cdot10^{4}$
4-NP AC-OX-380	0.090, – 2.000	0.632, – 2.745	0.279, – 3.686	0.951	392.1	0.041	$1.0\cdot10^{-5}$
4-NP AC-OX-480	0.241, – 1.892	0.643, – 2.654	0.116, – 3.468	0.971	258.4	0.662	$3.7\cdot10^{-4}$
4-NP AC-OX-640	0.153, – 1.814	0.737, – 2.623	0.110, – 3.388	0.985	235.8	0.533	$2.2\cdot10^{4}$
4-NP AC-OX-800	0.414, – 2.030	0.586, – 2.541	–	0.994	123.1	0.671	$3.5\cdot10^{-4}$
P AC-OX	0.181, – 1.230	0.419, – 1.945	0.400, – 4.087	0.217	682.1	0.474	$1.1\cdot10^{-4}$
P AC-OX-180	0.157, – 1.788	0.453, – 2.565	0.390, – 3.997	0.593	658.0	0.452	$7.8\cdot10^{4}$
P AC-OX-280	0.129, – 1.599	0.368, – 2.634	0.503, – 3.605	0.750	518.8	0.519	$5.2\cdot10^{-4}$
P AC-OX-380	0.187, – 1.929	0.300, – 2.665	0.513, – 3.557	0.867	465.1	0.515	$3.5\cdot10^{-4}$
P AC-OX-480	0.211, – 1.852	0.385, – 2.692	0.404, – 3.719	1.000	263.9	0.774	$6.6\cdot10^{4}$
P AC-OX-640	0.318, – 1.963	0.515, – 2.766	0.168, – 3.506	0.970	207.5	0.738	$6.2\cdot10^{-4}$
P AC-OX-800	0.336, – 1.960	0.557, – 2.693	0.107, – 3.462	1.000	141.7	0.837	$7.2\cdot10^{-4}$

= 286.6 °C (m_{loss1} = 4.02%) for AC-OX-180 can be found which confirms exothermic nature of these processes. It is related to the partial decomposition of surface groups connected to the desorption of a bit less-bonded oxygen species for both AC-OX and AC-OX-180 materials. It means that the surface functional groups of the tested materials are partially and systematically removed during the process of thermal modification of ACs samples at different temperatures (this effect is greatest in the case of material thermally treated at 800 °C (AC-OX-800)). The next decomposition step occurs at a temperature above 950 °C with a similar value of weight loss (m_{loss3} ~ 6%) for all studied carbons and is related to the removal of the most strongly surface-bonded oxygen functional groups (maxima on the DTG curve at ~1170 °C, Fig. 11). The total weight loss ($m_{loss,TOTAL}$), involving the three or optionally four stages, is related to the acidic-basic character of the surface of the materials. Overall, the total weight loss of ACs samples is in the range of 20–40% and confirms the high thermal stability of the analyzed materials.

To explain the thermal destruction routes and mechanism for investigated samples, the characteristics of the gaseous products yielded during their degradation of carbon materials were examined by the mass spectrometry (MS) technique which was coupled with TG. The 2D MS spectra of AC-OX, AC-OX-180, AC-OX-380, and AC-OX-800, and 3D MS spectra and gaseous products emitted during decomposition of ACs are shown in Fig. S5-S7 (Supplementary material). Generally, in the case of samples without adsorbed organic substances, the MS results (Fig. S5-S6) show that process of water removal takes place below 200 °C (m/z = 18, H_2O and m/z = 17, OH). Above 200 °C it starts to come away from various oxygen functional groups differently bonded (m/z = 44, CO_2). It can be seen that in the regions of medium temperatures, 180–350 °C, the slightly less-bonded functional groups are desorbed from the surface of the carbons. The quite strong-bonded groups with ACs surface are detached around T_{min2} ~700 °C (Table 7). At temperatures above 950 °C, the functional groups are still removed from the surface of carbon materials up to 1170 °C. It can be summarized the existence of very strong bonded functional groups onto the carbon's surface.

The comparison of the TG, DTG, and DSC data of thermal degradation of ACs after thermal modification and loaded with organic substances: phenol, nitrobenzene, and 4-nitrophenol with the initial support are present in Fig. 11, and Tables 7–8. Similarly, as oxidized carbon and thermally modified samples, the small mass losses in the range up to 180 °C for carbon material with adsorbed organic molecules were established, which is also related to the destruction of hydrogen bonds and removal of physically bound water from the solid surface. The stage of the carbons decomposition process with adsorbed P, NB, and 4-NP, regardless of the thermal modification temperature of the AC-OX initial material, shows the highest weight loss, $m_{loss2,}$ m_{loss3} (~12–24%, Tables 7, 8), and minimum peaks, T_{min2}, T_{min3}, (Tables 7, 8) on the DTG curves (Fig. 11) in the temperature range of 350–950 °C. It is related to thermodesorption of physically and partly chemically adsorbed P, NB, and 4-NP from carbon surface, their fragmentation, and partial oxidation of carbon surface (endothermic peaks in the area of 150–350 °C and exothermic peak at 350–500 °C on the DSC curve of 4-NP (Fig. 11)). Based on the analysis of the total weight loss ($m_{loss,\ TOTAL}$) for carbon adsorbents after organic solutes adsorption, it can be shown that the total weight losses systematically diminishes after thermal modification at higher temperatures as follows: P, NB, 4-NP AC-OX-180 >AC-OX-380 >AC-OX-800. However, this effect is greater in the case of oxidized ACs with adsorbed NB (Tables 7, 8).

Comparison of 3D MS spectra and gas profiles of pure carbon adsorbents (Figs. S6 and S7, Supplementary material) and carbons with adsorbed aromatic organic compounds (Figs. S8 and S9) showed that for the samples filled with P, 4-NP, and NB, additional signals related to degradation of adsorbed substances are reported. In addition to signals from physically bounded water (m/z = 17, 18) and carbon (IV) oxide (m/z = 44), signals from the nitrogen (II) oxide (m/z = 30), nitrogen (IV) oxide (m/z = 46), benzene ring (m/z = 77, 78), phenol (m/z = 94), nitrobenzene (m/z = 123), 4-nitrophenol (m/z = 139) can be found, however, the differences in their intensities are observed. Regarding m/z = 17 and 18 (Fig. 11), the signals below 200 °C, as was previously mentioned, are related to physically adsorbed water, however, peaks above 200 may be connected to the decay of P, 4-NP, and NB during the heating process. The peak with a maximum at ~280 °C ofm/z = 123 profile is clearly visible for NB, which means that nitrobenzene is tightly bound to the carbon and the interaction of nitrobenzene with the carbon surface groups is stable up to ~300 °C. This state is also confirmed by the presence of signals from benzene rings (m/z = 77, 78), and nitrogen (IV) dioxide (m/z = 46) that are the most intense for NB, and this substance is also detached from the carbon surface below 400 °C.The distinct peaks of phenol (m/z = 94) that elute at a slightly lower temperature (maximum at ~240 °C) than NB (m/z = 123, ~280 °C) are also noted. On the m/z = 94 gaseous profile 4-NP, and NB peaks with lower intensities than P are also visible which can be associated with braking down of 4-NP and NB molecules. For m/z = 30 the main peak is observed again below 400 °C (maximum at 310 °C) with higher intensity for 4-NP of AC-OX-180 and AC-OX-380 samples and similar

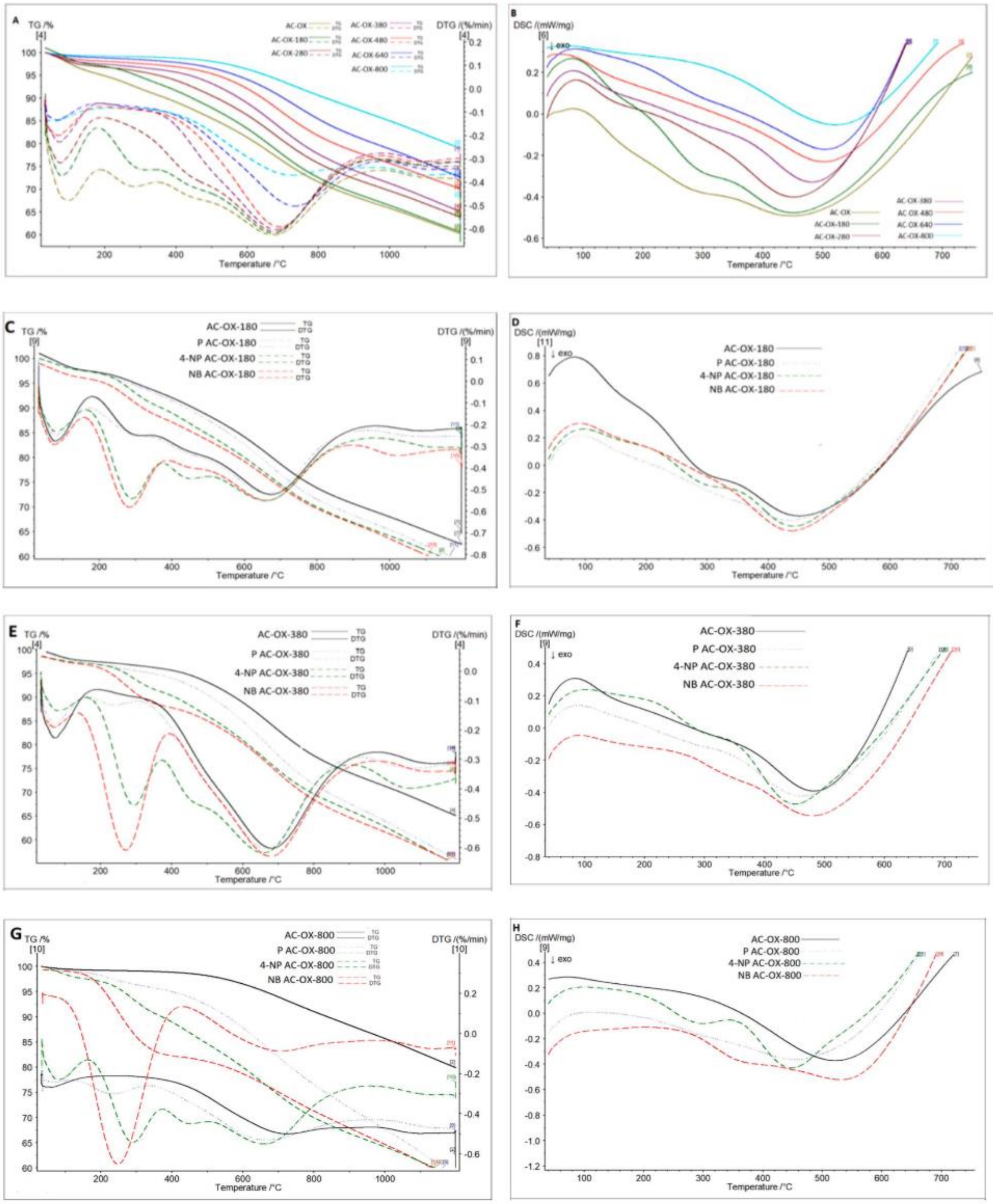

Fig. 11. TG, DTG and DSC curves of pure modified ACs (A-B), and AC-OX-180 (C-D), AC-OX-380 (E-F) and AC-OX-800 (G-H) and loaded with P, 4-NP, and NB.

intensity to that of nitrobenzene on AC-OX-800 sample. The presence of the $m/z = 30$ signal is also related to the decomposition of 4-NP and NB. For $m/z = 139$, the clear peaks cannot be seen, which could mean that 4-NP can be a less stable form than P or NB.

4. Conclusions

In this paper, the influence of chemical and thermal treatment of activated carbons on their porous, morphological, acid-base, adsorption, and thermal properties was examined. The applied modifications do not change significantly the pore structure, however, some differences in surface areas and pore volumes were evident as was confirmed by SAXS

Table 7
Comparison of thermal properties of pure modified ACs and loaded with P and NB.

Sample name	TG					DTG			DSC	
	$m_{loss, IDT}$ (%) 40–180 (°C)	m_{loss1} (%) 180–350 (°C)	m_{loss2} (%) 350–950 (°C)	m_{loss3} (%) 950–1170 (°C)	$m_{loss, TOTAL}$ (%) 40–1170 (°C)	$T_{min, IDT}$ (°C)	T_{min1} (°C)	T_{min2} (°C)	$\uparrow T_{peak1}$ (°C)	$\downarrow T_{peak2}$ (°C)
AC-OX	4.64	4.69	25.48	6.32	41.13	89.4	275.3	669.0	89.4	444.4
AC-OX-180	3.78	4.02	24.02	6.04	37.86	79,9	286.6	666.3	84.2	456.4
AC-OX-280	2.81	–	24.14	6.15	33.10	76.5	–	670.0	69.0	450.9
AC-OX-380	2.33	–	23.58	6.66	32.57	73.1	–	685.3	77.8	483.4
AC-OX-480	1.81	–	20.26	6.12	28.19	69.3	–	689.4	71.1	499.7
AC-OX-640	1.03	–	18.53	6.74	26.30	65.4	–	731.4	73.9	511.5
AC-OX-800	0.76	–	12.49	6.63	19.88	53.6	–	723.9	61.2	523.6
P AC-OX-180	2.88	4.01	24.94	4.54	36.37	81.9	302.5	667.6	87.5	434.9
P AC-OX-380	1.87	1.69	24.10	7.88	35.54	73.1	230.0	668.0	79.3	462.5
P AC-OX-800	0.61	1.87	15.67	5.92	24.07	68.7	227.4	665.3	–	451.5
NB AC-OX-180	3.09	8.26	23.21	7.94	42.50	76.7	279.9	664.0	83.8	432.1
NB AC-OX-380	1.41	8.16	22.65	6.21	38.43	70.6	270.3	675.6	79.7	476.6
NB AC-OX-800	0.23	8.46	12.29	5.60	26.58	74.5	243.0	706.1	–	529.7

Table 8
Thermal analysis data of ACs loaded with 4-NP.

Sample name	TG						DTG				DSC	
	$m_{loss, IDT}$ 40–150 (°C)	m_{loss1} 150–350 (°C)	m_{loss2} 350–500 (°C)	m_{loss3} 500–900 (°C)	$m_{loss4,}$ 900–1170 (°C)	$m_{loss, TOTAL}$ 40–1170 (°C)	$T_{min, IDT}$ (°C)	T_{min1} (°C)	T_{min2} (°C)	T_{min3} (°C)	$\uparrow T_{peak1}$ (°C)	$\downarrow T_{peak2}$ (°C)
4-NP AC-OX-180	2.43	6.94	5.89	18.50	6.82	33.76	80.8	289.8	443.2	652.8	88.8	440.4
4-NP AC-OX-380	1.30	5.59	5.20	19.75	7.95	31.84	80.1	293.8	456.1	662.4	88.6	447.2
4-NP AC-OX-800	0.83	6.12	4.69	12.84	6.41	24.48	81.8	288.4	443.3	683.6	82.8	446.1

and nitrogen adsorption-desorption measurements. The potentiometric titration studies revealed the differentiated acid-base character of the studied carbons from acidic to basic (changes of pH_{PZC}). It was confirmed by XPS results in which a decrease of surface oxygen groups in thermal treatment was reported.

The adsorption measurements were conducted for all modified carbons and three aromatic adsorbates: nitrobenzene, 4-nitrophenol, and phenol. Based on equilibrium studies the increase of maximum adsorption amounts was found with an increase in the modification temperature which was mainly correlated with carbon hydrophobicity enhancement. The conducted kinetic measurements revealed the effect of surface properties on the adsorption process. The adsorption half time ($t_{1/2}$), confirmed the highest adsorption rate for nitrobenzene showing the highest hydrophobicity and the strongest interactions with carbon basal planes. In the investigated experimental systems the dispersion interactions between the π electrons from the aromatic ring of the adsorbate and the π electrons in the adsorbent graphene layers prevailed. Thus, for 4-nitrophenol and phenol, characterized by lower hydrophobicity, the adsorption process was slower as a result of interactions with oxygen functional groups. It was also found that the adsorption half-time decreased with the increasing modification temperature of carbons. The higher number of acidic surface groups, the lower pH_{PZC}, the higher $t_{1/2}$ confirming the interactions of some solute molecules with adsorbent surface sites which resulted in extending the diffusion process.

The thermal analysis revealed that total weight loss systematically decreased with thermal modification temperature, and the surface functional groups were systematically removed during the process. The characteristics of gaseous products of thermal degradation of carbon materials were studied by the mass spectrometry technique coupled with thermogravimetry. The studies conducted for carbon samples loaded with organic substances revealed that the total weight losses systematically diminished after thermal modification at higher temperatures as follows: P, NB, 4-NP AC-OX-180 >AC-OX-380 >AC-OX-800. Moreover, it was stated that nitrobenzene was tightly bound to the carbon and its interactions with the carbon surface groups were stable up to higher temperatures.

Such complex characterization of porosity, morphology, chemistry, adsorption, and thermal stability supported by different techniques is needed both from the physicochemical point of view, and possible applications in purification or separation procedures. It allows the choice of the most effective adsorption system for specific applications. The studies will be extended to new materials of more complex structure and specific selectivity.

CRediT authorship contribution statement

Alicja Bosacka: Conceptualization, Methodology, Investigation, Formal analysis, Visualization, Writing - original draft. **Malgorzata Zienkiewicz-Strzalka:** Conceptualization, Methodology, Investigation, Formal analysis, Writing - review & editing, Validation, Supervision. **Anna Derylo-Marczewska:** Conceptualization, Writing - review & editing, Validation, Supervision. **Agnieszka Chrzanowska:** Methodology, Investigation, Formal analysis, Writing - review & editing. **Małgorzata Wasilewska:** Methodology, Formal analysis, Writing - review & editing. **Dariusz Sternik:** Investigation.

Declaration of Competing Interest

The authors declare that they have no known competing financial interests or personal relationships that could have appeared to influence the work reported in this paper.

Appendix A. Supporting information

Supplementary data associated with this article can be found in the online version at doi:10.1016/j.colsurfa.2022.129130.

References

[1] S. Liu, R. Wang, Modified activated carbon with an enhanced nitrobenzene adsorption capacity, J. Porous Mater. 18 (1) (2011) 99–106, https://doi.org/10.1007/s10934-010-9360-x.

[2] Z. Kecira, O. Benturki, A. Benturki, M. Daoud, P. Girods, High adsorption capacity of nitrobenzene from aqueous solution using activated carbons prepared from vegetable waste, Environ. Prog. Sustain Energy 39 (6) (2020), https://doi.org/10.1002/ep.13463.

[3] S. Álvarez-Torrellas, M. Martin-Martinez, H.T. Gomes, G. Ovejero, J. García, Enhancement of p-nitrophenol adsorption capacity through N 2 -thermal-based treatment of activated carbons, Appl. Surf. Sci. 414 (2017) 424–434, https://doi.org/10.1016/j.apsusc.2017.04.054.

[4] B. Xie, J. Qin, S. Wang, X. Li, H. Sun, W. Chen, Adsorption of phenol on commercial activated carbons: modelling and interpretation, Int J. Environ. Res Public Health 17 (3) (2020) 789, https://doi.org/10.3390/ijerph17030789.

[5] H.A. Arafat, M. Franz, N.G. Pinto, Effect of salt on the mechanism of adsorption of aromatics on activated carbon, Langmuir 15 (18) (1999) 5997–6003, https://doi.org/10.1021/la9813331.

[6] D. Li, Y. Wu, L. Feng, L. Zhang, Surface properties of SAC and its adsorption mechanisms for phenol and nitrobenzene, Bioresour. Technol. 113 (2012) 121–126, https://doi.org/10.1016/j.biortech.2012.02.130.

[7] F. Villacañas, M.F.R. Pereira, J.J.M. Órfão, J.L. Figueiredo, Adsorption of simple aromatic compounds on activated carbons, J. Colloid Interface Sci. 293 (1) (2006) 128–136, https://doi.org/10.1016/j.jcis.2005.06.032.

[8] S. Biniak, G. Szymański, J. Siedlewski, A. Światkoski, The characterization of activated carbons with oxygen and nitrogen surface groups, Carbon N.Y. 35 (12) (1997) 1799–1810, https://doi.org/10.1016/S0008-6223(97)00096-1.

[9] M. Pakuła, A. Świątkowski, M. Walczyk, S. Biniak, Voltammetric and FT-IR studies of modified activated carbon systems with phenol, 4-chlorophenol or 1,4-benzoquinone adsorbed from aqueous electrolyte solutions, Colloids Surf. A Physicochem. Eng. Asp. 260 (1–3) (2005) 145–155, https://doi.org/10.1016/j.colsurfa.2005.03.013.

[10] A. Derylo-Marczewska, A. Swiatkowski, S. Biniak, M. Walczyk, Effect of properties of chemically modified activated carbon and aromatic adsorbate molecule on adsorption from liquid phase, Colloids Surf. A Physicochem. Eng. Asp. 327 (1–3) (2008) 1–8, https://doi.org/10.1016/j.colsurfa.2008.05.026.

[11] P. Aggarwal, J.C. Kapoor, S.K. Kapoor, A.K. Bhalla, R.C. Bansal, Adsorption of nitrobenzene on activated carbon from dilute aqueous solutions, Indian J. Chem. Technol. 3 (4) (1996) 187–190.

[12] P. Su, J. Zhang, J. Tang, C. Zhang, Preparation of nitric acid modified powder activated carbon to remove trace amount of Ni(II) in aqueous solution, Water Sci. Technol. 80 (1) (2019) 86–97, https://doi.org/10.2166/wst.2019.248.

[13] M. Blachnio, A. Derylo-Marczewska, M. Seczkowska, Influence of pesticide properties on adsorption capacity and rate on activated carbon from aqueous solution. Sorption in 2020s, IntechOpen,, 2020, https://doi.org/10.5772/intechopen.88726.

[14] L. Giraldo, D.P. Vargas, J.C. Moreno-Piraján, Study of CO_2 adsorption on chemically modified activated carbon with nitric acid and ammonium aqueous, Front. Chem. 8 (2020), https://doi.org/10.3389/fchem.2020.543452.

[15] D. Hernández-Monje, L. Giraldo, J.C. Moreno-Piraján, Enthalpic characterization of activated carbons with different surface chemistry with organic solvents and water, J. Therm. Anal. Calor. 142 (4) (2020) 1511–1522, https://doi.org/10.1007/s10973-020-09255-0.

[16] T. Bohli, A. Ouederni, Improvement of oxygen-containing functional groups on olive stones activated carbon by ozone and nitric acid for heavy metals removal from aqueous phase, Environ. Sci. Pollut. Res. 23 (16) (2016) 15852–15861, https://doi.org/10.1007/s11356-015-4330-0.

[17] A. Derylo-Marczewska, A. Swiatkowski, S. Biniak, M. Walczyk, Effect of properties of chemically modified activated carbon and aromatic adsorbate molecule on adsorption from liquid phase, Colloids Surf. A Physicochem. Eng. Asp. 327 (2008) 1–8, https://doi.org/10.1016/j.colsurfa.2008.05.026 (Published online).

[18] C. Moreno-Castilla, Adsorption of organic molecules from aqueous solutions on carbon materials, Carbon N. Y. 42 (1) (2004) 83–94, https://doi.org/10.1016/j.carbon.2003.09.022.

[19] H. Naganawa, H. Matsuura, Y. Ogihara, S. Kusakabe, T. Sekine, Solvent extraction of p-nitrophenol into cyclohexane with phosphines and their derivatives, Anal. Sci. 6 (2) (1990) 287–289, https://doi.org/10.2116/analsci.6.287.

[20] A. Derylo-Marczewska, A. Swiatkowski, H. Grajek, S. Biniak, Z. Witkiewicz, Changes in the surface chemistry and adsorptive properties of active carbon previously oxidized and heat-treated at various temperatures. III. Studies of the adsorption of organic solutes from aqueous solutions, Adsorpt. Sci. Technol. 23 (10) (2005) 867–879, https://doi.org/10.1260/026361705777642025.

[21] M. Franz, H.A. Arafat, N.G. Pinto, Effect of chemical surface heterogeneity on the adsorption mechanism of dissolved aromatics on activated carbon, Carbon N. Y. 38 (13) (2000) 1807–1819, https://doi.org/10.1016/S0008-6223(00)00012-9.

[22] A. Bosacka, M. Zienkiewicz-Strzalka, M. Wasilewska, A. Derylo-Marczewska, B. Podkościelna, Physicochemical and adsorption characteristics of divinylbenzene-co-triethoxyvinylsilane microspheres as materials for the removal of organic compounds, Molecules 26 (8) (2021) 2396, https://doi.org/10.3390/molecules26082396.

[23] M.Z. Nashed, The theory of Tikhonov regularization for fredholm equations of the first kind (C. W. Groetsch), SIAM Rev. 28 (1) (1986) 116–118, https://doi.org/10.1137/1028033.

[24] E.P. Barrett, L.G. Joyner, P.P. Halenda, The determination of pore volume and area distributions in porous substances. I. Computations from nitrogen isotherms, J. Am. Chem. Soc. 73 (1) (1951) 373–380, https://doi.org/10.1021/ja01145a126 (Published online).

[25] G. Kupgan, T.P. Liyana-Arachchi, C.M. Colina, NLDFT pore size distribution in amorphous microporous materials, Langmuir 33 (42) (2017) 11138–11145, https://doi.org/10.1021/acs.langmuir.7b01961 (Published online).

[26] M. Blachnio, A. Derylo-Marczewska, B. Charmas, M. Zienkiewicz-Strzalka, V. Bogatyrov, M. Galaburda, Activated carbon from agricultural wastes for adsorption of organic pollutants, Molecules 25 (21) (2020) 5105, https://doi.org/10.3390/molecules25215105.

[27] A.W. Marczewski, M. Jaroniec, A new isotherm equation for single-solute adsorption from dilute solutions on energetically heterogeneous solids – short communication, Mon. für Chem. - Chem. Mon. 114 (6–7) (1983) 711–715, https://doi.org/10.1007/BF01134184.

[28] M. Jaroniec, A.W. Marczewski, Physical adsorption of gases on energetically heterogeneous solids I. Generalized Langmuir equation and its energy distribution, Mon. für Chem. Chem. Mon. 115 (8–9) (1984) 997–1012, https://doi.org/10.1007/BF00798768.

[29] M. Wasilewska, A.W. Marczewski, A. Deryło-Marczewska, D. Sternik, Nitrophenols removal from aqueous solutions by activated carbon – temperature effect of adsorption kinetics and equilibrium, J. Environ. Chem. Eng. 20 (2021), 105459, https://doi.org/10.1016/j.jece.2021.105459.

[30] M. Blachnio, T.M. Budnyak, A. Derylo-Marczewska, A.W. Marczewski, V. A. Tertykh, Chitosan-silica hybrid composites for removal of sulfonated azo dyes from aqueous solutions, Langmuir 34 (6) (2018) 2258–2273, https://doi.org/10.1021/acs.langmuir.7b04076.

[31] S. Azizian, Kinetic models of sorption: a theoretical analysis, J. Colloid Interface Sci. 276 (1) (2004) 47–52, https://doi.org/10.1016/j.jcis.2004.03.048.

[32] A.W. Marczewski, Kinetics and equilibrium of adsorption of organic solutes on mesoporous carbons, Appl. Surf. Sci. 253 (13) (2007), https://doi.org/10.1016/j.apsusc.2006.12.037.

[33] A.W. Marczewski, Application of mixed order rate equations to adsorption of methylene blue on mesoporous carbons, Appl. Surf. Sci. 256 (17) (2010) 5818–5826, https://doi.org/10.1016/j.apsusc.2009.12.078.

[34] A.W. Marczewski, A. Deryło-Marczewska, A. Słota, Adsorption and desorption kinetics of benzene derivatives on mesoporous carbons, Adsorption 19 (2) (2013) 391–406, https://doi.org/10.1007/s10450-012-9462-7.

[35] M. Haerifar, S. Azizian, Fractal-like adsorption kinetics at the solid/solution interface, J. Phys. Chem. C 116 (24) (2012) 13111–13119, https://doi.org/10.1021/jp301261h.

[36] A. Derylo-Marczewska, M. Blachnio, A.W. Marczewski, M. Seczkowska, B. Tarasiuk, Phenoxyacid pesticide adsorption on activated carbon – equilibrium and kinetics, Chemosphere 214 (2019) 349–360, https://doi.org/10.1016/j.chemosphere.2018.09.088.

[37] J. Crank, The Mathematics of Diffusion, second ed., Oxford Univ Press, 1975, pp. 69–88.

[38] G. Mckay, M.E.L. Geundi, M.M. Nassar, Pore diffusion during the adsorption of dyes onto bagasse pith, Process Saf. Environ. Prot. 74 (4) (1996) 277–288, https://doi.org/10.1205/095758296528635.

[39] Z.A. Alothman, A review: fundamental aspects of silicate mesoporous materials, in: Materials, MDPI, 2012, pp. 2874–2902, https://doi.org/10.3390/ma5122874.

[40] K.S.W. Sing, R.T. Williams, Physisorption hysteresis loops and the characterization of nanoporous materials, Adsorpt. Sci. Technol. 22 (10) (2004) 773–782, https://doi.org/10.1260/0263617053499032 (Published online).

[41] Charmas B., Zastosowanie metod termicznych i kalorymetrycznych do badania wybranych układów porowatych. Rozprawa habilitacyjna. UMCS 2015.

[42] A. Derylo-Marczewska, K. Miroslaw, A.W. Marczewski, D. Sternik, Studies of adsorption equilibria and kinetics of o-, m-, p-nitro- and chlorophenols on microporous carbons from aqueous solutions, Adsorption 16 (4) (2010) 359–375, https://doi.org/10.1007/s10450-010-9247-9 (Published online).

Supplementary material for the paper:

Title: Physicochemical, structural, and adsorption properties of chemically and thermally modified activated carbons

Authors: Alicja Bosacka, Małgorzata Zienkiewicz-Strzałka, Anna Deryło-Marczewska, Agnieszka Chrzanowska, Małgorzata Wasilewska,Dariusz Sternik

Affiliation: Institute of Chemical Sciences, Faculty of Chemistry, Maria Curie-Sklodowska University, Maria Curie-Sklodowska Sq. 3, 20-031 Lublin, Poland

***Corresponding authors:** alicja.bosacka@poczta.umcs.lublin.pl, annad@hektor.umcs.lublin.pl

Table S1. GAC description supported by the manufacturers and deliverers.

Product name	GAC1240W[1]
Producer	Norit N.V. Company[1]
Deliver	Sigma-Aldrich (USA)[1]
Form	Granules[1]
Moisture	Maximum 5%[2]
Ash content	<12%[2]
Activation	Steam activated[1]
Grade	1240W[1]
Water-soluble ash	0.1%[2]
Loss	≤5.0% loss on drying[1]

[1] https://www.sigmaaldrich.com/catalog/product/sigald/37771?lang=pl&region=PL (Accessed date: 01.12.2021)

[2] https://www.indiamart.com/proddetail/norit-gac-1240w-activated-carbon-21998601473.html (Accessed date: 01.12.2021)

Table S2. Physicochemical characteristics of adsorbates.

Adsorbatedescription	Chemical formula[*]
Compound name: Phenol (P) Molecular formula: C_6H_6O Molecular weight (g/mol): 94.11 Water solubility (g/100 mL at 20 ℃): 8.3 Ionization constant (pK_a): 9.99 Melting point (℃): 40.5 Boiling point (℃): 181.7	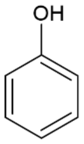

Compound name: Nitrobenzene (NB) Molecular formula: $C_6H_5NO_2$ Molecular weight (g/mol): 123.11 Water solubility (g/100 mL at 20 ℃): 0.19 Ionization constant (pK_a): - Melting point (℃): 5.7 Boiling point (℃): 279.0	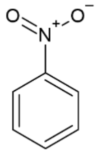
Compound name: 4-Nitrophenol (4-NP) Molecular formula: $C_6H_5NO_3$ Molecular weight (g/mol): 139.11 Water solubility (g/100 mL at 20 ℃): 1.6 Ionization constant (pK_a): 7.15 Melting point (℃): 113.0 Boiling point (℃): 210.9	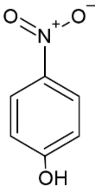

*The molecule structures of adsorbates were drawn up in ChemSketch/ACDLabs software (Toronto, Canada, USA)

Table S3. The adsorption kinetic equations and models.

Name and abbreviation	Short description	Kinetic equations
First-order equation and pseudo-first-order equation (FOE and PFOE)	Adsorption kinetics in the systems with a standard concentration gradient and processes based on the diffusion, but not intraparticle diffusion[30].	$ln(c_{eq} - c) = ln(c_{eq} - c_o) - k_1 t$ or $ln(a_{eq} - a) = ln a_{eq} - k_1 t$ (3) where c is the temporary concentration, a is the actual adsorbed amount, the o and eq subscripts are connected to the initial and equilibrium states, k_1 is the adsorption rate coefficient[29,30,31].
Second-order equation and pseudo-second-order equation (SOE and PSOE)	Suitable for the cases in which concentration changes proceedrapidly[30].	$a = a_{eq}[k_2 t/(1 + k_2 t)]$ (4) or $t/a = (1/a_{eq})(1/k_2 + t)$ and $a = a_{eq}[k_2 t/(1 + k_2 t)]$ where $k_2=k_{2a}\cdot a_{eq}$ and k_{2a} are the rate coefficients for pseudo-second-order kinetics[29,30,32].
1,2-mixed-order equation (MOE)	Generalization of the first- and second-order kinetic equations[29]. Relevant for the systems which behave in the middle of these two[30].	$F = a/a_{eq} = \frac{1-exp(-k_1 t)}{1-f_2 exp(-k_1 t)}$ or $ln\left(\frac{1-F}{1-f_2 F}\right) = -k_1 t$ (5) where F is the relative adsorption progress in time, $f_2<1$is the normalized share of the second-order process in the kinetics. In the special cases, the MOE equation may be degraded to the simple kinetic equations of the first ($f_2=0$) and the second-order ($f_2=1$) type[33].
Fractal-like MOE equation (f-MOE)	Includes probably distribution of rate coefficients[30]. Adequate for a description of the non-ideality effects[29].	$F = \frac{1 - exp(-k_1 t)^p}{1 - f_2 exp(-k_1 t)^p}$ (6) where p is the fractal coefficient[29,30,34,35].

Multi-exponential equation (m-exp)	Numerous first-order sequence processes[29]. Right for a description of the adsorption kinetics on energetically heterogeneous solids that could not be expressed by the FOE/SOE/MOE equations[30].	$c = \left(c_o - c_{eq}\right)\sum_{i=1}^{n} f_i exp(-k_i t) + c_{eq}$ (7) or $c = c_0 - c_0 u_{eq}\sum_{i=1}^{n} f_i[1 - exp(-k_i t)]$ where "i" is the term of the m-exp equation, k_i is the rate coefficient and $u_{eq}=1-c_{eq}/c_o$ is the relative loss of adsorbate from the solution[29,30,32,36].
Intraparticle Diffusion Model (IDM, Crank)	Adsorption on the spherical adsorbent grains[29].	$F = 1 - \frac{6}{\pi^2}\sum_{n=1}^{\infty}\frac{1}{n^2} exp\left(\frac{-\pi^2 \cdot n^2 \cdot D_a \cdot t}{r^2}\right)$ (8) where r is the radius of the adsorbent particle, D_a is the effective diffusion coefficient: $D_a = \frac{D}{\tau_p \cdot \left(1 + \rho \cdot K_H \cdot \varepsilon_p\right)}$ (9) where D is the molecular diffusion coefficient, τ_p – the dimensionless pore tortuosity factor, ρ is the particle density, ε_p is the particle porosity, K_H – the Henry adsorption constant[37].
Pore Diffusion Model (PDM, McKay)	Adsorption on porous solids (additional resistance connected to the transition through the solution/particle interfacial layer)[30].	$\frac{dF}{d\tau_s} = \frac{3\left(1 - u_{eq} \cdot F\right) \cdot (1 - F)^{\frac{1}{3}}}{1 - B \cdot (1 - F)^{\frac{1}{3}}}$ (10) where u_{eq} is the relative adsorbate loss, the parameter $B = 1-1/B_i$, *where*$B_i=K_f/D_p$ is the Biot number, D_p is the pore diffusion coefficient, K_f is the external mass transfer coefficient, τ_s is the undersized model time: $\tau_s = \frac{1}{6 \cdot u_{eq}}\left\{\left(2B - \frac{1}{b}\right) \cdot ln\left[\left\|\frac{x^3 + X^3}{1 + X^3}\right\|\right] + \frac{3}{a} ln\left[\left\|\frac{x + X}{1 + X}\right\|\right]\right\} + \left\{arc\tan\left(\frac{2 - X}{X \cdot \sqrt{3}}\right)\right\} - arc\tan\left(\frac{2 \cdot x - X}{X \cdot \sqrt{3}}\right)$ (11) where $x = (1 - F)^{\frac{1}{3}}, b = \left(\frac{1}{1-u_{eq}}\right)^{\frac{1}{3}}$[38]. (12)

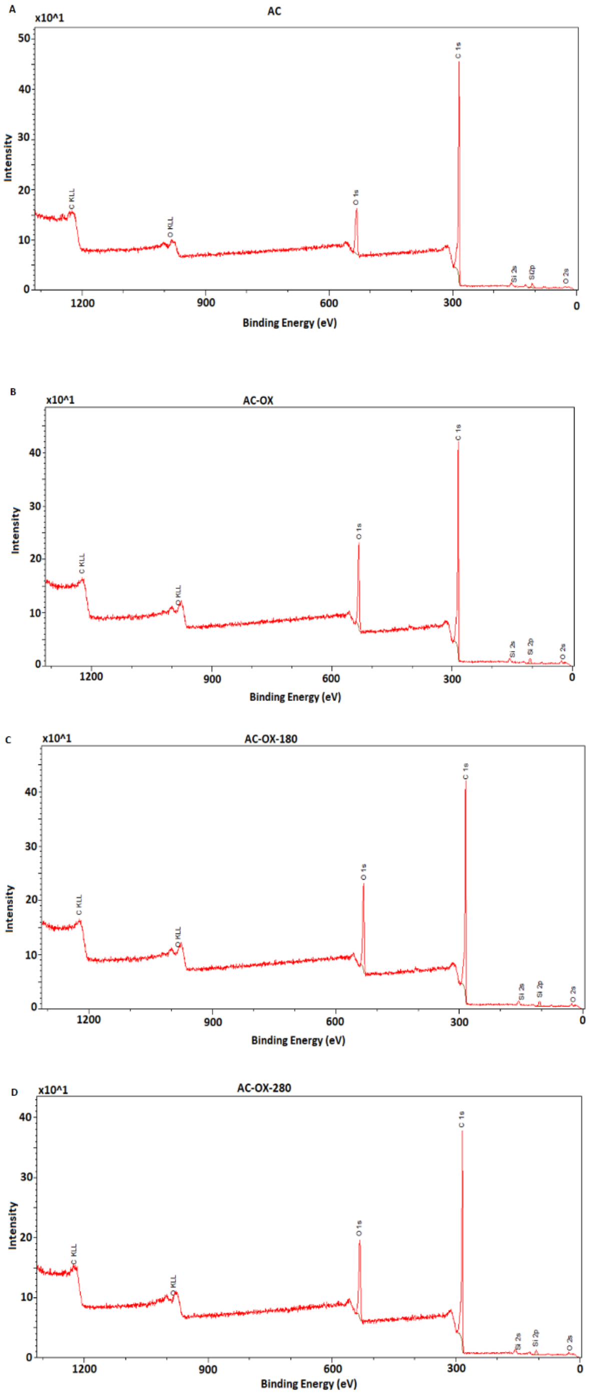
A
x10^1
AC
Intensity
Binding Energy (eV)
C KLL
O KLL
O 1s
C 1s
Si 2s
Si2p
O 2s
B
x10^1
AC-OX
Intensity
Binding Energy (eV)
C KLL
O KLL
O 1s
C 1s
Si 2s
Si 2p
O 2s
C
x10^1
AC-OX-180
Intensity
Binding Energy (eV)
C KLL
O KLL
O 1s
C 1s
Si 2s
Si 2p
O 2s
D
x10^1
AC-OX-280
Intensity
Binding Energy (eV)
C KLL
O KLL
O 1s
C 1s
Si 2s
Si 2p
O 2s
0
10
20
30
40
50
1200
900
600
300
0

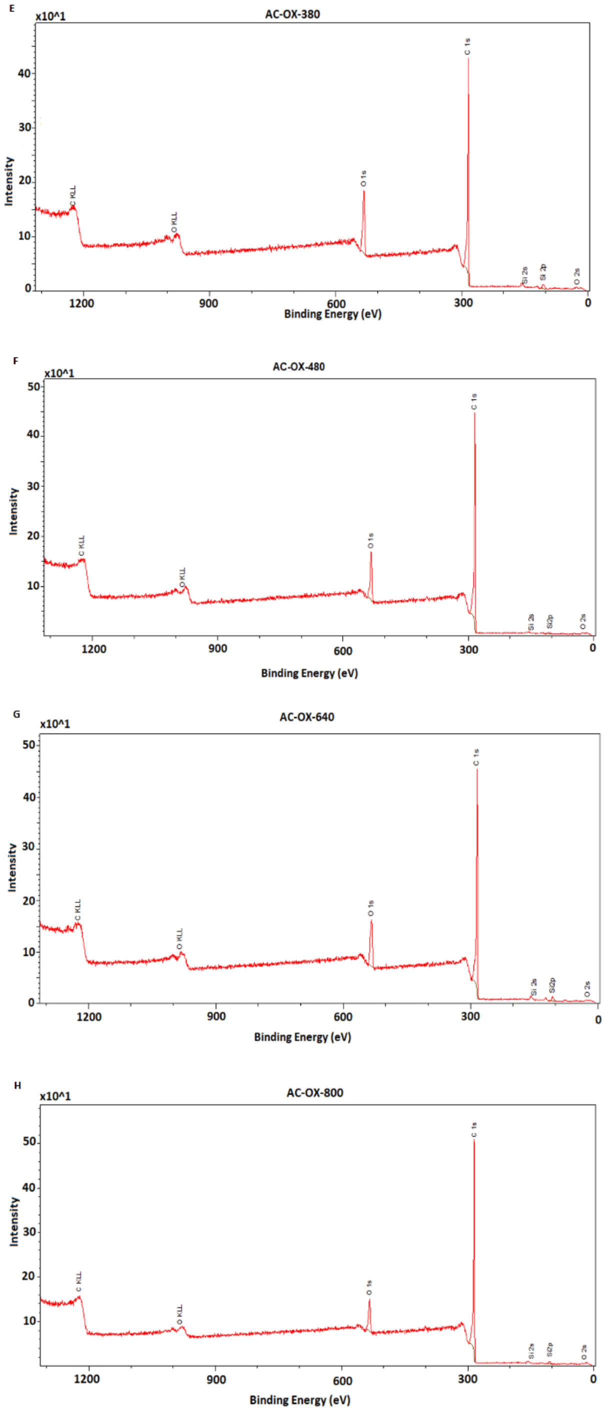

Figure S1. Survey spectra of AC (A), AC-OX (B), AC-OX-180 (C), AC-OX-280 (D), AC-OX-380 (E), AC-OX-480 (F), AC-OX-640 (G), and AC-OX-800 (H).

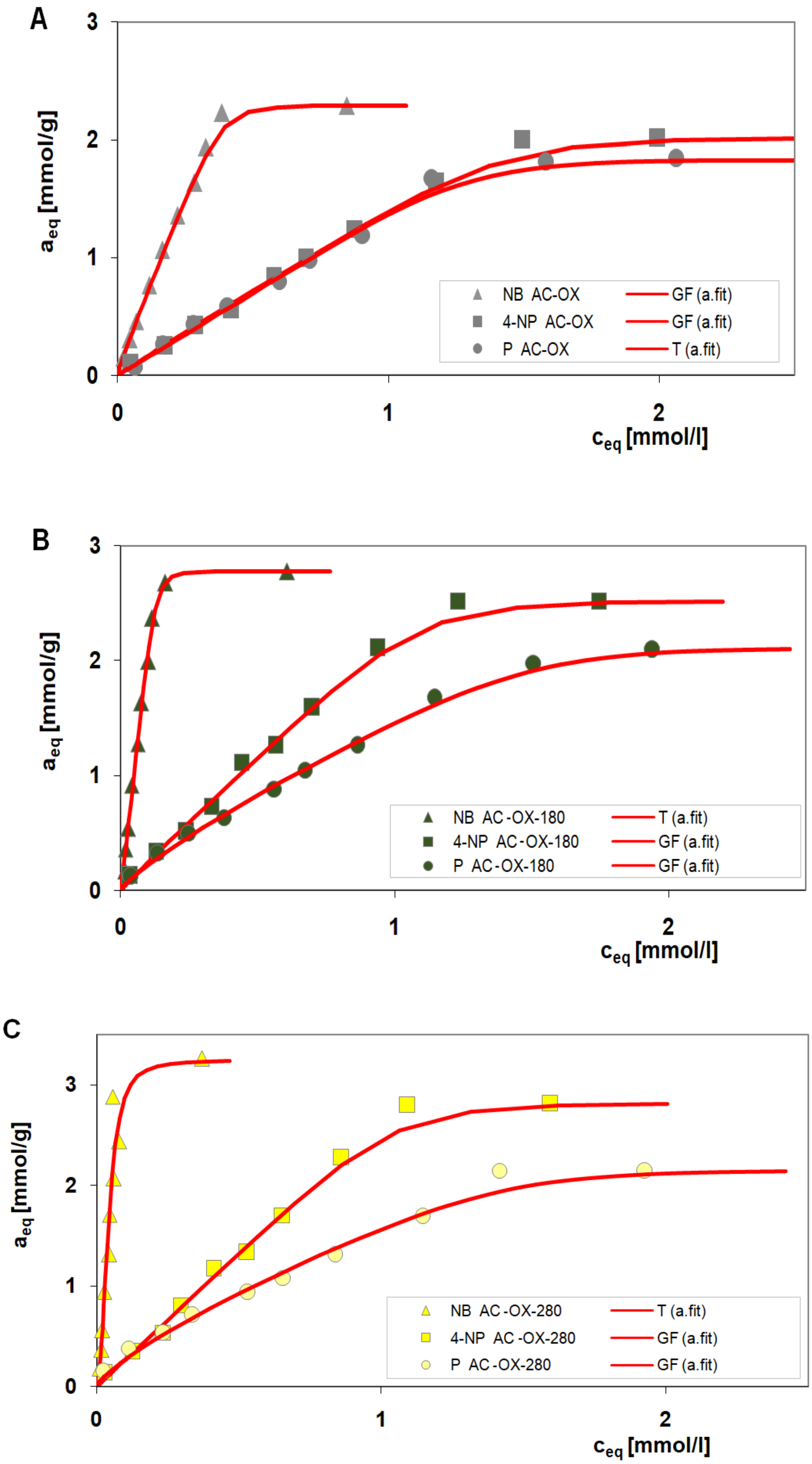
A
B
C
a_{eq} [mmol/g]
c_{eq} [mmol/l]
0
1
2
3
NB AC-OX
4-NP AC-OX
P AC-OX
GF (a.fit)
GF (a.fit)
T (a.fit)
NB AC-OX-180
4-NP AC-OX-180
P AC-OX-180
T (a.fit)
GF (a.fit)
GF (a.fit)
NB AC-OX-280
4-NP AC-OX-280
P AC-OX-280
T (a.fit)
GF (a.fit)
GF (a.fit)

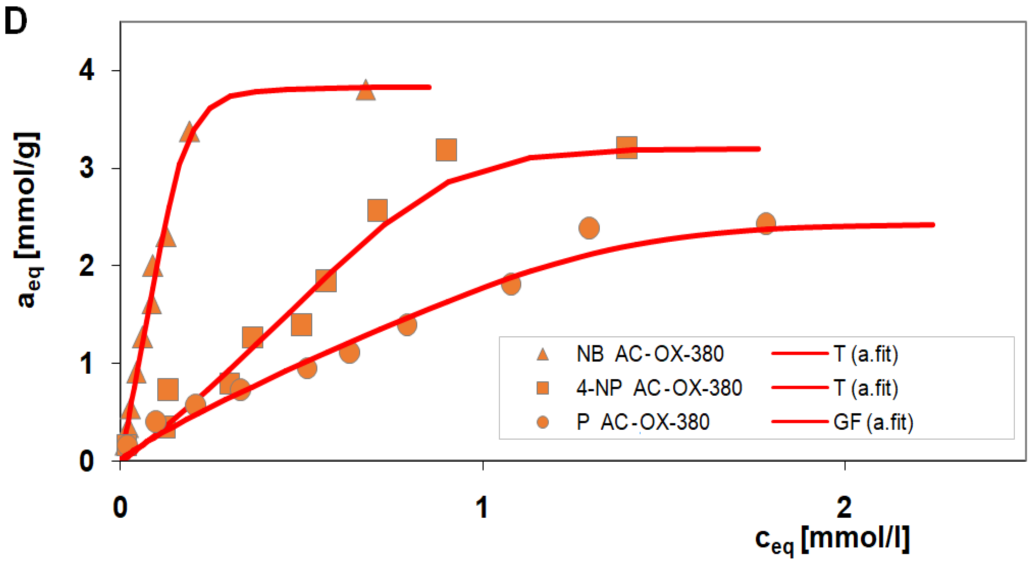
D
4
3
2
1
0
a_{eq} [mmol/g]
0
1
2
c_{eq} [mmol/l]
NB AC-OX-380
4-NP AC-OX-380
P AC-OX-380
T (a.fit)
T (a.fit)
GF (a.fit)

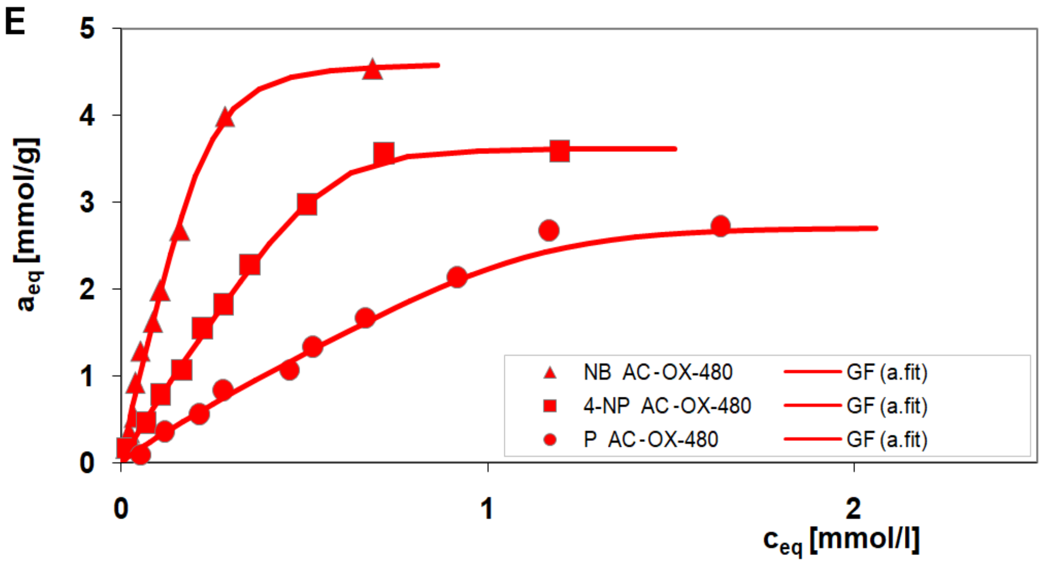
E
5
4
3
2
1
0
a_{eq} [mmol/g]
0
1
2
c_{eq} [mmol/l]
NB AC-OX-480
4-NP AC-OX-480
P AC-OX-480
GF (a.fit)
GF (a.fit)
GF (a.fit)

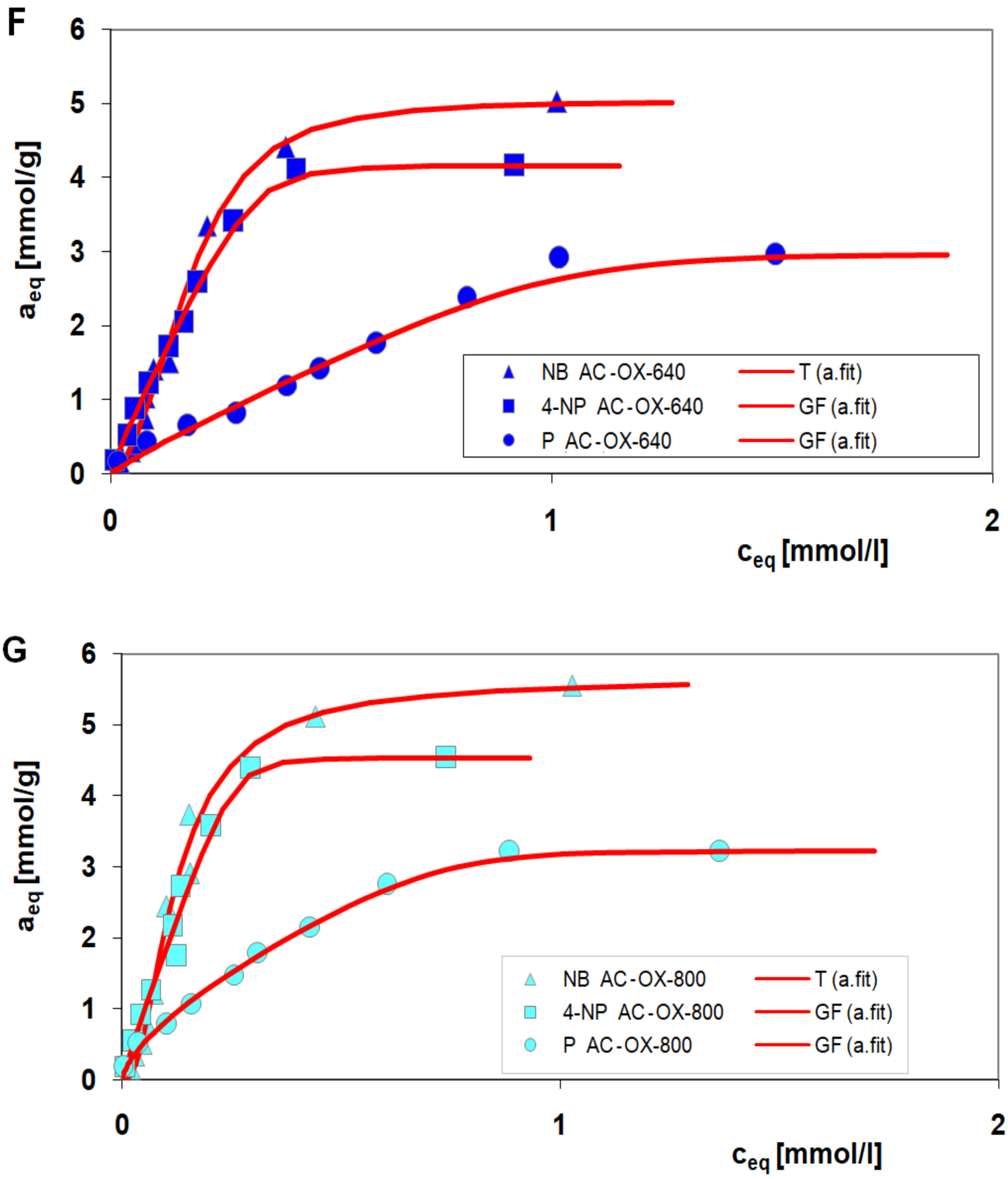

Figure S2. Adsorptionisotherms ofAC-OX (A), AC-OX-180 (B), AC-OX-280 (C), AC-OX-380 (D), AC-OX-480 (E), AC-OX-640 (F), AC-OX-800 (G) for NB, 4-NP, and P.

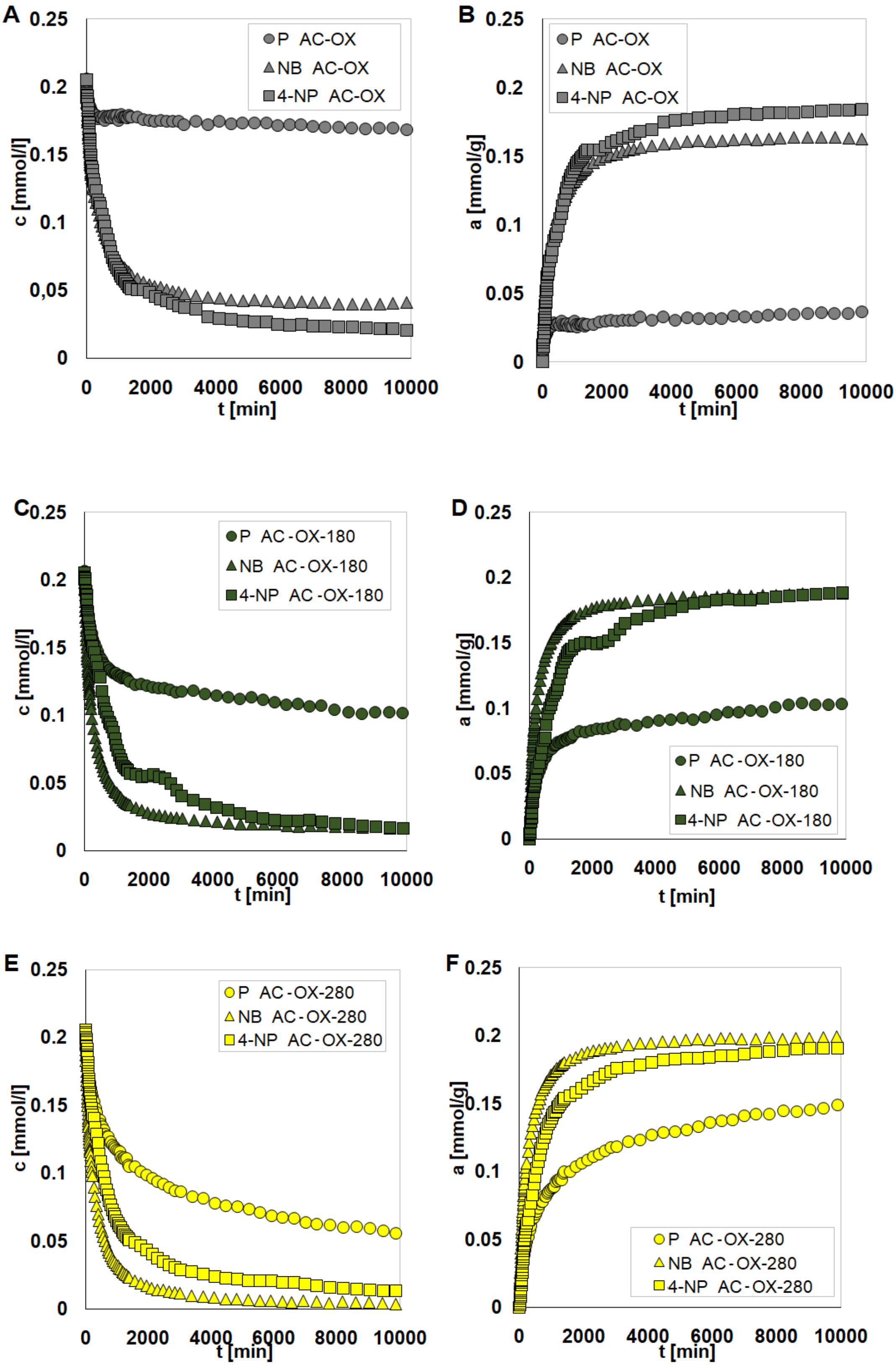
A
0.25
0.2
0.15
0.1
0,05
0
c [mmol/l]
0
2000
4000
6000
8000
10000
t [min]
P AC-OX
NB AC-OX
4-NP AC-OX
B
0.25
0.2
0.15
0.1
0.05
0
a [mmol/g]
0
2000
4000
6000
8000
10000
t [min]
P AC-OX
NB AC-OX
4-NP AC-OX
C
0.25
0.2
0.15
0.1
0.05
0
c [mmol/l]
0
2000
4000
6000
8000
10000
t [min]
P AC-OX-180
NB AC-OX-180
4-NP AC-OX-180
D
0.25
0.2
0.15
0.1
0.05
0
a [mmol/g]
0
2000
4000
6000
8000
10000
t [min]
P AC-OX-180
NB AC-OX-180
4-NP AC-OX-180
E
0.25
0.2
0.15
0.1
0.05
0
c [mmol/l]
0
2000
4000
6000
8000
10000
t [min]
P AC-OX-280
NB AC-OX-280
4-NP AC-OX-280
F
0.25
0.2
0.15
0.1
0.05
0
a [mmol/g]
0
2000
4000
6000
8000
10000
t [min]
P AC-OX-280
NB AC-OX-280
4-NP AC-OX-280

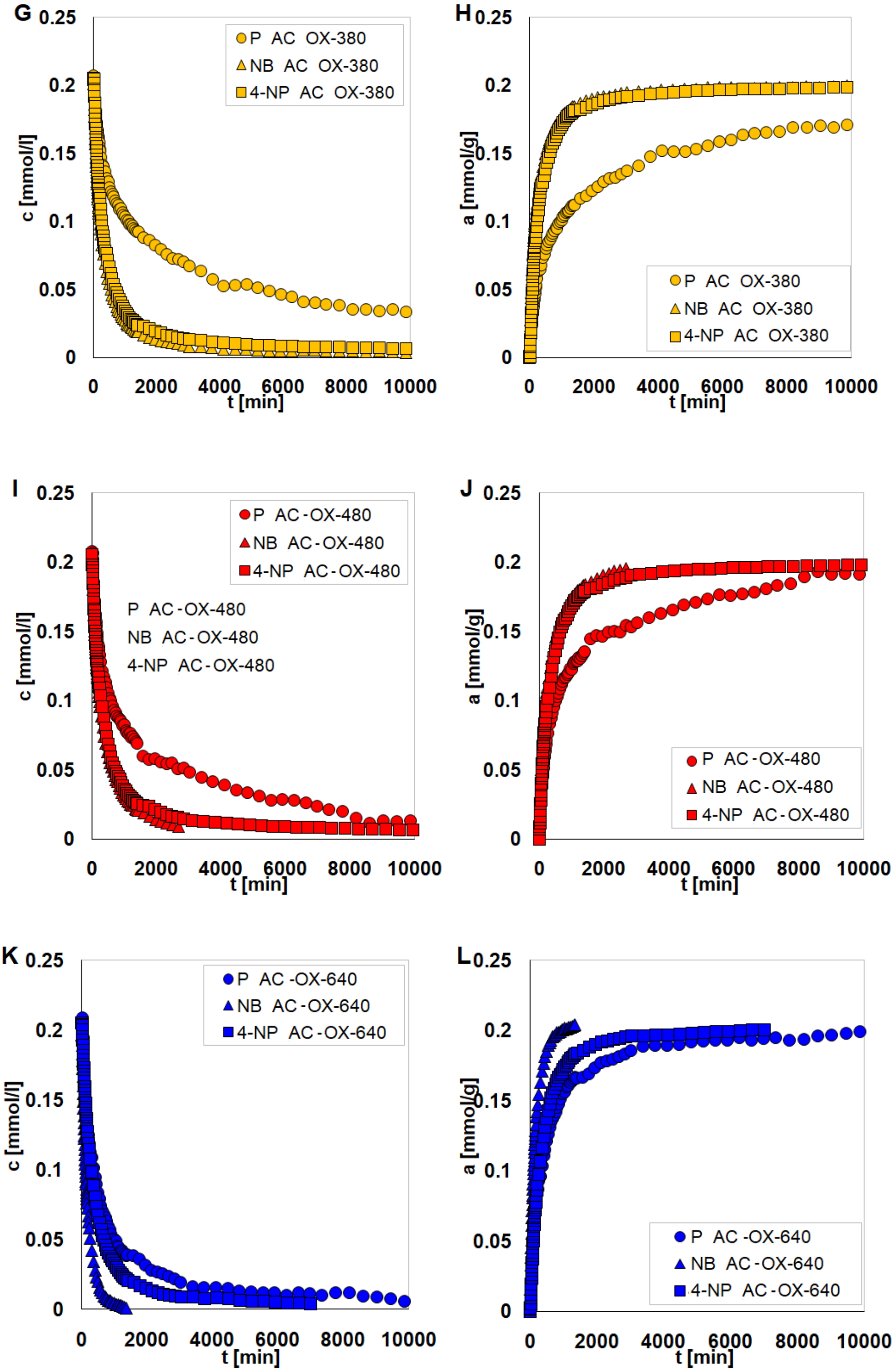
G
0.25
0.2
0.15
0.1
0.05
0
c [mmol/l]
0
2000
4000
6000
8000
10000
t [min]
P AC OX-380
NB AC OX-380
4-NP AC OX-380
H
0.25
0.2
0.15
0.1
0.05
0
a [mmol/g]
0
2000
4000
6000
8000
10000
t [min]
P AC OX-380
NB AC OX-380
4-NP AC OX-380
I
0.25
0.2
0.15
0.1
0.05
0
c [mmol/l]
0
2000
4000
6000
8000
10000
t [min]
P AC-OX-480
NB AC-OX-480
4-NP AC-OX-480
P AC-OX-480
NB AC-OX-480
4-NP AC-OX-480
J
0.25
0.2
0.15
0.1
0.05
0
a [mmol/g]
0
2000
4000
6000
8000
10000
t [min]
P AC-OX-480
NB AC-OX-480
4-NP AC-OX-480
K
0.25
0.2
0.15
0.1
0.05
0
c [mmol/l]
0
2000
4000
6000
8000
10000
t [min]
P AC -OX-640
NB AC-OX-640
4-NP AC-OX-640
L
0.25
0.2
0.15
0.1
0.05
0
a [mmol/g]
0
2000
4000
6000
8000
10000
t [min]
P AC -OX-640
NB AC-OX-640
4-NP AC-OX-640

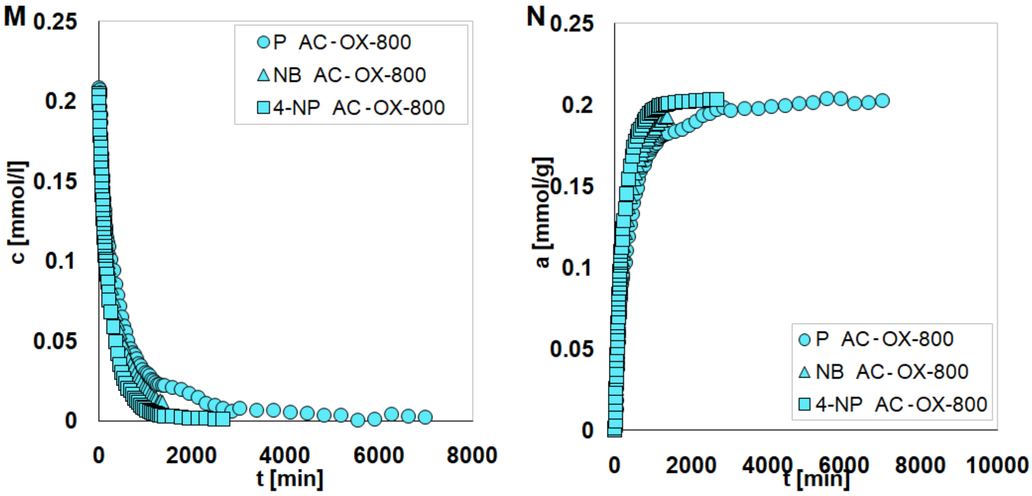

Figure S3. Adsorption kinetics on AC-OX (A-B), AC-OX-180 (C-D), AC-OX-280 (E-F), AC-OX-380 (G-H), AC-OX-480 (I-J), AC-OX-640 (K-L), AC-OX-800 (M-N) presented as changes in concentration (A, C, E, G, I, K, M), or adsorption over time (B, D, F, H, J, L, N) for NB, 4-NP, and P.

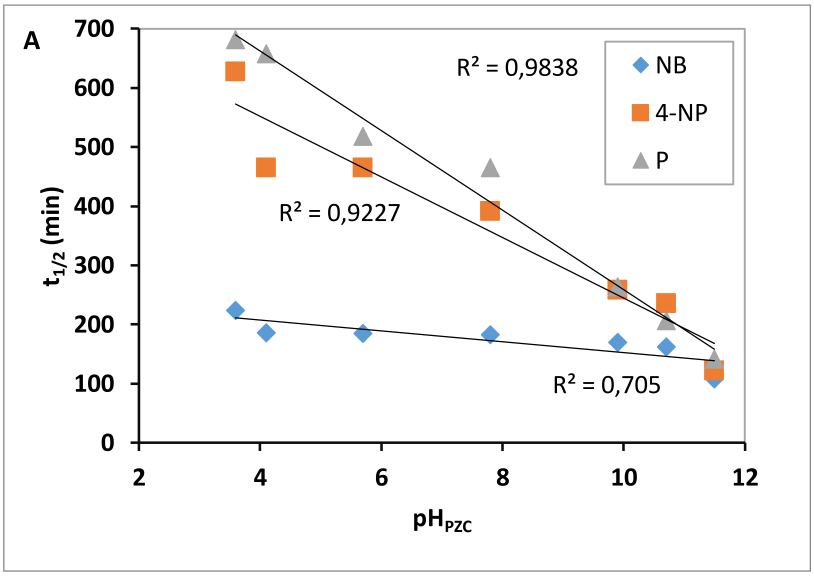
A
t1/2 (min)
700
600
500
400
300
200
100
0
2
4
6
8
10
12
pHPZC
R² = 0,9838
R² = 0,9227
R² = 0,705
◆ NB
■ 4-NP
▲ P

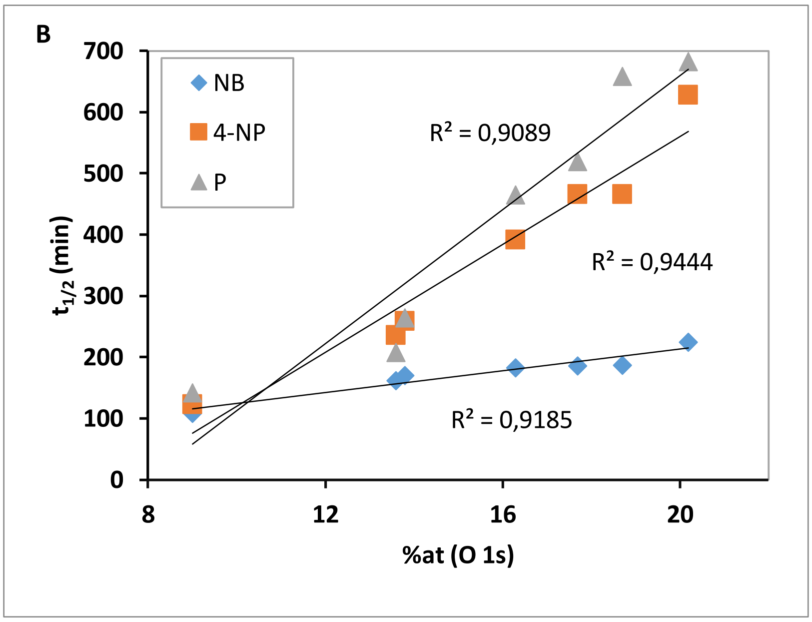
B
t1/2 (min)
700
600
500
400
300
200
100
0
8
12
16
20
%at (O 1s)
R² = 0,9089
R² = 0,9444
R² = 0,9185
◆ NB
■ 4-NP
▲ P

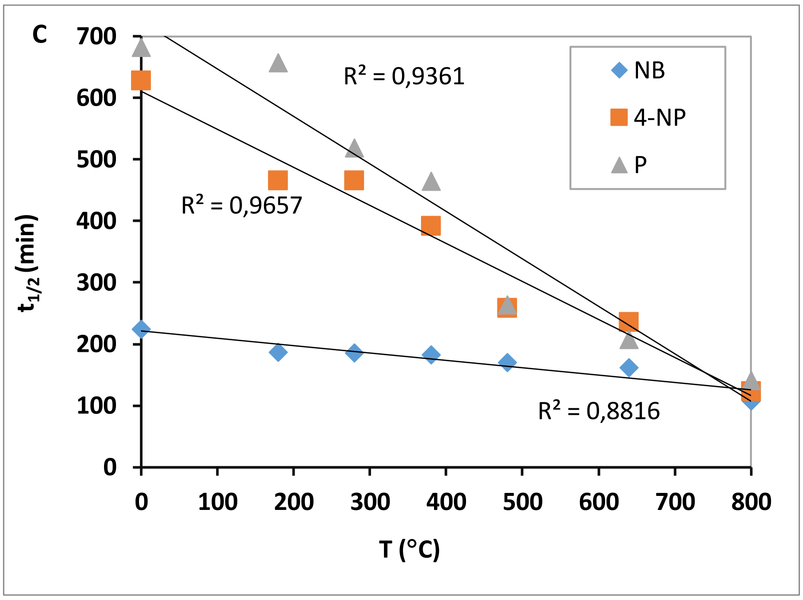

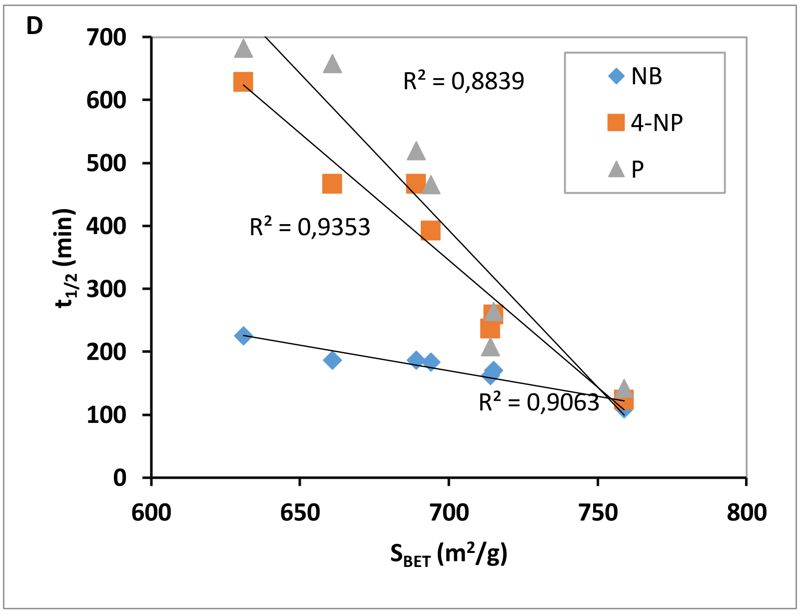

Figure S4. Half-time ($t_{1/2}$) dependence onthe point of zero charge (pH_{PZC}) (A), percentage of atomic concentration (%at) of O 1s (B), modification temperature (T) (C), and specific surface area (S_{BET}) (D).

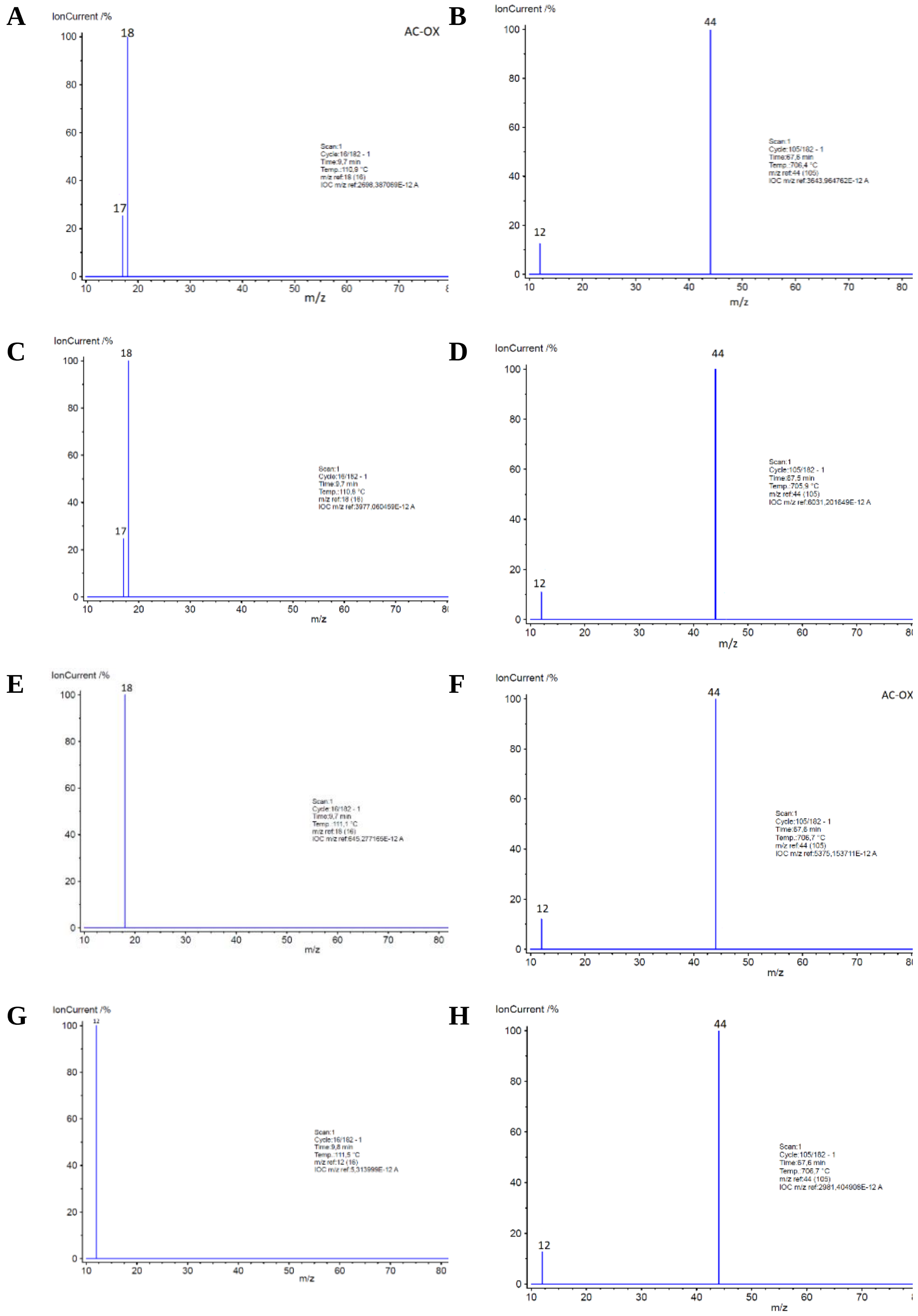

Figure S5. MS spectra of decomposition of AC-OX (A, B), AC-OX-180 (C, D), AC-OX-380 (E, F), and AC-XO-800 (G, H) samples at two different temperatures (∼111 °C – 16/1 cycle), ∼707 °C 105/1 cycle).

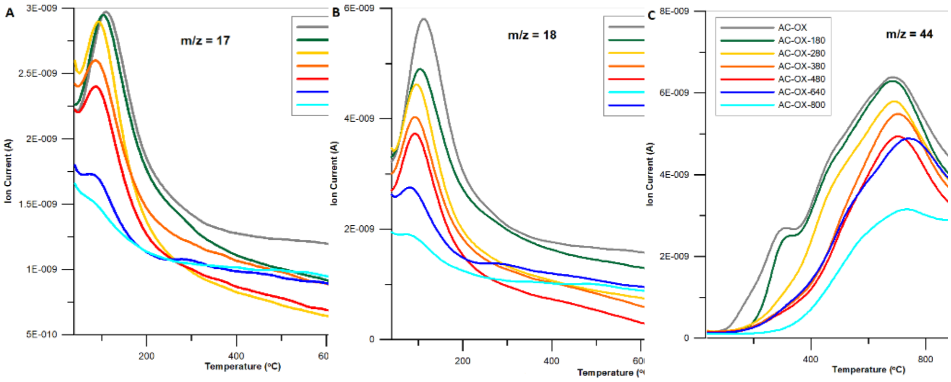

Figure S6. MS gaseous profiles registered during thermal decay of pure modified AC samples (m/z = 17, 18, and 44).

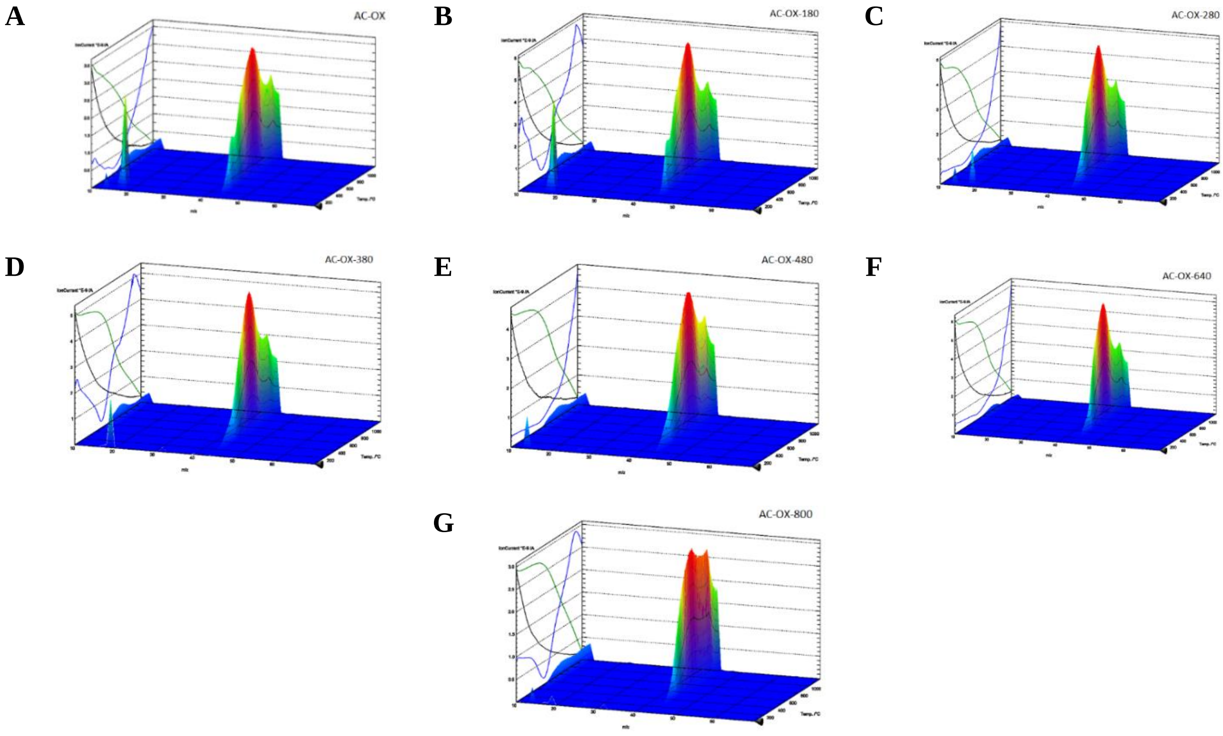

Figure S7. 3D MS profiles of decomposition of AC-OX (A), AC-OX-180 (B), AC-OX-280 (C), AC-OX-380 (D), AC-OX-480 (E), AC-OX-640 (F), and AC-OX-800 (G) samples.

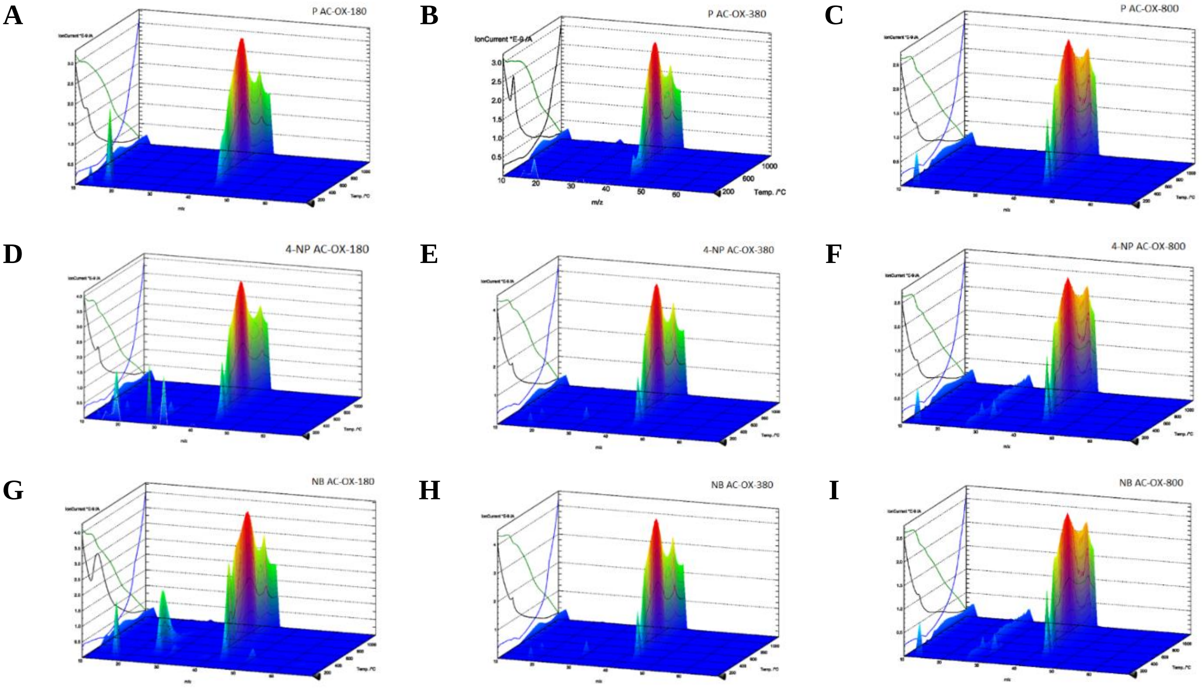

Figure S8. 3D MS profiles of decomposition of AC-OX-180 (A, D, G), AC-OX-380 (B, E, H), and AC-OX-800 (C, F, I) samples loaded with P, 4-NP, and NB.

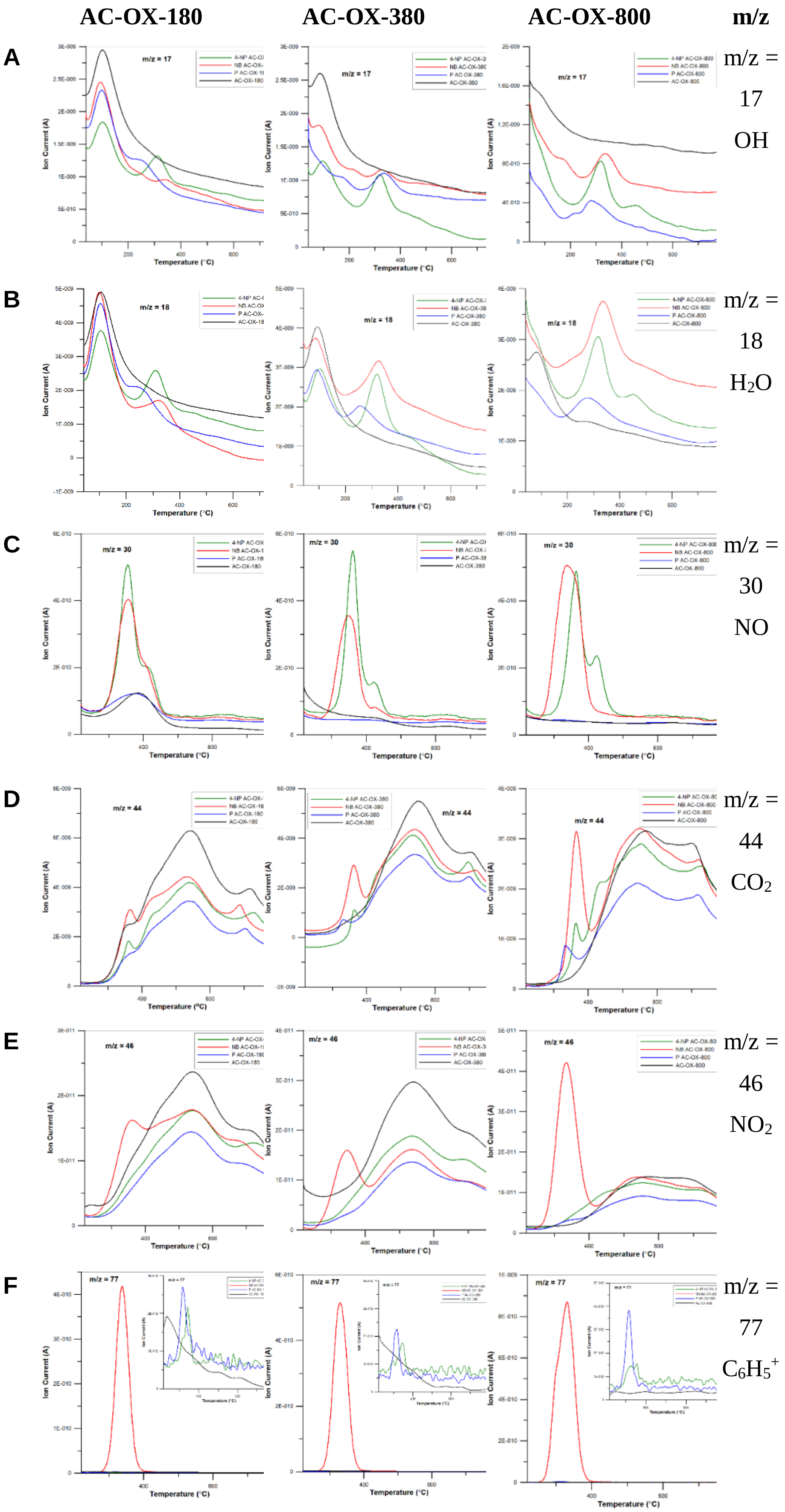
AC-OX-180
AC-OX-380
AC-OX-800
m/z
A
m/z = 17 OH
B
m/z = 18 H_2O
C
m/z = 30 NO
D
m/z = 44 CO_2
E
m/z = 46 NO_2
F
m/z = 77 $C_6H_5^+$
m/z = 17
m/z = 18
m/z = 30
m/z = 44
m/z = 46
m/z = 77
4-NP AC-OX-180
NB AC-OX-180
P AC-OX-180
AC-OX-180
4-NP AC-OX-380
NB AC-OX-380
P AC-OX-380
AC-OX-380
4-NP AC-OX-800
NB AC-OX-800
P AC-OX-800
AC-OX-800
Ion Current (A)
Temperature (°C)

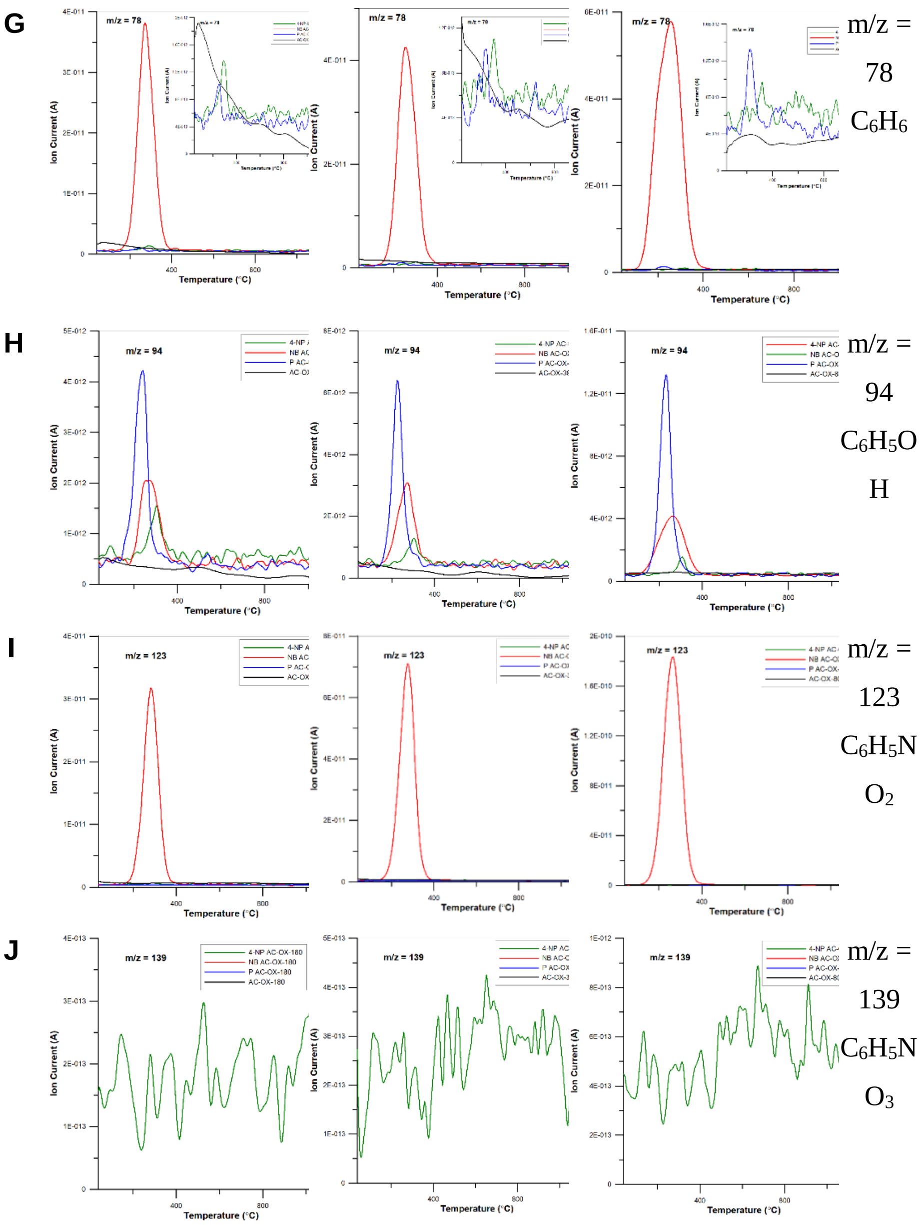

Figure S9. MS gaseous profiles registered during thermal decay of AC-OX-180, AC-OX-380, and AC-OX-800 samples (m/z = 17 (A), 18 (B), 30 (C), 44 (D), 46 (E), 77, (F), 78 (G), 94 (H), 123 (I), 139 (J) loaded with P, 4-NP and NB, and pure modified ACs as a reference.

[D3] Mariia Galaburda, Alicja Bosacka, Dariusz Sternik, Viktor Bogatyrov, Olena Oranska, Volodymyr Gun’ko, Anna Deryło-Marczewska, Development, Synthesis and Characterization of Tannin/Bentonite-Derived Biochar for Water and Wastewater Treatment from Methylene Blue, Water 2022, 14(15), 2407, https://doi.org/10.3390/w14152407

water

MDPI

Article

Development, Synthesis and Characterization of Tannin/Bentonite-Derived Biochar for Water and Wastewater Treatment from Methylene Blue

Mariia Galaburda [1,2], Alicja Bosacka [2,*], Dariusz Sternik [2], Viktor Bogatyrov [1], Olena Oranska [1], Volodymyr Gun'ko [1] and Anna Deryło-Marczewska [2]

[1] Chuiko Institute of Surface Chemistry, NAS of Ukraine, 17, General Naumov Street, 03164 Kyiv, Ukraine; mariia.galaburda@gmail.com (M.G.); vbogatyrov@gmail.com (V.B.); el.oranska@gmail.com (O.O.); vlad_gunko@ukr.net (V.G.)

[2] Institute of Chemical Sciences, Faculty of Chemistry, Maria Curie-Sklodowska University, 3, Maria Curie-Sklodowska Square, 20-031 Lublin, Poland; dariusz.sternik@mail.umcs.pl (D.S.); anna.derylo-marczewska@mail.umcs.pl (A.D.-M.)

* Correspondence: alicja.bosacka@poczta.umcs.lublin.pl

Abstract: Novel hybrid carbon–mineral materials were synthesized by the mechanochemical activation of a mixture of tannin and bentonite in a ball mill with further pyrolysis in an argon atmosphere at 800 °C. The influence of the initial mixture ingredients content on the structural, textural, and thermal characteristics of biochars has been described using X-ray diffraction, Raman and Fourier-transform infrared spectroscopy, nitrogen adsorption–desorption, and scanning electron microscopy. The influence of bentonite clay on the carbon phase characteristics due to the formation of more heat-resistant and structured nanocarbon particles in biochars has been proven. The adsorption effectiveness of the materials towards methylene blue was studied. The adsorption data were analyzed applying Langmuir and Freundlich isotherms with high determination coefficients (R^2) in the range of 0.983–0.999 (Langmuir) and 0.783–0.957 (Freundlich). The maximum adsorption amount of MB was 5.78 mg/g. The adsorption efficiency of biochars with respect to phenol was also examined. It was shown that the hybrid biochars show differentiated selectivity to the adsorption of organic compounds. It was concluded that the physicochemical properties of the surface of biochars play an important role in the adsorption effectiveness, making them a good candidate for water and wastewater remediation processes.

Keywords: tannin; bentonite; biochar; composite; pyrolysis; dye adsorption

check for updates

Citation: Galaburda, M.; Bosacka, A.; Sternik, D.; Bogatyrov, V.; Oranska, O.; Gun'ko, V.; Deryło-Marczewska, A. Development, Synthesis and Characterization of Tannin/Bentonite-Derived Biochar for Water and Wastewater Treatment from Methylene Blue. *Water* **2022**, *14*, 2407. https://doi.org/10.3390/w14152407

Academic Editor: Xike Tian

Received: 27 June 2022
Accepted: 1 August 2022
Published: 3 August 2022

1. Introduction

Dyes are substances of natural or synthetic origin that give color to other substances. Synthetic dyes, which are compounds with a complex aromatic structure of molecules, are especially hazardous and hard to be decomposed in water. One of the synthetic dyes is methylene blue (MB), also known as basic blue 9—whose chemical name is methylthioninium chloride—which is characterized by the basic character, the molar mass of 319.9 g/mol, the water solubility of 4.36 g/100 mL at 25 °C, and ionization constant (pKa) of 3.8. Methylene blue in the solid state is green crystalline powder, but dissolved in water is blue. Methylene blue is used in the textile industry, however, is considered as a toxic, carcinogenic, non-biodegradable, and environmentally dangerous substance, therefore, its removal from technological wastewater and water is of great importance [1–3]. There are many methods of purifying water and wastewater from dyes. The adsorption is one of the leading routes in terms of use simplicity, adsorption efficiency, and great possibilities in adsorbent design [4,5]. There are many various appropriate adsorbents. However, new, selective materials with enhanced adsorption effectiveness are still sought. In this work, the novel hybrid carbonized materials were prepared by the mechanochemical activation of ball-milled and subsequently carbonized blends of tannin and bentonite to be applied for the adsorption of methylene blue.

An initial mixture was prepared by the mechanochemical activation. It should be noted that mechanochemistry is a way of material receiving in which the chemical reaction's activation energy is supported by a mechanical force [6]. The chemical changes of solid-state starting materials are initialized by high-energy mills or grinders [7,8]. Additionally, mechanochemical activation using mills or grinders is one of the key methods for the synthesis of nanostructured materials [9,10].

One of the ingredients of the used blends is tannin, which is a natural, versatile, non-toxic aromatic polyphenolic compound. Tannin is an amorphous light-yellow powder with a slightly peculiar odor. Tannins are present in almost all parts of plants such as bark, wood, leaves, fruits, roots and seeds. Soluble tannin (tannic acid) consists of units with glucose linked by ester bonds with nine to ten molecules of gallic acid. The presence of poorly water-soluble polyphenols (phloroglucinol and resorcinol) in tannins or the formation of condensed tannins due to condensation of hydroxyls from neighboring molecules can reduce their solubility in water [11]. Tannins are one of the most common biomass compounds similar to cellulose, hemicelluloses, and lignin [11]. Drugs for internal and external use can be made using tannins immobilized on a surface of nanosilica [12]. Tannins can be used in many industrial domains: food [13], ecology [14], and medicine in the form of technical and pharmaceutical compounds [15,16]. They possess antimicrobial and immunomodulatory properties [17]. As a main raw material in the present work, grape seeds were used, separated from the unfermented pulp during the wine making season. In grapes, tannins are found in the skins, as well as in the seeds and stems. Grape and wine tannins are condensed tannins produced by the polymerization of several plant-derived flavonoid molecules [18]. Thus, given the above, the replacement of phenolic materials (i.e., phenol and resorcinol) with tannin for the synthesis of carbon sorbents can be beneficial to both the bioeconomy and environment due to its low-cost, bio-origin, non-toxic and non-carcinogenic properties.

The second component of the reaction mixture is bentonite, a natural origin clay that is formed from volcanic ash. Bentonite consists mainly of crystalline clay minerals belonging to the smectite group, which are hydrous aluminium silicates containing a mixture of sodium, magnesium, calcium, and iron. Structurally, a 2:1 layer of bentonite consists of two silica tetrahedral sheets with a central octahedral alumina sheet. The space between these layers is occupied by structural water and cations. The bentonite layers are negatively charged and held together by charge-balancing counterions such as Na^+ and Ca^{2+}. Water and counterions in the 2:1 layer in bentonite separate the clay layers [19]. Such a structure of the mineral makes it possible to modify it by filling interlayer spaces while maintaining the layered structure (2:1 layer) and increasing the specific surface area, pore volume, and amount of active centers on the surface of the material. Typically, montmorillonite is the main component of bentonite and consists of mainly SiO_2, Al_2O_3 with Fe_2O_3, MgO, Na_2O, and K_2O, which can promote the carbon yield [20]. Bentonite incorporated into biomass increases the pyrolysis gas yield, which can act as additional gas for activation during pyrolysis and carbon formation [21]. Bentonite can be used as a catalyst in pyrolysis, cracking, and biodiesel processes that may enhance their efficiency [21–23]. In a previous study, it was demonstrated how the way of incorporation of synthetic resorcinol–formaldehyde resins into bentonite clay can influence the porosity and activity of hybrid adsorbents [24]. Biochars produced at high temperatures (>700°C) are more effective for organic contaminant sorption because of their strong carbon structurization, relatively high specific surface area, and porosity [25]. Biochar surfaces become less polar and more aromatic after a high-temperature carbonization, which may affect the organic contaminant adsorption [26,27].

The starting mixture of tannin and bentonite was pyrolyzed at a high temperature and an inert gas atmosphere to produce the biochars. It is worth mentioning that the carbonaceous materials are considered to be effective sorption systems for the removal of organic pollutants from water and wastewater because of their well-developed surface area and porosity. The biochars could be produced due to the thermochemical decomposition of agricultural residues under restricted oxygen conditions. In the process of carbonaceous materials production, the initial components are subjected to pyrolysis and activation which are extremely important preparation steps in the formation of porous materials with appropriate chemical properties increasing adsorption efficiency [28–30]. Furthermore, pyrolysis of certain blends allows for the synthesis of novel hybrid materials retaining the structural advantages of bentonite (mesoporosity) and adding new structural characteristics due to a carbon component.

In the presented paper, the structural, textural, morphological, and thermal characteristics of biochars prepared by mechanochemical activation and pyrolysis at 800 °C in an inert gas atmosphere of blends of tannin and bentonite of differentiated compositions have been investigated by several techniques: low-temperature nitrogen sorption, thermogravimetry (TG), X-ray diffraction (XRD), Fourier transform-infrared (FT-IR) and Raman spectroscopies, and scanning electron microscopy (SEM). The adsorption equilibrium studies of the carbonized materials towards methylene blue were carried out. The adsorption data were analyzed by applying Langmuir and Freundlich isotherms. The phenol adsorption studies were also performed for a better understanding of the sorption mechanism by biochars. The adsorption studies revealed the applicability of the obtained adsorbents in water and wastewater treatments to remove the organic substances of various properties.

2. Materials and Methods

2.1. Materials and Chemicals

The experiments were conducted using bentonite (Sigma-Aldrich, Gillingham, UK). Tannin products (soluble in alcohol, extracted from grapes purchased from a local wine merchant in the Republic of Moldova. The hydrochloric acid (35–38%), sodium hydroxide, and sodium chloride were bought from Chempur (Piekary Slaskie, Poland). The methylene blue (MB) was purchased from Merck (Darmstadt, Germany). The solutions for adsorption studies were prepared with the use of deionized water (deionizer Polwater, Labpol, Cracow, Poland).

2.2. Materials Preparation

A two-stage method of synthesis was used: (i) mechanochemical activation of a mixture and (ii) pyrolysis. In the first part, the certain weights of tannin and bentonite were placed into a stainless steel jar (250 mL) containing stainless steel balls (5 mm in diameter) and milled for 6 h in a laboratory ball mill. The second step was pyrolysis in the quartz cells of the vertical reactor in an argon flow (100 mL/min) at 800 °C. The heating rate was 10 °C/min and a sample was maintained for 2 h at the set temperature. Cooling was carried out to room temperature in an argon flow. The names of the samples and the initial ratios of the components are given in Table 1.

Table 1. The ratios of the initial components used to prepare materials.

Sample	Component Ratio, g	
	Tannin	Bentonite
TC (control)	10	-
TBC-1	10	10
TBC-2	20	10
TBC-3	30	10
TBC-0.5	6	10

2.3. Methods

X-ray diffraction (XRD) patterns were recorded at 2θ = 5–80° using a DRON-4-07 diffractometer with filtered Cu Kα radiation in the geometry of Bragg–Brentano. The phases were identified using the PDF-2 X-ray database of standards.

The Raman spectra were recorded over the 3200–150 cm^{-1} range using a Via Reflex Microscope DMLM Leica Research Grade, Reflex (Renishaw, Gloucestershire, UK) with laser excitation at λ_0 = 785 nm.

The FT-IR spectra were registered in the range of 400–4000 cm^{-1} using Tensor 27 apparatus (Bruker, Selb, Germany) with an ATR attachment equipped with a diamond crystal.

A morphological analysis of the studied materials was carried out using a Quanta 250 FEG scanning electron microscope (FEI, Hillsboro, OR, USA) equipped with an EDS attachment.

To compute the textural characteristics, the low-temperature (77 K) nitrogen adsorption–desorption isotherms were recorded using an ASAP 2405N (Micromeritics, Norcross, GA, USA) adsorption analyzer. The specific surface area, S_{BET}, was calculated according to the standard BET method [31]. The total pore volume, V_p, was evaluated from the nitrogen adsorption at p/p_0 = 0.98–0.99 (p and p_0 denote the equilibrium and saturation pressure of nitrogen at 77.4 K, respectively). The nitrogen desorption data were used to compute the pore size distributions (PSD, differential $f_V(R) \sim dV_p/dR$ and $f_S(R) \sim dS/dR$), using a model with slit-shaped pores for carbon–bentonites [32]. The differential PSD concerning pore volume, $f_V(R) \sim dV_p/dR$ and $\int fV(R)dR \sim V_p$, were recalculated as incremental PSD (IPSD), $\sum \Phi_{v,i}(R) = V_p$. The $f_V(R)$ and $f_S(R)$ functions were also used to calculate the contributions of micropores (V_{micro} and S_{micro} at radius $R \leq 1$ nm), mesopores (V_{meso} and S_{meso} at 1 nm < R < 25 nm) and macropores (V_{macro} and S_{macro} at 25 nm < R < 100 nm) to the total pore volume and specific surface area.

A potentiometric titration of suspension was carried out using a multicomponent system equipped with a pH meter (PHM240 Radiometer, Copenhagen, Denmark), an autoburet 765 Dosimat (Metrohm, Herisau, Switzerland), a thermostat (Ecoline RE207, Lauda, Germany), a degassing system (nitrogen atmosphere), and a quartz vessel. In the first step was 30 mL of 0.1 mol/dm^3 NaCl (an electrolyte) with the addition of 300 μL of 0.2 HCl, the solution then equilibrated for 1 h at 25 °C to achieve constant temperature and pH value, then it was titrated with 0.1 mol/dm^3 NaOH. In the second step, the same procedure was repeated but with the addition of 1 g of solid sample. Finally, the surface charge density and the point of zero charge (pH_{PZC}) were determined.

The thermal stability of samples, as well as the carbon content, was determined using an STA 449 Jupiter F1 (Netzsch, Selb, Germany) apparatus. The samples (~12 mg) were heated at a rate of 10 °C/min in the range of 30–950 °C in the atmosphere of synthetic air (flow of 50 mL/min) in an alumina crucible, and sensor thermocouple type S TG–DSC. An empty Al_2O_3 crucible was used as a reference. Thermogravimetry (TG and DTG) curves were registered during the analysis.

Adsorption equilibrium studies were performed applying a Carry 4000 UV-Vis spectrophotometer (Varian, Melbourne, Australia). Initially, the 50 mL conical flask with an adsorbent of mass ~0.05 g and 25 mL solution of MB with the desired concentration in the range of 1.25–40 mg/L and pH~7was placed into the incubator shaker for 2 days at 25 °C (110 rpm) (New Brunswick Scientific, Edison, NJ, USA). After the equilibrium achievement, the absorbance was measured at 200–800 nm, and the organic substance concentration was determined from the maximum absorbance peak A = f(λ).

The adsorbed amount (a) was calculated based on the mass balance equation:

$$a = \frac{(C_0 - C_{eq}) \cdot V}{m} \tag{1}$$

where: a is the adsorption amount (mg/g), C_0—the initial concentration of dye (mg L^{-1}), C_{eq}—the equilibrium concentration of dye (mg L^{-1}), V—the volume of solution, and m—the mass of adsorbent.

The analysis of the adsorption process was carried out based on the Langmuir (1) and Freundlich (2) isotherms using the equations:

$$\frac{C_{eq}}{a} = \frac{C_{eq}}{a_m} + \frac{1}{K_L \cdot a_m} \tag{2}$$

$$\ln a = \ln K_F + \frac{1}{n} \cdot \ln C_{eq} \tag{3}$$

where: a_m is the adsorption capacity (mg/g), C_{eq}—the equilibrium dye concentration (mg L^{-1}), K_L—the Langmuir constant related to the rate of adsorption (L/mg), K_F—the Freundlich constant (mg/g), and n—the parameter describing the favorableness of the sorption process.

To compare, the additional adsorption studies towards phenol were carried out using a similar procedure. The adsorbent of mass 0.02 g was placed in 50 mL Erlenmeyer flasks with 10 mL of phenol solution (C_0 = 1.054 mmol/L) and maintained for 24 h in an incubator shaker (New Brunswick Scientific, Edison, NJ, USA, 110 rpm, 25 °C). Then carbon slurry was centrifugated (MPM 252R, 10,000 rpm for 10 min). The absorbance was measured at 200–450 nm, and the phenol concentration was determined from the maximum absorbance peak measured using the Carry 4000 UV-Vis spectrometer (λ = 270 nm).

The effect of pH on the percent of removal of MB was analyzed using TBC-0.5 sample. The mixtures were prepared in plastic containers (10 mL) by addition of the methylene blue solution with a defined pH (5 mL of MB with an initial concentration of 10 mg/L) to 0.01 g of adsorbent. The adsorption in the examined system was carried out at pH: 3, 5, 7, 9, and 11 (corrected by the addition of 0.1 mol/dm^3 HCl or 0.1 mol/dm^3 NaOH solution). The solution was stirred using a shaker (New Brunswick Scientific, Edison, NJ, USA, 110 rpm, 25 °C). When equilibrium was attained, the adsorbent was separated bycentrifugation. Then, the supernatant was analyzed in terms of residual concentration.

The influence of contact time on the MB removal (%) was also investigated taking into account the TBC-0.5. The suspensions were prepared in plastic containers (10 mL) by the addition of the MB solution (5 mL, C_0 = 20 mg/L) to 0.01 g of adsorbent. The adsorption was carried out for selected times: 1, 3, 6, 12, 24, and 48 h. When equilibrium was achieved, the adsorbent was separated by centrifugation. Analogous to the pH studies, the residual concentration was determined.

3. Results

3.1. Structural Characteristics

XRD patterns of the samples are given in Figure 1. The characteristic peaks on the pattern of the natural bentonite indicate that the clay is composed primarily of montmorillonite with some impurities corresponding to quartz and muscovite (JCPDS No. 3-19, 85-795, 7-42, respectively, Figure 1a, Table 2). After pyrolysis at 800 °C a partial destruction of the layered and crystalline structure of montmorillonite took place that is accompanied by the disappearance of the basal peak (001) at 2θ = 6° (interplanar distance 1.47 nm) and other peaks. The patterns of carbonized samples indicate that the structure of bentonite remains the same as in treated bentonite alone. The raise in tannin content lead to an increase in the content of carbon during carbonization. An increase in the intensity of the diffuse halo at 2θ = 25° and a decrease in the intensity of the quartz and muscovite peaks indicate an increase in the content of amorphous carbon in the biochar. Considering the carbonized raw tannin, there are two typical diffuse halos at 2θ = 25° and 50°, characteristic of amorphous carbon, and are well recorded in the spectrum. Thus, the synthesized materials are a combination of particles of bentonite with a destructed structure and amorphous carbon, which is partially formed in the interplanar space of bentonite layers.

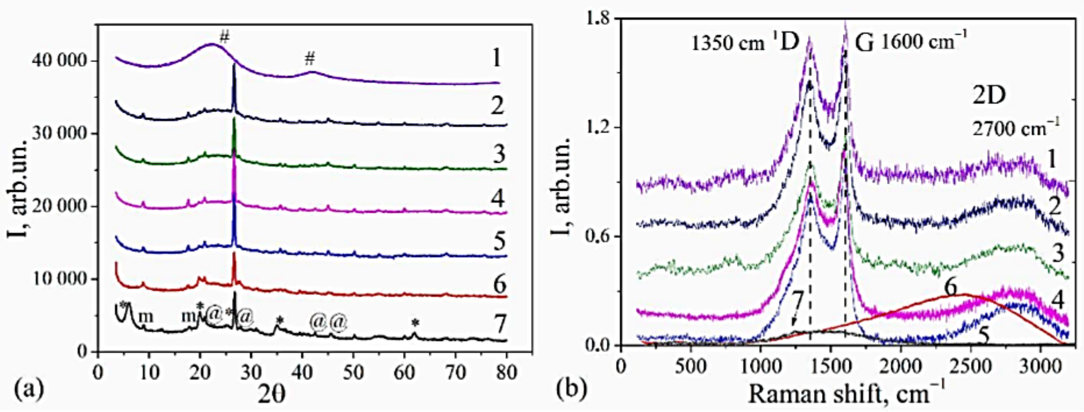

Figure 1. X-ray diffraction patterns (**a**) and Raman spectra of the pyrolyzed materials (**b**): 1—TC (control), 2—TBC-3, 3—TBC-2, 4—TBC-1, 5—TBC-0.5, 6—bentonite pyrolyzed, 7—bentonite (*—montmorillonite, @ quartz, m—muscovite, and #—amorphous carbon).

Table 2. Structural characteristics of pyrolyzed tannin–bentonite materials.

No.	Sample	PDF-2 Card No.	Phase	FWHM (cm^{-1})		Center (cm^{-1})		D/G Intensity Ratio (I_D/I_G)
				D-Band	G-Band	D-Band	G-Band	
1	TC (control)	-	Amorphous carbon	126.3	126.3	1340.4	1598.0	0.8
2	TBC-1	- 85–795 7–42 -	Montmorillonite$_{destr.}$ Quartz Muscovite Amorphous carbon	145.3	145.3	1354.8	1590.0	0.8
3	TBC-2	- 85–795 7–42 -	Montmorillonite$_{destr.}$ Quartz Muscovite Amorphous carbon	155.6	154.8	1349.6	1600.2	0.8
4	TBC-3	- 85–795 7–42 -	Montmorillonite$_{destr.}$ Quartz Muscovite Amorphous carbon	144.0	144.0	1340.8	1600.2	0.8
5	TBC-0.5	- 85–795 7–42 -	Montmorillonite$_{destr.}$ Quartz Muscovite Amorphous carbon	145.3	145.3	1352.9	1600.2	0.9
6	Bentonite	3–19 85–795 7–42	Montmorillonite Quartz Muscovite	-	-	-	-	-
7	Bentonite (pyrolyzed)	- 85–795 7–42	Montmorillonite$_{destr.}$ Quartz Muscovite	-	-	-	-	-

Raman spectroscopy was used to obtain additional information about the carbon phase in biochars. The spectra were collected in the most informative range for carbon materials of 200–3200 cm^{-1} (Figure 1b). The spectra of biochar were characterized by two distinctive bands, G (at ~1600 cm^{-1}), and D (at ~1350 cm^{-1}) [33]. The G-band represents in-plane vibrations of sp^2 hybridized carbon atoms in the graphitic structure, and the D-band is derived from the partial carbon lattice defects that can be mainly due to the structural distortion (breathing mode of aromatic rings) [34]. During graphite amorphisation, both bands changed. The broad G, as well as D bands of high relative intensity, indicate high disordering of carbon. The ratio of the intensities of the D- and G-bands (I_D/I_G) is often used as an indicator of graphitization degree, i.e., the contribution of plane polyaromatic structures in the materials. As can be seen in Table 2 the materials were graphitized with defects and disorders. The I_D/I_G value did not show significant change and thus, one can state that bentonite does not affect the structural features of the carbon phase.

Moreover, a series of peaks in the region of 2500–3000 cm^{-1} could be detected. In particular, the broad 2D peak at ~2700 cm^{-1}, which is called the overtone mode of the D mode, indicates a highly amorphous skeleton containing graphitic domains in biochar of a few nanometres in size (less than 5 nm due to the XRD data). The higher the intensity of this bend, the smaller the size of the carbon crystalline. Thus, the size of graphitic component increased with the following tendency: TBC-0.5 < TBC-1 < TBC-2 < TBC-3 < TC (control).

The spectrum of raw bentonite corresponds to the spectrum of montmorillonite (the main mineral in bentonite) according to the Raman spectroscopy databases, which includes the stretching vibrations of hydroxyls and water (ν3 vibration of H_2O, ν3(Me–H_2O) [35]. After carbonization, the overlapped and not so intensive bands could be observed in the region of 900–2000 cm^{-1}, which correspond to ν3(SiO_4) and ν1(SiO_4) vibrations. The weak bands in the spectrum at 580 and 850 cm^{-1} could be referred to Al–O and Fe–O fragments.

The FT-IR spectra of bentonite and tannin–bentonite biochars are shown in Figure 2. The intensive and sharp band at 3600 cm^{-1} and broad band at 3400 cm^{-1} belonged to OH stretching vibrations (ν3) of structural hydroxyl groups and water present in the raw bentonite due to hydroxyl bonding between octahedral and tetrahedral layers in the mineral [36]. Another sharp peak at 1630 cm^{-1} was assigned to the asymmetric OH of water (deformation vibrations of bound water). The intensive bands centered at ~1000 cm^{-1} and ~1020 cm^{-1} were assigned to the silicate montmorillonite mineral and attributed to the Si-O stretching vibrations ν3 (in-plane) [34]. The OH deformation mode of Al-O-Al-OH or Al-OH-Al was recorded at 914 cm^{-1} [37]. The band centered at 690 cm^{-1} belonged to the deformation and bending modes of the Si–O bonds, while at 548 cm^{-1}, to the deformation mode of the Al-O-Si group. Several bands in the lower region were due to the vibrational modes of the SiO_4 units [34].

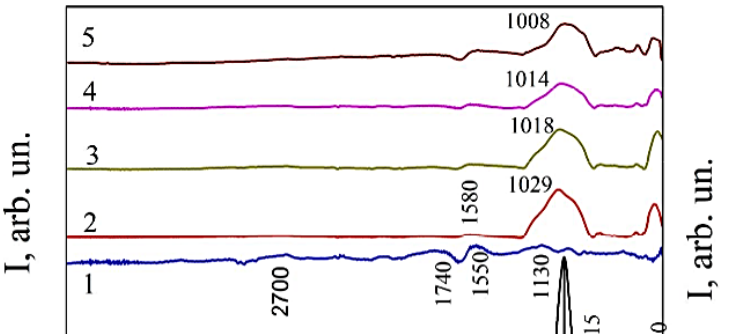

Figure 2. FT-IR spectra of carbonized tannin–bentonite materials: 1—TC (control), 2—TBC-3, 3—TBC-2, 4—TBC-1, 5—TBC-0.5, 6—bentonite.

In the biochar, significant changes in the surface structure could be seen in the IR-spectra due to the dehydration and decarboxylation processes associated with the formation of structures containing aromatic carbon. The characteristic C–H stretching vibrations of the alkyl structure of the aliphatic group (C–H stretching) in the TC (control) sample could be seen in the region of 2580–2950 cm^{-1}. In addition, the presence of a skeletal vibration spectrum, typical for aromatic lignin fragments (C=C and $-OCH_3$) could be observed in the region of 1510–1450 cm^{-1} [38]. A band at 1580 cm^{-1} was related to the C=C aromatic ring stretching vibrations. The band occurring in the region of 1500–1600 cm^{-1} could be attributed to the C=C stretching vibrations of aromatic components and to a smaller extent to the C=O stretching vibrations in quinones and ketonic acids [38], and the aromatic C–C and C–O stretching vibrations of conjugated ketones (quinones). A band at 1580 cm^{-1} belonged to COO− asymmetric stretching vibrations. The wide band at 1740 cm^{-1} could be attributed to the C=O stretching vibrations which indicates the presence of the carboxylic group in the surface of biochar [39]. A band at 1550 cm^{-1} could be referred to the COO– asymmetric stretching vibrations while the band occurring at 1130 cm^{-1} was characteristic to the C–O–C stretching vibrations [40]. Analyzing the spectra of mineral-containing biochars, it can be seen that the surface of the TBC-0.5 sample (Figure 2, curve 5) had more intensive bands in the region of 1500–1800 cm^{-1} due to the greater aromatic character of the carbon component and a high degree of carbonization. The decrease in peak intensity in the lower region with almost complete disappearance at 3000–3700 cm^{-1}, as well as bands shift indicated significant changes and damages of the layered structure of bentonite (dihydroxylation) in the biochar after carbonization at 800 °C. However, a significant broadening of a peak at ~1000 cm^{-1} in the pyrolyzed materials, with simultaneous shift to the red region (1028–1008 cm^{-1}) may indicate the formation of chemical bonds, such as in the Si–O–C groups [39–41].

3.2. Thermal Properties

The TG curves for the carbonized materials (Figure 3) present a major mass loss step in the temperature range of 350–650 °C with a corresponding effect on the DTG curves. This mass loss was related to the decomposition of the carbon skeleton with the release of CO_2, while the final residue corresponds to the dehydrated bentonite. The content of carbon in the samples after carbonization changed in proportion to the amount of tannin in the initial blends. The amount of physically adsorbed water was less than 1 wt% (desorbed up to 300 °C), so it was not taken into account in the calculations. Bentonite content enhanced the temperature of the thermo-oxidative destruction of carbon. The control sample (TC) had the lowest T_{max} = 550 °C, and in the case of other samples with different carbon content in the material, a slight differentiation of T_{max} was observed.

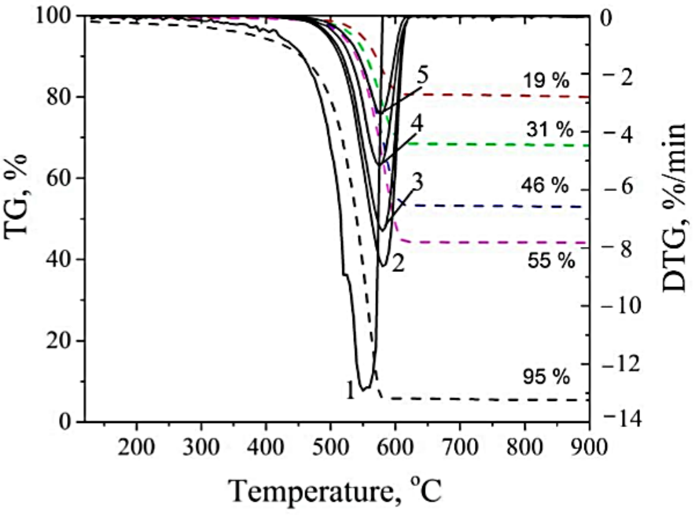

Figure 3. TG and DTG curves of biochars: 1—TC (control), 2—TBC-3, 3—TBC-2, 4—TBC-1, 5—TBC-0.5.

It can be noted that with increasing bentonite content in the material, an increase in the oxidation temperature was observed from 577 °C (TBC-3 sample) to 585 °C (TBC-0.5). Thus, the enhancement of thermal stability of biochar took place due to the creation of Si-O-C bonds in the samples and location of carbon layers between clay layers.

3.3. Morphological Properties

Scanning electron microscopy (SEM) was used to evaluate the morphology of the carbonized materials. The SEM images (Figure 4) of the pyrolyzed samples show that carbon is in the form of irregularly shaped particles of 1–1.5 μm sizes and consists of X-ray amorphous carbon structures (Figure 1), formed on lamellar polygonal bentonite flakes. With an increase in the content of tannin (a carbon source), the size of particles practically did not change, but their density increased. Moreover, the original structure of the clay mineral was broken after carbonization, and the polygonal lamellar morphology was disturbed with decreasing size and shape of individual plate particles. As a result of the introduction of carbon into the interplanar spacing of clay during modification processes and pyrolysis, the structural degradation of bentonite was observed. The residues become much looser, and the pore sizes decreased. This statement was checked further based on nitrogen sorption studies.

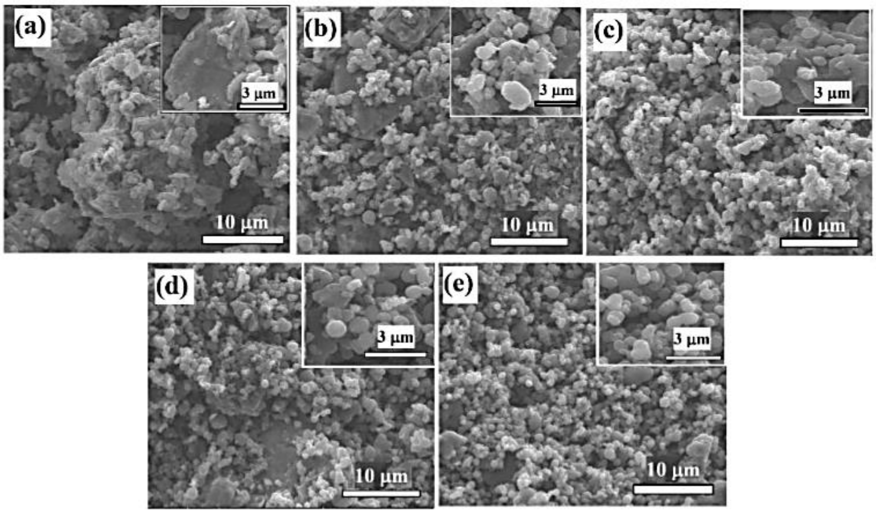

Figure 4. SEM images of TBC-0.5 (**a**), TBC-1 (**b**), TBC-2 (**c**), TBC-3 (**d**), and TC (control) (**e**).

3.4. Porosity and Acid–Base Properties

Nitrogen sorption isotherms of pyrolyzed tannin–bentonite materials can be classified as a mixture of Type I and IV isotherms (IUPAC) and are characterized by rapidly increased adsorption at low relative pressure (p/p_0) and slowing down at higher relative pressures. Thus, monolayer adsorption at low relative pressure, multilayer adsorption at a higher relative pressure, and capillary condensation in mesopores (Figure 5a). This hysteresis loop may be classified as a type H4, which can be associated with narrow slit-like pore structures and its elongation to lower relative pressures, indicating the presence of micropores in the material. The raw bentonite shows Type IV adsorption isotherms with a large uptake near saturation pressure, indicating the mesopores structure.

The BET surface area of the investigated materials and porosity data are summarized in Table 3. It is worth noting that the layered structure of bentonite collapsed after pyrolysis due to the removal of interlamellar water and dihydroxylation, and as a result, it became less porous. Compared to raw bentonite (Table 3), the carbonized biochars are characterized by a higher BET surface area and the contribution of micropores to the total porosity of the materials (Figure 5b). It was shown that an increase in the tannin content raised the volume of nanopores due to the formation of the carbon phase during the pyrolysis process occurring in the interlayer space of bentonite.

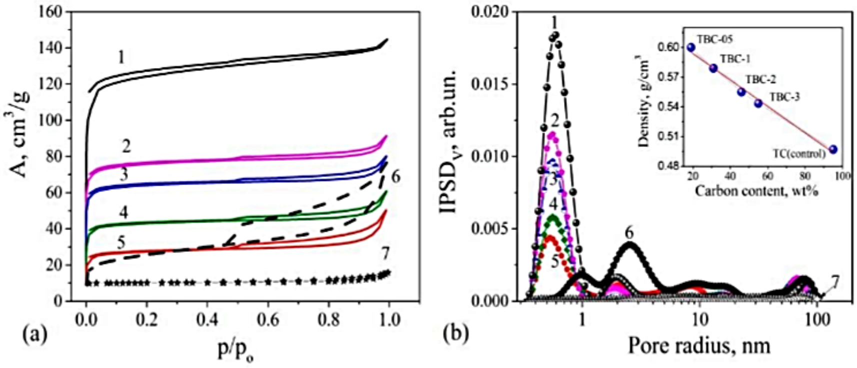

Figure 5. Nitrogen adsorption/desorption isotherms (**a**) and pore size distributions (**b**) of biochars: 1—TC (control), 2—TBC-3, 3—TBC-2, 4—TBC-1, 5—TBC-0.5, 6—bentonite, 7—bentonite pyrolyzed. Bulk density versus carbon content is in the insertion.

Table 3. Porous characteristics and pH_{PZC} for the studied materials.

No.	**Sample**	S_{BET} (m^2/g)	S_{micro}, m^2/g	S_{meso}, m^2/g	S_{macro}, m^2/g	V_p (cm^3/g)	V_{micro} (cm^3/g)	V_{meso} (cm^3/g)	V_{macro} (cm^3/g)	V_{micro}/V_p	V_{meso}/V_p	pH_{PZC}
1	TBC-0.5	86	75.2	9.0	-	0.08	0.05	0.03	0.00	0.61	0.39	8.55
2	TBC-1	128	121.1	6.2	0.2	0.09	0.06	0.02	0.01	0.72	0.20	6.41
3	TBC-2	194	188.2	5.4	0.2	0.13	0.10	0.02	0.01	0.80	0.13	6.39
4	TBC-3	230	223.4	6.2	0.2	0.14	0.11	0.02	0.01	0.81	0.12	5.84
5	TC(control)	380	368.5	10.8	0.1	0.23	0.20	0.02	0.01	0.86	0.10	6.95
6	Bentonite	86	28.3	57.0	0.6	0.12	0.01	0.08	0.02	0.08	0.70	7.90
7	Bentonite pyrolyzed	3	0.6	1.9	0.2	0.01	-	0.01	0.00	0.59	0.39	8.42

With an increase in carbon content, an increase in the hydrophobicity of biochar took place, which lead to a decrease in their wetting by water. The TBC-0.5 sample is characterized by the highest wettability of the series of pyrolyzed materials due to a smaller amount of carbon, carbonization, and a lower degree of graphitization (I_D/I_G = 0.9). Higher hydrophilicity can be due to a small content of hydrophobic aromatic carbon structures (19%) and a significant contribution of bentonite (81%).

The bulk density of a particulate filler depends on the size, shape, surface structure, and particle packing. A change in the bulk density in the samples is directly proportional to the carbon content since the carbon phase has bulk and true densities smaller than that of clay. This fact confirms that the porosity of the samples is affected by the filling with carbon in the process of pyrolysis of tannin (Figure 5b, insertion).

The acid–base properties of tannin–bentonite biochars were investigated by potentiometric titration of the aqueous suspension. Generally, the values of point of zero charge (pH_{PZC}) for investigated samples are given in Table 3 and are in the range of 5.84–8.55. The changes in the pH_{PZC} values are associated with the different composition of the initial mixtures. For the TC (control) sample, the pH_{PZC} value is ~7 which identifies an inert character of its surface. During the pyrolysis of the TC sample, the most surface functional groups (e.g., phenolic) were removed. For TBC-3, TBC-2, and TBC-1, the pH_{PZC} values are 5.84, 6.39, and 6.41 that are related to the existence of certain oxygen species of acidic character. The TBC-0.5, bentonite, and pyrolyzed bentonite are characterized by higher pH_{PZC} values (8.55, 7.90, and 8.42) that reveal the presence of some amount of basic centers on their surfaces [41].

3.5. Adsorption Characteristics

The scheme of synthesis of biochars from tannin and bentonite with possible mechanisms for methylene blue and phenol adsorption is presented in Figure 6. Figure 7a presents the isotherms of methylene blue (MB) adsorption on biochars. The effect of pH and contact time on MB removal by the adsorbent is shown in Figure 7b. The results of phenol removal by TBC-0.5, TBC-1, TBC-2, TBC-3 and bentonite are shown in Figure 8. The effect of contact time and pH on phenol removal by TBC-0.5 is shown in Figure 9. The studies showed a significant increase in the adsorption capacity of the materials prepared with the addition of aluminosilicate in the reaction blends in comparison to the control sample (TC). It may be correlated with the highest share of micropores in TC porosity (0.86) which hinder diffusion and diminishes adsorption of large dye molecules. The best adsorption properties were found for TBC-0.5 material with the highest contribution of bentonite which is characterized by the highest share of mesoporosity (0.39) in comparison to microporosity (0.61). In the case of the three other samples TBC-1, TBC-2, and TBC-3, one could find the comparable representation of micro- (0.71–0.81) and mesopores (0.20–0.12), however, there were larger differences in specific surface area values. Thus, it results in the following differentiation of the adsorption values: TBC-3 > TBC-2 > TBC-1. The experimental data were described by Langmuir and Freundlich isotherms. The determined L and F parameters are summarized in Table 4. The high R^2 values (above 0.98) show that the Langmuir model describes well the experimental data for all adsorption systems. The R^2 in the range of 0.783–0.957 proved that the Freundlich model also well describes the experimental systems. The optimized adsorption capacities a_m and n parameters of the biochars containing bentonite in the structure were 3 to 5 times higher than for the material obtained by tannin pyrolysis. The highest a_m value was obtained for the TBC-0.5 sample with the lowest micropore contribution, but the highest proportion of mesopores from the obtained materials, therefore, in the case of the carbonized material, the dye molecules can well penetrate pores. In addition, it was observed that in the case of carbonized material with the highest tannin content, the increase in MB adsorption was likely also affected by an increase in the specific surface area. The L and F parameters were compared to the literature data and shown in Table 5.

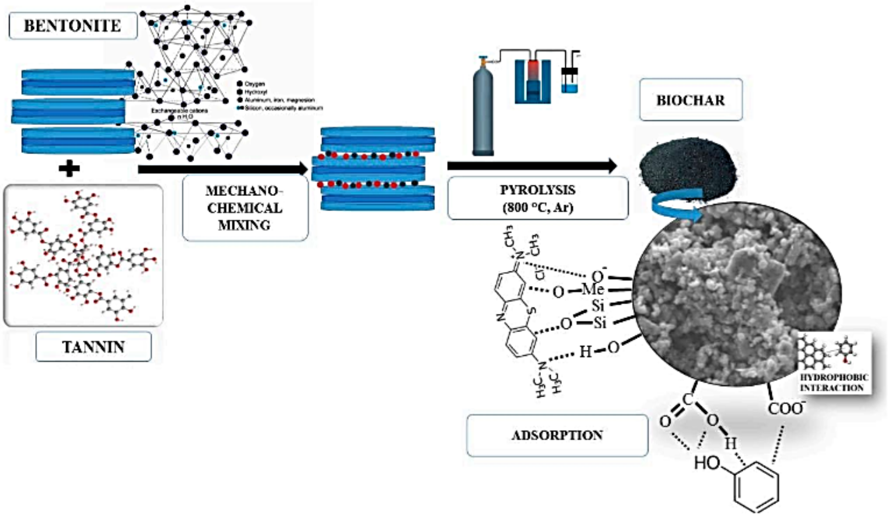

Figure 6. The scheme of synthesis of biochars from tannin and bentonite with possible mechanisms for methylene blue and phenol adsorption.

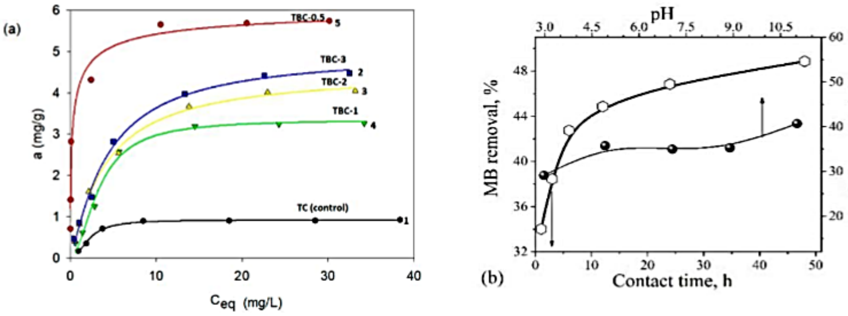

Figure 7. Comparison of adsorption isotherms of MB on the biochars: 1—TC (control), 2—TBC-3, 3—TBC-2, 4—TBC-1, 5—TBC-0.5 (**a**), and the effect of contact time and pH of the solution of MB on the removal by TBC-0.5 (C_0 = 20 mg/L, m = 10 mg, V_s = 5 mL) (**b**).

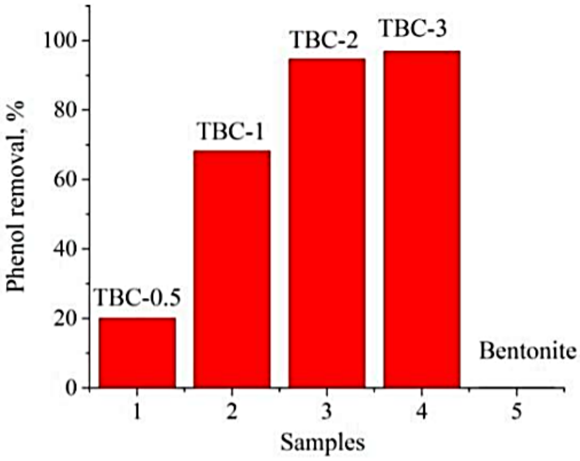

Figure 8. Phenol removal by TBC-0.5, TBC-1, TBC-3, and bentonite (C_0 = 20 mg/L, m = 10 mg, V_s = 5 mL).

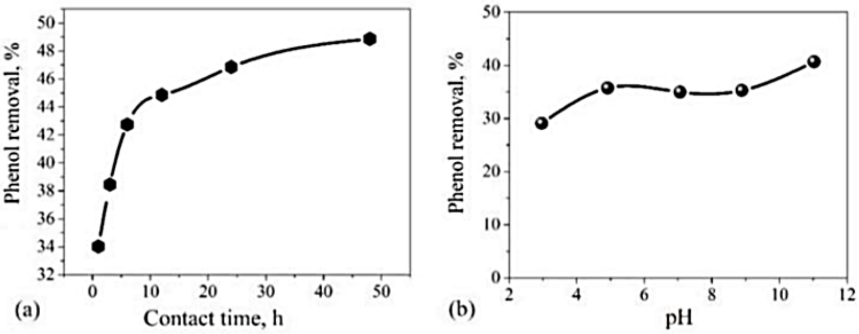

Figure 9. Effect of contact time (**a**) and pH (**b**) on the removal of phenol by TBC-0.5 (C_0 = 20 mg/L, m = 10 mg, V_s = 5mL).

Table 4. Isotherm parameters for adsorption of MB from water solutions.

No.	Sample	Langmuir Isotherm		
		R^2	K_L (L/mg)	a_m (mg/g)
1	TC (control)	0.994	0.39	1.00
2	TBC-0.5	0.999	3.61	5.78
3	TBC-1	0.983	0.19	3.90
4	TBC-2	0.996	0.21	4.74
5	TBC-3	0.995	0.20	5.26
		Freundlich Isotherm		
No.	Sample	R^2	K_F(mg/g)	n
1	TC (control)	0.783	0.28	2.50
2	TBC-0.5	0.847	3.03	4.21
3	TBC-1	0.907	0.60	1.77
4	TBC-2	0.928	0.78	1.83
5	TBC-3	0.957	0.87	1.85

Some differentiation in the sorption mechanisms of the cationic dyes should be taken into account: the hydrophobic interactions, electrostatic repulsion/attraction, oxidation-reduction reactions, or complex formation. Especially when taking into account the differentiation of acid–base properties of studied materials, the electrostatic interactions were of great importance. The MB was positively charged at the working pH and it interacted electrostatically with negatively charged and electron-rich functional groups of the adsorbents. To clarify this issue, additional measurements for phenol adsorption (Figure 8), as an organic compound with both hydrophobic and hydrophilic properties, were performed too. As can be seen in Figure 8, the mineral-rich biochars showed the opposite tendency toward phenol adsorption and the highest adsorption effectiveness was found for the samples with the highest carbon loading, while phenol poorly adsorbs on the raw bentonite. From the obtained data, it follows that the surface functional groups of the synthesized materials have a significant influence on the adsorption capacity if adsorbents have appropriate textural characteristics. In particular, in the case of methylene blue adsorption, the main centers involved in the interaction were the functional groups from clay: hydrogen bond between hydroxyl groups (Si-O-H) and nitrogen atoms of MB; π-π/n-π interaction between the aromatic structure of MB and carbons, as well as electron clouds of the Si-O-Si bridges; hydrogen bonding between hydroxyls (C-OH) and nitrogen of the dye molecule could also be attributed to it adsorption [42]. Thus, the mineral-enriched biochar (with higher bentonite content, sample TBC-0.5) shows a higher adsorption capacity for MB compared to the carbon-rich biochar (sample TBC-3). Schematic interpretation of MB interactions with biochar structures is shown in Figure 6. Phenol removal can take place due to the presence of carbon phase in the pyrolyzed materials: π–π dispersion interaction derived from phenol aromatic rings and carbon layers; physical adsorption based on π–π interaction; and via an electron donor-acceptor complex between surface C-C, C-O and C=O groups which can act as the electron donors and phenol aromatic rings (acceptors), that may occur simultaneously. Additionally, the C-OH group from phenol can form hydrogen bonds with O-containing carbon functionalities. Since phenol interacts with the carbon surface through the aromatic ring, the interactions will be weaker as carbon content decreases, which is observed in the case of the TBC-0.5 sample.

Table 5. Isotherm parameters for adsorption of MB from water solutions for selected adsorbents based on the literature data.

No.	Sample	Langmuir Isotherm			
		R^2	K_L (L/mg)	a_m (mg/g)	Literature Source
1	EDTA modified bentonite	0.998	3.45	160.00	[43]
2	Modified Pumice Stone	0.992	0.13	15.87	[44]
3	Pumice	0.975	-	0.02	[45]
4	SAC	0.991	0.14	126.60	[46]
5	NR90CS10 blend	-	0.94	1.12	[47]
6	Natural clay	-	-	4.98–50.00	[48]
		Freundlich Isotherm			
No.	Sample	R^2	K_F(mg/g)	n	Literature Source
1	EDTA modified bentonite	0.774	84.8	3.61	[43]
2	Modified Pumice Stone	0.999	3.45	2.18	[44]
3	Pumice	0.986	-	1.47	[45]
4	SAC	0.987	41.7	4.76	[46]
5	NR90CS10 blend	-	0.47	2.32	[47]

4. Conclusions

In this work, textural, structural, morphological, and thermal characteristics of novel hybrid biochars prepared by mechanochemical activation and pyrolysis of natural origin constituents (tannin and bentonite), with an application as a sorbent system for methylene blue dye were described. Additionally, the phenol adsorption studies were performed for a better understanding of the sorption mechanism.

The XRD diffraction data confirm that the main crystalline phase of the studied materials corresponds to montmorillonite. An increase in tannin content in the reaction blends leads to an increase in the carbon content in the biochars. The Raman analysis reveals that the crystalline structure of bentonite undergoes significant changes during the tannin pyrolysis, with the simultaneous formation of a carbon phase with a disordered structure (D/G ratio is ~0.8), confirming that the carbon layers are mainly amorphous with many defects. The FT-IR analysis confirms the existence of characteristic stretching and deformation vibrations of the bentonite phase. Changes in peaks intensity and bands shifts are due to the destruction of the layered structure of bentonite during tannin carbonization. The SEM analysis shows that the carbon forms irregularly shaped particles of 1–1.5 μm sizes, and consists of amorphous carbon crystallites. With increasing the tannin content (a carbon source), the size of carbon globules does not practically change, but the bulk density of the biochars increases. The low-temperature nitrogen sorption studies indicate that materials are characterized by the BET specific surface area from 84 to 380 m^2/g. The changes in the textural characteristics of pyrolyzed materials are connected to the differences in the initial blend compositions. Potentiometric titration studies reveal an inert of TC (control) ($pH_{PZC} = 6.95$), acidic of TBC-3 ($pH_{PZC} = 5.84$), TBC-2 ($pH_{PZC} = 6.39$), and TBC-1 ($pH_{PZC} = 6.41$), and basic character of TBC-0.5 ($pH_{PZC} = 8.55$), and bentonite and pyrolyzed bentonite (pH_{PZC} = 7.90 and 8.42) surfaces. The thermal analysis of biocarbons shows that the main destruction of analyzed materials follows at the temperature range of 350–650°C. The carbon obtained only from tannin has the lowest $T_{max} = 550°C$, however, for the materials with different carbon content, a slight differentiation of T_{max} is observed. Generally, data obtained by XRD, Raman and FT-IR spectroscopies, potentiometric titration, SEM microscopy, and porosimetry are in good agreement. The presented studies confirm that bentonite affects the structurization of carbon, and the thermal stability of the materials is due to the Si–O–C bond formation in the sample and nanocarbon intercalation between the clay layers during the carbonization.

The adsorption data were examined by the Langmuir and Freundlich isotherms. The high R^2 values in the range of 0.983–0.999 show that the Langmuir model describes well the experimental data for all adsorption systems. The R^2 in the range of 0.783–0.957 proved that the Freundlich model also well describes the experimental systems. The adsorption properties of obtained materials towards methylene blue are differentiated and correlations with their structural characteristics are found. Much better adsorption effectiveness is observed for the materials obtained with the addition of aluminosilicate with a maximum adsorption capacity of 5.78 mg/g compared to the carbon synthesized only from tannin (a_m = 1.00). The obtained results indicate that the surface functional groups of the adsorbent are more critical for the adsorption of the studied organic substances than the surface area and porosity. They show differentiated affinity towards organic substances. The obtained materials are very good adsorbents for typical organics of hydrophobic properties which are poorly adsorbed on raw clay. The investigated materials can be used as an effective selective adsorbent for the removal of organic substances of differentiated properties from the aqueous solutions.

From a practical point of view, the obtained materials may be valuable adsorbents in water and wastewater purification technologies.

Author Contributions: Conceptualization, M.G. and V.B.; Material synthesis, M.G.; Investigation, M.G., A.B., D.S. and O.O.; Methodology, M.G., A.B., D.S., O.O., V.G. and A.D.-M.; Writing—original draft, M.G., A.B. and D.S.; Writing—review and editing, A.D.-M. and V.G. All authors have read and agreed to the published version of the manuscript.

Funding: This research received no external funding.

Institutional Review Board Statement: Not applicable.

Informed Consent Statement: Informed consent was obtained from all subjects involved in the study.

Data Availability Statement: The data and samples are available from the authors.

Acknowledgments: The authors are grateful for the National Academy of Science of Ukraine and the Polish Academy of Science, International Research Staff Exchange Scheme between NAS of Ukraine and PAS (2022–2024) for financial support of the project Pesticide removal from aqueous solutions using innovative composites.The authors thank Wojciech Franus from the Faculty of Civil Engineering and Architecture at the Lublin University of Technology for SEM analysis of the samples.

Conflicts of Interest: The authors declare no conflict of interest.

References

1. Youcef, L.D.; Belaroui, L.S.; López-Galindo, A. Adsorption of a cationic methylene blue dye on an Algerian palygorskite. *Appl. Clay Sci.* **2019**, *179*, 105145. [CrossRef]
2. Khan, I.; Saeed, K.; Zekker, I.; Zhang, B.; Hendi, A.H.; Ahmad, A.; Ahmad, S.; Zada, N.; Ahmad, H.; Shah, L.A.; et al. Review on Methylene Blue: Its Properties, Uses, Toxicity and Photodegradation. *Water* **2022**, *14*, 242. [CrossRef]
3. Deng, H.; He, H.; Li, W.; Abbas, T.; Liu, Z. Characterization of amphoteric bentonite-loaded magnetic biochar and its adsorption properties for Cu^{2+} and tetracycline. *PeerJ* **2022**, *10*, e13030. [CrossRef] [PubMed]
4. Hameed, B.H.; Ahmad, A.L.; Latiff, K.N.A. Adsorption of basic dye (methylene blue) onto activated carbon prepared from rattansaw dust. *Dye. Pigment.* **2007**, *75*, 143–149. [CrossRef]
5. Bosacka, A.; Zienkiewicz-Strzalka, M.; Wasilewska, M.; Deryło-Marczewska, A.; Podkościelna, B. Physicochemical and Adsorption Characteristics of Divinylbenzene-co-Triethoxyvinylsilane Microspheres as Materials for the Removal of Organic Compounds. *Molecules* **2021**, *8*, 2396. [CrossRef] [PubMed]
6. Do, J.L.; Friščić, T. Mechanochemistry: A Force of Synthesis. *ACS Cent. Sci.* **2017**, *3*, 13–19. [CrossRef] [PubMed]
7. AbdEl-Magied, M.O.; Hassan, A.M.A.; Gad, H.M.H.; Mohammaden, T.F.; Youssef, M.A.M. Removal of nickel (II) ions from aqueous solutions using modified activated carbon: Akinetic and equilibrium study. *J. Dispers. Sci. Technol.* **2018**, *39*, 862–873. [CrossRef]
8. Kumar, A.; Lingfa, P. Sodium bentonite and kaolin clays: Comparative study on their FT-IR, XRF, and XRD. *Mater. Today Proc.* **2020**, *22*, 737–742. [CrossRef]
9. Xu, C.; De, S.; Balu, A.M.; Ojeda, M.; Luque, R. Mechanochemical synthesis of advanced nanomaterials for catalytic applications. *Chem. Commun.* **2015**, *51*, 6698–6713. [CrossRef] [PubMed]
10. Tsuzuki, T. Mechanochemical synthesis of metal oxide nanoparticles. *Commun. Chem.* **2021**, *4*, 143. [CrossRef]

11. Krupska, T.; Golovan, A.; Lupashku, T.; Povar, I.; Spinu, O.; Kartel, M.; Turov, V. The nanocomposite system based on tannin and methylsilica for the activation of development of seeds. *Dopov. Nac. Akad. Nauk.* **2017**, *10*, 83–90. [CrossRef]
12. Arbenz, A.; Avérous, L. Chemical modification of tannins to elaborate aromatic biobased macromolecular architectures. *Green Chem.* **2015**, *17*, 2626–2646. [CrossRef]
13. Kozakevych, R.; Bolbukh, Y.; Lupascu, L.; Lupascu, T.; Tertykh, V. Polymeric Composite Films with Controlled Release ofNatural Antioxidant Enoxil. In *NANO 2017 Nanochemistry, Biotechnology, Nanomaterials, and Their Applications*; Springer Proceedings in Physics; Fesenko, O., Yatsenko, L., Eds.; Springer: Cham, Switzerland, 2017; Volume 214, pp. 149–164.
14. Hintz, T.; Matthews, K.K.; Di, R. The Use of Plant Antimicrobial Compounds for Food Preservation. *BioMed Res. Int.* **2015**, *2015*, 246264. [CrossRef]
15. Sánchez-Martín, J.; Beltrán-Heredia, C.; Solera-Hernández, C. Surface water and wastewater treatment using a new tannin-based coagulant. *J. Environ. Manag.* **2010**, *91*, 2051–2058. [CrossRef]
16. Vu, T.T.; Kim, H.; Tran, V.K.; Vu, H.D.; Hoang, T.X.; Han, J.W.; Choi, Y.H.; Jang, K.S.; Choi, G.J.; Kim, J.-C. Antibacterial activity of tannins isolated from Sapium baccatumextractanduse for control of tomato bacterial wilt. *PLoS ONE* **2017**, *12*, e0181499. [CrossRef] [PubMed]
17. Yang, B.; Liu, P. Composition and biological activities of hydrolysable tannins of fruits of phyllanthusemblica. *J. Agric. Food Chem.* **2014**, *62*, 529–541. [CrossRef] [PubMed]
18. Gonta, A.; Lupascu, T.; Timbaliuc, N.; Meghea, A. Obtaining and characterizing modified tannins by physical-chemical methods. *Open Chem.* **2014**, *12*, 757–762. [CrossRef]
19. Ismadji, S.; Tong, D.S.; Soetaredjo, F.E.; Ayucitra, A.; Yu, W.H.; Zhou, C.H. Bentonite hydrochar composite for removal of ammonium from Koifishtank. *Appl. Clay Sci.* **2016**, *119*, 146–154. [CrossRef]
20. Available online: https://forum.md/ru/741258 (accessed on 30 May 2022).
21. Aprianti, N.; Faizal, M.; Said, M.; Nasir, S. Catalytic gasification of oil palm empty fruit bunch by using Indonesian bentonite as the catalyst. *J. Appl. Eng. Sci.* **2021**, *2*, 334–343. [CrossRef]
22. Moosavi, M. Bentonite clay as a natural remedy: A brief review. *Bentonite Clay A Nat. Rem. A Brief Rev.* **2017**, *46*, 1176–1183.
23. Dou, G.; Goldfarb, J.L. In situ upgrading of pyrolysis biofuels by bentonite clay with simultaneous production of heterogeneous adsorbents for watertreatment. *J. Appl. Eng. Sci.* **2017**, *195*, 273–283.
24. Sternik, D.; Galaburda, M.; Bogatyrov, V.M.; Gun'Ko, V.M. Influence of the Synthesis Method on the Structural Characteristics of Novel Hybrid Adsorbents Based on Bentonite. *Colloids Interfaces* **2019**, *3*, 18. [CrossRef]
25. Chen, Z.; Chen, B. Sorption of naphthalene and 1-naphthol by biochars of orange peels with different pyrolytic temperatures. *Chemosphere* **2009**, *76*, 127–133. [CrossRef] [PubMed]
26. Uchimiya, M.; Wartelle, L.H.; Lima, I.M.; Klasson, K.T. Sorption of Deisopropylatrazine on Broiler Litter Biochars. *J. Agric. Food Chem.* **2009**, *58*, 12350–12356. [CrossRef]
27. Ahmad, M.; Rajapaksha, A.U.; Lim, J.E.; Zhang, M.; Bolan, N.; Mohan, D.; Vithanage, M.; Lee, S.S.; Ok, Y.S. Biochar as a sorbent for contaminant management in soil and water: A review. *Chemosphere* **2014**, *99*, 19–33. [CrossRef] [PubMed]
28. Islam, T.; Li, Y.; Cheng, H. Biochars and engineered biochars for water and soil remediation: A review. *Sustainability* **2021**, *13*, 9932. [CrossRef]
29. Yahaya Bermakai, M.; Farahin Jafri, N.; Abdul Hadi, N. Biomass activated carbon properties through activation method forsupercapacitor- a mini-review. *Sustainability* **2021**, *9*, 8–13.
30. Kumar, A.; Jena, H.M. Preparation and characterization of high surface area activated carbon from Fox nut (Euryaleferox) shell by chemical activation with H3PO4. *Results Phys.* **2016**, *6*, 651–658. [CrossRef]
31. Ambroz, F.; Macdonald, T.J.; Martis, V.; Parkin, I.P. Evaluation of the BET Theory for the Characterization of Meso and Microporous MOFs. *Small Methods* **2018**, *2*, 1800173. [CrossRef]
32. Gun'ko, V.M.; Mikhalovsky, S.V. Evaluation of slitlike porosity of carbon adsorbents. *Carbon* **2004**, *42*, 843–849. [CrossRef]
33. Ferrari, A.C.; Robertson, J. Raman spectroscopy of amorphous, nanostructured, diamond-like carbon, and nanodiamond. *Philos. Trans. R. Soc. Lond. A Math. Phys. Eng. Sci.* **2004**, *362*, 2477–2512. [CrossRef]
34. Fang, Y.; Lv, Y.; Che, R.; Wu, H.; Zhang, X.; Gu, D.; Zheng, G.; Zhao, D. Two-Dimensional Mesoporous Carbon Nanosheets and Their Derived Graphene Nanosheets: Synthesis and Efficient Lithium Ion Storage. *J. Am. Chem. Soc.* **2013**, *135*, 1524–1530. [CrossRef] [PubMed]
35. Sergeeva, A.V.; Zhitova, E.S.; Nuzhdaev, A.A.; Zolotarev, A.A.; Bocharov, V.N.; Ismagilova, R.M. Infrared and Raman Spectroscopy of Ammonio voltaite,$(NH_4)_2Fe^{2+}{}_5Fe^{3+}{}_3Al(SO_4)_{12}(H_2O)_{18}$. *Minerals* **2020**, *10*, 781. [CrossRef]
36. Reddy, T.R.; Kaneko, S.; Endo, T.; Reddy, S.L. Spectroscopic Characterization of Bentonite. *J. Lasers Opt. Photonics* **2017**, *4*, 171.
37. Koswojo, R.; Utomo, R.P.; Ju, Y.H.; Ayucitra, A.; Soetaredjo, F.E.; Sunarso, J.; Ismadji, S. AcidGreen 25 removal from wastewater by organo-bentonite fromPacitan. *Appl. Clay Sci.* **2010**, *48*, 81–86. [CrossRef]
38. Mierzwa-Hersztek, M.; Gondek, K.; Nawrocka, A.; Pińkowska, H.; Bajda, T.; Stanek-Tarkowska, J.; Szostek, M. FT-IR analysis and the content of phenolic compounds in exogenous organic matter produced from plant biomass. *J. Elem.* **2019**, *24*, 879–896. [CrossRef]
39. Tomczyk, A.; Sokolowska, Z.; Boguta, P. Biochar physicochemical properties: Pyrolysis temperature and feedstock in deffects. *Rev. Environ. Sci. Bio/Technol.* **2020**, *19*, 191–215. [CrossRef]

40. Zhao, S.; Na, T.; Wang, X. Effect of temperature on the structural and physicochemical properties of biochar with apple treebranches as feed stock material. *Energies* **2017**, *10*, 1293. [CrossRef]
41. Blachnio, M.; Derylo-Marczewska, A.; Charmas, B.; Zienkiewicz-Strzalka, M.; Bogatyrov, V.; Galaburda, M. Activated Carbon from Agricultural Wastes for Adsorption of Organic Pollutants. *Molecules* **2020**, *25*, 5105. [CrossRef]
42. Zhu, Y.; Yi, B.; Yuan, Q.; Wu, Y.; Wang, M.; Yan, S. Removal of methylene blue from aqueous solution by cattlemanure-derived low temperature biochar. *Molecules* **2018**, *8*, 19917–19929.
43. DeCastro, M.L.F.A.; Abad, M.L.B.; Sumalinog, D.A.G.; Abarca, R.R.M.; Paoprasert, P.; Luna, M.D.G.d. Adsorption of Methylene Blue dye and Cu(II) ions on EDTA-modified bentonite: Isotherm, kinetic and thermodynamic studies. *Sustain. Environ. Res.* **2018**, *28*, 197–205. [CrossRef]
44. Derakhshan, Z.; Baghapour, M.A.; Ranjbar, M.; Faramarzian, M. Adsorption of Methylene Blue Dye from Aqueous Solutions by Modified Pumice Stone: Kinetics and Equilibrium Studies. *Health Scope* **2013**, *3*, 136–144. [CrossRef]
45. Veliev, T.; Öztürk, S.; Veli, A.; Fatullayev, A.G. Application of Diffusion Model for Adsorption of Azo Reactive Dye on Pumice. *Pol. J. Environ. Stud.* **2006**, *15*, 345–353.
46. Jawad, A.H.; Rashid, R.A.; Ishak, M.A.M.; Wilson, L.D. Adsorption of methylene blue onto activated carbon developed from biomass waste by H_2SO_4 activation: Kinetic, equilibrium and thermodynamic studies. *Desalination Water Treat.* **2016**, *57*, 25194–25206. [CrossRef]
47. Vijayalakshmi, R.; Jobish, J. Adsorption of Methylene Blue onto Natural Rubber/Chitosan Blends. *Int. J. Polym. Mater.* **2011**, *60*, 766–775.
48. Fatiha, M.; Belkacem, B. Adsorption of methylene blue from aqueous solutions using natural clay. *J. Matter Environ. Sci.* **2016**, *7*, 285–292.

[D4] Mariia Galaburda, Alicja Bosacka, Dariusz Sternik, Olena Oranska, Mykola Borysenko Volodymyr Gun’ko, Anna Derylo-Marczewska, Physicochemical and Sorption Characteristics of Carbon Biochars Based on Lignin and Industrial Waste Magnetic Iron Dust, Water 2023, 15(1), 189, https://doi.org/10.3390/w15010189

water

MDPI

Article

Physicochemical and Sorption Characteristics of Carbon Biochars Based on Lignin and Industrial Waste Magnetic Iron Dust

Mariia Galaburda [1,2], Alicja Bosacka [1,3,*], Dariusz Sternik [1], Olena Oranska [2], Mykola Borysenko [2], Volodymyr Gun'ko [2] and Anna Derylo-Marczewska [1,*]

[1] Faculty of Chemistry, Institute of Chemical Sciences, Maria Curie-Sklodowska University, Maria Curie-Sklodowska Sq. 3, 20-031 Lublin, Poland
[2] Institute of Surface Chemistry, National Academy of Sciences, General Naumov Street 17, 03164 Kyiv, Ukraine
[3] Faculty of Production Engineering, University of Life Sciences, Gleboka Street 28, 20-612 Lublin, Poland
* Correspondence: alicja.bosacka@up.lublin.pl (A.B.); anna.derylo-marczewska@mail.umcs.pl (A.D.-M.)

Abstract: Magnetosensitive biochars were prepared with mechanochemical ball-milling of lignin and blast furnace dust with further pyrolysis at 800 °C under an inert gas atmosphere. The physicochemical and sorption characteristics of the materials were analyzed using several techniques: low-temperature nitrogen adsorption–desorption, X-ray powder diffraction, Raman spectroscopy, elemental analysis, potentiometric titration, and thermal analysis. All the synthesized biocarbons were characterized by their specific surface areas (S_{BET}) in the range of 290–330 m^2/g and microporous structures with certain contribution of mesopores in the total porosity. Equilibrium adsorption studies revealed the potential applicability of the materials in water remediation from hazardous organic substances modelled with methylene blue (MB) dye. Generally, this study illustrates the effective conversion of sustainable waste into a functional carbon material.

Keywords: metallurgical dust; lignin; magnetosensitive biochars; carbons; mechanochemical activation

check for updates

Citation: Galaburda, M.; Bosacka, A.; Sternik, D.; Oranska, O.; Borysenko, M.; Gun'ko, V.; Derylo-Marczewska, A. Physicochemical and Sorption Characteristics of Carbon Biochars Based on Lignin and Industrial Waste Magnetic Iron Dust. *Water* **2023**, *15*, 189. https://doi.org/10.3390/w15010189

Academic Editors: Konstantinos Simeonidis and Kiriaki Kalaitzidou

Received: 30 November 2022
Revised: 21 December 2022
Accepted: 29 December 2022
Published: 2 January 2023

1. Introduction

Dyes and pigments are applied in various industries; for example, printing, leather tanning, the production of textiles, paper, rubber, food, cosmetics, etc. Unfortunately, colored substances strongly and negatively affect the quality of water. The coloration of water can occur even with very low dye concentration. Moreover, numerous dyes, mainly of synthetic origin, are considered hazardous substances for aquatic life, animals, and people and are hard to decompose in water. Therefore, the removal of these substances from water and wastewater is of great importance. Adsorption is one of the most frequently used methods for the removal of organic substances because of its simplicity, high efficiency, high variety of available adsorbents, and low ability to produce pollutants [1,2].

On the material market, a wide range of adsorbents (e.g., silicas, zeolites, carbons, polymers, clays, etc.) are available, but these materials may have some restrictions [3–5]. Novel materials with improved properties that are characterized by high adsorption efficiency, thermal stability, longevity, selectivity, resistance to microbes, and relatively inexpensive production are the subject of this research. Adsorption efficiency depends on some key factors caused by types of adsorbates, adsorbents, and solvents. The adsorption process depends on the structure and size of adsorbate molecules, the presence of various functional groups, adsorbate solubility, dissociation ability, adsorbent surface and structural characteristics (e.g., porous structure, surface chemistry, and ash content), and solution properties (e.g., solvent type, pH, and ionic strength) [1,2,6–8]. Functional groups that are present on the adsorbent surface can play a key role in the interactions between adsorbent and adsorbate. For carbons, the basic or acidic surface sites affect the charge, hydrophobicity, and electric density of carbon layers. Based on the aforementioned factors, which may affect the adsorption efficiency of carbon materials, different absorption mechanisms occur, including dispersion, hydrogen bonding, donor–acceptor interactions, or competitive water adsorption [7,8].

Biochar-based materials with strictly defined surface properties and characteristics have reached scientists' attention because of their high adsorption efficiency of organic pollutants (e.g., dyes) and environmental friendliness due to their reuse of organic wastes [1]. In this work, biochars based on lignin and industrial iron dust blends were prepared using pyrolysis at a high temperature under restricted oxygen conditions. Pyrolysis and activation are crucial stages in the formation of the texture and structure of biochars that affect adsorption effectiveness. Generally, pyrolysis of selected blends enables the preparation of materials with unique textural, structural, thermal, and adsorption characteristics [9].

Lignin was chosen as a carbon source for several reasons. Firstly, it was chosen due to its prevalence and availability. Lignin is the second most abundant natural amorphous polymer after cellulose [10]. A huge amount of technical lignin is produced every day all over the world. Lignin is commonly viewed as a useless and low-cost industrial solid waste separated from the biomass feedstocks of papermaking industries, such as wood and grass. Secondly, it was chosen because of its aromatic molecular structure. Lignin is a complex biopolymer composed of different amounts of three monolignols, including p-coumarylalcohol, coniferyl alcohol, and sinapyl alcohol [11]. Compared with other bioresources, it consists of a large number of aromatic benzene rings and possesses the highest carbon content of up to 60%, which favour the highly efficient production of biochar. However, due to the complex structure, low chemical reactivity, and presence of organic and inorganic impurities, its further applications are limited, and currently, most lignin is burned for energy. Hence, it can be an optimal choice to use as the feedstock of biochar.

In recent years, researchers have paid great attention to the production of biochars from lignocellulosic biomass to reduce the cost of biomass utilization [12,13]. Different methods for the preparation of carbon sorbents from lignin were reviewed, such as pyrolysis at high temperatures, steam activation, or chemical activation aiming to increase biochar porosity or structure. Chatterjee described [14] that the content of lignin controlled the char yield and consequently controlled the activated carbon yield. Thus, the type of lignin as well as the microstructure of the char yield depend on the source of biomass and the amount of cellulose and lignin. Lignin-derived biochar is a promising, sustainable alternative to petroleum-based carbon powders (e.g., carbon black) for polymer composite and energy storage applications for high-performance capacitors [15,16]. Demir M. and co-authors reported the economic and sustainable syntheses of functional lignin-derived carbons for supercapacitor and CO_2 capture applications [17]. In another work, Demir M. successfully obtained graphitic carbon via the hydrothermal carbonization and catalytic graphitization of biochar using nitrates Fe(II), Co(II), or Mn(II) as catalysts at 900–1100 °C [18]. Zijun Yi et al. investigated the impact of different pyrolysis atmospheres on the prop-erties of lignin-derived biochar and determined that CO_2 accelerated the removal of the aliphatic structures and rendered the biochar of hydrophobic surface, but formed less fragmentized structures than that obtained in N_2 [19]. Thus, the potential of biochar and lignin-based adsorbents for wastewater treatment (to remove dyes, antibiotics, organics, and heavy metals) has received particular attention in recent years [20–24].

Different methods of modifications that changed the adsorption, catalytic, and magnetic properties of biochar were mainly conducted by mixing metal oxides, metal salts, carbonaceous materials, and biochars [25]. The magnetic properties of biochars are usually enhanced by iron salt or iron metal oxide. To the best of our knowledge, no report on lignin-derived biochars filled with magnetic metallurgical dust exists. That is why such a possibility is considered in this work.

According to the World Steel Association, world crude steel production in 64 countries was 143.3 million tons in November 2021 [26]. Ukraine was in 14th place on the list of "Major steel-producing countries 2021 and 2020" with 21.4 million tons of crude steel production as well as 21.2 million tons of pig iron.

The main product of blast furnace production is cast iron, and by-products include slag and blast furnace gas. Smelting products released from the furnace are sent for processing, including cast iron that is processed for pouring into ingots on a filling machine, slag that is processed for granulation, and blast furnace gas that is processed for purification [27]. Blast furnace production is considered to be the most ecologically dirty link of the technological cycle as it generates 60–65% of wastes. Gravity dust collectors, cyclone dust collectors, bag dust collectors, and other devices are used to obtain flue dust. The sludge is recycled as a waste product after wet cleaning of blast furnace gas. It is used for the blast furnace charge due to its high content of iron oxides. These solid wastes contain many valuable products that can be reused. They usually contain zinc, iron, carbon, and other ferrous and non-ferrous metals and are classified as a secondary resource of zinc and iron. The chemical composition of dust varies to a large extent. Dust from a furnace under high pressure contains 14.6 SiO_2, 4.35 MgO, 4.35 Al_2O_3, 11.85 CaO, 0.74 S, and 3.75 MnO wt.%, and the rest is iron oxides. From a technological point of view, the sludge is very difficult to process due to the high content of non-ferrous metals. By separating particles into fine and coarse fractions, 50–60% of zinc and lead can be removed, and 80% of the total annual volume of generated sludge can be recycled. The particle size of blast furnace dust is about 5–120 μm. The composition of the sludge includes heavy non-ferrous metals—mainly zinc, lead, fluids, chlorides, and sulphates. They have a good flow ability and cause secondary pollution which can be suspended in the air for a long time [28]. Many steel plants around the world have already taken innovative measures to recycle 100% of these wastes with the ultimate goal of improving the efficiency of the steel industry. Blast furnace slags in some countries do not even have the status of waste but belong to secondary raw materials due to effective use as raw materials in several areas (e.g., road construction, the production of cement and concrete in the form of crushed stone, and mixtures without binders or with binders) [29–32]. However, it remains relevant for Ukraine [33].

The disposal of technological waste is a complex resource and environmental problem. The recovery and reuse of this solid waste in an enterprise or industrial facility is mainly necessary to protect the environment and conserve metals and minerals. Studies on improving waste processing technologies and the disposal of metallurgical slags, including dust, are of considerable interest. The problem of organizing zero-waste technology using waste from adjacent industries, the return of waste, shavings, and other dispersed metal waste to metal circulation, and the use of secondary resources in powder metallurgy are promising directions of resource conservation [26–32].

In this paper, we present a new approach based on the carbonization of lignin in the presence of metallurgical dust to obtain magnetically sensitive carbon sorbents via an efficient solvent-free mechanochemical synthesis [9,34]. Our strategy is based on the use of dust as a filler, which plays the role of a graphitization catalyst and a porosity activator, and at the same time allows us to prepare magnetosensitive carbon sorbents. The advantage of such adsorbents is that in the contact purification of solutions, the use of magnetic sorbents greatly simplifies the separation of the sorbent by magnetic separation and the completeness of its processing [35,36]. The influence of the initial composition of lignin–magnetic dust blends on the textural, structural, thermal, and adsorption properties of final materials was evaluated. Adsorption studies regarding methylene blue on lignin–iron dust biochars were conducted. This work may expand ways to design and develop carbon sorbents and present a promising prospect for the application of carbon to wastewater decontamination.

2. Materials and Methods

2.1. Materials and Chemicals

The kraft lignin used in this study was from Indulin AT, MeadWestvaco Corp. (Charleston, SC, USA). The magnetic blast furnace dust was provided by the Blast furnace workshop of the Donetsk Metallurgical Plant Research. The hydrochloric acid (35–38%), sodium hydroxide, and sodium chloride were purchased from Chempur (Piekary Slaskie, Poland). The methylene blue was bought from Merck (Darmstadt, Germany). All solutions were prepared using deionized water (0.05 μS/cm, Polwater, Labpol, Cracow, Poland).

2.2. Materials Preparation

As in the previous paper [9], the materials were synthesized by mechanochemical activation and high-temperature pyrolysis. The first step of the procedure was a mechanochemical activation of kraft lignin and industrial waste magnetic iron dust blends that were loaded into a stainless-steel jar (250 mL) containing stainless steel balls with a 5 mm diameter for 2 h. The second stage was pyrolysis in a reactor at 800 °C and inert gas condition with a flow rate of 100 mL/min. The heating rate was 10 °C/min, and the samples were preserved in the reactor at the established temperature for 1 h, and then they were cooled at room temperature [9].

The names of the samples and the initial ratios of the components are given in Table 1.

Table 1. The ratios of the initial components used to prepare biochars.

Samples	Components Ratios			
	Kraft Lignin (g)	**Kraft Lignin (%)**	**Magnetic Iron Dust (g)**	**Magnetic Iron Dust (%)**
STInd–1	12.5	71.0	5.0	29.0
STInd–2	12.5	76.0	4.0	24.0
STInd–3	12.5	81.0	3.0	19.0
STInd–4	12.5	91.0	1.3	9.0
Indulin/Carbon	12.5	100.0	0.0	0.0

2.3. Methods

2.3.1. Low-Temperature Nitrogen Adsorption-Desorption

To determine the textural characteristics, the nitrogen adsorption–desorption isotherms at 77 K were recorded using a Micromeritics ASAP 2405N adsorption analyzer (Micrometric, Nocross, GA, USA). The specific surface area, S_{BET}, was calculated according to the standard BET method [37]. The total pore volume, V_p, was evaluated based on the nitrogen adsorption at $p/p_0 = 0.98$–0.99 (where p and p_0 denote the equilibrium and saturation pressure of nitrogen at 77 K, respectively). Nitrogen desorption data were used to compute pore size distributions (PSD, differential $f_V(R) \sim dV_p/dR$ and $f_S(R) \sim dS/dR$), using a model with slit-shaped pores [38]. Differential PSD concerning pore volume, $f_V(R) \sim dV_p/dR$ and $\int f_V(R)dR \sim V_p$, were recalculated to incremental PSD (IPSD), $\sum\Phi_{v,i}(R) = V_p$. The $f_V(R)$ and $f_S(R)$ functions were also used to calculate the contributions of micropores (V_{micro} and S_{micro} at radius $R \leq 1$ nm) and mesopores (V_{meso} and S_{meso} at $1 \text{ nm} < R < 25$ nm).

2.3.2. Potentiometric Titration

Potentiometric titration was performed using a system composed of a 765 Dosimat Metrohm autoburet (Herisau, Switzerland), a PHM240 Radiometer pH-meter (Copenhagen, Denmark), an Ecoline RE207 thermostat (Lauda, Germany) to maintain the 25 °C temperature, a degassing system (an inert gas atmosphere), and a 50 mL quartz container. Thirty mL of 0.1 mol/L electrolyte (sodium chloride), 0.3 mL of 0.2 mol/L hydrochloric acid, and 0.1 g of solid sample (biochar) were added to the quartz vessel to conduct the experiment. After achieving a constant temperature and pH value, the 0.1 mol/L sodium hydroxide was gradually titrated. Analogous titration was performed without the addition of the solid. Based on the collected data, the surface charge and the point of zero charge (pH_{PZC}) were established for all carbonized samples [9].

2.3.3. X-ray Diffraction (XRD)

The XRD patterns were recorded using a DRON UM1 diffractometer (Burevestnik, Saint Petersburg, Russia) at 2θ from 10 to 90° with filtered Co K_α radiation and Bragg–Brentano geometry.

2.3.4. X-ray Fluorescence (XRF)

The XRF was used for an elemental composition analysis of bulk samples using an Expert 3L XRF desktop high-precision express analyzer in helium atmosphere.

2.3.5. Raman Spectroscopy

The Raman spectra were recorded at 3200–150 cm^{-1} using Via Reflex Microscope DMLM Leica Research Grade, Reflex (Renishaw, UK) with laser excitation at $\lambda_0 = 785$ nm.

2.3.6. Thermal Analysis (TA)

The thermogravimetric (TG) measurements with differential thermal analysis (DTA) of samples (with a mass of 100–150 mg) placed in a ceramic crucible were performed at a temperature range between 25 and 1000 °C in the air atmosphere using a Derivatograph Q 1500D (Paulik, Paulik & Erdey, MOM, Budapest, Hungary) with a heating rate of 10 °C/min.

2.3.7. Equilibrium Adsorption Studies

Adsorption equilibrium studies of methylene blue (MB) on indulin–magnetic dust adsorbents were carried out using a Carry 4000, Varian UV-Vis spectrophotometer (Melbourne, Australia). Adsorbent with a mass of 0.05 g was placed into a 100 mL conical flask. Then, 50 mL of methylene blue aqueous solutions (pH ~7) with initial concentrations from 0.005 to 0.1 mmol/L (1.6 to 32 mg/L) were shaken for 2 days at 25 °C with 110 rpm in a New Brunswick Scientific Shaker (Edison, NJ, USA). When equilibrium was established, the absorbance was measured at 450–200 nm, and the methylene blue concentration was evaluated based on the maximum of the absorbance peak. The adsorbed amount (*a*) was determined using the Mass Balance Equation (1), and the percentages of removal of methylene blue from solutions were determined applying Equation (2). The adsorption data were analyzed based on modified Langmuir (3) and Freundlich (4) isotherms.

$$a = \frac{\left(c_0 - c_{eq}\right) \cdot V}{m} \tag{1}$$

$$\%\ removal_{MB} = \frac{\left(c_0 - c_{eq}\right)}{C_0} \cdot 100 \tag{2}$$

$$a = a_m \frac{K_{ML} \cdot C_{eq}}{\left(C_S - C_{eq}\right) + \left(K_{ML} \cdot C_{eq}\right)} \tag{3}$$

$$a = K_F \cdot C_{eq}{}^{\frac{1}{n}} \tag{4}$$

where a is the adsorption amount at equilibrium (mg/g); C_0 is the initial concentration of dye (mg/L); C_{eq} is the equilibrium concentration of dye (mg/L); V is the volume of solution; m is the mass of adsorbent; $\%\ removal_{MB}$ is the percentage of methylene blue removal; a_m is the maximum adsorption amount; K_{ML} is the modified Langmuir equilibrium constant; C_S is the value of saturated concentration of solute [mg/L], (dimensionless quantity); K_F is the Freundlich constant (mg/g); and n is the heterogeneity factor.

The influence of pH and contact time were checked before the adsorption studies of methylene blue. The effect of pH on the percent of methylene blue removal was taken into account. Biochars with a mass of 0.05 g were placed in 100 mL plastic containers and contacted with 50 mL of 12.8 mg/L methylene blue solution at pH 2, 4, 7, and 10. The pH value was preserved by adding 0.1 mol/L hydrochloric acid or 0.1 mol/L sodium hydroxide solutions and shaken for 2 days at 25 °C with 110 rpm in a New Brunswick Scientific Shaker to achieve equilibrium. Additionally, the effect of time was examined on two selected materials, including STInd–1 and STInd–4. The samples of mass of 0.05 g were situated in 100 mL Erlenmeyer flasks and contacted with 50 mL of 12.8 mg/L at pH ~7, and the solution was measured at appropriate time intervals. In all cases, the adsorbent was centrifuged for 10 min with 10,000 rpm at 25 °C using an MPW-352R centrifuge (Warsaw, Poland), and the supernatant was analyzed [9].

3. Results and Discussion

3.1. Low-Temperature Nitrogen Adsorption-Desorption

Nitrogen adsorption–desorption isotherms were collected to verify the textural properties of biochars (Figure 1a). The specific surface area (S_{BET}) of carbonized indulin–iron dust materials is in the range between 290 and 330 m^2/g, while pyrolyzed indulin is characterized by a specific surface area of only 7 m^2/g. The adsorption–desorption data are summarized in Table 2.

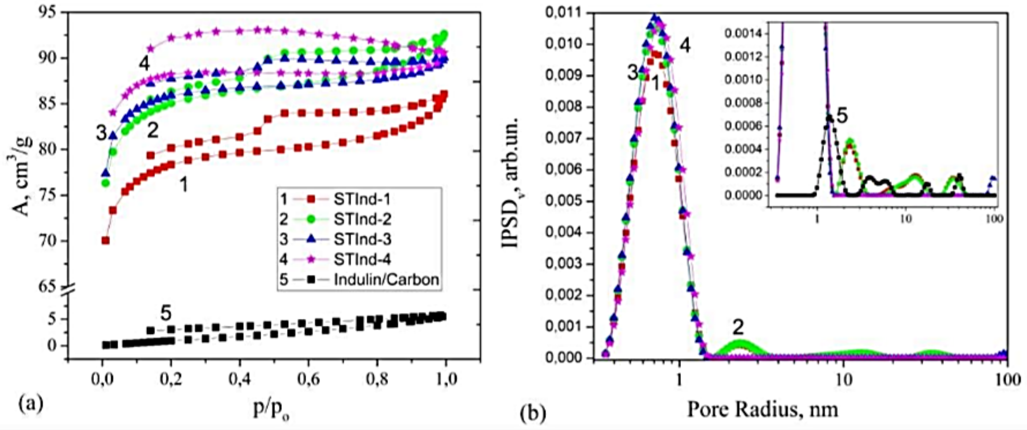

Figure 1. (**a**) Nitrogen adsorption–desorption isotherms and (**b**) pore size distributions of 1: STInd–1; 2: STInd–2; 3: STInd–3; 4: STInd–4; and 5: indulin/carbon.

Table 2. Textural characteristics of biochars.

Sample	S_{BET} (m^2/g)	V_{micro} (cm^3/g)	V_{meso} (cm^3/g)	V_p (cm^3/g)	V_{micro}/V_p	V_{meso}/V_p
STInd–1	290	0.118	0.014	0.132	0.894	0.106
STInd–2	315	0.128	0.014	0.142	0.901	0.099
STInd–3	313	0.129	0.011	0.140	0.921	0.079
STInd–4	330	0.131	0.008	0.139	0.942	0.058
Indulin/Carbon	7	-	0.007	0.007	-	-

The nitrogen adsorption–desorption isotherms of the indulin-based samples can be ascribed as a mixture of I and IV types with a combination of the hysteresis loops of H1 and H4 according to IUPAC classification, which is associated with the occurrence of microporous and mesoporous structures of biochar surfaces. The desorption curves of the STInd–1, STInd–2, and STInd–3 samples show an inflection point in the relative pressure range between 0.4 and 0.6, which indicates that a high amount of adsorbed gas is instantly desorbed due to the presence of special ink bottle-like pore structures or the deformation of the coal body by filler [39,40].

The adsorption and desorption curves of the STInd–4 sample do not come together at a relatively low pressure in the isotherm. This may be caused by the irreversible uptake of nitrogen molecules in pores through very narrow pore entrances and some swelling of the adsorbents. The micropores are extremely developed in this sample, and their pore area gives a majority share to the total pore area. The STInd–4 sample shows a higher surface area than STInd–1 which is most likely due to the partial pore blocking by the filler. Generally, a small decrease in S_{BET}, V_{mic} values is observed with an increase in the filler content, and the mesopore volume increases at the same time. The pore size distribution curves (Figure 1b with insert Table 2) show that the pore size distributions are mostly in the microporous range, which indicates that the resulting carbons have a microporous structure; however, the mesopores of different sizes also contribute to the total porosity.

3.2. X-ray Investigations

The main chemical composition of the blast furnace dust probe was analyzed using X-ray fluorescence, and the data are presented in Table 3.

Table 3. The chemical composition of the blast furnace dust.

Component	**Fe**	**Ca**	**Si**	**Cl**	**S**	**Mg**	**Mn**	**Pb**	**Zn**	**Al**
Content (wt%)	79.763 (±0.100)	9.965 (±0.031)	3.951 (±0.080)	3.843 (±0.050)	2.166 (±0.058)	0.134 (±0.010)	0.089 (±0.017)	0.045 (±0.006)	0.027 (±0.004)	0.015 (±0.003)

According to the XRF and XRD data (Tables 3 and 4 and Figure 2), it can be concluded that the main components of the blast furnace dust include the Fe_3O_4, α-Fe_2O_3, SiO_2, and $CaCO_3$ phases. The sample does not contain appreciable amounts of Pb and Zn as was reported by Das B. et al. [31] for samples from other parts of the world. The carbonization of indulin–iron dust blends at 800 °C; therefore, iron oxides are partly reduced to α-Fe. Furthermore, FeO and Fe_3O_4 phases are also present in small amounts. In addition to amorphous carbon, graphite is observed in carbonized samples as evidenced by the presence of the (002) peak at $2\theta = 31°$. Data regarding the phase composition are given in Table 4. The highest content of amorphous carbon is in the STInd–4 sample.

Table 4. Structural characteristics of biochars.

Sample	**Phase Composition**	**Center (cm^{-1})**		**FWHM (cm^{-1})**		**I_D/I_G**	**Carbon Content (%)**
		D	**G**	**D**	**G**		
DustST	Fe_3O_4, α-Fe_2O_3, SiO_2, $CaCO_3$	-	-	-	-	-	-
STInd–1	Fe, FeO, Fe_3O_4, SiO_2, C_{amorph}	1310	1600	84.8	57.2	0.9	46.0
STInd–2	Fe, FeO, Fe_3O_4, C SiO_2, C_{amorph}	1312	1598	120.3	64.6	1.0	51.0
STInd–3	Fe, FeO, Fe_3O_4, C SiO_2, C_{amorph}	1314	1598	120.8	64.7	1.2	56.0
STInd–4	Fe, Fe_3O_4, FeO, SiO_2, C_{amorph}	1316	1598	121.5	63.2	1.3	66.0
Indulin/Carbon	C_{amorph}	1319	1586	90.5	58.1	1.2	100.0

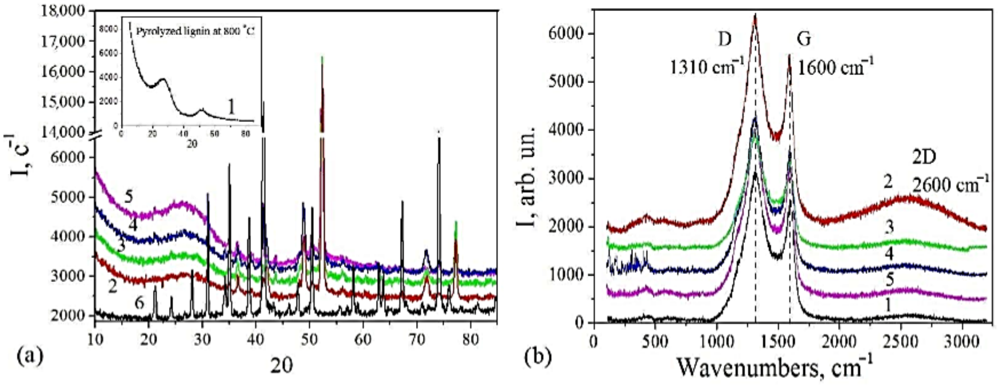

Figure 2. (**a**) XRD patterns and (**b**) Raman spectra of carbonized materials and furnace dust. 1: indulin/carbon; 2: STInd–1; 3: STInd–2; 4: STInd–3; 5: STInd–4; and 6: DustST.

The formation of Zn and Mn ferrite phases as well as Al_2O_3, MgO, and Ca_2SiO_4 (as was reported by Li et al. [41]) cannot be precisely established to see the crystalline compounds due to the sensitivity of this method and their very low content. As shown in Figure 2a (insertion), the pyrolyzed lignin is amorphous due to the presence of two broad and non-intense maxima of the halo at around $2\theta = 26°$ and 50° in the pattern that is characteristic of amorphous carbon.

Additional information about the carbon phase in biochar is provided by the Raman spectroscopy. As can be seen in Figure 2b, the Raman spectra show characteristic D and G peaks with the maxima at wavenumbers of ~1310 and ~1600 cm^{-1}, respectively. The G band is due to bond stretching of all pairs of sp^2 atoms in both rings and chains and is associated with the vibration of the ideal graphite lattice (E2g symmetry, C-C in-plane stretching mode), while the D band is due to the breathing modes of sp^2 atoms in rings (A1g symmetry) [42]. The wide intensive G band in the samples indicates the increasing degree of carbon disordering.

The intensity ratio of the D and G peaks (I_D/I_G) is commonly used to measure the degree of graphitization of carbon structures. Only STInd–1 and STInd–2 samples have an I_D/I_G ratio ≤ 1 (Table 4), whereas other STInd samples have values above 1, which indicates the presence of amorphous phases. This value is higher than or comparable to previously reported data [43]. Apart from the D and G peaks, a 2D peak appears at regions 2200–2800 cm^{-1} as the overtones of fundamental modes, which was assigned by Y. Wang et al. as a highly ordered pyrolytic graphite [44]. Moreover, the D band maximum moves toward the higher wavenumber, and the broadening of FWHM of all peaks takes place due to increasing disordering via changes in the crystallite structure (i.e., the arrangement or reconstruction of a boundary carbon atom) (Figure 2b). Thus, an increase in the filler content leads to an intensifying of the crystallinity of the graphite-like fraction.

3.3. Thermal Analysis

Weight losses in the temperature range of 25–1000 °C is observed on the TG curves during the thermo-oxidative destruction of the samples. The first mass loss, which is visible on the TG curves for all samples (Figure 3) at a temperature of ~100 °C, corresponds to the desorption of physisorbed water. This low temperature weight loss is not accompanied by DTA effects, but it is clearly visible on the DTG curves. Moreover, it can be seen that TG and DTA shift toward higher temperatures with an increase in the content of magnetic fillers in the samples.

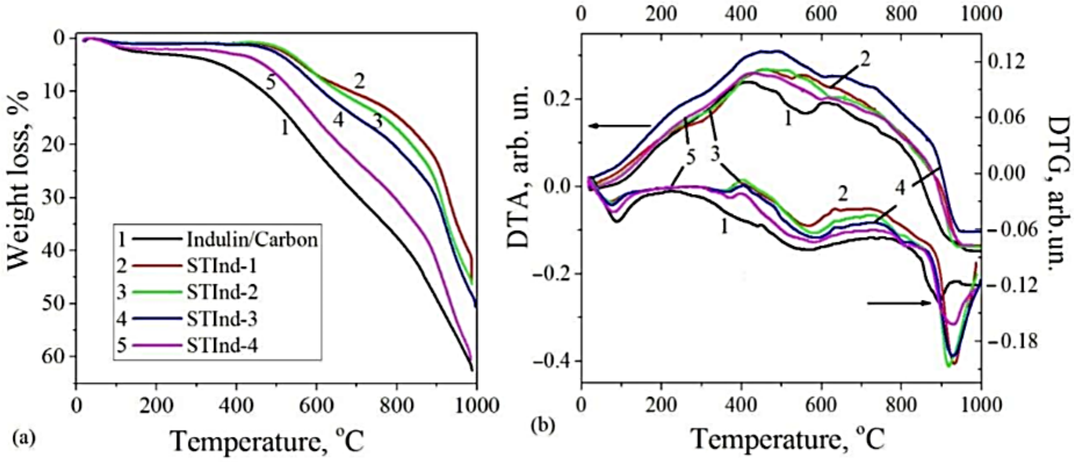

Figure 3. TG (**a**) and DTG and DTA (**b**) curves of biochars.

The DTA curves of modified samples have a broad peak in the temperature range of 200–950 °C and consist of several overlapping picks that result from a series of processes, including the adsorption of oxygen on carbon and metals (at $T > 200$ °C) and carbon combustion with CO_2 removal (DTA_{max} at 400–800 °C). The DTG curves demonstrate that three mass loss steps occurred during the thermal degradation of the modified samples in this region. The weight decrease phenomenon that is visible in this range on the TG curves is due to the decomposition of functional groups of biochars [45,46], the oxidation of metal nano-particles in the air with the formation of oxides forms above 700 °C, and the thermo-oxidations of graphene structures on the surface of biochar. When comparing the TG and DTA curves of indulin/carbon to the modified samples, the magnetic dust filler gives the carbons a higher thermal resistance. The wide temperature range of the oxidation of modified samples can be explained by the presence of carbon nanoparticle aggregates of higher densities. According to the literature [8,47], the presence of two exothermic peaks on the DTA curves (during analysis in a static atmosphere in air) is related to the oxidation of carbon atoms on the surface and oxygen diffusion and reaction in the pores. The distinctive T_{max} at temperatures above 800 °C can be attributed to the high external thermal energy that must be applied to the system to overcome strong bonding in the carbon lattice structures. The low T_{max} in the indulin/carbon indicates that less heat energy is necessary to destroy the weak non-graphitic sp^3 hybridized carbon atoms with a high density of defects during thermooxidative reactions compared with STInd–1 and STInd–2 samples; in these samples, sp^2 hybridized carbon atoms are ordered by covalent bonds in a hexagonal carbon framework. These results correspond precisely with the Raman spectroscopy data. Moreover, weight loss at temperatures above 800 °C can be associated with the decomposition of residual ash, the volatilization of heavy metals, and further oxidation of metals.

The carbon retention of lignin is 65 wt.%, which indicates a high yield of carbon and the prospect of its use for obtaining carbon biochars by pyrolysis. The carbon content in the carbonized samples was calculated [48] according to the TG data and took into account the fact that DustST contains ~20% impurities (Table 4).

3.4. Potentiometric Titration

Potentiometric titration was used to determine the acid base properties of indulin–iron dust biochars. The surface charge dependences as a function of pH are presented in Figure 4. The values of the pH_{PZC} (point of zero charge) of the STInd–1, STInd–2, STInd–3, STInd–4, and indulin/carbon samples are 7.38, 7.81, 8.32, 8.58, and 9.41, respectively. All examined carbonized materials are positively and negatively charged and can interact with both cations and anions, depending on the pH region. Overall, the pH_{PZC} values reveal the alkaline nature of the carbonized materials; moreover, the alkaline properties decrease with iron magnetic dust filler content. This result may be related to a lower degree of carbonization with an increasing filler amount. Generally, the potentiometric titration results are in good agreement with data obtained by Raman spectroscopy, X-ray diffraction, and thermal analysis. Besides, a good correlation between the percentage of carbon and pH_{PZC} were found since the pH_{PZC} is higher when the carbon content in the pyrolyzed material is higher [9].

3.5. Adsorption Studies

The adsorption properties of carbonized indulin–iron dust materials were tested using a cationic thiazine dye known as methylene blue. The measurements of adsorption isotherms were conducted using a wide pH range.

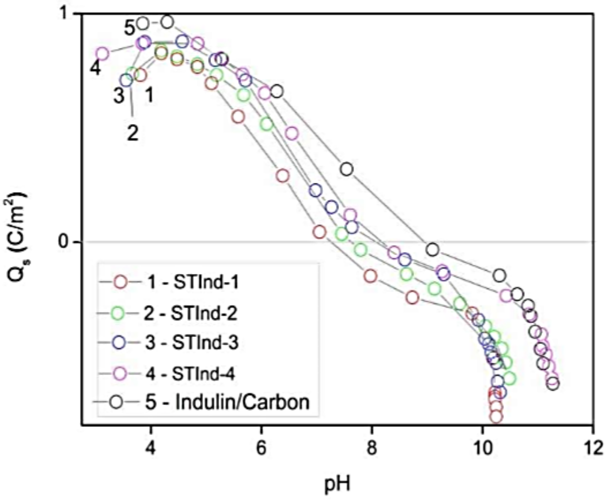

Figure 4. Surface charge density as a function of pH (Qs vs. pH) of carbonized indulin-based biochars.

The effect of pH on the removal of methylene blue from solutions with an initial concentration of 12.8 mg/L is presented in Figure 5a. It can be seen that pH only slightly affects adsorption efficiency. The effect of contact time on the adsorption of methylene blue from solutions at pH ~7 on the selected carbonized materials is visible in Figure 5b. It can be concluded that the adsorption equilibrium is achieved in 1 day. The percentage of methylene blue removal by indulin–based adsorbents from solutions at pH ~7 is shown in Figure 5c. It is visible that the change in the value of the removed substance is related to the adsorbent structural and surface properties. Generally, the adsorption data reveal a meaningful increase in the adsorption uptake for materials with iron dust filler (STInd–1, STInd–2, STInd–3, and STInd–4) compared with the sample with pyrolyzed indulin (indulin/carbon) which shows a very weakly developed pore structure. The carbonized indulin samples with the addition of the magnetic filler are characterized by high values of specific surface area (S_{BET}) of ~300 m^2/g, while indulin is only 7 m^2/g. Taking into account the filler influence, the effectiveness of the adsorption process may be ordered as follows: STInd–1 > STInd–2 > STInd–3 > STInd–4. The differences in adsorption capacity can be related, firstly, to the structure characteristics (e.g., the specific surface area, microporosity, and mesporosity contribution) and, secondly, to the surface properties (i.e., the acid base properties). The share of mesopores in the STInd–1 sample is the highest (0.106), and the micropores share is the lowest (0.894). On the contrary, for STInd–4, the contribution of mesopores is the lowest (0.058), and micropores share is the highest (0.942). The mesoporosity gradually diminishes as the filler content of the initial mixture of blends decreases. It may be that the presence of mesopores facilitates the penetration of the internal adsorbent space by a large molecule of dye.

The parameters calculated based on modified Langmuir [49] and Freundlich isotherms are summarized in Table 5. Both equations show correlation coefficients above 0.9, which allows them to be used to characterize the adsorption process. The tests show that the maximum adsorption of methylene blue for the indulin–lignin dust biochars is 10 to 20 times higher than that of the reference sample (indulin/carbon) (Figure 5d).

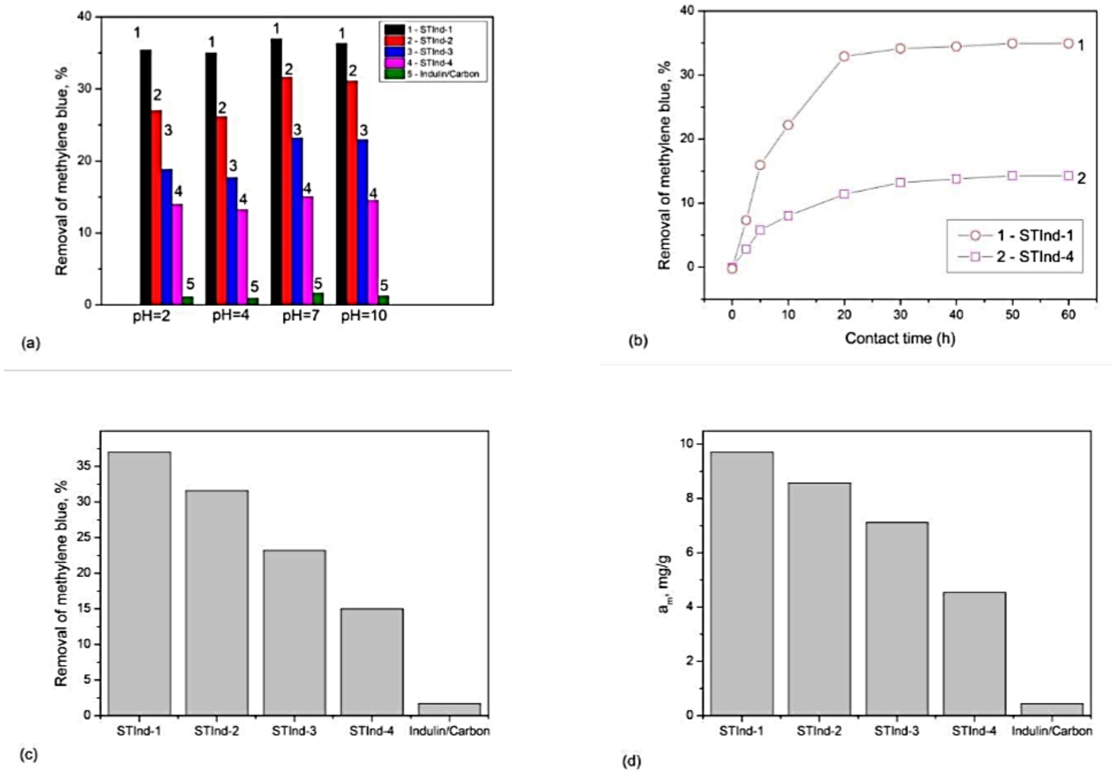

Figure 5. The effect of (**a**) pH (C_0 = 12.8 mg/L, pH = 2, 4, 7), (**b**) contact time C_0 = 12.8 mg/L, pH = 7), (**c**) the percent of methylene blue removal (C_0 = 12.8 mg/L, pH ~7) and (**d**) maximum adsorption (a_m) (mg/g) for the investigated adsorbents.

Table 5. Parameters of modified Langmuir and Freundlich isotherms for methylene blue adsorption on biochars.

Sample	**Modified Langmuir Isotherm**			**Freundlich Isotherm**		
	R^2	K_{ML} (Dimensionless)	a_m (mg/g)	R^2	K_F (mg/g)	N
STInd–1	0.911	4336	9.71	0.933	0.949	1.49
STInd–2	0.980	5139	8.57	0.953	1.045	1.66
STInd–3	0.905	4285	7.12	0.951	0.838	1.72
STInd–4	0.979	5960	4.53	0.972	0.669	1.89
Indulin/Carbon	0.988	5,889,834	0.44	0.184	0.361	12.71

The results of the literature overview regarding the adsorption of methylene blue on biochars and commercially available activated carbons are shown in Table 6. One can state that the indulin–iron dust materials show comparable or, in some cases, even higher adsorption effectiveness toward methylene blue solutions compared with other biochars. Besides, it has been reported that lignin-based biochars with the addition of magnetic filler show a higher adsorption efficiency than carbonized lignin [3,9,50–57].

Table 6. Comparison of literature data regarding methylene blue adsorption on biochars and commercial activated carbons.

Lp.	Sample	a_m (mg/g)	Literature
1	Zeolite-Waste Materials	10	[3]
2	Tannin/Bentonite-Derived Biochar (TBC-3)	5	[9]
3	Compost Biochar	13	[50]
4	Biomass Biochar	12	[50]
5	Optimal Biochar from Argan Shells Powder	31	[51]
6	Biochar from Pongamia Glabra Seed Cover	2	[52]
7	Ouricuri Endocarp Biochar	2	[53]
8	Biochar from Anaerobic Digestion Residue (BC-R)	10	[54]
9	Biochar from Palm Bark (BC-PB)	3	[54]
10	Biochar from Eucalyptus (BC-E)	2	[54]
11	Composite Based on Ca/Al Layered Double Hydroxide-biochar	19	[55]
12	GAC	131	[56]
13	CAC	980	[57]

Regarding the adsorption mechanisms of the studied systems (i.e., biochar and methylene blue), one can take into account mainly hydrophobic and electrostatic interactions, but also hydrogen bonding. The scheme of biochars synthesis with the possible mechanisms of methylene blue adsorption is presented in Figure 6. Methylene blue is a positively charged molecule which may interact electrostatically with negatively charged or electron-rich moieties. The formation of hydrogen bonding between hydrogen containing groups (Si-O-H, Me-O-H, C-O-H) and nitrogen atoms of methylene blue can also occur. One can expect that the π-π interactions between the aromatic rings of dye molecules and graphene structures of biochars prevail [9].

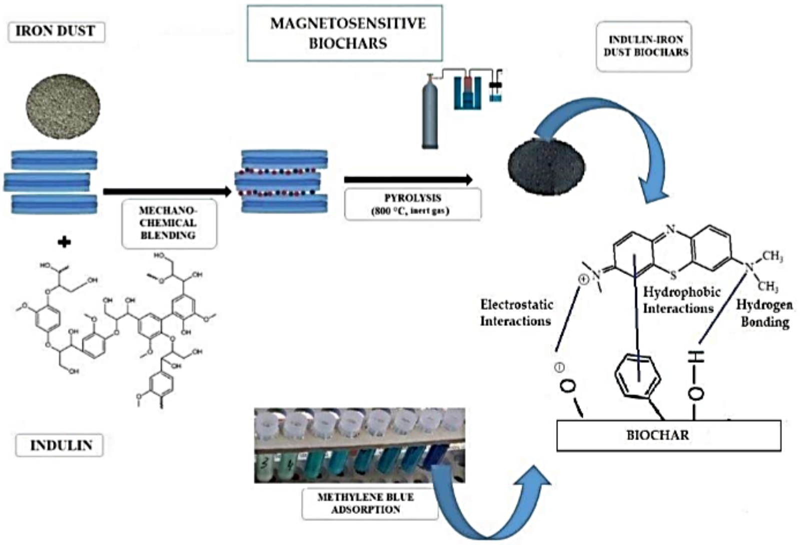

Figure 6. The scheme of biochars synthesis with the possible mechanism of methylene blue adsorption.

4. Conclusions

The present work successfully explored the potential utilization of abundant lignin and industrial magnetic dust as precursors to magneto-sensitive carbon systems. Lignin and industrial magnetic dust blends were successfully converted into magnetic carbon sorbents via catalytic carbonization. The synthesized indulin–iron dust biochars exhibited surface areas of ~300 m^2/g and a high degree of microporosity with a certain mesoporosity contribution and high thermal stability. Compared with the indulin–iron dust biochars, the carbonized inulin was characterized by a surface area of only 7 m^2/g.

The obtained materials showed a maximum adsorption in a range between 4.53 and 9.71 mg/g toward methylene blue, while it was only 0.44 mg/g for pyrolyzed indulin. A strong increase in adsorption uptake was observed for materials that contained iron dust filler. The differentiation of adsorption effectiveness was related to structure and surface characteristics. The best adsorption properties were found for the STInd-1 material with 29% iron filler content and the highest share of mesopores in the pore structure. However, other materials with a lower filler content (9–24%) and a lower contribution of micropores also showed quite good adsorption efficiency.

The utility of magnetosensitive sorbents may be very promising regarding the purification of waters; therefore, reducing the cost of magnetite for its synthesis is an urgent task. Thus, production that uses iron-containing wastes seems to be a very effective method. Overall, this study expands the understanding of the development of lignin-derived magnetosensitive biochar as a renewable substitute for commercial carbons in various industries.

Author Contributions: Conceptualization, M.G. and M.B.; material synthesis, M.G. and M.B.; investigation, M.G., A.B., D.S., M.B. and O.O.; methodology, M.G., A.B., D.S., O.O., M.B., V.G. and A.D.-M.; writing—original draft, M.G., A.B., D.S., O.O. and M.B.; writing—review and editing, A.D.-M. and V.G. All authors have read and agreed to the published version of the manuscript.

Funding: This research received no external funding.

Institutional Review Board Statement: Not applicable.

Informed Consent Statement: Informed consent was obtained from all subjects involved in the study.

Data Availability Statement: The data and samples are available from the authors.

Acknowledgments: This work was implemented within the Scholarship of the International Visegrad Fund (contract number 52211439).

Conflicts of Interest: The authors declare no conflict of interest.

References

1. Budarin, H.L.V.; Clark, J.H. Rapid and Efficient Adsorption of Methylene Blue Dye From Aqueous Solution by Hierarchically Porous, Activated Starbons®: Mechanism and Porosity Dependence. *J. Hazard. Mater.* **2022**, *436*, 129174. [CrossRef]
2. Chen, J.; Tang, C.; Li, X.; Sun, J.; Liu, Y.; Huang, W.; Wang, A.; Lu, Y. Preparation and Modification of Rape Straw Biochar and Its Adsorption Characteristics for Methylene Blue in Water. *Water* **2022**, *14*, 3761. [CrossRef]
3. Imessaoudene, A.; Cheikh, S.; Bollinger, J.C.; Belkhiri, L.; Tiri, A.; Bouzaza, A.; El Jery, A.; Assadi, A.; Amrane, A.; Mouni, L. Zeolite Waste Characterization and Use as Low-Cost, Ecofriendly, and Sustainable Material for Malachite Green and Methylene Blue Dyes Removal: Box–Behnken Design, Kinetics, and Thermodynamics. *Appl. Sci.* **2022**, *12*, 7587. [CrossRef]
4. Zamouchea, M.; Mouni, L.; Ayachia, A.; Merniza, I. Use of commercial activated carbon for the purification of synthetic water polluted by a pharmaceutical product. *Desalination Water Treat.* **2019**, *172*, 86–95. [CrossRef]
5. Zhu, S.; Khan, M.A.; Kameda, T.; Xu, H.; Wang, F.; Xia, M.; Yoshioka, T. New insights into the capture performance and mechanism of hazardous metals Cr3+ and Cd2+ onto an effective layered double hydroxide based material. *J. Hazard. Mater.* **2022**, *426*, 128062. [CrossRef]
6. Bosacka, A.; Zienkiewicz-Strzalka, M.; Wasilewska, M.; Derylo-Marczewska, A.; Podkoscielna, B. Physicochemical and Adsorption Characteristics of Divinylbenzene-co-Triethoxyvinylsilane Microspheres as Materials for the Removal of Organic Compounds. *Molecules* **2021**, *26*, 2396. [CrossRef]
7. Bosacka, A.; Zienkiewicz-Strzalka, M.; Derylo-Marczewska, A.; Chrzanowska, A.; Wasilewska, M.; Sternik, D. Physicochemical, structural, and adsorption properties of chemically and thermally modified activated carbons. *Colloids Surf. A Physicochem. Eng. Asp.* **2022**, *647*, 129130. [CrossRef]
8. Derylo-Marczewska, A.; Sternik, D.; Swiatkowski, A.; Kusmierek, K.; Gac, W.; Buczek, B. Adsorption of phenol from aqueous and cyclohexane solutions on activated carbons with differentiated surface chemistry. *Thermochim. Acta* **2022**, *715*, 179299. [CrossRef]
9. Galaburda, M.; Bosacka, A.; Sternik, D.; Bogatyrov, V.; Oranska., O.; Gun'ko, V.M.; Derylo-Marczewska, A. Development, Synthesis and Characterization of Tannin/Bentonite-Derived Biochar for Water and Wastewater Treatment from Methylene Blue. *Water* **2022**, *14*, 2407. [CrossRef]
10. Norgren, M.; Edlund, H. Lignin: Recent advances and emerging applications. *Curr. Opin. Colloid Interface Sci.* **2014**, *19*, 409–416. [CrossRef]

11. Kakroodi, A.R.; Sain, M. Lignin-Reinforced Rubber Composites. In *Lignin in Polymer Composites*, 1st ed.; Faruk, O., Sain, M., Eds.; William Andrew Elsevier: Amsterdam, The Netherlands, 2016; pp. 195–206. [CrossRef]
12. Mammar, A.C.; Mouni, L.; Bollinger, J.C.; Belkhiri, L.; Bouzaza, A.; Assadi, A.A.; Belkacemi, H. Modeling and optimization of process parameters in elucidating the adsorption mechanism of Gallic acid on activated carbon prepared from date stones. *Sep. Sci. Technol.* **2020**, *55*, 3113–3125. [CrossRef]
13. Bouchelkia, N.; Mouni, L.; Belkhiri, L.; Bouzaza, A.; Bollinger, J.C.; Madani, K.; Dahmoune, F. Removal of lead(II) from water using activated carbon developed from jujube stones, a low-cost sorbent. *Sep. Sci. Technol.* **2016**, *51*, 1645–1653. [CrossRef]
14. Chatterjee, S.; Saito, T. Lignin-Derived Advanced Carbon Materials. *ChemSusChem* **2015**, *8*, 3941–3958. [CrossRef] [PubMed]
15. Kane, S.; Ulrich, R.; Harrington, A.; Stadie, N.P.; Ryan, C. Physical and chemical mechanisms that influence the electrical conductivity of lignin-derived biochar. *Carbon Trends* **2021**, *5*, 100088. [CrossRef]
16. Zhu, L.; Liu, X.; Wu, Y.; Wang, Q.; Wang, H.; Li, D. Fast-pyrolysis lignin-biochar as an excellent precursor for high-performance capacitors. *Renew. Energy* **2022**, *198*, 1318–1327. [CrossRef]
17. Demir, M.; Tessema, T.; Farghaly, A.A.; Nyankson, E.; Saraswat, S.K.; Aksoy, B.; Islamoglu, T.; Collinson, M.M.; El-Kaderi, H.M.; Gupta, R. Lignin-derived heteroatom-doped porous carbons for supercapacitor and CO_2 capture applications. *Int. J. Energy Res.* **2018**, *42*, 2686–2700. [CrossRef]
18. Demir, M.; Kahveci, Z.; Aksoy, B.; Palapati, N.K.R.; Subramanian, A.; Cullinan, H.T.; El-Kaderi, H.M.; Harris, C.T.; Gupta, R.B. Graphitic Biocarbon from Metal-Catalyzed Hydrothermal Carbonization of Lignin. *Ind. Eng. Chem. Res.* **2015**, *54*, 10731–10739. [CrossRef]
19. Yi, Z.; Li, C.; Zhang, L.; Zhang, S.; Gao, W.; Wang, S.; Li, B.; Hu, X. Impacts of CO_2 atmosphere on property of the biochar from pyrolysis of lignin. *J. Anal. Appl. Pyrolysis* **2022**, *167*, 105689. [CrossRef]
20. Dai, Q.; Liu, Q.; Zhang, X.; Cao, L.; Hu, B.; Shao, J.; Ding, F.; Guo, X.; Gao, B. Synergetic effect of co-pyrolysis of sewage sludge and lignin on biochar production and adsorption of methylene blue. *Fuel* **2022**, *324*, 124587. [CrossRef]
21. Wu, F.; Chen, L.; Hu, P.; Zhou, X.; Zhou, H.; Wang, D.; Lu, X.; Mi, B. Comparison of properties, adsorption performance and mechanisms to Cd(II) on lignin-derived biochars under different pyrolysis temperatures by microwave heating. *Environ. Technol. Innov.* **2022**, *25*, 102196. [CrossRef]
22. Liu, D.; Gu, W.; Zhou, L.; Lei, J.; Wang, L.; Zhang, J.; Liu, Y. From biochar to functions: Lignin induced formation of Fe3C in carbon/Fe composites for efficient adsorption of tetracycline from wastewater. *Sep. Purif. Technol.* **2023**, *304*, 122217. [CrossRef]
23. Liu, X.J.; Li, M.F.; Singh, S.K. Manganese-modified lignin biochar as adsorbent for removal of methylene blue. *J. Mater. Res. Technol.* **2021**, *12*, 1434–1445. [CrossRef]
24. Li, Y.; Wang, F.; Miao, Y.; Mai, Y.; Li, H.; Chen, X.; Chen, J. A lignin-biochar with high oxygen-containing groups for adsorbing lead ion prepared by simultaneous oxidization and carbonization. *Bioresour. Technol.* **2020**, *307*, 123165. [CrossRef]
25. Sun, Y.; Wang, T.; Sun, X.; Bai, L.; Han, C.; Zhang, P. The potential of biochar and lignin-based adsorbents for wastewater treatment: Comparison, mechanism, and application—A review. *Ind. Crops Prod.* **2021**, *166*, 113473. [CrossRef]
26. World Steel Association AISBL. Available online: https://worldsteel.org/steel-topics/statistics/world-steel-in-figures-2022 (accessed on 10 November 2022).
27. World Steel Association AISBL. Available online: https://worldsteel.org/publications/policy-papers/co-product-position-paper/2022 (accessed on 10 November 2022).
28. Nayak, N.P. Characterization of blast furnace flue dust- an assessment for its utilization. *Mater. Today. Proc.* **2022**, *50*, 2078–2083. [CrossRef]
29. Lepa, V.V.; Prognimak, O.D. Blast Furnace Slag Disposal Problems in the Context of the Transition to a Circular Economy. *Econ. Her. Donbass* **2021**, *1*, 129–145. [CrossRef]
30. Özbay, E.; Erdemir, M.; Durmu, H. Utilization and efficiency of ground granulated blast furnace slag on concrete properties—A review. *Constr. Build. Mater.* **2016**, *105*, 423–434. [CrossRef]
31. Das, B.; Prakash, S.; Reddy, P.S.R.; Biswal, S.K.; Mohapatra, B.K.; Misra, V.N. Effective utilization of blast furnace flue dust of integrated steel plants. *Eur. J. Miner. Process. Environ. Prot.* **2002**, *2*, 61–68.
32. Li, Y.; Liu, Y.; Gong, X.; Nie, Z.; Cui, S.; Wang, Z.; Chen, W. Environmental impact analysis of blast furnace slag applied to ordinary Portland cement production. *J. Clean. Prod.* **2016**, *120*, 221–230. [CrossRef]
33. Drachuk, Y.; Stalinskaya, E.; Snitko, E.; Zavgorodnyaya, E.; Jaworska, M.; Savyuk, L.; Cheylyakh, D. Slag waste of metallurgical production. Environmental and economic justification of their use in industry in Ukraine. *Polityka Energetyczna Energy Policy J.* **2021**, *24*, 169–182. [CrossRef]
34. Galaburda, M.; Kovalska, E.; Hogan, B.T.; Baldycheva, A.; Nikolenko, A.; Dovbeshko, G.I.; Oranska, O.I.; Bogatyrov, V.M. Mechanochemical synthesis of carbon-stabilized Cu/C, Co/C and Ni/C nanocomposites with prolonged resistance to oxidation. *Sci. Rep.* **2019**, *9*, 17435. [CrossRef] [PubMed]
35. Galaburda, V.; Bogatyrov, V.M.; Skubiszewska-ZiĿba, J.; Oranska, O.I.; Sternik, D.; Gun'ko, V.M. Synthesis and structural features of resorcinol formaldehyde resin chars containing nickel nanoparticles. *Appl. Surf. Sci.* **2016**, *360*, 722–730. [CrossRef]
36. Galaburda, M.; Bogatyrov, V.; Sternik, D.; Oranska, O.; Borysenko, M.; Škorvánek, I.; Skwarek, E.; Deryło-Marczewska, A.; Gun'ko, V. Magneto-sensitive carbon-inorganic composites based on particleboard and plywood wastes. *Chem. J. Mold.* **2021**, *16*, 68–78. [CrossRef]

[D5] Alicja Bosacka, Małgorzata Zienkiewicz-Strzałka, Anna Derylo-Marczewska, Małgorzata Śliwińska-Bartkowiak, Angelina Sterczyńska, Dariusz Sternik, Konrad Rotnicki *The influence of chemical and thermal modifications of ordered mesoporous carbon on the melting processes of water confined in pores*, Microporous and Mesoporous Materials, 2023, 351, 112477, https://doi.org/10.1016/j.micromeso.2023.112477 wraz z materiałem dodatkowym [S5]

Microporous and Mesoporous Materials 351 (2023) 112477

Contents lists available at ScienceDirect

Microporous and Mesoporous Materials

journal homepage: www.elsevier.com/locate/micromeso

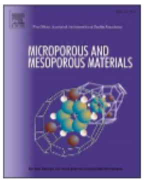

The influence of chemical and thermal modifications of ordered mesoporous carbon on the melting processes of water confined in pores

A. Bosacka [a,b,*], M. Zienkiewicz-Strzalka [b], A. Derylo-Marczewska [b], M. Sliwinska-Bartkowiak [c], A. Sterczynska [c], D. Sternik [b], K. Rotnicki [c]

[a] *Faculty of Production Engineering, University of Life Sciences, Gleboka Street 28, 60-612, Lublin, Poland*
[b] *Faculty of Chemistry, Institute of Chemical Sciences, Maria Curie-Sklodowska University, Maria Curie-Sklodowska Sq. 3, 20-031, Lublin, Poland*
[c] *Faculty of Physics, Adam Mickiewicz University, Uniwersytetu Poznanskiego Street 8, 61-614, Poznan, Poland*

ARTICLE INFO

Keywords:
Ordered mesoporous carbon
Surface functionalization
Chemical and thermal treatment
Water melting inside the pores

ABSTRACT

In this work, the mesoporous carbon (MC) of the ordered structure was synthesized using silica (SBA-15) as a template and glucose as a carbon precursor. The received MC was subjected to wet oxidation in nitric acid and thermal treatment at 150, 400, 600 and 800 °C to differ its hydrophobic/hydrophilic character. The obtained unmodified (MC), oxidized (MC-OX) and thermally modified oxidized carbon (MC-OX-150, MC-OX-400, MC-OX-600 and MC-OX-800) were investigated by various techniques: transmission electron microscopy (TEM), scanning electron microscopy (SEM), and low-temperature nitrogen adsorption to characterize material porosity, X-ray photoelectron spectroscopy (XPS) and suspension potentiometric titration (SPT) to provide the statement of quality and quantity of groups presented onto the surface and the surface charge, and dielectric spectroscopy (DS) and differential scanning calorimetry (DSC) to register the changes in the water melting processes in carbon pores. The DS and DSC studies revealed the correlation between the water melting temperature inside the pores of MCs and their chemical characteristics, which were determined mainly by surface functional groups and only slightly by textural properties.

1. Introduction

Porous media are intensively studied because of their unique physical, chemical, electrical, mechanical, catalytic or adsorption properties [1–4]. Generally, materials with good adsorption characteristics are described by well-developed specific surface areas, high total pore volumes and appropriate surface properties for specific applications [5]. Pores are defined as various types of concavities in the material: holes, interstices, fissures or channels are empty spaces with a depth greater than the width. These spaces can be filled by liquids or gases [6,7]. Adsorption is a process of bonding molecules, atoms or ions on a surface or interface of physical phases causing local changes in a concentration [8]. As effective adsorbents, zeolites [9], activated carbons [10], silica gels [11], and ordered mesoporous materials [12] are widely used. This work is focused on chemically and thermally treated mesoporous carbons (MCs) with the presence of both meso- and micropores, which were obtained based on a silica hard template (SBA-15) and glucose as a carbon precursor.

The first ordered mesoporous carbon (CMK-1) was obtained by Ryoo et al., in 1999 using MCM-41 with Ia3d symmetry as a hard template and sucrose as a carbon precursor [12]. In 2000, ordered mesoporous carbon (CMK-3) was also studied by Ryoo et al. using SBA-15 with P6 mm symmetry and sucrose as the carbon precursor [13]. The MCM-41 material has a hexagonal arrangement of cylindrical pores, which are characterized by a relatively large diameter and narrow distribution because of the use of a cationic surfactant as a pore directing agent. In the SBA-15 silica, the surfactant was replaced by a block copolymer. In this way, the material with thicker walls and larger pore diameters than MCM-41 was received, with a certain amount of micropores, and was more thermally and mechanically stable. Because of that, SBA-15 is a great material itself and is also an excellent scaffolding for obtaining ordered mesoporous carbon. In addition, the presence of micropores in SBA-15 and the materials based on it (CMK-3) strongly influence an increase in the sorption properties of the adsorbent in comparison to the materials containing only mesopores [14–18].

Even though it has been a long time since the synthesis of the first

---

[*] Corresponding author. Faculty of Production Engineering, University of Life Sciences, Gleboka Street 28, 60-612, Lublin, Poland.
E-mail address: alicja.bosacka@up.lublin.pl (A. Bosacka).

https://doi.org/10.1016/j.micromeso.2023.112477
Received 19 October 2022; Received in revised form 19 January 2023; Accepted 2 February 2023

ordered mesoporous carbons, due to their unique properties, these materials have a wide range of potential applications [19]. As already mentioned, ordered mesoporous carbon systems are characterized by a uniform porous structure, chemical inertness, good electrical conductivity, low toxicity, high mechanical and thermal stability and relatively inexpensive synthesis. These materials are also characterized by high surface areas and large pore volumes; therefore, they are commonly used as adsorbents [20,21], sensors [22], energy stores [23], nanomaterials [24], and catalysts [25]. However, ordered mesoporous materials with improved characteristics are still being developed. The neutral chemical character of the carbon surface is caused by a small number of functional groups. For this reason, the functionalization process, in many cases, is desired to improve the adsorption or other properties of these materials [26]. One of the most powerful methods of surface functionalization is an oxidation process, in which hydroxyl, carboxyl, carbonyl, ether groups, quinones, and other functional groups can be provided [27,28]. Frequently used oxidizers are nitric, phosphoric, sulfuric acids [28] and magnate potassium [19]. The presence of various functional groups impacts the character of the carbon surface (hydrophobic or hydrophilic) and the nature of the interaction between the adsorbent and adsorbate [29–31].

From year to year, the growing interest of researchers in the study of fluid and solid transitions in porous systems has been noticeable [32]. Phases confined in the narrow pores repeatedly exposed a physical and chemical behaviour that significantly varied from that of the bulk phase. This effect emerges from the decreased dimensionality and strong interactions of the adsorbate molecules in the nanophase with the confining walls [33]. This phenomenon differs due to the size effect, wall forces, and liquid–liquid and liquid-wall interactions [34]. The scientist's melting and freezing considerations involve the nature of the phase transitions, the direction of shifts in the melting temperature (T_m), or the morphological transitions of the condensed phases in the restricted pore geometries. A better understanding of confinement effects on melting and freezing processes is crucial in many fields connected to adhesion, adsorption, lubrications, and nanotechnology [35]. It was suggested that for pore widths significantly larger than the diameter of the adsorbate molecules, the shift in the melting points $\Delta T = T_{m,p} - T_{m,b}$ is associated with the pore width H in the Gibbs-Thomson equation: $\frac{T_{m,b}-T_{m,p}}{T_{m,b}} = 2\frac{(\gamma_{ws}-\gamma_{wf})\nu}{H\gamma_{m,b}}$, where $T_{m,b}$ and $T_{m,p}$ are the melting temperatures of the bulk of the confined sample, γ_{ws} and γ_{wf} are the wall-solid and wall-fluid surface tensions, ν is the molar volume of the liquid phase, and $\lambda_{m,b}$ is the bulk latent heat of melting [36]. Many experiments conducted for pores above 6 nm exhibited a linear dependence between the shift in the melting temperature and the 1/H pore width. However, for lower pore diameters, deviations from the Gibbs-Thomson equation were registered [37].

The surface character also influences the melting and freezing processes occurring inside the pores. An increase in the number of oxygen groups leads to a reduction in the hydrophobicity of carbon, which determines the interaction of molecules with a hydrophobic surface, whereas the decreased number of oxygen groups enhances the hydrophobic character of the samples [38,39]. Consequently, some modification processes, such as oxidation and further thermal treatment, are expected to cause shifts in the melting and freezing temperatures of carbon materials. The distinctions in the number of oxygen groups on the carbon surfaces cause a transition in the interactions of the adsorbate molecules with the nanopore walls of the materials.

In this paper, MC was synthesized, chemically modified by nitric acid oxidation and subjected to thermal modifications. The main aim of this work was to investigate the influence of the concentration of the oxygen functional groups located on the carbon surface and silica residues on the melting processes occurring inside the pores. For this purpose, two complementary techniques were used: dielectric spectroscopy (DS) and differential scanning calorimetry (DSC). Moreover, microscopic analysis, low-temperature nitrogen sorption, suspension potentiometric titration (SPT), and X-ray photoelectron spectroscopy (XPS) techniques were applied to provide structural data, evaluate the effectiveness of chemical and thermal modifications and support knowledge about the type of functional groups occurring on the surfaces of the materials.

2. Experimental

2.1. Chemicals

Pluronic P123, triblock copolymer (poly(ethylene oxide)-poly (propylene oxide)-poly(ethylene oxide), $EO_{20}PO_{70}EO_{20}$, $M_w = 5800$) and tetraethyl orthosilicate ($Si(OC_2H_5)_4$, TEOS, 98%) were purchased from Merck (Darmstadt, Germany), hydrochloric acid (HCl, 35–38%) and sulfuric acid (H_2SO_4, 95%) were purchased from Chempur (Piekary Slaskie, Poland), potassium hydroxide (KOH, powder), sodium hydroxide (NaOH, powder), sodium chloride (NaCl, powder), ethyl alcohol (C_2H_5OH, 96%) and nitric acid (HNO_3, 65%) were acquired from Avantor Performance Materials Poland S.A. (Gliwice, Poland), and glucose ($C_6H_{12}O_6$, D-glucose, powder) was purchased from Microfarm (Zabierzow, Poland). Solutions were prepared by the usage of deionized water.

2.2. Materials synthesis

2.2.1. Preparation of SBA-15

SBA-15 was prepared based on the procedure proposed by Zhao et al. [40,41]. To synthesize the SBA-15 template, 12 g of copolymer Pluronic P123 was dissolved in a mixture of 360 mL of HCl (2 mol/L) and 90 mL of deionized water with stirring at 35 °C. Furthermore, 27.4 mL of TEOS was dropped, and the mixture was preserved at a temperature of 35 °C for 24 h under stirring. The solution with precipitate was transferred to an autoclave and heated at 85 °C for 48 h. After that, the precipitate was filtered, washed with deionized water, dried under vacuum and calcined at 550 °C for 4 h in a muffle furnace under air conditions.

2.2.2. Preparation of MC

The impregnation was carried out in two stages using glucose as a precursor and sulfuric acid as a catalyst. In the first step, 50 mL of water, 12.5 g of glucose and 0.8 mL of sulfuric acid were added to 10 g of SBA-15. The mixture of SBA-15 material with glucose and sulfuric acid in a 500 mL flask was inserted into the vacuum dryer and heated at 100 °C for 6 h. In the second step, 50 mL of water, 7.5 g of glucose and 0.4 mL of sulfuric acid were added to the 500 mL flask with the partially carbonized carbon precursor. The mixture was again placed in a vacuum dryer and heated at 160 °C for 13 h. The silica-organic composite was moved to a mortar to homogenize the material, placed in a tube flow furnace and heated at 700 °C for 6 h with a 2.5 °C/min heating rate under a nitrogen atmosphere to protect the material against combustion. To remove the silica matrix from the carbonized material, an etching solution was used. For this purpose, the carbonizate was placed in a 250 mL round-bottom flask and filled with a mixture of 50 mL of 95% ethyl alcohol and 50 mL of deionized water with 6.6 g of potassium hydroxide. Using the system supported by a reflux condenser and magnetic stirrer, the carbonized material was activated by heating at 100 °C for 1 h. After etching, the material was moved to the Büchner funnel, washed with at least 4 L of deionized water and dried.

2.2.3. Surface oxidation and thermal treatment

Mesoporous carbon material was oxidized with 65% nitric acid at 80 °C for 3 h in a system equipped with a reflux condenser and mixed by a magnetic stirrer according to the procedure proposed by Swiatkowski et al. [42]. After oxidizing, the material was moved to the Büchner funnel, washed with a minimum of 4 L of deionized water and dried. Finally, the oxidized material was subjected to thermal modifications. For this target, the sample was divided into portions. Each of the portions of the oxidized sample was introduced into the tube flow furnace and heated at 150, 400, 600 and 800 °C for 3 h with a 5 °C/min heating rate under a nitrogen atmosphere.

2.3. *Measurements and calculations*

2.3.1. *Nitrogen sorption and electron microscopy*

The porosity properties of the initial and thermally modified carbon materials low-temperature nitrogen adsorption-desorption isotherms at 77 K over the whole range of relative pressures obtained by using a sorption analyser (ASAP 2020, Micromeritics, Norcross, USA). The specific surface area (S_{BET}) was assessed from experimental isotherms according to the standard BET method [43]. The pore-size distribution curves were obtained from the adsorption or desorption branch of the isotherm using the Barrett−Joyner−Halenda (BJH) [44] model with cylindrical pores and Faas correction without smooth differentials and nonlocal density functional theory (NLDFT) [45]. The total pore volume (V_t) was obtained from the amount of nitrogen adsorbed at $p/p_o = 0.99$. The pore volume of micropores (V_{mic}) was estimated from the *t*-plot method [46]. Before the analysis, all samples were outgassed at 90 °C and a pressure of 1 mmHg for 24 h in a degas port of the analyser.

The textural properties of the initial carbon were analysed by two microscopic techniques: a high-resolution transmission electron microscope (HR-TEM) Titan G2 60–300 (FEI Company, Hillsboro, Oregon, USA) with an accelerating voltage of 200 kV and a scanning electron microscope (SEM) Quanta™ 3D FEG (FEI Company, Hillsboro, Oregon, USA) with a 5 kV speed-up voltage.

2.3.2. *SAXS investigations*

The SAXS analysis was carried out by Empyrean diffractometer (PANalytical) with CuKα radiation source as SAXS/WAXS capillary mode configuration. The SAXS configuration includes a 2θ range of 0.1–2° of 2θ. The corresponding range of q values was 0.0095–0.15 Å^{-1}. The length of the scattering vector q is defined as $q = 4\pi \sin\theta/\lambda$, where 2θ is the scattering angle, λ is the X-ray wavelength (1.5418 Å). The device was powered by a 4 kW high-voltage X-ray generator and generator settings of 40 kV and 40 mA. The incident beam path consisted of a line focus type, W/Si, graded X-ray mirror with an elliptic shape. The primary beam was measured using a beam attenuator Cu 0.2 mm. The measurements were taken using a PIXcel1D detector and receiving slit with 0.05 mm active length. Background scattering was performed by air scattering measure with an empty sample holder. The EasySAXS software was applied for SAXS calculations. Dv(*R*) calculations were performed using the indirect Fourier transformation technique with algorithm based on Tikhonov's regularization method.

2.3.3. *X-ray photoelectron spectroscopy (XPS) and potentiometric titration of suspension (SPT)*

The surface composition and interaction between elements in the initial, oxidized and thermally treated carbons were characterized by X-ray photoelectron spectroscopy (XPS) applying a multichamber ultrahigh vacuum (UHV) system (Prevac 2009, Rogow, Poland) with a hemispherical analyser (VG Scienta R4000). The average depth of analysis was approximately 5 nm. The data processing and high-resolution deconvolution of the (C1s) and (O1s) peaks were performed by CasaXPS software (Casa Software Ltd., License for Maria-Sklodowska University, Lublin, Poland.).

The surface charge properties were determined by potentiometric titration of the suspension. The potentiometric titration experiment was conducted with a 765 Dosimat Autoburette (Metrohm, Herisau, Switzerland) combined with a PHM240 pH-meter (Radiometer, Copenhagen, Denmark). Additionally, a constant temperature of 25 °C was provided by the thermostat (Ecoline RE207, Lauda, Germany). As an electrolyte, 30 mL of 0.1 mol/L NaCl was used and placed in a thermostatic quartz vessel. The initial pH was achieved by the addition of 0.3 mL of 0.5 mol/L HCl. After 2 h the temperature and initial pH were stabilized, and 0.05 g of solid sample was added (previously dried for 3 h at 60 °C). Then, the suspension was titrated gradually with 0.2 mol/L NaOH, and pH changes were registered by the custom computer program (Titr_v3 written by Marczewski and Janusz, Faculty of Chemistry, Maria Curie-Sklodowska University, Lublin, Poland). The measurements were supported by protecting the gas atmosphere (nitrogen) to defeat the problem of carbon dioxide contamination. The titration curves were transformed into surface charge density curves based on the relation $Q_s = \frac{F\Delta n}{S_{BET}}$, in which Q_s is the surface charge density, Δn is the change in H^+/OH^- balance per mass of the solid and *F* is the Faraday number [16].

2.3.4. *Differential scanning calorimetry (DSC) and dielectric spectroscopy (DS)*

Differential scanning calorimetry (DSC) and dielectric spectroscopy (DS) were applied to melting studies of the water confined in pore systems of MCs. The DS measurements were conducted using a parallel plate capacitor built of stainless steel equipped with a Solartron 1260 impedance analyser (England, UK) to measure the capacitance (C) as a function of the temperature (T) and the frequency (ω) of the subsequent cyclic electric field in the frequency range from 1 to 10^6 Hz at different temperatures (from 140 K to 304 K) and a temperature rate of 0.8 K/min and 0.6 K/min during the cooling and heating processes, respectively. The samples were placed between the capacitor plates as a suspension of carbon with water; therefore, permittivity measurements originate from the bulk as well as confined water. Complex electric permittivity is defined as $\varepsilon^* = \varepsilon' + i\varepsilon''$. The melting temperature T_m was determined as a change in the value of electric permittivity ε' (or electric capacity C) of the melting point $\varepsilon' = \frac{C}{C_o}$, in which C_o is the capacitance of the empty capacitor. ε'' is an imaginary part of the permittivity and is expressed by the dependence $\varepsilon'' = tg\delta \bullet \varepsilon'$, where $tg\ \delta$ are the dielectric losses. The dielectric relaxation time was evaluated by fitting the Debye model of orientational relaxation to the dispersion spectrum of the complex permittivity near resonance: $\varepsilon^D = \varepsilon'_\infty + \frac{\varepsilon'_s + \varepsilon'}{1 + if\tau}$, where *f* is the frequency of the potential, τ is the orientational relaxation time of a dipolar molecule, and the *s* and ∞ indices correspond to the static (low frequency) and optical (induced) permittivity. DSC measurements were carried out with a TG/DTA/DSC apparatus (STA 449 Jupiter F1, Netzsch, Selb, Germany). For this purpose, 20 mg of filtrated suspension was placed in an aluminium crucible covered with an aluminium lid and encapsulated. The empty one was used as a reference. The measurements were led in the presence of synthetic air with a flow rate of 50 mL/min in the temperature range from −100 to +60 °C and a heating rate of 5 °C/min. Before measurements, the samples were dried for 12 h at 60 °C.

3. Results and discussion

3.1. *Porosity characteristics*

Two electron microscopy techniques, SEM and TEM, were applied to assess the quality of the textural properties of the initial carbon (MC). The SEM micrographs at different magnifications show the irregular structure of grains of the ordered mesoporous carbon (Fig. 1A and B). The TEM images (Fig. 1C and D) show the well-developed ordered structure of the ordered mesoporous carbon with uniform pore sizes of ~ 4 nm. Hexagonal-ordered arrays of circles arranged in the parallel direction to the pore channels are observed. Moreover, in Fig. 1C, pairs of light and dark lines arranged in parallel are apparent. The light-dark lines correspond to the two-dimensional hexagonal ordered array of carbon tubes. The well-ordered structure of the MC is the inverted replica of SBA-15, which is the template used to synthesize the MC. Generally, microscopic studies confirm the effective method of preparing carbons with ordered and well-expanded surface structures [47].

The experimental nitrogen adsorption-desorption isotherms, the Barett, Joyner and Halenda (BJH), and pore size distributions calculated using nonlocal density functional theory (NLDFT) for the mesoporous

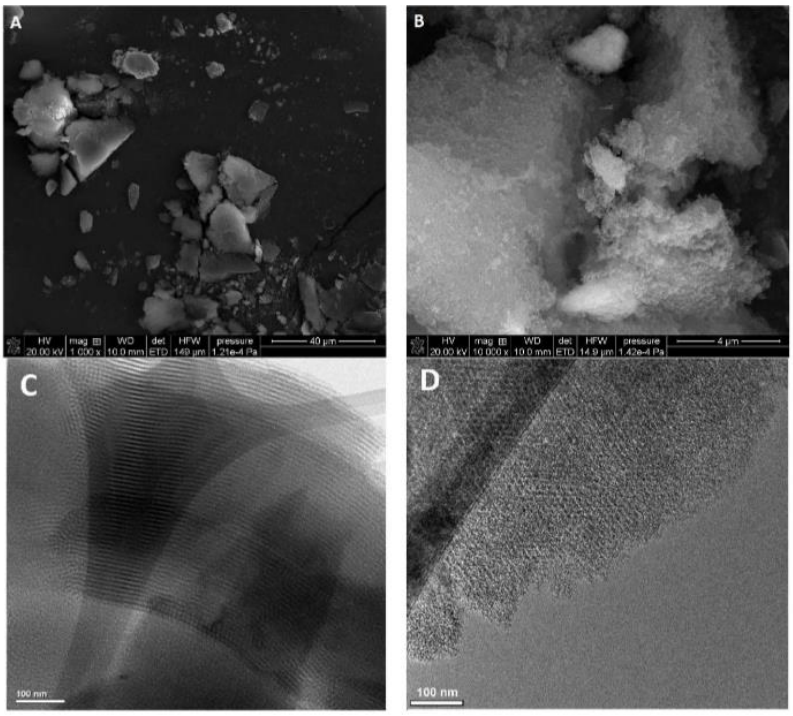

Fig. 1. SEM (A, B) and TEM (C, D) images of the initial mesoporous carbon of ordered structure (MC) at different magnifications.

carbon (MC), oxidized mesoporous carbon (MC-OX) and oxidized thermally treated mesoporous carbons at 150, 400, 600 and 800 °C (MC-OX-150, MC-OX-400, MC-OX-600 and MC-OX-800) are presented in Fig. 2.

The experimental low-temperature isotherms of N_2 adsorption/desorption are typical for mesoporous materials of type IV according to the IUPAC classification. The characteristic hysteresis loop visible for the initial mesoporous carbon (MC) was not preserved for the modified samples. This suggests that the shapes of the isotherms and their porous structure after chemical and thermal modifications are transformed, especially in the range of the capillary condensation. It proves a decrease or loss of pore ordering (hexagonal arrays of tubes) during the oxidation process in HNO_3 and thermal treatment.

The SAXS analysis of pore structure for MC, MC-OX, MC-OX-150, and MC-OX-800 is shown in Fig. 3. The structural ordering according to hexagonal symmetry *P*6mm characteristic for the SBA-15 replica was confirmed by three well-resolved reflections registered at small diffraction angles and indexed as (100), (110), and (200) for the MC and MC-OX samples (Fig. 3A). The disappearance of these signals on the SAXS curves for the chemically and thermally treated materials (MC-OX-150, MC-OX-800) confirm a change of their structure from well-ordered to partly disordered. Fig. 3B shows the volume-weighted particle size distribution Dv(R) from the scattering curve of an ensemble of scattering objects. For the discussed scattering objects (pores) the function is smooth with a lack of minor oscillations (for MC and MC-OX samples, Fig. 3C and D), thus revealing the presence of well-defined symmetric pores with dimensions of approximately 5 nm (maximum of the Dv(R) function). For the oxidized and heat-treated samples (MC-OX-150 and MC-OX-800), the calculated Dv(R) curves indicate the disappearance of the previously observed pore structure (Fig. 3E and F). In addition, for these samples, the enhancement of this function for the micropore area can be indicated. Interestingly, this is consistent with the adsorption data, including the experimentally determined micropore volume. Due to the fact that the SAXS method is sensitive to structural changes and not to surface physicochemistry, the obtained data confirm that in the first stage of modification of carbon samples with nitric acid the number of surface functional groups change within the pores, which translates into the porosity characteristics of the material observed as decrease of specific surface area and pore volume. The ordering of pore structure itself is degraded at the stage of thermal treatment.

The values of the structural parameters of the studied carbons calculated from nitrogen sorption isotherms are presented in Table 1. The unmodified carbon has a quite high specific surface area of nearly 400 m^2/g and a total pore volume equal to 0.40 cm^3/g. The nitric acid surface oxidation of MC causes a significant reduction in the value of the specific surface area and total pore volume (both values are approximately halved); however, changes after thermal treatments are not as significant. The obtained materials also have a certain amount of micropores (V_{mic} from 0.04 to 0.08 cm^3/g). The adsorption-desorption BJH pore size distributions for MC are presented in Fig. 2B. The adsorption and desorption BJH pore size distributions for modified samples are shown in Fig. 2C and D. The pore size distributions of pores below 2 nm calculated by NLDFT theory are presented in Fig. 2E.

The strong reduction of the surface area and pore volumes after treatment in nitric acid may be mainly associated with blocking the entrance of pores by surface groups, and only to a small extent with porosity changes as observed on the SAXS curves which confirm the structure ordering after oxidation. The increase in surface areas and pore volumes after thermal treatment at high temperatures is caused by structure changes, the collapse of some pore walls, and by the removal of surface groups. It should be noted that the oxygen surface groups can partly block the entrances of pores restricting the available space of materials. The thermal treatment results in opening internal space because of the removal of oxygen surface groups, however, it may enhance the material porous structure disordering as observed by SAXS. Generally, the modification in nitric acid and further thermal treatment may cause partial destruction of some pore walls deforming the regular

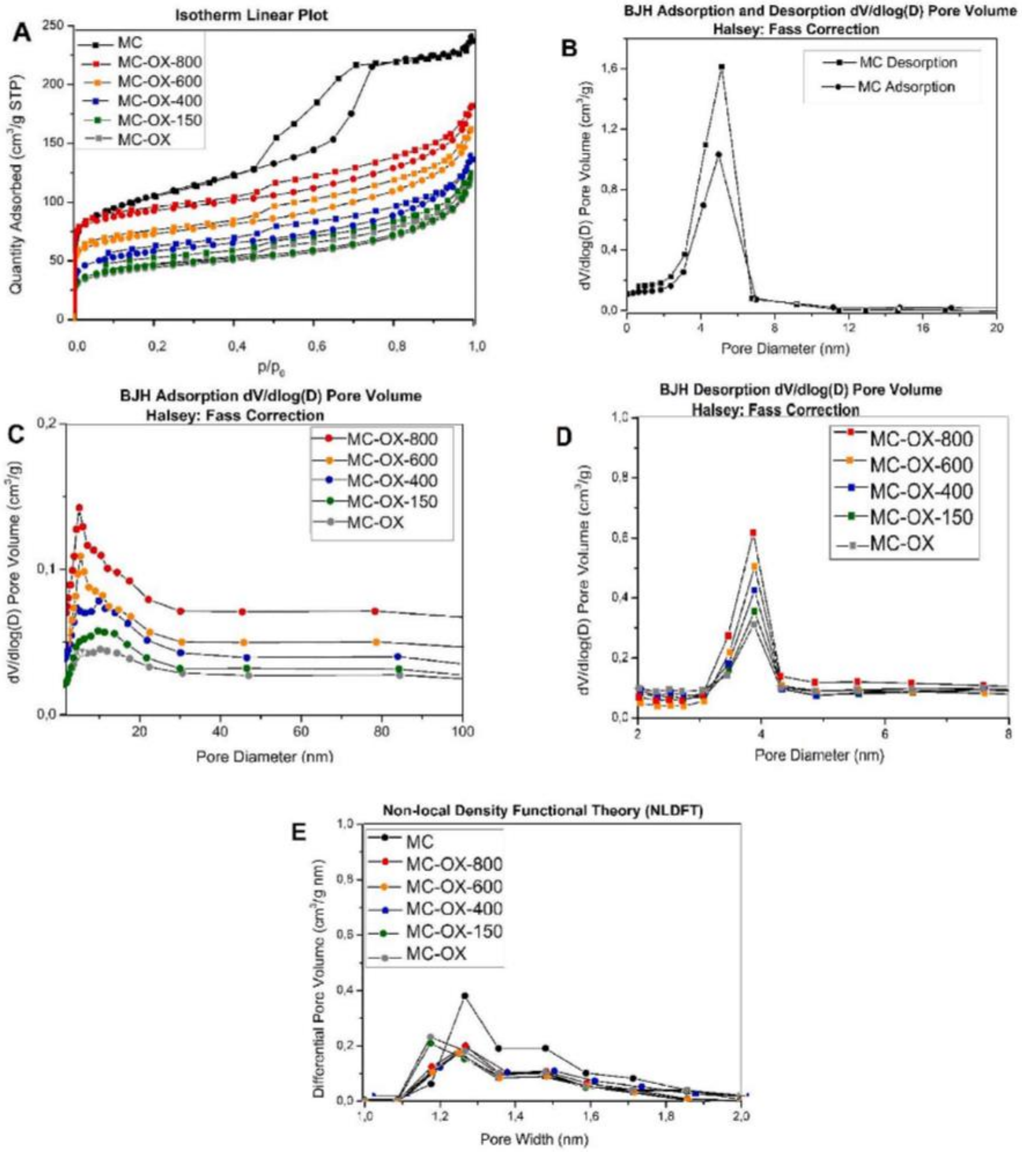

Fig. 2. Nitrogen adsorption-desorption isotherms at 77 K (A), BJH (B, C, D), and NLDFT pore size distributions (<2 nm) (E) for MC, MC-OX, MC-OX-150, MC-OX-400, MC-OX-600 and MC-OX-800.

carbon structure [39,42,48]. The detailed information about the type and character of functional groups of materials is given further based on the XPS data.

3.2. Functional group determination

The surface composition analysis of the chemical binding state of MC, MC-OX and MC-OX-800 was carried out by X-ray photoelectron spectroscopy (XPS). To identify and quantify elements and types of functional groups on the carbon surface, XPS spectra are taken into consideration. The survey spectra of (C 1s), (O 1s) and (Si 2p) of the MC, MC-OX and MC-OX-800 samples are presented in Figs. S1A–C, S1D-F and S1G-I (Supplementary Material), respectively. The quantitative results of the overview analysis of MC, MC-OX and MC-OX-800 are presented in Table S1 (Supplementary Material).

The overview spectra peak positions from (C 1s), (O 1s) and (Si 2p) are at binding energies of ~285, 533 and 103 eV, respectively. Based on the analysis of survey spectra (Figs. S1A, D, G) and calculations (percentage atomic and mass concentrations presented in Table S1), it is found that during oxidation, the share of carbon (C 1s) and silicon (Si 2p) atoms decreases. On the other hand, the number of oxygen atoms (O 1s) increases. After the thermal treatment, the oxygen content decreased. Even the sample heated at 800 °C is not completely depleted of oxygen groups. Moreover, for all studied carbons, the silica content is registered (Si 2p), which is an SBA-15 template residue (Supplementary Material) [49–57]. SBA-15 material usually contains the following silicon-oxygen groups: mainly siloxanes, but also vicinal, germinal, and free silanols. Siloxanes rather fill the interior of the material, while

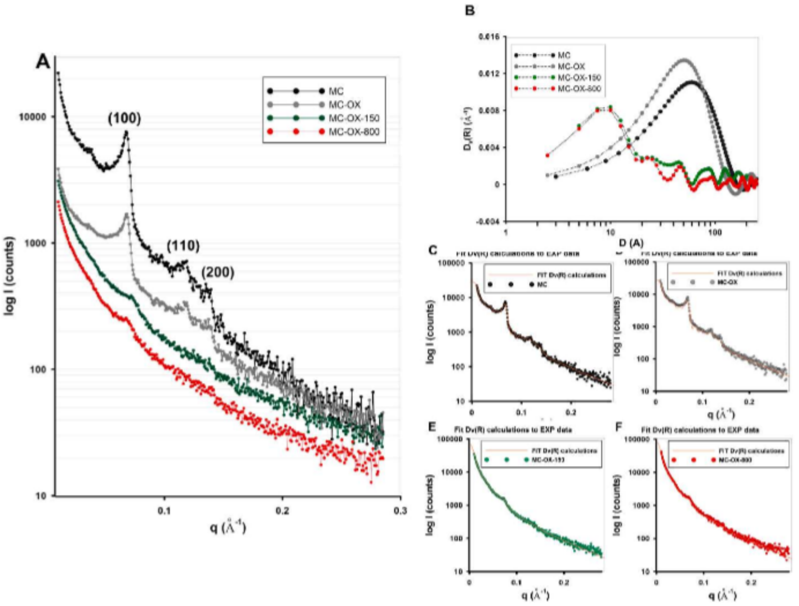

Fig. 3. SAXS profiles for MC, MC-OX, MC-OX-150 and MC-OX-800 (A). The SAXS curves are shifted on the Y-axis for better data presentation. Analysis of particle size distribution by volume for investigated samples (B) and corresponding fit curves of Dv(R) calculations (solid lines) toward experimental data (points) (C–F).

Table 1
The values of structural parameters of the studied MCs.

Sample name	S_{BET}[a] [m^2/g]	V_t[b] [cm^3/g]	V_{mic}[c] [cm^3/g]
MC	375	0.40	0.06
MC-OX	174	0.19	0.04
MC-OX-150	178	0.20	0.04
MC-OX-400	214	0.24	0.04
MC-OX-600	317	0.27	0.08
MC-OX-800	325	0.32	0.08

[a] S_{BET}, BET specific surface area.
[b] V_t, total pore volume.
[c] V_{mic}, micropore volume.

silanols are present on the surface and may react with different chemical species. The formation of silicon-oxygen groups on the surface takes place during the calcination process at a high temperature (~550 °C), in which the ordered mesoporous structure of the SBA-15 is developed. Thus, the silica residues in the obtained carbons contribute to the total number of surface oxygen groups. Based on the obtained results it should be marked that the general contribution of Si decreases after modification in nitric acid and backward increases after heating as a result of strong changes in a number of oxygen groups introduced or removed during oxidation and thermal treatments. This effect is related to the removal of oxygen groups as well as the destruction of carbon at high temperatures (drop in O 1s and C1s). Meanwhile, silica residue forms a hard-to-destroy structure even at very high temperatures that may partially affect the MC's physicochemical properties and translate into the melting processes of water in the pores.

The detailed analysis of XPS spectra (presented in the Supplementary Material) reveals the type of present groups on the surface and therefore the sample character [58–61]. A summary of the data from the particular XPS analysis is given in Table 2. In general, XPS analysis confirms the efficiency of the chemical and thermal modification.

3.3. Surface acidity

The acid-base features of carbon samples were analysed by potentiometric titration. The surface charge density dependence on pH exposed the differences in the electrochemical nature of the studied carbon samples. In general, the pH of the point of zero charge (pH_{PZC}) supports information about the amount of acidic-basic sites on the sample surface and is established by crossing out the electrolyte titration curve and registered curve of the studied material and the intersection of the surface charge density curve with the abscissa axis equal to zero. The pH_{PZC} point separates the positively and negatively charged side. If the pH of the suspension of solids is above the pH_{PZC} point, then its surface is negatively charged and can adsorb cations and take part in their exchange reaction. On the other hand, when the pH is lower than the pH_{PZC} point, then the surface is positively charged and has an anion exchange capacity. The relation of charge density as a function of pH is shown in Fig. 4. The results imply that the initial ordered mesoporous carbon has inert properties concerning the presence of oxygen functional groups on the surface ($pH_{PZC} = 7.0$). The inert character of the carbon surface could be caused by the thermal treatment of the sample during the synthesis, which removed most of the oxygen functional groups mainly originating from silica. The acidity of the sample is strictly connected to the presence of oxygen groups on the sample surface [39,42]. A decrease in the pH_{PZC} value of the carbon sample after nitric acid oxidation ($pH_{PZC} = 4.4$) was combined with an increase in the number of acidic sites on the sample surface. Furthermore, surface thermal treatments at 150, 400, 600 and 800 °C caused changes in the pH_{PZC} values (from 4.8 to 6.6) due to the removal of oxygen functional groups from the surface of the samples. Along with the higher heating temperature of the studied carbons, their character changes from acidic to close to neutral. The highest differences in acid-base character of the obtained samples is observed between the oxidized MC-OX, and the initial and MC-OX-800 materials. The remaining samples heated at lower temperatures are characterized by differentiated pH_{PZC} values increasing with modification temperature growth. The potentiometric titration results are in good agreement with the data from XPS. However, the XPS technique provides more detailed knowledge about the

Table 2
Detailed XPS analysis of MC, MC-OX and MC-800.

Sample name			Name	Position/Binding Energy [eV]			Fwhm			Raw area			% Atomic concentration			Functional group	Short description
MC	**MC-OX**	**MC-OX-800**	C 1s A	284.4	284.4	284.2	0.6	0.5	0.6	85.1	57.8	36.5	19.7	11.1	10.1	C=C	sp^2 carbon
			C 1s B	284.8	284.8	284.6	0.6	0.5	0.6	203.9	95.7	76.3	47.1	18.4	21.1	C–C/C–H	sp^3 carbon/ primary carbon peak
			C 1s C	285.2	285.3	285.0	0.7	0.6	0.7	13.0	94.6	98.6	3.0	18.1	27.3	C–C	"High" carbon
			C 1s D	285.7	285.7	285.5	0.9	0.7	0.8	35.3	91.0	56.9	8.2	17.5	15.7	C–O–C	Ether groups
			C 1s E	286.4	286.3	286.2	1.3	1.2	1.1	43.9	44.40	48.9	10.2	8.5	13.5	C–OH	Hydroxyl groups
			C 1s F	287.6	287.5	287.1	1.4	1.3	0.9	13.7	22.70	8.9	3.2	4.4	2.5	C=O	Carbonyl groups
			C 1s G	289.6	289.1	288.6	1.5	1.4	1.2	4.4	78.0	12.6	1.0	15.0	3.5	COOH	Carboxyl groups
			C 1s H	284.0	284.0	283.8	0.6	0.5	0.8	29.0	30.7	17.4	6.6	5.8	4.7	C–C	"Low" carbon
			C 1s I	283.6	283.6	283.3	0.6	0.5	0.9	4.2	6.4	5.9	1.0	1.2	1.6		
			O 1s A	533.0	532.9	533.1	1.2	1.0	1.0	757.2	466.9	630.0	56.7	36.3	43.8	Si–O–Si	Silicon dioxide
			O 1s B	532.4	532.3	532.5	1.3	1.0	0.9	48.4	179.0	134.2	3.6	13.9	11.3	C=O	Carbonyl groups
			O 1s C	531.7	531.6	531.8	1.3	1.0	1.2	22.4	89.9	73.0	1.7	7.0	5.1	COOH	Carboxyl groups
			O 1s D	533.5	533.4	533.6	1.3	0.9	1.0	407.4	270.7	281.4	30.5	21.0	19.6	Si–OH	Silanol groups
			O 1s E	534.0	533.9	534.1	1.4	1.0	1.1	45.9	185.7	189.5	3.4	14.4	11.2	C–O–C/ C–OH	Ether/hydroxyl groups
			O 1s F	534.7	534.5	534.8	1.8	1.3	1.5	40.4	79.5	99.72	3.0	6.2	6.9	O_2/H_2O	Adsorbed oxygen (water)
			O 1s G	530.8	530.7	530.9	1.2	1.1	1.4	14.3	15.9	30.1	1.1	1.2	2.1	O = ≤> = O	Quinones

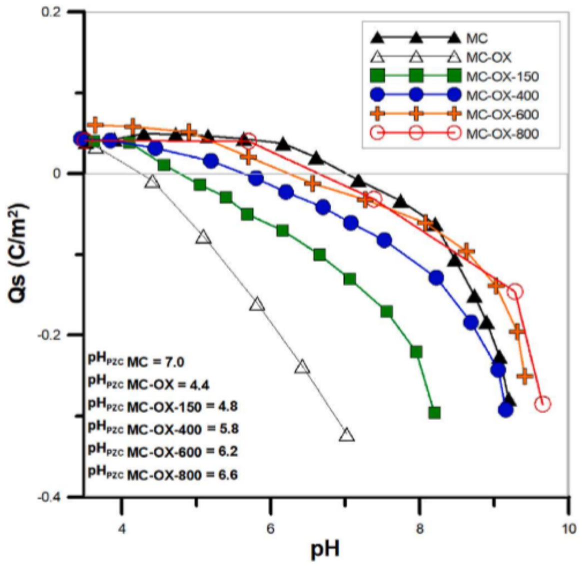

Fig. 4. Surface charge density as a function of pH for MC, MC-OX, MC-OX-150, MC-OX-400, MC-OX-600 and MC-OX-800.

type of oxygen groups present on the surface of carbon samples (oxidation state, type of chemical bonds) in comparison to potentiometric titration.

3.4. *Melting of water confined in carbon samples*

Differential scanning calorimetry (DSC) and dielectric spectroscopy (DS) techniques were used to determine the melting temperatures of water confined in the pores of the MCs. The DSC (Fig. 5 and Fig. S2 in the Supplementary Material) and DS (Fig. 6 and Fig. S3 in the Supplementary Material) studies reveal the existence of shifts in water melting temperatures in the pores of the obtained carbons with differentiated surface properties. The melting temperature data obtained from both techniques are presented in Table 3. As previously mentioned, the porosity characteristics indicate that these carbons, except for the presence of mesopores, also have a certain amount of micropores; therefore, DS and DSC studies provided two main values of water melting temperatures in the pores in two different ranges. The shifts (Δ T) are calculated from the positions of the pore and bulk melting temperatures. The large endothermic peaks at DSC curves at ~ 274 K (Fig. 5 and Fig. S2 in the Supplementary Material) correspond to the melting of the bulk water in which the MCs are suspended, whereas two smaller peaks at 217–226 K and 239–254 K are associated with the melting process of adsorbed water inside the micro- (<2 nm) and mesopores (~ 4 nm) of MCs. The melting temperatures in both types of pores obtained from the DS and DSC measurements are in good agreement [62]. Analysing the data presented in Table 3, we can state that the highest melting temperature is observed for MC carbon. After oxidation connected with the creation of a large amount of oxygen functional groups, a strong decrease in melting temperature is found. However, after the thermal treatment connected with strong changes in acid/base properties (decrease in the number of surface acid groups), an increasing trend in melting temperature changes is observed in comparison to MC-OX. Generally, one can state that the shifts in melting temperatures are caused mainly by changes in the surface chemistry of all modified samples.

To confirm this observed relationship between the surface acidity and melting temperatures in micro- and mesopores, the dependence of the difference between the melting temperatures of water in micro- and mesopores and bulk water, Δ T vs. pH_{PZC}, is presented in Fig. 7. One can easily find a good correlation between these values. In the case of hydrophobic carbons with some surface groups of hydrophilic character (introduced by chemical modification and originated from silica template), different types of interactions are found between the adsorbent and adsorbate. The adsorbate of hydrophobic character interacts strongly with carbon graphene groups; however, the adsorbate of hydrophilic properties has a great affinity to oxygen surface layers. Thus, when the studied modified materials with different acid/base properties are immersed in water, the differentiation of a share of both types of interactions is observed. This results in a decrease in lateral interactions between water molecules in the case of oxidized carbons because of their involvement in interactions with surface groups. In contrast, for

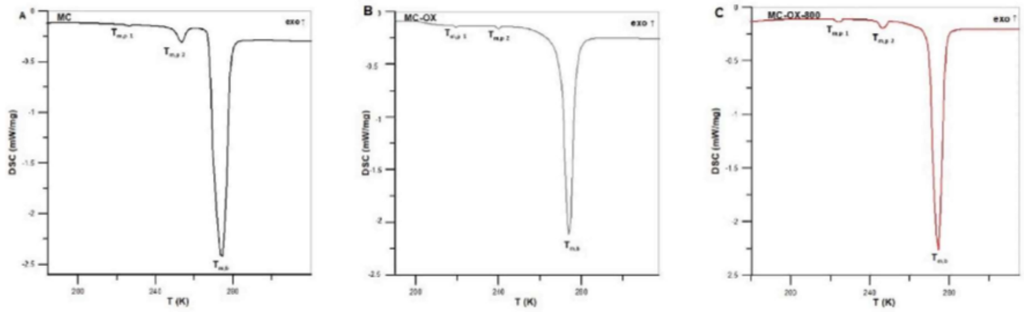

Fig. 5. Dissipation power as a function of temperature mW/mg = f(T) for water confined in MC (A), MC-OX (B) and MC-OX-800 (C).

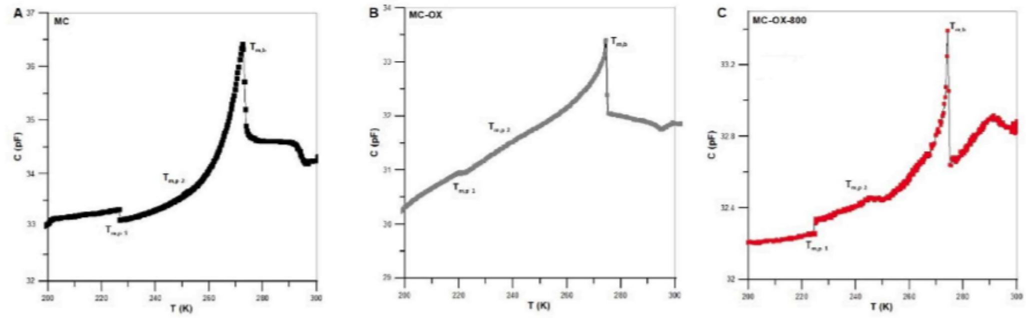

Fig. 6. Capacitance as a function of temperature C = f(T) for water confined in MC (A), MC-OX (B) and MC-OX-800.

Table 3
Melting temperatures of bulk water and water in the pores of carbons MC, MC-OX, MC-OX-150, MC-OX-600 and MC-OX-800; the data received from DSC/DS measurements.

Sample name	$T_{m,\,b}$ [K]	$T_{m,\,p1}$[K]	$T_{m,\,p2}$ [K]	ΔT_1 [K]	ΔT_2 [K]
MC	274_{DSC}/ 273_{DS}	226_{DSC}/ 226_{DS}	254_{DSC}/ 253_{DS}	-48_{DSC}/ -47_{DS}	-20_{DSC}/ -20_{DS}
MC-OX	274_{DSC}/ 274_{DS}	217_{DSC}/ 217_{DS}	239_{DSC}/ 239_{DS}	-57_{DSC}/ -57_{DS}	-35_{DSC}/ -35_{DS}
MC-OX-150	274_{DSC}/ 274_{DS}	217_{DSC}/ 217_{DS}	239_{DSC}/ 239_{DS}	-57_{DSC}/ -57_{DS}	-35_{DSC}/ -35_{DS}
MC-OX-400	274_{DSC}/ 274_{DS}	221_{DSC}/ 221_{DS}	242_{DSC}/ 242_{DS}	-53_{DSC}/ -53_{DS}	-32_{DSC}/ -32_{DS}
MC-OX-600	274_{DSC}/ 274_{DS}	223_{DSC}/ 224_{DS}	243_{DSC}/ 243_{DS}	-51_{DSC}/ -50_{DS}	-31_{DSC}/ -31_{DS}
MC-OX-800	274_{DSC}/ 274_{DS}	225_{DSC}/ 225_{DS}	246_{DSC}/ 247_{DS}	-49_{DSC}/ -48_{DS}	-28_{DSC}/ -29_{DS}

$T_{m,b}$ – melting temperature of bulk water.
$T_{m,p1}$ – pore melting temperature of water confined in micropores.
$T_{m,p2}$ – pore melting temperature of water confined in mesopores.
ΔT_1 – difference between $T_{m,p1}$ and $T_{m,b}$.
ΔT_2 – difference between $T_{m,p2}$ and $T_{m,b}$.
DSC – data obtained from DSC measurements.
DS – data received from DS measurements.

materials with a low number of oxygen groups, lateral interactions between water molecules prevail, and their interactions with carbon graphene layers are weaker. Thus, the observed decrease in water melting temperatures in the pores of oxidized materials may relate to a decrease in these lateral interactions necessary for the formation of a solid phase. However, the increase in interactions between water molecules and carbon surface groups results in a melting temperature increase. Overall, the data obtained from the DSC and DS methods are in good compliance. Taking into account an averaged silica residue amount in all carbon samples in fact we observe the total effect on water melting of all oxygen groups originating from sample carbon and silica parts, as is presented in the dependences Δ T vs. pH_{PZC} (Fig. 7).

In the following section, the electric permittivity (ε') and imaginary electric permittivity (ε") were calculated, and their spectra in the logarithm function of frequency (*f*) were obtained from the electric capacity and temperature data C(T) received in the wide range of frequencies (*f*). The fitting to the Debye model calculated by (ε^D) provided the characteristics of the phase transitions in pores. The relaxation time was determined as the reciprocal of the frequency of the saddle point of ε'or the maximum of the ε" function (Fig. 8A–C). The relaxation spectra of MC, MC-OX-150, and MC-OX-800 are presented in Fig. 9A–C, in which some relaxation times are visible and are connected mainly to the existence of certain types of ice characteristics for bulk and pore confined ice, respectively [32]. As shown in Fig. 9A–C, three different branches of relaxation time can be observed. At the temperature range higher than the bulk melting point, the Maxwell-Wagner interfacial polarization marked by the relaxation time $\tau 2$ is shown. Two branches of relaxation time are observed at the temperature ranges below the pore melting points. The values in the range of 10^{-3} s are typical for the hexagonal form of ice, and they appear below the bulk melting point [32–34, 63–65]. At the temperature range below the melting point in the pore system, an additional branch of relaxation times in the range of 10^{-5} s is observed. This branch represents cubic ice present in pores [32,34, 63–65]. We should mention that recent X-ray and neutron diffraction studies suggested that this cubic ice does not have a structure consistent with either the cubic crystal system or with the hexagonal system [32, 37,53]. It is considered stacking-disordered ice, Isd [65]. This ice is not a simple mixture of the two but a combination of intertwined cubic and hexagonal sequences with a symmetry *P*3m1 (the symmetry of hexagonal ice is *P*63/mmc, of cubic ice is Fd3m) [65]. Recent investigations

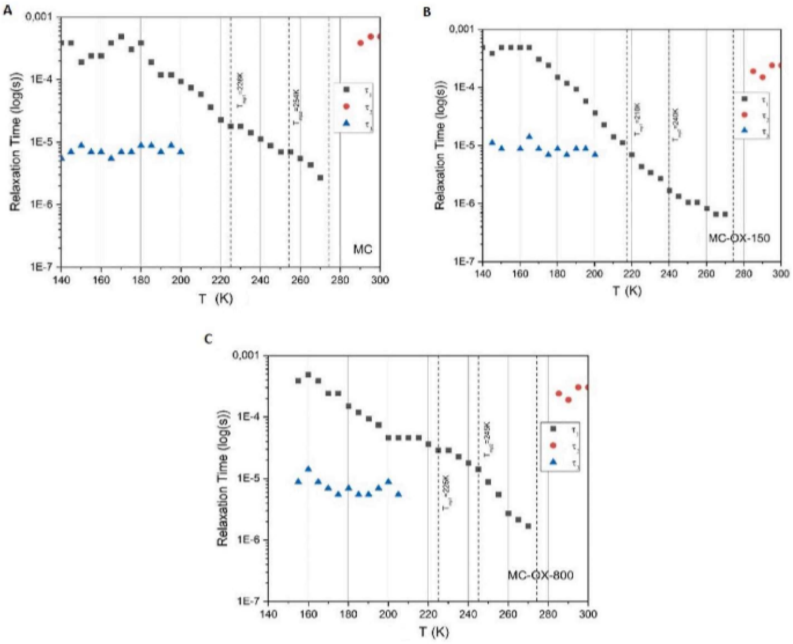

Fig. 9. Dielectric relaxation time τ as a function of temperature logτ = f(T) for water confined in MC (A), MC-OX-150 (B) and MC-OX-800 (C) pores.

surface composition were also confirmed. It was found that during oxidation, the number of carbon decreases, and the number of oxygen increases. After the thermal treatment, the oxygen content decreased. However, the general contribution of Si decreases after modification in nitric acid and backward increases after heating as a result of strong changes in a number of oxygen groups introduced or removed during oxidation and thermal treatments. The silica residues in the obtained carbons contribute to the total number of surface oxygen groups and partially affect the MC's physicochemical properties and may translate into the melting processes of water in the pores.

Differential scanning calorimetry (DSC) and dielectric spectroscopy (DS) techniques were used to investigate the melting processes in the pores of all studied materials. The melting temperatures of water confined in the micro- and mesopores of the MCs were determined. Both experimental techniques indicated shifts in water melting temperatures in the pores of the carbons with differentiated surface properties, and these values were comparable. The highest melting temperature was observed for the MC carbon; after oxidation, it decreased, and with an increase in thermal treatment temperature, its increase was found. Such a trend in melting temperature changes was strictly connected with the changes in the amount of oxygen surface groups originating from carbonaceous and siliceous parts of the obtained materials. This general trend was confirmed by the relationship between pH_{PZC} and ΔT. This observation was explained by the differentiation between water−water and water-carbon interactions in the case of materials with different acid-base properties. Generally, a weakening of lateral interactions between water molecules for the oxidized materials and their increase for more hydrophobic adsorbents were assumed. Based on the relaxation time, three different structural forms of ice confined in the pores of modified carbonaceous materials were found. Further studies are needed to analyse these crystal forms in the pore system of differentiated surface chemistry. Taking into account the porous materials applications in technology, research on phase transitions in a wide temperature range is of great importance.

CRediT authorship contribution statement

A. Bosacka: Writing – original draft, Visualization, Methodology, Investigation, Formal analysis, Data curation, Conceptualization. **M. Zienkiewicz-Strzalka:** Validation, Supervision, Software, Methodology, Investigation, Formal analysis, Data curation, Conceptualization. **A. Derylo-Marczewska:** Writing – review & editing, Writing – original draft, Validation, Supervision, Methodology, Conceptualization. **M. Sliwinska-Bartkowiak:** Writing – review & editing, Validation, Supervision, Methodology, Conceptualization. **A. Sterczynska:** Software, Methodology, Investigation, Formal analysis, Data curation. **D. Sternik:** Software, Investigation, Formal analysis, Data curation. **K. Rotnicki:** Software, Formal analysis, Data curation.

Declaration of competing interest

The authors declare that they have no known competing financial interests or personal relationships that could have appeared to influence the work reported in this paper.

Data availability

Data will be made available on request.

Appendix A. Supplementary data

Supplementary data to this article can be found online at https://doi.org/10.1016/j.micromeso.2023.112477.

References

[1] F. Roquerol, J. Rouquerol, K. Sing, Adsorption by Powders and Solids: Principles, Methodology, and Applications, 1999.
[2] U. Ciesla, F. Schüth, Ordered mesoporous materials, Microporous Mesoporous Mater. (1999), https://doi.org/10.1016/S1387-1811(98)00249-2.
[3] W. Li, D. Zhao, An overview of the synthesis of ordered mesoporous materials, Chem. Commun. 49 (10) (2013) 943–946, https://doi.org/10.1039/c2cc36964h.

[4] M. Marciniak, J. Goscianska, R. Pietrzak, Physicochemical characterization of ordered mesoporous carbons functionalized by wet oxidation, J. Mater. Sci. (2018), https://doi.org/10.1007/s10853-017-1960-2.

[5] W. Libbrecht, et al., Tuning the pore geometry of ordered mesoporous carbons for enhanced adsorption of bisphenol-A, Materials (2015), https://doi.org/10.3390/ma8041652.

[6] B.D. Zdravkov, J.J. Čermák, M. Šefara, J. Janků, Pore classification in the characterization of porous materials: a perspective, Cent. Eur. J. Chem. 5 (2) (2007) 385–395, https://doi.org/10.2478/s11532-007-0017-9.

[7] E.J.W. Visser, G.M. Bögemann, Measurement of porosity in very small samples of plant tissue, Plant Soil (2003), https://doi.org/10.1023/A:1024560322835.

[8] A. Dabrowski, Adsorption - from theory to practice, Adv. Colloid Interface Sci. (2001), https://doi.org/10.1016/S0001-8686(00)00082-8.

[9] S. Wang, Y. Peng, Natural zeolites as effective adsorbents in water and wastewater treatment, Chem. Eng. J. (2010), https://doi.org/10.1016/j.cej.2009.10.029.

[10] J.L. Figueiredo, M.F.R. Pereira, M.M.A. Freitas, J.J.M. Órfão, Modification of the surface chemistry of activated carbons, Carbon N. Y. (1999), https://doi.org/10.1016/S0008-6223(98)00333-9.

[11] A.M. Buckley, M. Greenblatt, The sol-gel preparation of silica gels, J. Chem. Educ. (1994), https://doi.org/10.1021/ed071p599.

[12] J.M. Kim, S. Jun, R. Ryoo, Improvement of hydrothermal stability of mesoporous silica using salts: reinvestigation for time-dependent effects, J. Phys. Chem. B 103 (30) (1999), https://doi.org/10.1021/jp990394k.

[13] S. Jun, et al., Synthesis of new, nanoporous carbon with hexagonally ordered mesostructure [5], J. Am. Chem. Soc. 122 (43) (2000), https://doi.org/10.1021/ja002261e.

[14] A. Galarneau, et al., SBA-15 versus MCM-41: are they the same materials? Stud. Surf. Sci. Catal. 141 (January 2018) (2002) 395–402, https://doi.org/10.1016/s0167-2991(02)80567-5.

[15] B. Szcze, Major Advances in the Development of Ordered Mesoporous Materials, 2020, pp. 7836–7848, https://doi.org/10.1039/d0cc02840a.

[16] A. Sterczyńska, A. Deryło-Marczewska, M. Zienkiewicz-Strzałka, M. Śliwińska-Bartkowiak, K. Domin, Surface properties of Al-functionalized mesoporous MCM-41 and the melting behavior of water in Al-MCM-41 nanopores, Langmuir (2017), https://doi.org/10.1021/acs.langmuir.7b02172.

[17] N.B. Ab Rahman, H. Md Rasid, H. Mohammad Hassan, M. Noor Jalil, Synthesis and characterization of mesoporous silica mcm-41 and sba-15 from power plant bottom ash, Malaysian J. Anal. Sci. 20 (3) (2016) 539–545, https://doi.org/10.17576/mjas-2016-2003-11.

[18] M.M. Titirici, A. Thomas, M. Antonietti, Aminated hydrophilic ordered mesoporous carbons, J. Mater. Chem. 17 (32) (2007) 3412–3418, https://doi.org/10.1039/b703569a.

[19] R. Janus, P. Natkański, M. Wądrzyk, B. Dudek, M. Gajewska, P. Kuśtrowski, Synthesis of pseudo-CMK-3 carbon replicas by precipitation polycondensation of furfuryl alcohol in the pore system of SBA-15 detemplated using KMnO4, Mater. Today Commun. 13 (August) (2017) 6–22, https://doi.org/10.1016/j.mtcomm.2017.07.009.

[20] W. Shou, R. Guo, H. Pan, D.D. Gang, Ordered mesoporous carbon: fabrication, characterization, and application as adsorbents, in: Dekker Encyclopedia of Nanoscience and Nanotechnology, third ed., 2015.

[21] W. Teng, Z. Wu, J. Fan, W.X. Zhang, D. Zhao, Amino-functionalized ordered mesoporous carbon for the separation of toxic microcystin-LR, J. Mater. Chem. (2015), https://doi.org/10.1039/c5ta05320j.

[22] J.C. Ndamanisha, L. ping Guo, Ordered mesoporous carbon for electrochemical sensing: a review, Anal. Chim. Acta 747 (Oct. 17, 2012) 19–28, https://doi.org/10.1016/j.aca.2012.08.032. Elsevier.

[23] A. Eftekhari, Z. Fan, Ordered mesoporous carbon and its applications for electrochemical energy storage and conversion, Mater. Chem. Front. (2017), https://doi.org/10.1039/c6qm00298f.

[24] C. Zheng, et al., Hydrophilic modification of ordered mesoporous carbon supported Fe nanoparticles with enhanced adsorption and heterogeneous Fenton-like oxidation performance, RSC Adv. (2015), https://doi.org/10.1039/c5ra15156b.

[25] S.H. Joo, et al., Ordered mesoporous carbons with controlled particle sizes as catalyst supports for direct methanol fuel cell cathodes, Carbon N. Y. (2008), https://doi.org/10.1016/j.carbon.2008.08.015.

[26] C. He, X. Hu, Functionalized Ordered Mesoporous Carbon for the Adsorption of Reactive Dyes, 2012, https://doi.org/10.1007/s10450-012-9410-6.

[27] R. Burgess, et al., The functionalisation of graphite surfaces with nitric acid: identification of functional groups and their effects on gold deposition, J. Catal. (2015), https://doi.org/10.1016/j.jcat.2014.12.021.

[28] M. Marciniak, J. Goscianska, M. Frankowski, R. Pietrzak, Optimal synthesis of oxidized mesoporous carbons for the adsorption of heavy metal ions, J. Mol. Liq. (2019), https://doi.org/10.1016/j.molliq.2018.12.042.

[29] X. Yang, et al., Surface functional groups of carbon-based adsorbents and their roles in the removal of heavy metals from aqueous solutions: a critical review, Chem. Eng. J. (2019), https://doi.org/10.1016/j.cej.2019.02.119.

[30] A. Deryło-Marczewska, A.W. Marczewski, Effect of Adsorbate Structure on Adsorption from Solutions, 2002, https://doi.org/10.1016/S0169-4332(02)00064-8.

[31] K. Morishige, Influence of pore wall hydrophobicity on freezing and melting of confined water, J. Phys. Chem. C (2018), https://doi.org/10.1021/acs.jpcc.8b00538.

[32] M. Jażdżewska, et al., Structural properties of ice in confinement, J. Mol. Liq. (2019), https://doi.org/10.1016/j.molliq.2019.03.080.

[33] Y. Long, et al., On the molecular origin of high-pressure effects in nanoconfinement: the role of surface chemistry and roughness, J. Chem. Phys. (2013), https://doi.org/10.1063/1.4824125.

[34] K. Domin, et al., Structure of ice in confinement: water in mesoporous carbons, J. Chem. Eng. Data (2016), https://doi.org/10.1021/acs.jced.6b00607.

[35] M. Sliwinska-Bartkowiak, J. Gras, R. Sikorski, R. Radhakrishnan, L. Gelb, K. E. Gubbins, Phase transitions in pores: experimental and simulation studies of melting and freezing, Langmuir 15 (18) (1999) 6060–6069, Jan, https://doi.org/10.1021/la9814642.

[36] K.E. Gubbins, Y. Long, M. Śliwinska-Bartkowiak, Thermodynamics of confined nano-phases, J. Chem. Thermodyn. (2014), https://doi.org/10.1016/j.jct.2014.01.024.

[37] J. Czwartos, M. Sliwinska-Bartkowiak, B. Coasne, K.E. Gubbins, Melting of Mixtures in Silica Nanopores, 2009, https://doi.org/10.1351/PAC-CON-09-01-15.

[38] Y. Liu, et al., Performance of mesoporous silicas (MCM-41 and SBA-15) and carbon (CMK-3) in the removal of gas-phase naphthalene: adsorption capacity, rate and regenerability, RSC Adv. (2016), https://doi.org/10.1039/c5ra27289k.

[39] A. Derylo-Marczewska, B. Buczek, A. Swiatkowski, Effect of oxygen surface groups on adsorption of benzene derivatives from aqueous solutions onto active carbon samples, Appl. Surf. Sci. (2011), https://doi.org/10.1016/j.apsusc.2011.06.036.

[40] D. Zhao, et al., Triblock copolymer syntheses of mesoporous silica with periodic 50 to 300 angstrom pores, Science 80 (1998), https://doi.org/10.1126/science.279.5350.548.

[41] D. Zhao, Q. Huo, J. Feng, B.F. Chmelka, G.D. Stucky, Nonionic triblock and star diblock copolymer and oligomeric sufactant syntheses of highly ordered, hydrothermally stable, mesoporous silica structures, J. Am. Chem. Soc. (1998), https://doi.org/10.1021/ja974025i.

[42] A. Derylo-Marczewska, A. Swiatkowski, H. Grajek, S. Biniak, Z. Witkiewicz, Changes in the surface chemistry and adsorptive properties of active carbon previously oxidized and heat-treated at various temperatures. III. Studies of the adsorption of organic solutes from aqueous solutions, Adsorpt. Sci. Technol. (2005), https://doi.org/10.1260/026361705777642025.

[43] F. Ambroz, T.J. Macdonald, V. Martis, I.P. Parkin, Evaluation of the BET theory for the characterization of meso and microporous MOFs, Small Methods 2 (11) (Nov. 2018), 1800173, https://doi.org/10.1002/smtd.201800173.

[44] E.P. Barrett, L.G. Joyner, P.P. Halenda, The determination of pore volume and area distributions in porous substances. I. Computations from nitrogen isotherms, J. Am. Chem. Soc. (1951), https://doi.org/10.1021/ja01145a126.

[45] G. Kupgan, T.P. Liyana-Arachchi, C.M. Colina, NLDFT pore size distribution in amorphous microporous materials, Langmuir (2017), https://doi.org/10.1021/acs.langmuir.7b01961.

[46] A. Galarneau, F. Villemot, J. Rodriguez, F. Fajula, B. Coasne, Validity of the t-plot method to assess microporosity in hierarchical micro/mesoporous materials, Langmuir (2014), https://doi.org/10.1021/la5026679.

[47] K.S. Xia, Q.M. Gao, Synthesis and hydrogen adsorption properties of templated nanoporous carbons, Advanced Matrial Research (2011). www.scientific.net/AMR.239-242.2116.

[48] F. Villacañas, M.F.R. Pereira, J.J.M. Órfão, J.L. Figueiredo, Tunable Effect of the Calcination of the Silanol Groups of KIT-6 and SBA-15 Mesoporous Materials, Applied Sciences, 2020, https://doi.org/10.1016/j.jcis.2005.06.032.

[49] A.M. Basso, B.P. Nicola, K. Bernardo-Gusmão, S.B.C. Pergher, Adsorption of Simple Aromatic Compounds on Activated Carbons, Applied Sciences, 2017, https://doi.org/10.3390/app10030970.

[50] R. Ojeda-López, I.J. Pérez-Hermosillo, J. Marcos Esparza-Schulz, et al., SBA-15 materials: calcination temperature influence on textural properties and total silanol ratio, Adsorption (2015), https://doi.org/10.1007/s10450-015-9716-2.

[51] C. Pavan, M. Delle Piane, M. Gullo, et al., The puzzling issue of silica toxicity: are silanols bridging the gaps between surface states and pathogenicity? Particle and Fiber Toxicology (2015) https://doi.org/10.1007/s10450-015-9716-2.

[52] S. Güneş, F. Çiğdem Güldür, Synthesis of OMC supported Pt catalysts and the effect of the metal loading technique on their PEM fuel cell performances, Chem. Eng. Commun. (2020), https://doi.org/10.1080/00986445.2019.1635464.

[53] W. Liu, H. Yuan, Y. Ke, Preparation and characterization of ordered mesoporous carbon based on soybean oil, J. Mater. Sci. (2020), https://doi.org/10.1007/s10853-020-04480-2.

[54] W. Libbrecht, K. Vandaele, K. De Buysser, A. Verberckmoes, et al., Tuning the pore geometry of ordered mesoporous carbons for enhanced adsorption of bisphenol-A, Materials (2015), https://doi.org/10.3390/ma8041652.

[55] Z. Uddin Ahmad, Q. Lian, M.E. Zappi, P.R. Buchireddy, D.D. Gang, Adsorptive removal of resorcinol onto surface modified ordered mesoporous carbon: kinetics and equilibrium study, Environ. Prog. Sustain. Energy (2019), https://doi.org/10.1002/ep.13070.

[56] L.A. Perreault, S. Giret, M. Gagnon, J. Florek, D. Lariviere, Functionalization of mesoporous carbon materials for selective separation of lanthanides under acidic conditions, ACS Appl. Mater. Interfaces (2017), https://doi.org/10.1021/acsami.6b16650.

[57] S.H. Yoo, S.Y. Yoon, K.H. Woo, J.S. Kim, S.Y. Cho, S.S. Lee, et al., Psychological effects of a disastrous hydrogen fluoride spillage on the local community, Annals of Occupational and Environmental Medicine (2017), https://doi.org/10.1186/s40557-017-0196-6.

[58] B. Lesiak, et al., C sp 2/sp 3 hybridisations in carbon nanomaterials – XPS and (X) AES study, Appl. Surf. Sci. (2018), https://doi.org/10.1016/j.apsusc.2018.04.269.

[59] M.J. Calaway, M.D. Fries, Adventitious carbon on primary sample containment metal surfaces, 46th Lunar Planet. Sci. Conf. (2015), Available on-line on: 03.02.2023 (https://www.hou.usra.edu/meetings/lpsc2015/pdf/1517.pdf).

[60] A. Barinov, et al., Initial stages of oxidation on graphitic surfaces: photoemission study and density functional theory calculations, J. Phys. Chem. C (2009), https://doi.org/10.1021/jp902051d.
[61] Y.J. Oh, et al., Oxygen functional groups and electrochemical capacitive behavior of incompletely reduced graphene oxides as a thin-film electrode of supercapacitor, Electrochim. Acta (2014), https://doi.org/10.1016/j.electacta.2013.11.040.
[62] M. Jazdzewska, et al., Novel ice structures in carbon nanopores: pressure enhancement effect of confinement, Phys. Chem. Chem. Phys. (2011), https://doi.org/10.1039/c0cp02797a.
[63] M. Sliwinska-Bartkowiak, M. Jazdzewska, M. Domin, K.E. Gubbins, Effect of confinement on melting in nanopores, in: Spin Orbitronics and Topological Properties of Nanostructures - Lecture Notes of the Twelfth International School on Theoretical Physics: Symmetry and Structural Properties of Condensed Matter, 2017.
[64] M. Jażdżewska, et al., Structure of ice confined in carbon and silica nanopores, Bull. Mater. Sci. 42 (4) (2019), https://doi.org/10.1007/s12034-019-1846-9.
[65] T.L. Malkin, B.J. Murray, C.G. Salzmann, V. Molinero, S.J. Pickering, T.F. Whale, Stacking disorder in ice i, Phys. Chem. Chem. Phys. 17 (1) (2015), https://doi.org/10.1039/c4cp02893g.

Supplementary material for the paper

Title: The influence of chemical and thermal modifications of ordered mesoporous carbon on the melting processes of water confined in pores.

Authors: A. Bosacka[1,2*], M. Zienkiewicz-Strzalka[2], A. Derylo-Marczewska[2], M. Sliwinska-Bartkowiak[3], A. Sterczynska[3], D. Sternik[2], K. Rotnicki[3]

[1]Faculty of Production Engineering, University of Life Sciences, Gleboka Street 28, 60-612 Lublin, Poland

[2]Faculty of Chemistry, Institute of Chemical Sciences, Maria Curie-Sklodowska University, Maria Curie-Sklodowska Sq. 3, 20-031 Lublin, Poland

[3]Faculty of Physics, Adam Mickiewicz University, Uniwersytetu Poznanskiego Street 8, 61-614 Poznan, Poland

*Corresponding author: alicja.bosacka@up.lublin.pl

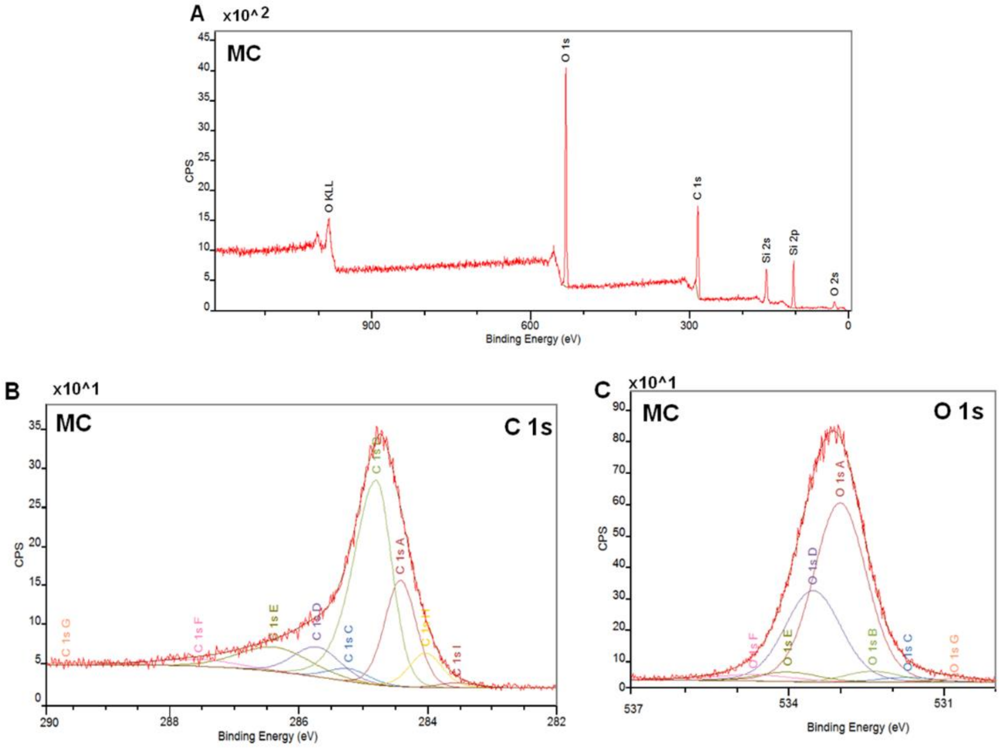

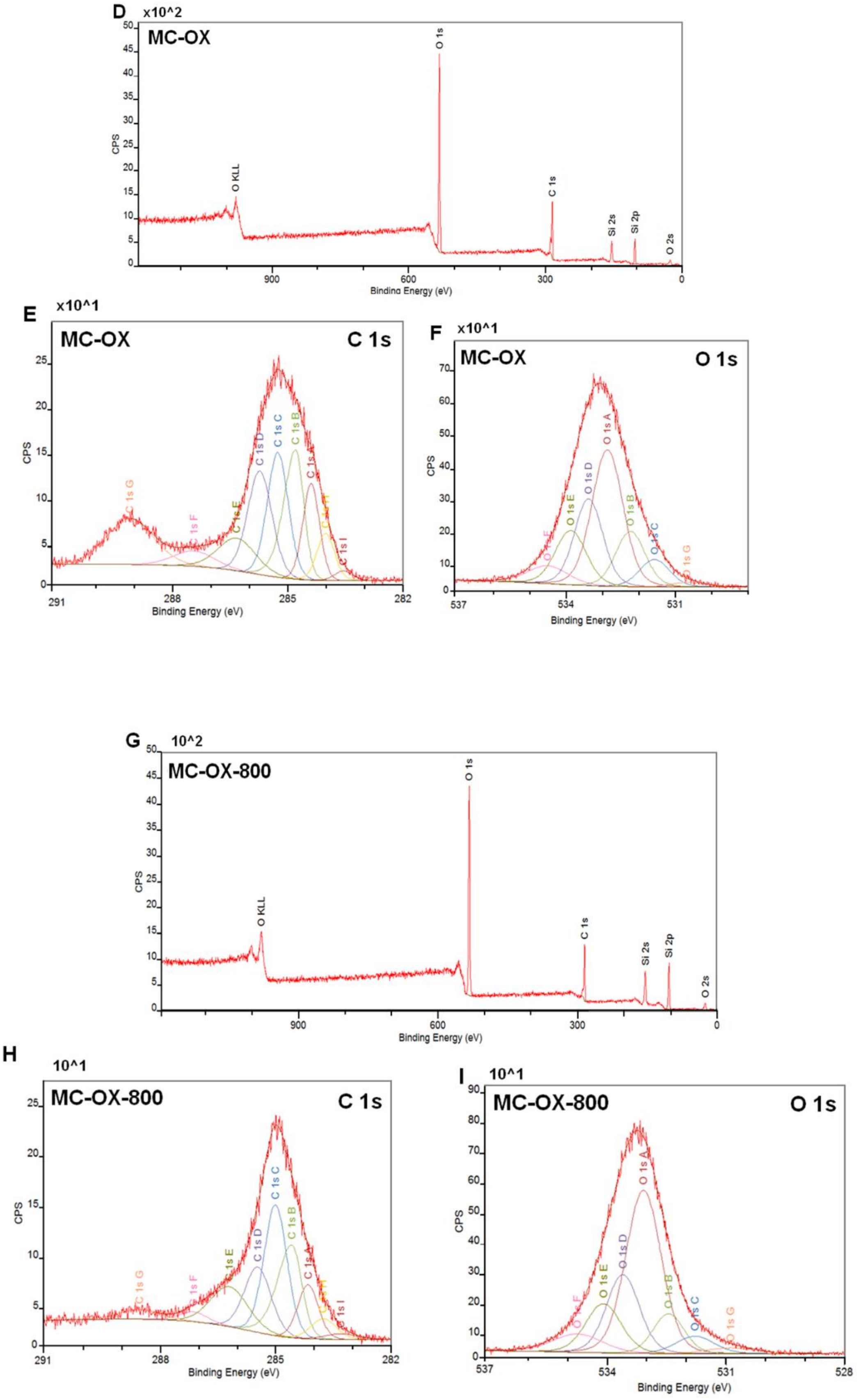

Figure S1. Overview and detailed XPS spectra of (C 1s) and (O 1s) of MC (A-C), MC-OX (D-E) and MC-OX-800 (G-I).

Table S1. Quantitative results of XPS analysis for MC,MC-OX and MC-OX-800.

Sample name			**Name**	**Position/Binding Energy [eV]**			**Raw area**			**% Atomic concentration**			**% Mass concentration**		
MC	**MC-OX**	**MC-OX-800**	C 1s	284.39	284.92	284.94	5173.9	3583.3	2787.9	43.7	38.2	29.2	30.7	27.6	22.6
			O 1s	532.89	532.92	532.94	11323.7	11960.1	12672.8	32.7	43.6	38.2	30.6	41.8	33.2
			Si 2p	103.39	103.42	103.44	2277.3	1391.1	2568.0	23.6	18.2	32.6	38.7	30.6	44.2

Generally, the SBA-15 material usually contains the following silicon-oxygen groups: mainly siloxanes, but also vicinal, germinal, and free silanols. Siloxanes rather fill the interior of the material, while silanols are present on the surface and may react with different chemical species. The formation of silicon-oxygen groups on the surface takes place during the calcination process at a high temperature (~550 °C), in which the ordered mesoporous structure of the SBA-15 is developed. The silanol groups are considered a good medium in surface functionalization that may create strong covalent bonds with various functional groups [49-51]. Based on the obtained results it should be marked the general contribution of Si decreases after modification in nitric acid and backward increases after applying thermal treatment. This is related to the removal of oxygen groups as well as the destruction of carbon at high temperatures (drop in O 1s and C1s). Meanwhile, silica residue forms a hard-to-destroy structure even at very high temperatures that may partially affect the MC's physicochemical properties and translate into the melting processes of water in the pores.

Generally, the SBA-15 template can be removed by different solutions of acids or bases from which the most commonly used are appropriate solutions of NaOH, KOH or HF [52-56]. In this work, ~1 mol/L KOH (v_{C6H5OH}/v_{H2O} = 1:1) was used. The usage of 10-15% HF is more efficient than various KOH solutions, but the negative aspect on human health of working with HF solutions is described in the literature [57].

The detailed XPS analysis reveals the type of present groups on the surface and therefore the sample character. A summary of the data from the particular XPS analysis is given in Table 2. Based on the position/binding energy and full-width-at-half-maximum (FWHM) of the bands (C 1s A-I) and (O 1s A-G) and literature data [58-61], the types of functional groups are assigned. The peak (C 1s A) at ~284 eV corresponds to the existence of carbon in hybridization sp^2 (C=C). The peak (C 1s B), which is shifted by approximately 0.8 eV from (C 1s A) to the higher binding energy, confirms the presence of the "primary" carbon in hybridization sp^3 (C-C or C-H). Peak (C 1s C) (~285 eV) is associated with the occurrence of "high" carbon (C-C), whereas the (C 1s H-I) bands in the positions ~283.6 and 284 eV have "low" carbon (C-C). The (C 1s D-G) peaks at binding energies of ~285.7, 286, 288 and 289 eV testify to the presence of ether (C-O-C), hydroxyl (C-OH), carbonyl (C=O) and carboxyl (COOH) groups, respectively [58-60]. The bands (O 1s A) and (O 1s D) at ~533 and 533.5 eV are from the silica template (Si-O-Si and Si-OH). The (O 1s B) and (O 1s C) peaks moved by approximately 0.5 and 1.0 eV to the lower binding energy from (O 1s A) are associated with the appearance of carbonyl (C=O) and carboxyl groups (COOH), respectively. The (O 1s E) peaks shifted by approximately 0.5 eV to the higher binding energy from (O 1s A) are connected to the presence of ether (C-O-C) or hydroxyl groups (C-OH). The (O 1s F) peak indicates the presence of adsorbed water. The (O 1s G) peak (~530 eV) came from quinones (O≤=>=O) [61].

Most carbon on the surface of the MC occurs in hybridization sp^3 ("primary" carbon) (47.1%). In addition, the surface of MC is rich in carbon in the hybridization sp^2 (19.7%), carbon occurring in the connection with hydroxyl groups (10.2%) and carbon from ether groups (8.2%). The "high" and "low" carbon and carbonyl and carboxyl groups account for less than 10% of the MC surface. Taking oxygen into account, the MC sample contains the greatest number of oxygen from the Si-O-Si (56.7%) and Si-OH groups (30.5%). Carbonyl, carboxyl, hydroxyl and ether groups with atomic concentrations less than 4% are also present on the MC surface.

Nitrogen (V) acid oxidation causes a change in the proportions of functional groups on the surface. For the MC-OX sample, the amount of sp^2, "high" and carbon from the ether group is approximately equal to 18%. Hydroxyl and carboxyl groups are also present on this sample surface with atomic concentrations of 8.5 and 15.0%, respectively. On the MC-OX carbon surface, a significant increase in the amount of oxygen from ether and hydroxyl groups is noticed (from 3.4 to 14.4%) in comparison to the MC. Taking into consideration the MC-OX-800 carbon, an increase in the number of "high" carbons (27.3%) (MC – 3.0%, MC-OX – 18.1%) and carbon from hydroxyl groups (13.5%) (MC – 10.2%, MC-OX – 8.5%) and a reduction in the amount of oxygen from the ether and hydroxyl groups (from 14.4 after oxidation to 11.2% after thermal treatment) are reported. In general, XPS analysis confirms the efficiency of the chemical and thermal modification.

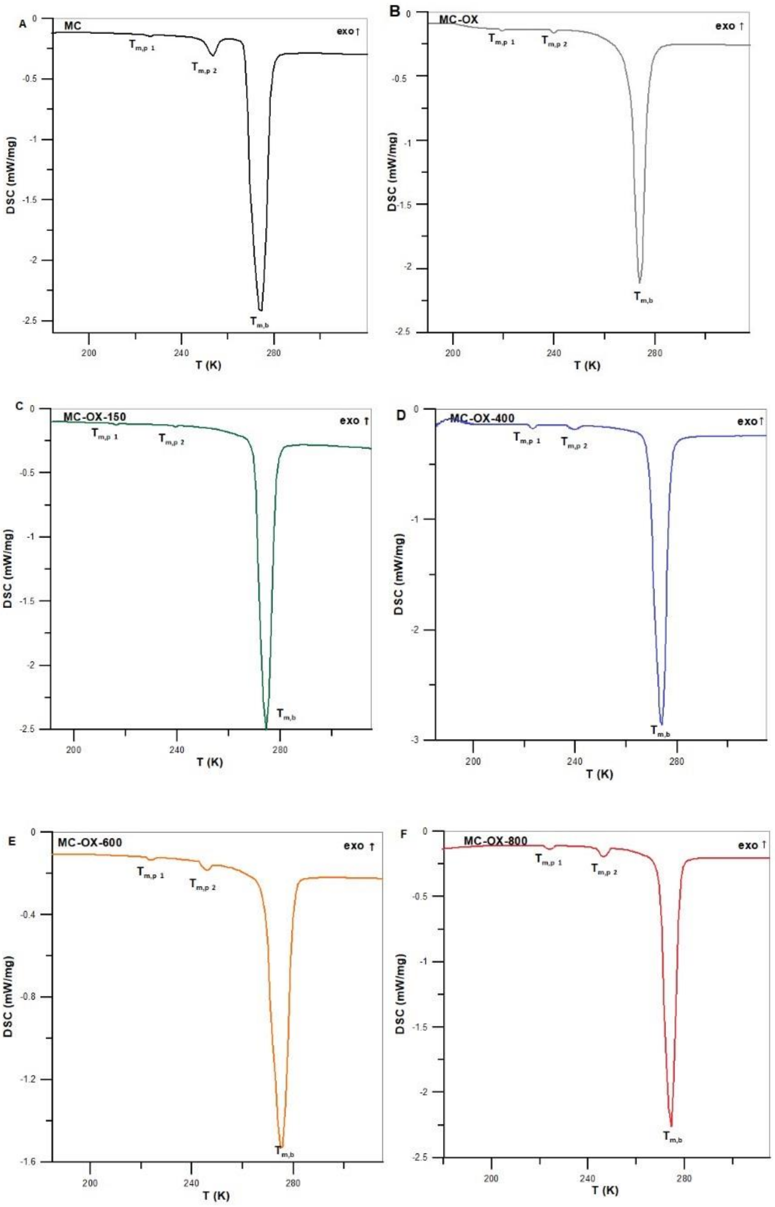

Figure S2. Dissipation power as a function of temperature mW/mg=f(T) for water confined in MC (A), MC-OX (B), MC-OX-150 (C), MC-OX-400 (D), MC-OX-600 (E) and MC-OX-800 (F).

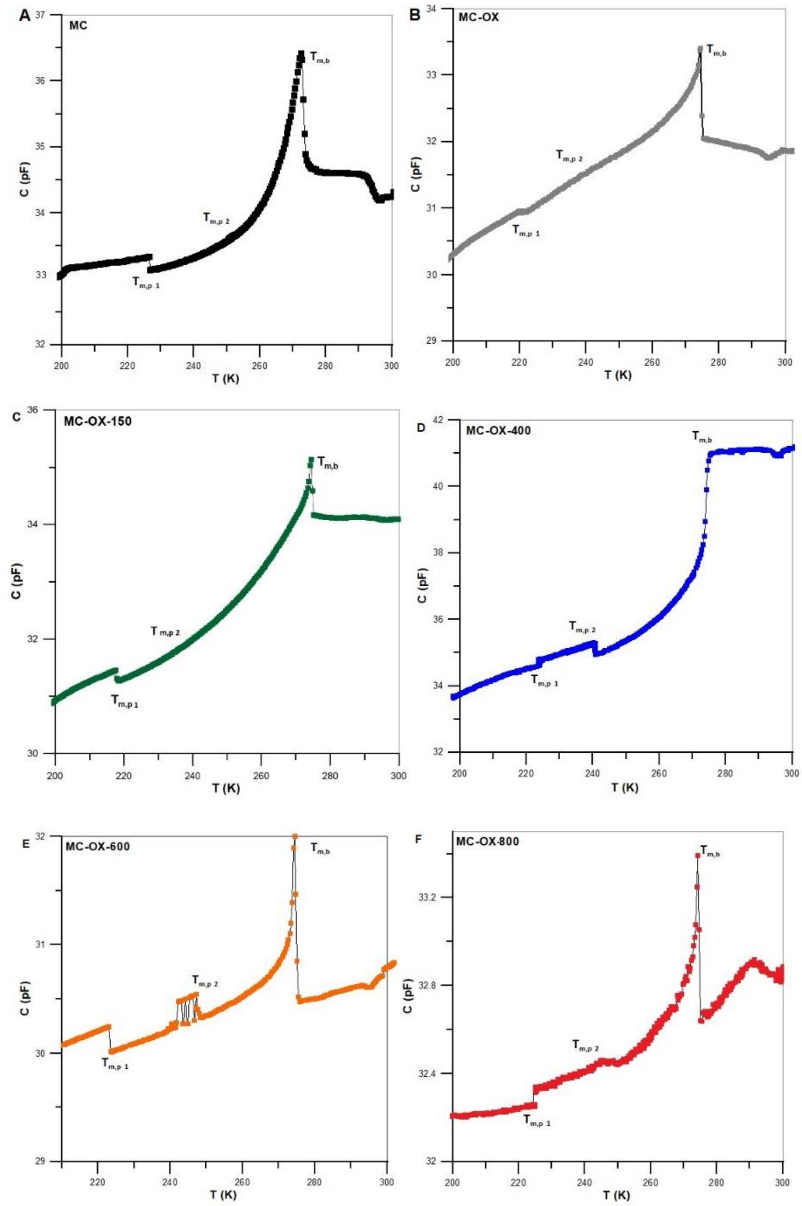

Figure S3. Capacitance as a function of temperature C=f(T) for water confined in MC (A), MC-OX (B), MC-OX-150 (C), MC-OX-400 (D), MC-OX-600 (E) and MC-OX-800 (F).

UMCS

UNIWERSYTET MARII CURIE-SKŁODOWSKIEJ W LUBLINIE
Wydział Chemii, Instytut Nauk Chemicznych

Lublin, 3.02.2023

mgr Alicja Bosacka
Katedra Chemii Fizycznej
Instytut Nauk Chemicznych
Wydział Chemii
Uniwersytet Marii Curie-Skłodowskiej w Lublinie
alicja.bosacka@mail.umcs.pl

Oświadczenie o współautorstwie

Niniejszym oświadczam, że w pracy:

Alicja Bosacka, Małgorzata Zienkiewicz-Strzałka, Anna Deryło-Marczewska, Małgorzata Wasilewska, Beata Podkościelna, Physicochemical and Adsorption Characteristics of Divinylbenzene-co-Triethoxyvinylsilane Microspheres as Materials for the Removal of Organic Compounds, Molecules 2021, 26(8), 2396 wraz z materiałem dodatkowym, mój udział polegał na współtworzeniu wspólnej koncepcji, wykonaniu badań laboratoryjnych, pisaniu oryginalnego manuskryptu, przygotowaniu odpowiedzi do recenzentów.

Alicja Bosacka, Małgorzata Zienkiewicz-Strzałka, Anna Deryło-Marczewska, Agnieszka Chrzanowska, Małgorzata Wasilewska, Dariusz Sternik, Physicochemical, structural, and adsorption properties of chemically and thermally modified activated carbons, Colloids and Surfaces A: Physicochemical and Engineering Aspects 2022, 647, 12913 wraz z materiałem dodatkowym, mój udział polegał na współtworzeniu wspólnej koncepcji pracy, modyfikacji chemicznej i termicznej materiałów, wykonaniu badań laboratoryjnych, pisaniu oryginalnego manuskryptu, przygotowaniu odpowiedzi do recenzentów, pełnieniu roli autora korespondencyjnego.

Mariia Galaburda, Alicja Bosacka, Dariusz Sternik, Viktor Bogatyrov, Olena Oranska, Volodymyr Gun'ko, Anna Deryło-Marczewska, Development, Synthesis and Characterization of Tannin/Bentonite-Derived Biochar for Water and Wastewater Treatment from Methylene Blue, Water 2022, 14(15), 2407, mój udział polegał na wykonaniu badań laboratoryjnych oraz przygotowywaniu ich interpretacji, pisaniu oryginalnego manuskryptu, przygotowaniu odpowiedzi do recenzentów, pełnieniu roli autora korespondencyjnego.

Mariia Galaburda, Alicja Bosacka, Dariusz Sternik, Olena Oranska, Mykola Borysenko Volodymyr Gun'ko, Anna Derylo-Marczewska, Physicochemical and Sorption Characteristics of Carbon Biochars Based on Lignin and Industrial Waste Magnetic Iron Dust, Water 2023, 15(1), 189 polegał na wykonaniu badań laboratoryjnych i analizie wyników oraz ich interpretacji, pisaniu oryginalnego manuskryptu, przygotowaniu odpowiedzi do recenzentów, pełnieniu roli autora korespondencyjnego.

Alicja Bosacka, Małgorzata Zienkiewicz-Strzalka, Anna Derylo-Marczewska, Małgorzata Śliwińska-Bartkowiak, Angelina Sterczyńska, Dariusz Sternik, Konrad Rotnicki The influence of chemical and thermal modifications of ordered mesoporous carbon on the melting processes of water confined in pores, Microporous and Mesoporous Materials 2023, Available online 3 February 2023, 112477, mój udział polegał na pisaniu i edycji oryginalnego manuskryptu, wykonaniu badań laboratoryjnych oraz analizie wyników i ich interpretacji, przygotowaniu odpowiedzi do recenzentów, pełnieniu roli autora korespondencyjnego.

Alicja Bosacka

UMCS

UNIWERSYTET MARII CURIE-SKŁODOWSKIEJ W LUBLINIE
Wydział Chemii, Instytut Nauk Chemicznych

Lublin, 3.02.2023

Prof. dr hab. Anna Deryło-Marczewska
Katedra Chemii Fizycznej
Instytut Nauk Chemicznych
Wydział Chemii
Uniwersytet Marii Curie-Skłodowskiej w Lublinie
anna.derylo-marczewska@mail.umcs.pl

Oświadczenie o współautorstwie

Niniejszym oświadczam, że w pracy:

Alicja Bosacka, Małgorzata Zienkiewicz-Strzałka, Anna Deryło-Marczewska, Małgorzata Wasilewska, Beata Podkościelna, *Physicochemical and Adsorption Characteristics of Divinylbenzene-co-Triethoxyvinylsilane Microspheres as Materials for the Removal of Organic Compounds*, Molecules 2021, 26(8), 2396, mój udział polegał na współtworzeniu wspólnej koncepcji, udziale w pisaniu oryginalnego maszynopisu, korekcie tekstu po recenzjach oraz udziale w przygotowaniu odpowiedzi do recenzentów, pełnieniu funkcji autora korespondencyjnego.

Alicja Bosacka, Małgorzata Zienkiewicz-Strzałka, Anna Deryło-Marczewska, Agnieszka Chrzanowska, Małgorzata Wasilewska, Dariusz Sternik, *Physicochemical, structural, and adsorption properties of chemically and thermally modified activated carbons*, Colloids and Surfaces A: Physicochemical and Engineering Aspects 2022, 647, 12913 wraz z materiałem dodatkowym, mój udział polegał na współtworzeniu wspólnej koncepcji, udziale w pisaniu oryginalnego maszynopisu, korekcie tekstu po recenzjach oraz udziale w przygotowaniu odpowiedzi do recenzentów, pełnieniu roli autora korespondencyjnego.

Mariia Galaburda, Alicja Bosacka, Dariusz Sternik, Viktor Bogatyrov, Olena Oranska, Volodymyr Gun'ko, Anna Deryło-Marczewska, *Development, Synthesis and Characterization of Tannin/Bentonite-Derived Biochar for Water and Wastewater Treatment from Methylene Blue*, Water 2022, 14(15), 2407, mój udział polegał na czytaniu i poprawianiu manuskryptu, udziale w korekcie tekstu po recenzjach oraz w odpowiedziach dla recenzentów.

Mariia Galaburda, Alicja Bosacka, Dariusz Sternik, Olena Oranska, Mykola Borysenko Volodymyr Gun'ko, Anna Derylo-Marczewska, *Physicochemical and Sorption Characteristics of Carbon Biochars Based on Lignin and Industrial Waste Magnetic Iron Dust*, Water 2023, 15(1), 189, mój udział polegał na czytaniu i poprawianiu manuskryptu, udziale w korekcie tekstu po recenzjach oraz w odpowiedziach dla recenzentów oraz pełnieniu funkcji autora korespondencyjnego.

Alicja Bosacka, Małgorzata Zienkiewicz-Strzałka, Anna Deryło-Marczewska, Małgorzata Śliwińska-Bartkowiak, Angelina Sterczyńska, Dariusz Sternik, Konrad Rotnicki, *The influence of chemical and thermal modifications of ordered mesoporous carbon on the melting processes of water confined in pores, Microporous and Mesoporous Materials* 2023, https://doi.org/10.1016/j.micromeso.2023.112477, mój udział polegał na współtworzeniu wspólnej koncepcji, udziale w pisaniu oryginalnego maszynopisu, korekcie tekstu po recenzjach oraz udziale w przygotowaniu odpowiedzi do recenzentów, pełnieniu roli autora korespondencyjnego.

A. Deryło-Marczewska
....
Podpis

UMCS

UNIWERSYTET MARII CURIE-SKŁODOWSKIEJ W LUBLINIE
Wydział Chemii, Instytut Nauk Chemicznych

Lublin, 3.02.2023

Dr Małgorzata Zienkiewicz-Strzałka
Katedra Chemii Fizycznej
Instytut Nauk Chemicznych
Wydział Chemii
Uniwersytet Marii Curie-Skłodowskiej w Lublinie
malgorzata.zienkiewcz.strzalka@mail.umcs.pl

Oświadczenie o współautorstwie

Niniejszym oświadczam, że w pracy:

Alicja Bosacka, Małgorzata Zienkiewicz-Strzałka, Anna Deryło-Marczewska, Małgorzata Wasilewska, Beata Podkościelna, *Physicochemical and Adsorption Characteristics of Divinylbenzene-co-Triethoxyvinylsilane Microspheres as Materials for the Removal of Organic Compounds*, Molecules 2021, 26(8), 2396, mój udział polegał na współtworzeniu wspólnej koncepcji, udziale w pisaniu oryginalnego manuskryptu, udziale w opracowywaniu grafiki, analizie materiałów oraz interpretacji wyników techniką SAXS, udziale w pomiarach metodą niskotemperaturowej adsorpcji-desorpcji azotu oraz interpretacji tych wyników, korekcie tekstu po recenzjach oraz udziale w przygotowaniu odpowiedzi do recenzentów.

Alicja Bosacka, Małgorzata Zienkiewicz-Strzałka, Anna Deryło-Marczewska, Agnieszka Chrzanowska, Małgorzata Wasilewska, Dariusz Sternik, *Physicochemical, structural, and adsorption properties of chemically and thermally modified activated carbons*, Colloids and Surfaces A: Physicochemical and Engineering Aspects 2022, 647, 12913 wraz z materiałem dodatkowym, mój udział polegał na współtworzeniu wspólnej koncepcji, udziale w pisaniu oryginalnego manuskryptu, udziale w opracowywaniu grafiki, analizie materiałów oraz interpretacji wyników techniką SAXS oraz SEM, korekcie tekstu po recenzjach, oraz udziale w przygotowaniu odpowiedzi do recenzentów.

Alicja Bosacka, Małgorzata Zienkiewicz-Strzałka, Anna Deryło-Marczewska, Małgorzata Śliwińska-Bartkowiak, Angelina Sterczyńska, Dariusz Sternik, Konrad Rotnicki, *The influence of chemical and thermal modifications of ordered mesoporous carbon on the melting processes of water confined in pores, Microporous and Mesoporous Materials* 2023, https://doi.org/10.1016/j.micromeso.2023.112477, mój udział polegał na współtworzeniu wspólnej koncepcji, udziale w pisaniu oryginalnego manuskryptu, udziale w przygotowywaniu abstraktu, analizie materiałów oraz interpretacji wyników techniką SAXS, TEM oraz SEM, korekcie tekstu po recenzjach, oraz udziale w przygotowaniu odpowiedzi do recenzentów.

Małgorzata Zienkiewicz-Strzałka
Podpis

UMCS

UNIWERSYTET MARII CURIE-SKŁODOWSKIEJ W LUBLINIE
Wydział Chemii, Instytut Nauk Chemicznych

Lublin, 3.02.2023

Dr Agnieszka Chrzanowska
Katedra Chemii Fizycznej
Instytut Nauk Chemicznych
Wydział Chemii
Uniwersytet Marii Curie-Skłodowskiej w Lublinie
agnieszka.chrzanowska@mail.umcs.pl

Oświadczenie o współautorstwie

Niniejszym oświadczam, że w pracy:

Alicja Bosacka, Małgorzata Zienkiewicz-Strzałka, Anna Deryło-Marczewska, Agnieszka Chrzanowska, Małgorzata Wasilewska, Dariusz Sternik, *Physicochemical, structural, and adsorption properties of chemically and thermally modified activated carbons*, Colloids and Surfaces A: Physicochemical and Engineering Aspects 2022, 647, 12913 wraz z materiałem dodatkowym, mój udział polegał na udziale w pisaniu manuskryptu, pomiarach próbek metodą niskotemperaturowej adsorpcji-desorpcji azotu oraz udziale w opisie i interpretacji wyników, udziale w opracowywaniu danych z analizy termicznej oraz udziale w przygotowaniu odpowiedzi do recenzentów.

Agnieszka Chrzanowska
Podpis

UMCS
UNIWERSYTET MARII CURIE-SKŁODOWSKIEJ W LUBLINIE
Wydział Chemii, Instytut Nauk Chemicznych

Lublin, 3.02.2023

Dr Małgorzata Wasilewska
Katedra Chemii Fizycznej
Instytut Nauk Chemicznych
Wydział Chemii
Uniwersytet Marii Curie-Skłodowskiej w Lublinie
malgorzata.wasilewska@mail.umcs.pl

Oświadczenie o współautorstwie

Niniejszym oświadczam, że w pracy:

Alicja Bosacka, Małgorzata Zienkiewicz-Strzałka, Anna Deryło-Marczewska, Małgorzata Wasilewska, Beata Podkościelna, *Physicochemical and Adsorption Characteristics of Divinylbenzene-co-Triethoxyvinylsilane Microspheres as Materials for the Removal of Organic Compounds*, Molecules 2021, 26(8), 2396, mój udział polegał na współtworzeniu wspólnej koncepcji, udziale w pisaniu manuskryptu, ustaleniu początkowych warunków pomiarowych układów adsorpcyjnych, udziale w pomiarach kinetycznych, opracowaniu danych adsorpcyjnych (kinetyka adsorpcji) oraz interpretacji tych wyników, udział w pomiarach i interpretacji wyników z niskotemperaturowej adsorpcji-desorpcji azotu oraz udziale w przygotowywaniu odpowiedzi do recenzentów.

Alicja Bosacka, Małgorzata Zienkiewicz-Strzałka, Anna Deryło-Marczewska, Agnieszka Chrzanowska, Małgorzata Wasilewska, Dariusz Sternik, *Physicochemical, structural, and adsorption properties of chemically and thermally modified activated carbons*, Colloids and Surfaces A: Physicochemical and Engineering Aspects 2022, 647, 12913 wraz z materiałem dodatkowym, mój udział polegał na udziale w powstaniu wspólnej koncepcji, pisaniu manuskryptu, wstępnym przygotowaniu materiału wyjściowego (przesianie, odmycie), przygotowaniu danych dla materiału niemodyfikowanego (niskotemperaturowa adsorpcja-desorpcja azotu, XPS), opracowaniu danych adsorpcyjnych (kinetyka i równowaga adsorpcji) oraz interpretacji tych wyników, udziale w przygotowaniu odpowiedzi do recenzentów.

Małgorzata Waniewska

Podpis

UMCS

UNIWERSYTET MARII CURIE-SKŁODOWSKIEJ W LUBLINIE
Wydział Chemii, Instytut Nauk Chemicznych

Lublin, 3.02.2023

Dr Dariusz Sternik
Katedra Chemii Fizycznej
Instytut Nauk Chemicznych
Wydział Chemii
Uniwersytet Marii Curie-Skłodowskiej w Lublinie
dariusz.sternik@mail.umcs.pl

Oświadczenie o współautorstwie

Niniejszym oświadczam, że w pracy:

Alicja Bosacka, Małgorzata Zienkiewicz-Strzałka, Anna Deryło-Marczewska, Agnieszka Chrzanowska, Małgorzata Wasilewska, Dariusz Sternik, *Physicochemical, structural, and adsorption properties of chemically and thermally modified activated carbons*, Colloids and Surfaces A: Physicochemical and Engineering Aspects 2022, 647, 12913 wraz z materiałem dodatkowym, mój udział polegał na udziale w pomiarach próbek z wykorzystaniem analizy termicznej sprzężonej z MS (przygotowaniu sprzętu do pomiaru, kalibracji, oraz ustaleniu wstępnych warunków pomiarów) oraz pomocy merytorycznej w interpretacji danych.

Mariia Galaburda, Alicja Bosacka, Dariusz Sternik, Viktor Bogatyrov, Olena Oranska, Volodymyr Gun'ko, Anna Deryło-Marczewska, *Development, Synthesis and Characterization of Tannin/Bentonite-Derived Biochar for Water and Wastewater Treatment from Methylene Blue*, Water 2022, 14(15), 2407, mój udział polegał na pisaniu oryginalnego maszynopisu, udziale w badaniach adsorpcyjnych, analizie danych oraz interpretacji wyników, udział w korekcie tekstu po recenzjach oraz udział w przygotowaniu odpowiedzi do recenzentów.

Mariia Galaburda, Alicja Bosacka, Dariusz Sternik, Olena Oranska, Mykola Borysenko Volodymyr Gun'ko, Anna Derylo-Marczewska, *Physicochemical and Sorption Characteristics of Carbon Biochars Based on Lignin and Industrial Waste Magnetic Iron Dust*, Water 2023, 15(1), 189, mój udział polegał na pisaniu oryginalnego maszynopisu, udziale w badaniach adsorpcyjnych i termicznych, analizie danych oraz interpretacji wyników, udział w korekcie tekstu po recenzjach oraz udział w przygotowaniu odpowiedzi do recenzentów.

Alicja Bosacka, Małgorzata Zienkiewicz-Strzałka, Anna Deryło-Marczewska, Małgorzata Śliwińska-Bartkowiak, Angelina Sterczyńska, Dariusz Sternik, Konrad Rotnicki, *The influence of chemical and thermal modifications of ordered mesoporous carbon on the melting processes of water confined in pores, Microporous and Mesoporous Materials* 2023, https://doi.org/10.1016/j.micromeso.2023.112477, mój udział polegał na udziale w pomiarach próbek techniką DSC (kalibracja sprzętu przed pomiarem, dobór odpowiednich warunków prowadzenia pomiarów), oraz wsparciu merytorycznym podczas interpretacji wyników.

Sternik

Podpis

UMCS

UNIWERSYTET MARII CURIE-SKŁODOWSKIEJ W LUBLINIE
Wydział Chemii, Instytut Nauk Chemicznych

Lublin, 3.02.2023

Dr hab. Beata Podkościelna
Katedra Chemii Polimerów
Instytut Nauk Chemicznych
Wydział Chemii
Uniwersytet Marii Curie-Skłodowskiej w Lublinie
beata.podkoscielna@mail.umcs.pl

Oświadczenie o współautorstwie

Niniejszym oświadczam, że w pracy:

Alicja Bosacka, Małgorzata Zienkiewicz-Strzałka, Anna Deryło-Marczewska, Małgorzata Wasilewska, Beata Podkościelna, *Physicochemical and Adsorption Characteristics of Divinylbenzene-co-Triethoxyvinylsilane Microspheres as Materials for the Removal of Organic Compounds*, Molecules 2021, 26(8), 2396, mój udział polegał na współtworzeniu wspólnej koncepcji, syntezie materiałów, korekcie manuskryptu, udziale w przygotowaniu odpowiedzi do recenzentów.

Beata Podkościelna
....
Podpis

UMCS

UNIWERSYTET MARII CURIE-SKŁODOWSKIEJ W LUBLINIE
Wydział Chemii, Instytut Nauk Chemicznych

Lublin, 3.02.2023

Dr Mariia Galaburda
Katedra Chemii Fizycznej
Instytut Nauk Chemicznych
Wydział Chemii
Uniwersytet Marii Curie-Skłodowskiej w Lublinie
mariia.galaburda@gmail.com

Oświadczenie o współautorstwie

Niniejszym oświadczam, że w pracy:

Mariia Galaburda, Alicja Bosacka, Dariusz Sternik, Viktor Bogatyrov, Olena Oranska, Volodymyr Gun'ko, Anna Deryło-Marczewska, *Development, Synthesis and Characterization of Tannin/Bentonite-Derived Biochar for Water and Wastewater Treatment from Methylene Blue*, Water 2022, 14(15), 2407, mój udział polegał na współtworzeniu wspólnej koncepcji, udziale w pisaniu oryginalnego manuskryptu, wykonywaniu badań laboratoryjnych, analizie materiałów oraz interpretacji wyników, korekcie tekstu po recenzjach, oraz udziale w przygotowaniu odpowiedzi do recenzentów.

Mariia Galaburda, Alicja Bosacka, Dariusz Sternik, Olena Oranska, Mykola Borysenko Volodymyr Gun'ko, Anna Derylo-Marczewska, *Physicochemical and Sorption Characteristics of Carbon Biochars Based on Lignin and Industrial Waste Magnetic Iron Dust*, Water 2023, 15(1), 189, mój udział polegał na współtworzeniu wspólnej koncepcji, udziale w pisaniu oryginalnego manuskryptu, wykonywaniu badań laboratoryjnych, analizie materiałów oraz interpretacji wyników, korekcie tekstu po recenzjach, oraz udziale w przygotowaniu odpowiedzi do recenzentów.

Galaburda M.

....
Podpis

UMCS

UNIWERSYTET MARII CURIE-SKŁODOWSKIEJ W LUBLINIE
Wydział Chemii, Instytut Nauk Chemicznych

Lublin, 3.02.2023

Dr Viktor Bogatyrov
Chuiko Institute of Surface Chemistry
National Academy of Science of Ukraine
General Naumov Str. 17
Kyiv 03164
Ukraine

Oświadczenie o współautorstwie

Niniejszym oświadczam, że w pracy:

Mariia Galaburda, Alicja Bosacka, Dariusz Sternik, Viktor Bogatyrov, Olena Oranska, Volodymyr Gun'ko, Anna Deryło-Marczewska, *Development, Synthesis and Characterization of Tannin/Bentonite-Derived Biochar for Water and Wastewater Treatment from Methylene Blue*, Water 2022, 14(15), 2407, mój udział polegał na współudziale w opracowywaniu koncepcji pracy oraz wsparciu merytorycznym.

Pan Dr. V. Bogatyrov nie żyje
Podpisuje się w imieniu Dr.
Galaburda M.
Podpis

Maria Curie-Skłodowska Sq. 2, 20-031 Lublin, www.umcs.lublin.pl
tel: +48 81 537 57 16, fax: +48 81 533 33 48
e-mail: chemia@poczta.umcs.lublin.pl

UMCS

UNIWERSYTET MARII CURIE-SKŁODOWSKIEJ W LUBLINIE
Wydział Chemii, Instytut Nauk Chemicznych

Lublin, 3.02.2023

Dr Mykola Borysenko
Katedra Chemii Fizycznej
Instytut Nauk Chemicznych
Wydział Chemii
Uniwersytet Marii Curie-Skłodowskiej w Lublinie

Oświadczenie o współautorstwie

Niniejszym oświadczam, że w pracy:

Mariia Galaburda, Alicja Bosacka, Dariusz Sternik, Olena Oranska, Mykola Borysenko Volodymyr Gun'ko, Anna Derylo-Marczewska, *Physicochemical and Sorption Characteristics of Carbon Biochars Based on Lignin and Industrial Waste Magnetic Iron Dust*, Water 2023, 15(1), 189, mój udział polegał na współtworzeniu koncepcji oraz udziale w syntezie materiałów.

W imieniu Dr. M. Borysenko

Galaburda Mariia ....

Podpis

UMCS

UNIWERSYTET MARII CURIE-SKŁODOWSKIEJ W LUBLINIE
Wydział Chemii, Instytut Nauk Chemicznych

Lublin, 3.02.2023

Dr Olena Oranska
Chuiko Institute of Surface Chemistry
National Academy of Science of Ukraine
General Naumov Str. 17
Kyiv 03164
Ukraine

Oświadczenie o współautorstwie

Niniejszym oświadczam, że w pracy:

Mariia Galaburda, Alicja Bosacka, Dariusz Sternik, Viktor Bogatyrov, Olena Oranska, Volodymyr Gun'ko, Anna Deryło-Marczewska, *Development, Synthesis and Characterization of Tannin/Bentonite-Derived Biochar for Water and Wastewater Treatment from Methylene Blue*, Water 2022, 14(15), 2407, mój udział polegał na analizie materiałów techniką XRD oraz interpretacji tych wyników.

Mariia Galaburda, Alicja Bosacka, Dariusz Sternik, Olena Oranska, Mykola Borysenko Volodymyr Gun'ko, Anna Derylo-Marczewska, *Physicochemical and Sorption Characteristics of Carbon Biochars Based on Lignin and Industrial Waste Magnetic Iron Dust*, Water 2023, 15(1), 189, mój udział polegał na analizie materiałów techniką XRD oraz interpretacji tych wyników.

W imieniu Dr. O. Oranska
Galaburda

Maria Curie-Skłodowska Sq. 2, 20-031 Lublin, www.umcs.lublin.pl
tel: +48 81 537 57 16, fax: +48 81 533 33 48
e-mail: chemia@poczta.umcs.lublin.pl

UMCS

UNIWERSYTET MARII CURIE-SKŁODOWSKIEJ W LUBLINIE
Wydział Chemii, Instytut Nauk Chemicznych

Lublin, 3.02.2023

Prof. Volodymyr Gun'ko
Chuiko Institute of Surface Chemistry
National Academy of Science of Ukraine
General Naumov Str. 17
Kyiv 03164
Ukraine

Oświadczenie o współautorstwie

Niniejszym oświadczam, że w pracy:

Mariia Galaburda, Alicja Bosacka, Dariusz Sternik, Viktor Bogatyrov, Olena Oranska, Volodymyr Gun'ko, Anna Deryło-Marczewska, *Development, Synthesis and Characterization of Tannin/Bentonite-Derived Biochar for Water and Wastewater Treatment from Methylene Blue*, Water 2022, 14(15), 2407, mój udział polegał na czytaniu i poprawianiu manuskryptu, udziale w korekcie tekstu po recenzjach oraz udziale w odpowiedziach na sugestie recenzentów.

Mariia Galaburda, Alicja Bosacka, Dariusz Sternik, Olena Oranska, Mykola Borysenko Volodymyr Gun'ko, Anna Derylo-Marczewska, *Physicochemical and Sorption Characteristics of Carbon Biochars Based on Lignin and Industrial Waste Magnetic Iron Dust*, Water 2023, 15(1), 189, mój udział polegał na czytaniu i poprawianiu manuskryptu, udziale w korekcie tekstu po recenzjach oraz udziale w odpowiedziach na sugestie recenzentów, wsparciu merytorycznym podczas pisania manuskryptu.

W imieniu Prof. V. Gun'ko
Galaburda M.

....
Podpis

Maria Curie-Skłodowska Sq. 2, 20-031 Lublin, www.umcs.lublin.pl
tel: +48 81 537 57 16, fax: +48 81 533 33 48
e-mail: chemia@poczta.umcs.lublin.pl

UMCS

UNIWERSYTET MARII CURIE-SKŁODOWSKIEJ W LUBLINIE
Wydział Chemii, Instytut Nauk Chemicznych

Poznań, 3.02.2023

Prof. dr hab. Małgorzata Śliwińska-Bartkowiak
Zakład Fizyki Dielektryków
Wydział Fizyki
Uniwersytet im. Adama Mickiewicza w Poznaniu
msb@amu.edu.pl

Oświadczenie o współautorstwie

Niniejszym oświadczam, że w pracy:

Alicja Bosacka, Małgorzata Zienkiewicz-Strzałka, Anna Deryło-Marczewska, Małgorzata Śliwińska-Bartkowiak, Angelina Sterczyńska, Dariusz Sternik, Konrad Rotnicki, *The influence of chemical and thermal modifications of ordered mesoporous carbon on the melting processes of water confined in pores, Microporous and Mesoporous Materials* 2023, https://doi.org/10.1016/j.micromeso.2023.112477, mój udział polegał na współtworzeniu wspólnej koncepcji, udziale w pisaniu oryginalnego maszynopisu, wsparciu merytorycznym podczas realizacji badań, analizy otrzymanych wyników i przygotowywaniu manuskryptu.

Małgorzata Śliwińska-Bartkowiak
Podpis

UNIWERSYTET MARII CURIE-SKŁODOWSKIEJ W LUBLINIE
Wydział Chemii, Instytut Nauk Chemicznych

Poznań, 3.02.2023

Dr Angelina-Sterczyńska
Zakład Fizyki Dielektryków
Wydział Fizyki
Uniwersytet im. Adama Mickiewicza w Poznaniu
aster3@amu.edu.pl

Oświadczenie o współautorstwie

Niniejszym oświadczam, że w pracy:

Alicja Bosacka, Małgorzata Zienkiewicz-Strzałka, Anna Deryło-Marczewska, Małgorzata Śliwińska-Bartkowiak, Angelina Sterczyńska, Dariusz Sternik, Konrad Rotnicki, *The influence of chemical and thermal modifications of ordered mesoporous carbon on the melting processes of water confined in pores, Microporous and Mesoporous Materials* 2023, https://doi.org/10.1016/j.micromeso.2023.112477, mój udział polegał na obsłudze sprzętu oraz udziale w pomiarach metodą spektroskopii dielektrycznej (DS), wstępnej analizie danych eksperymentalnych, wsparciu merytorycznym podczas opracowywania wyników badań oraz przygotowywaniu manuskryptu.

w.z. M. Śliwińska-Bartkowiak
Podpis

UMCS
UNIWERSYTET MARII CURIE-SKŁODOWSKIEJ W LUBLINIE
Wydział Chemii, Instytut Nauk Chemicznych

Poznań, 3.02.2023

Mgr Konrad Rotnicki
Zakład Fizyki Dielektryków
Wydział Fizyki
Uniwersytet im. Adama Mickiewicza w Poznaniu
info3@amu.edu

Oświadczenie o współautorstwie

Niniejszym oświadczam, że w pracy:

Alicja Bosacka, Małgorzata Zienkiewicz-Strzałka, Anna Deryło-Marczewska, Małgorzata Śliwińska-Bartkowiak, Angelina Sterczyńska, Dariusz Sternik, Konrad Rotnicki, *The influence of chemical and thermal modifications of ordered mesoporous carbon on the melting processes of water confined in pores, Microporous and Mesoporous Materials* 2023, https://doi.org/10.1016/j.micromeso.2023.112477, mój udział polegał na udziale w pomiarach próbek techniką DSC (kalibracja sprzętu przed pomiarem, dobór odpowiednich warunków prowadzenia pomiarów), oraz wsparciu merytorycznym podczas interpretacji wyników.

Konrad Rotnicki
Podpis

9. Bibliografia

Artykuły z cyklu publikacji:

[D1] Alicja Bosacka, Małgorzata Zienkiewicz-Strzałka, Anna Deryło-Marczewska. Małgorzata Wasilewska, Beata Podkościelna, Physicochemical and Adsorption Characteristics of Divinylbenzene-co-Triethoxyvinylsilane Microspheres as Materials for the Removal of Organic Compounds, *Molecules 2021*, 26(8), 2396, https://doi.org/10.3390/molecules26082396
[S1] Materiał uzupełniający do pracy [D1]
[D2] Alicja Bosacka, Małgorzata Zienkiewicz-Strzałka, Anna Deryło-Marczewska, Agnieszka Chrzanowska, Małgorzata Wasilewska, Dariusz Sternik, Physicochemical, structural, and adsorption properties of chemically and thermally modified activated carbons, *Colloids and Surfaces A: Physicochemical and Engineering Aspects* 2022, 647, 129130, https://doi.org/10.1016/j.colsurfa.2022.129130
[S2] Materiał uzupełniający do pracy [D2]
[D3] Mariia Galaburda, Alicja Bosacka, Dariusz Sternik, Viktor Bogatyrov, Olena Oranska, Volodymyr Gun'ko, Anna Deryło-Marczewska, Development, Synthesis and Characterization of Tannin/Bentonite-Derived Biochar for Water and Wastewater Treatment from Methylene Blue, *Water 2022*, 14(15), 2407, https://doi.org/10.3390/w14152407
[D4] Mariia Galaburda, Alicja Bosacka, Dariusz Sternik, Olena Oranska, Mykola Borysenko Volodymyr Gun'ko, Anna Derylo-Marczewska, Physicochemical and Sorption Characteristics of Carbon Biochars Based on Lignin and Industrial Waste Magnetic Iron Dust, *Water 2023*, 15(1), 189, https://doi.org/10.3390/w15010189
[D5] Alicja Bosacka, Małgorzata Zienkiewicz-Strzałka, Anna Derylo-Marczewska, Małgorzata Śliwińska-Bartkowiak, Angelina Sterczyńska, Dariusz Sternik, Konrad Rotnicki, The influence of chemical and thermal modifications of ordered mesoporous carbon on the melting processes of water confined in pores, *Microporous and Mesoporous Materials 2023*, 351, 112477, https://doi.org/10.1016/j.micromeso.2023.112477

Bibliografia:

[1] S. Srivastava, E.N. Zare, P. Makvandi, X. Zheng, S. Iftekhar, A. Wu, V.V.T. Padil, B. Mokhtari, R.S. Varma, F.R. Tay, et al.,. Cytotoxic aquatic pollutants and their removal by nanocomposite-based sorbents, *Chemosphere* 2020, 258, 127324
[2] F. Younas, A. Mustafa, Z.U.R. Faroogi, X. Wang, S. Younas, W. Mohy-Ud-Din, M.A. Hameed, M.M. Abrar, A.A. Maitlo, S. Noree, et al. Current and Emerging Adsorbent Technologies for Wastewater Treatment: Trends, Limitations, and Environmental Implications, *Water* 2021, 13, 215
[3] S. Liu, R. Wang, Modified activated carbon with an enhanced nitrobenzene adsorption capacity, *J. Porous Mater.* 18 (1) (2011) 99–106, https://doi.org/10.1007/s10934-010-9360-x

[4] Z. Kecira, O. Benturki, A. Benturki, M. Daoud, P. Girods, High adsorption capacity of nitrobenzene from aqueous solution using activated carbons prepared from vegetable waste, *Environ. Prog. Sustain Energy* 39 (6) (2020), https://doi.org/ 10.1002/ep.13463

[5] Y. Sheth, S. Dharaskar, M. Khalid, S. Sonawane, An environment friendly approach for heavy metal removal from industrial wastewater using chitosan based biosorbent: A review, *Sustain. Energy Technol. Assess.* 2021, 43, 100951

[6] A. Derylo-Marczewska, A. Swiatkowski, H. Grajek, S. Biniak, Z. Witkiewicz, Changes in the surface chemistry and adsorptive properties of active carbon previously oxidized and heat-treated at various temperatures. III. Studies of the adsorption of organic solutes from aqueous solutions, *Adsorpt. Sci. Technol.* 23 (10) (2005) 867–879, https://doi.org/10.1260/026361705777642025

[7] M. Franz, H.A. Arafat, N.G. Pinto, Effect of chemical surface heterogeneity on the adsorption mechanism of dissolved aromatics on activated carbon, *Carbon* 38 (13) (2000) 1807–1819, https://doi.org/10.1016/S0008-6223(00)00012-9

[8] C. Moreno-Castilla, Adsorption of organic molecules from aqueous solutions on carbon materials, *Carbon* 42 (1) (2004) 83–94, https://doi.org/10.1016/j. carbon.2003.09.022.

[9] H. Naganawa, H. Matsuura, Y. Ogihara, S. Kusakabe, T. Sekine, Solvent extraction of p-nitrophenol into cyclohexane with phosphines and their derivatives, *Anal. Sci.* 6 (2) (1990) 287–289, https://doi.org/10.2116/analsci.6.287

[10] M. Wang, L. Gengxian, X. Chunlong, J. Xudong, W. Rubing, L. Qingquan, C. Xiyun, Facile preparation of cyclodextrin polymer materials with rigid spherical structure and flexible network for sorption of organic contaminants in water, *Chem. Eng. J.* 2021, 411, 128489

[11] M. Jażdżewska, K. Domin, M. Śliwińska-Bartkowiak, A.I. Beskrovnyi, D.N. Chudoba, T.V. Nagorna, K. Ludzik, D.S. Neov, Structural properties of ice in confinement, *J. Mol. Liq.*, 2019, doi: 10.1016/j.molliq.2019.03.080

[12] K. E. Gubbins, Y. Long, M. Śliwinska-Bartkowiak, Thermodynamics of confined nano-phases, *J. Chem. Thermodyn.* 2014, doi: 10.1016/j.jct.2014.01.024

[13] K. Domin, K.Yu. Chan, H. Yung, K. Gubbins, M. Jarek, A. Sterczyńska, M. Śliwinska-Bartkowiak, "Structure of ice in confinement: Water in mesoporous carbons," *J. Chem. Eng. Data* 2016, doi: 10.1021/acs.jced.6b00607

[14] M. Sliwinska-Bartkowiak, J. Gras, R. Sikorski, R. Radhakrishnan, L. Gelb, and K. E. Gubbins, "Phase transitions in pores: experimental and simulation studies of melting and freezing," *Langmuir* 15, 18, 6060–6069, doi: 10.1021/la9814642

[15] N.P. Nayak, Characterization of blast furnace flue dust- an assessment for its utilization, *Mater. Today. Proc.* 2022, 50, 2078–2083

[16] Z. Yi, C. Li, L. Zhang, S. Zhang, W. Gao, S. Wang, B. Li, X. Hu, Impacts of CO_2 atmosphere on property of the biochar from pyrolysis of ligni, *J. Anal. Appl. Pyrolysis* 2022, 167, 105689

[17] D. Zhao *et al.*, Triblock copolymer syntheses of mesoporous silica with

periodic 50 to 300 angstrom pores, *Science 80*, doi: 10.1126/science.279.5350.548

[18] D. Zhao, Q. Huo, J. Feng, B. F. Chmelka, and G. D. Stucky, Nonionic triblock and star diblock copolymer and oligomeric sufactant syntheses of highly ordered, hydrothermally stable, mesoporous silica structures, *J. Am. Chem. Soc.* 1998, doi: 10.1021/ja974025i

[19] F. Ambroz, T.J. Macdonald, V. Martis, I.P. Parkin, Evaluation of the BET Theory for the Characterization of Meso and Microporous MOFs, *Small Methods* 2018, 2, 1800173

[20] G. Kupgan, T.P. Liyana-Arachchi, C.M. Colina, NLDFT pore size distribution in amorphous microporous materials, *Langmuir* 33 (42) (2017) 11138–11145

[21] E.P. Barrett, L.G. Joyner, P.P. Halenda, The determination of pore volume and area distributions in porous substances. I. Computations from nitrogen isotherms, *J. Am. Chem. Soc.* 73 (1) (1951) 373–380, https://doi.org/10.1021/ja01145a126 (Published online)

[22] M. Blachnio, A. Derylo-Marczewska, B. Charmas, M. Zienkiewicz-Strzalka, V. Bogatyrov, M. Galaburda, Activated Carbon from Agricultural Wastes for Adsorption of Organic Pollutants, *Molecules* **2020**, *25*, 5105. https://doi.org/10.3390/molecules25215105

[23] M. Zienkiewcz-Strzalka, S. Pikus, The study of palladium ions incorporation into the mesoporous ordered silicates, *Appl. Surf. Sci.* 2012, 261, 616–622

[24] A.M. Motoc, S. Valsan, A.E. Slobozeanu, M. Corban, D. Valerini, M. Prakasam, M. Botan, V. Dragut, B.S. Vasile, A.V. Surdu, R. Trusca, M.L. Grilli, R.R. Piticescu, Design, Fabrication, and Characterization of New Materials Based on Zirconia Doped with Mixed Rare Earth Oxides: Review and First Experimental Results, *Metals* 2020, 10, 746. https://doi.org/10.3390/met10060746

[25] A. Sterczyńska, A. Deryło-Marczewska, M. Zienkiewicz-Strzałka, M. Śliwińska-Bartkowiak, K. Domin, Surface Properties of Al-Functionalized Mesoporous MCM-41 and the Melting Behavior of Water in Al-MCM-41 Nanopores, *Langmuir* 2017 33 (42), 11203-11216 DOI: 10.1021/acs.langmuir.7b02172

[26] W. Urbaniak-Domagala, The Use of the Spectrometric Technique FTIR-ATR to Examine the Polymers Surface. Advanced Aspects of Spectroscopy. IntechOpen, Rijeka, 2012, (Ed. Muhammad Akhyar Farrukh), Chapter https://doi.org/10.5772/48143

[27]A. Deryło-Marczewska, K. Skrzypczyńska, K. Kuśmierek, A. Swiatkowski,M. Zienkiewicz-Strzalka, The adsorptive properties of oxidized activated carbons and their applications as carbon paste electrode modifiers, *Adsorption* 25, 357–366 (2019). https://doi.org/10.1007/s10450-019-00016-6

[28] O. Oranska, Yu. I. Gornikov, X-ray diffraction and thermal studies on some food and cosmetic bentonite clays, *Himia, Fizika ta Tehnologia Poverhni* 2019

[29] D. Sternik, M. Wiśniewska, P. Nowicki, Thermal degradation of peat-based activated carbons covered with mixed adsorption layers of PAA polymer

---

and SDS surfactant, *Thermochimica Acta*, 2019, 676, 71-83, ,https://doi.org/10.1016/j.tca.2019.03.039

[30] A.W. Marczewski, A. Deryło-Marczewska, A. Słota, Adsorption and desorption kinetics of benzene derivatives on mesoporous carbons, *Adsorption* 2013, 19, 391–406, https://doi.org/10.1007/s10450-012-9462-7

[31] A. Deryło-Marczewska, A.W. Marczewski, A general model for adsorption of organic solutes from dilute aqueous solutions on heterogeneous solids : Application for prediction of multisolute adsorption, *Langmuir* 1997, 13, 1245-1250

[32] M. Wasilewska, A.W. Marczewski, A. Deryło-Marczewska, D. Sternik, Nitrophenols removal from aqueous solutions by activated carbon – temperature effect of adsorption kinetics and equilibrium, *Journal of Environmental Chemical Engineering*, 2021, 9, 4, 105459, https://doi.org/10.1016/j.jece.2021.105459

[33] A. Derylo-Marczewska, D. Sternik, A. Swiatkowski, K. Kusmierek, W. Gac, B. Buczek, Activated Carbon from Agricultural Wastes for Adsorption of Organic Pollutants. *Termochemica Acta* 2022, 215, 179299, https://doi.org/10.3390/molecules25215105

[34] A. Derylo-Marczewska, A.W. Marczewski, Effect of adsorbate structure on adsorption from solutions, *Appl. Surf. Sci.* 2002, 196, 264–272

[35] M. Blachnio, A. Derylo-Marczewska, A.W. Marczewski, M. Seczkowska, Phenoxyacid pesticide adsorption on activated carbon–equilibrium and kinetics, *Chemosphere* 2019, 214, 349–360

[36] J.N. Hamid, D. Fariba, M.A. Reza, Effects of triethoxy and triphenylvinylsilanes on the porous structure of cross-linkedpoly(methylmethacrylate) beads, *e-Polymers* 2008, 1–11

[37] H. Naghash, A. Karimzadeh, A. Momeni, A. Massah, H. Alian, Preparation and Properties of Triethoxyvinylsilane-Modified Styrene-Butyl Acrylate Emulsion Copolymers, *Turk. J. Chem.* 2007, 31, 257–269

[38] B. Podkoscielna, M. Sobiesiak, Synthesis and characterization of organic–inorganic hybrid microspheres, *Adsorption* 2016, 22, 631–638

[39] K. Fila, Y. Bolbukh, M. Goliszek, B. Podkoscielna, M. Gargol, B. Gawdzik, Synthesis and characterization of mesoporous polymeric microspheres of methacrylic derivatives of aromatic thiols, *Adsorption* 2019, 35, 429–442

[40] M. Goliszek, B. Poskoscielna, K. Fila, A.V. Riazanova, S. Aminzadeh, O. Sevastyanova, V.M. Gunko, Synthesis and structure characterization of polymeric nanoporous microspheres with lignin, *Cellulose* 2018, 25, 5843–5862

[41] B. Podkoscielna, K. Fila, M. Gil, J. Nowak, J. Synthesis and characterization of new hybrid microspheres with amide functionalization, *Adsorpt. Sci. Technol.* 2017, 35, 422–431

[42] D. Li, Y. Wu, L. Feng, L. Zhang, Surface properties of SAC and its adsorption mechanisms for phenol and nitrobenzene, *Bioresour. Technol.* 2012, 113, 121–126, https://doi.org/10.1016/j.biortech.2012.02.130

[43] S. Biniak, G. Szymanski, J. Siedlewski, A. Swiatkowski, The characterization of activated carbons with oxygen and nitrogen surface groups, *Carbon* 1997, 35, 1799-1810, https://doi.org/10.1016/S0008-6223(97)00096-1

[44] A.W. Marczewski, Kinetics and equilibrium of adsorption of organic solutes on mesoporous carbons, *Appl. Surf. Sci.* 2007, 253, https://doi.org/10.1016/j. apsusc.2006.12.037

[45] A. Derylo-Marczewska, K. Miroslaw, A.W. Marczewski, D. Sternik, Studies of adsorption equilibria and kinetics of o-, m-, p-nitro- and chlorophenols on microporous carbons from aqueous solutions, *Adsorption* 2010, 16, 359–375, https://doi.org/10.1007/s10450-010-9247-9

[46] V.M. Gun'ko, S.V. Mikhalovsky, Evaluation of slitlike porosity of carbon adsorbents, *Carbon* 2004, 42, 843–849

[47] A.C. Ferrari, J. Robertson, Raman spectroscopy of amorphous, nanostructured, diamond-like carbon, and nanodiamond, *Philos.Trans. R. Soc. Lond. A Math. Phys. Eng. Sci.* 2004, 362, 2477–2512

[48] M. Mierzwa-Hersztek, K. Gondek, A. Nawrocka, H. Pienkowska, T. Bajda, J. Stanek-Tarkowska, M. Szostek, FT-IR analysis and the content of phenolic compounds in exogenous organic matter produced from plant biomass, *J. Elem.* 2019, 24, 879–896

[49] A. Tomczyk, Z. Sokolowska, P. Boguta, Biochar physicochemical properties: Pyrolysis temperature and feedstock in defects, *Rev. Environ. Sci. Bio/Technol.* 2020, 19, 191–215

[50] S. Zhao, T. Na, X. Wang, Effect of temperature on the structural and physicochemical properties of biochar with apple treebranches as feed stock material, *Energies* 2017, 10, 1293

[51] Y. Zhu, B. Yi, Q.Yuan, Y. Wu, M. Wang, S. Yan, Removal of methylene blue from aqueous solution by cattlemanure-derived low temperature biochar, *Molecules* 2018, 8, 19917–19929

[52] A.V. Neimark, P.I. Ravikovitch, A. Vishnyakov, Adsorption hysteresis in nanopores, *Phys. Rev. E* 2000, 62, R1493

[53] P.I. Ravikovitch, S.Ó. Domhnaill, A.V. Neimark, Capillary hysteresis in nanopores: Theoretical and experimental studies of nitrogen adsorption on MCM-41, *Langmuir* 1995, 11, 4765–4772

[54] B. Das, S. Prakash, P.S.R. Reddy, S.K. Biswal, B.K. Mohapatra, V.N. Misra, Effective utilization of blast furnace flue dust of integrated steel plants, *Eur. J. Miner. Process. Environ. Prot.* 2002, 2, 61–68

[55] Y. Wang, D.C. Alsmeyer, R.L. McCreery, Raman spectroscopy of carbon materials: Structural basis of observed spectra, *Chem. Mater.* 1990, 2, 557–563

[56] E. Gul, K.A.B. Alrawashdeh, O. Masek, O. Skreiberg, A. Corona, M. Zampilli, L. Wang, P. Samaras, Q. Yang, H. Zhou, H. et al., Production and use of biochar from lignin and lignin-rich residues (such as digestate and olive stones) for wastewater treatment, *J. Anal. Appl. Pyrolysis* 2021, 158, 105263

[57] J. Kujawska, H. Wasag, Biochar: A low-cost adsorbent of Methylene Blue from aqueous solutions, *J. Phys. Conf. Ser.* 2021, 1736, 012002

[58] N. Kannan, M. Sundaram, Kinetics and mechanism of removal of methylene blue by adsorption on various carbons – A comparative study, *Dyes Pigments* 2001, 51, 25–40

[59] S. Azizian, S. Eris, L.D. Wilson, Re-evaluation of the century-old Langmuir isotherm for modeling adsorption phenomena in solution, *Chem. Phys.* 2018, 513, 99–104